

# Exploiting phonon and Coulomb interactions in semiconductor quantum dots

## Inauguraldissertation

zur  
Erlangung der Würde eines Doktors der Philosophie  
vorgelegt der  
Philosophisch-Naturwissenschaftlichen Fakultät  
der Universität Basel

von

**Clemens Spinnler**

2023

The original document is saved on the University of Basel document server  
<http://edoc.unibas.ch>



This work is licensed under a Creative Commons Attribution-NonCommercial-NoDerivatives 4.0 International License.

The complete text may be reviewed here:

<http://creativecommons.org/licenses/by-nc-nd/4.0/>



Genehmigt von der Philosophisch-Naturwissenschaftlichen Fakultät auf Antrag von

Erstbetreuer: Prof. Dr. Richard J. Warburton

Zweitbetreuer: Prof. Dr. Martino Poggio

Externer Experte: PD Dr. Julien Claudon

Basel, den 20. Juni 2023

Prof. Dr. Marcel Mayor  
Dekan

## Abstract

Semiconductor quantum dots have been investigated in many different aspects, from fundamental semiconductor physics to advanced quantum technologies. After many years of growth improvements, the quantum dot emits single photons of high purity and high indistinguishability. The noise in the semiconductor is reduced to a level where it starts to be negligible (compared to other measurement errors). Recently advances also have been made in controlling a single electron(hole)-spin confined by the quantum dot. This makes the quantum dot a perfect candidate for any application involving single photons and also a spin, for example, boson sampling and cluster state generation, respectively.

The quantum dot can also be used to study its coupling to additional degrees of freedom, such as for example the surrounding nuclear spins or coupling to an optical cavity. In this thesis, two individual studies are presented. First, the interaction of the quantum dot with the mechanical surrounding, i.e. phonons, and second, radiative Auger processes due to Coulomb interactions.

The quantum dot naturally couples to its mechanical environment by deformation-potential coupling. The interaction is exploited by engineering the mechanical environment (density of states) by patterning a mechanical resonator (mechanical cavity). The main focus lies on reaching gigahertz mechanical frequencies, the so-called resolved-sideband regime. However, this is not trivial for two reasons. First, fabricating a mechanical resonator at such high frequencies is challenging due the small size. Second, measuring such a fast modulation of the quantum dot requires a special measurement parameter set. Nonetheless, the coupling to mechanical resonators from a few megahertz to more than a gigahertz mechanical frequency is shown. Furthermore, an in-depth study of the exciton-phonon interaction is presented which includes a semi-classical master-equation description of the coupled system as well as the observation of acoustic sideband emission. The current limit, for applications such as optomechanical cooling, is the coupling rate between the two systems. However, such experiments are within reach with a five- to ten-fold increase in the coupling rate.

The quantum dot itself presents a coupled system if charged with an additional electron (or hole). Then, in the excited state, three carriers (one hole and two electrons) are tightly confined inside the dot which are coupled to each other via Coulomb interactions. The effect of this coupling is studied which gives rise to the so-called radiative Auger process. During the decay of the trion, one of the carriers (the Auger electron) is promoted to a higher energy state inside the quantum dot (p- and d-shell) and the emitted photon is correspondingly red-shifted. In more detail, it is found that the wavefunction of the trion is composed of admixtures of higher shells and the emitted photon projects the state of the remaining electron to the corresponding shell. Furthermore, the radiative Auger process gives rise to an optical transition which can be addressed with a laser. In a two-laser experiment ( $\Lambda$ -configuration), the radiative Auger transition is optically driven. This leads to a coherent superposition of the auger carrier being in two different quantum dot shells. These measurements pose a first step toward coherent control of the orbital state of the Auger carrier.



---

# Contents

---

<b>1</b>	<b>Introduction</b>	<b>1</b>
<b>2</b>	<b>Background theory and device fabrication</b>	<b>7</b>
2.1	A solid-state artificial atom . . . . .	8
2.2	Optical excitation scheme . . . . .	10
2.3	The optical two-level system . . . . .	11
2.4	Mechanical harmonic oscillator . . . . .	15
2.5	An optical two-level system coupled to a mechanical resonator . . . . .	17
2.6	Fabrication of the mechanical resonators . . . . .	19
<b>3</b>	<b>Quantum-dot optomechanics in the unresolved-sideband regime</b>	<b>21</b>
3.1	Introduction . . . . .	22
3.2	A quantum dot coupled to a mechanical resonator . . . . .	23
3.3	Quantum dot localisation and mechanical mode profile . . . . .	24
3.4	Mechanically modulated resonance fluorescence . . . . .	25
3.5	Amplitude and phase of the quantum dot modulation . . . . .	27
3.6	Model for quantum dot resonance modulation . . . . .	29
3.7	Time-resolved measurement in a magnetic field . . . . .	31
3.8	Brownian-motion measurement with single quantum dots . . . . .	33
3.9	Estimation of the exciton-phonon coupling rate . . . . .	35
3.10	Time-trace and autocorrelation measurements . . . . .	36
3.11	Conclusion . . . . .	38
3.12	Supplementary note I: Quantum dot characterisation . . . . .	39
3.13	Supplementary note II: Finite-element simulations . . . . .	41
3.14	Supplementary note III: Electric-field antenna characterisation . . . . .	43
3.15	Supplementary note IV: Measurement setup . . . . .	45
<b>4</b>	<b>Mechanical damping in a quantum-dot optomechanical device</b>	<b>47</b>
4.1	Introduction . . . . .	48

4.2	Optomechanical device . . . . .	48
4.3	Optical cavity characterisation . . . . .	50
4.4	Optomechanical coupling rate . . . . .	51
4.5	Pump-probe optomechanical experiments . . . . .	51
4.6	Mechanical damping measurements . . . . .	53
4.7	Conclusion . . . . .	55
4.8	Supplementary note I: Optomechanical cooling . . . . .	56
4.9	Supplementary note II: Device characterisation and clamping loss . . . . .	57
<b>5</b>	<b>Quantum-dot optomechanics in the sideband regime</b>	<b>59</b>
5.1	Introduction . . . . .	60
5.2	Optimised mechanical resonator design . . . . .	60
5.3	Mechanical pre-characterisation . . . . .	64
5.4	Quantum dot characterisation . . . . .	64
5.5	Master-equation simulations of the exciton-phonon coupling . . . . .	67
5.6	Brownian-motion measurement . . . . .	70
5.7	Mechanical actuation . . . . .	72
5.7.1	Plateau broadening . . . . .	72
5.7.2	Phase response to individual modes . . . . .	73
5.7.3	Quantum dot lifetime . . . . .	75
5.7.4	Autocorrelation measurement . . . . .	77
5.7.5	Resonant linewidth scan . . . . .	78
5.7.6	Time-resolved measurement . . . . .	80
5.7.7	Emission spectrum . . . . .	82
5.8	Conclusion . . . . .	87
5.9	Supplementary note I: Electric-field antenna and sample setup . . . . .	88
5.10	Supplementary note II: Mechanical parameters . . . . .	90
5.11	Supplementary note III: Quantum dot characterisation . . . . .	91
5.12	Supplementary note IV: Time-resolved measurements . . . . .	93
5.13	Supplementary note V: Emission spectrum measurements . . . . .	98
5.14	Supplementary note VI: 25 $\mu\text{m}$ mechanical resonator . . . . .	100
5.15	Supplementary note VII: A comment on charge and spin noise . . . . .	101
<b>6</b>	<b>Quantum-dot optomechanics in the resolved-sideband regime</b>	<b>103</b>
6.1	Introduction . . . . .	104
6.2	Finite-element simulations . . . . .	104
6.3	Optical device characterisation . . . . .	107
6.4	Numerical master-equation simulations . . . . .	109
6.5	High-power resonant excitation . . . . .	111
6.6	Brownian-motion measurement . . . . .	112
6.7	Conclusion and future directions . . . . .	115
6.8	Supplementary note I: From autocorrelation to power spectral density . . . . .	117
6.9	Supplementary note II: A comment on optical device optimisation . . . . .	119
<b>7</b>	<b>Radiative Auger process in the single-photon limit</b>	<b>121</b>
7.1	Introduction . . . . .	122
7.2	The radiative Auger process . . . . .	122

---

7.3	Magnetic field dependence . . . . .	125
7.4	Modelling the magnetic field dispersion . . . . .	126
7.5	Time-dynamics of the radiative Auger process . . . . .	128
7.6	Cross-correlation theory . . . . .	130
7.7	Evaluation of correlation measurements . . . . .	133
7.8	Power dependent excitation and radiative Auger linewidth . . . . .	134
7.9	Conclusion . . . . .	136
7.10	Supplementary note I: Methods . . . . .	137
7.11	Supplementary note II: List of definitions . . . . .	138
7.12	Supplementary note III: Radiative Auger process theory . . . . .	139
7.13	Supplementary note IV: Spin pumping and Rabi oscillations . . . . .	141
<b>8</b>	<b>Optically driving the radiative Auger transition</b>	<b>143</b>
8.1	Introduction . . . . .	144
8.2	Driving the radiative Auger transition . . . . .	144
8.3	Autler-Townes splitting in single-laser experiments . . . . .	146
8.4	Two-laser experiments in a $\Lambda$ -configuration . . . . .	148
8.5	Modelling the $\Lambda$ -system . . . . .	149
8.6	Cross-correlation measurements . . . . .	151
8.7	Magnetic field dispersion . . . . .	153
8.8	Conclusion and future directions . . . . .	154
8.9	Supplementary note I: Methods . . . . .	155
8.10	Supplementary note II: Additional Autler-Townes splitting . . . . .	157
<b>9</b>	<b>Summary</b>	<b>159</b>
	<b>Bibliography</b>	<b>163</b>
	<b>Acknowledgements</b>	<b>177</b>
	<b>List of Publications</b>	<b>179</b>
	<b>Curriculum Vitae</b>	<b>181</b>



## CHAPTER 1

---

# Introduction

---



Optically active semiconductor quantum dots have been part of fundamental research for a long time and important optical observations have been made, for example, resonance fluorescence [1], dressed states [2–4], Rabi-oscillations [5], anti-bunching [3–5], two-photon indistinguishability [3], and coherent scattering [6, 7]. Recently, quantum dots are investigated in the direction of photonic quantum technologies [8, 9]. Optically active quantum dots are also part of the first quantum revolution and can be found in quantum dot laser devices [10]. Nevertheless, there is still a lot of room for further investigations, especially when coupling the quantum dot to other systems. For example, when coupling the quantum dot to an optical cavity, the light-matter interaction can be strongly enhanced [11–14]. Naturally the quantum dot couples to its environment, such as the surrounding nuclear spins [15–18] and mechanical vibrations in the crystal lattice, i.e., phonons [19, 20]. Furthermore, the quantum dot itself also presents a coupled few-particle system, where the carriers confined inside the dot couple to each other via Coulomb interactions [21–23]. In general, if the interaction between the quantum dot and the coupled system is strong enough, the optical interaction with the dot can be exploited to control the state of the coupled system. For example, fluctuations in the nuclear spins can be reduced [18], a mechanical resonator can be cooled down [24], and the orbital degree of freedom of a confined electron can be controlled [22, 23].

The first part of the thesis (Chapter 3-6) investigates the interaction between a solid-state quantum emitter and a mechanical resonator. The coupling of an optical system to a mechanical system has been shown many times, from optical cavities [25–30] to microwave resonators [31–34], and hybrid system such as superconducting qubits [35–37], cold atoms [38–40], defect centres [41, 42], rare-earth emitters [43], 2D-materials [44–46], and also semiconductor quantum dots [20, 47–65]. The advantage of self-assembled semiconductor quantum dots is that they emit single photons with almost perfect optical properties and close-to-lifetime-limited linewidths [66]. Furthermore, they can be embedded in various types of mechanical resonators. In recent years there have been great advances in this direction by coupling quantum dots to cantilevers [47, 48], beams [49, 50], nanowires [51, 67], trumpet resonators [20, 52–56, 68, 69], photonic-crystal membranes [57], and surface-acoustic waves [58–65].

What is missing so far is a scalable mechanical platform in the gigahertz regime. Inspired by the cavity-optomechanical community [27, 70] we introduce a mechanical-membrane platform, suitable for combination with photonic-crystal cavities [71], and photonic or phononic waveguides [72–75]. Besides the scalable platform, measuring gigahertz quantum dot optomechanics without additional mechanical driving still needs to be achieved. We approach this with a set of master equation simulations and a step-by-step increase of the mechanical frequency from 0.5 MHz to 1.5 GHz.

Whereas for cavity optomechanics the linearised interaction (low coupling regime) is dominated by the classical properties of the optical resonator [29], here, the interaction is governed by the inherent non-linearity of the quantum emitter [20]. This means that only one photon at a time can scatter from the dot (elastically or inelastically). On the one hand, this allows the deterministic generation of single photons (and phonons) [13, 72, 76, 77]. On the other hand, it also brings a lot of challenges. For example, the count rate is limited due to the saturation behaviour of

the quantum dot which means that measurements can take a long time. Furthermore, when working with high excitation powers the linewidth becomes power broadened, transforming the system from the resolved- to the unresolved-sideband regime. Nevertheless, in this thesis, the coupling to highly-confined GHz-mechanical modes is achieved, only based on Brownian motion. This presents a first step in the direction of controlling the state of the mechanical resonator using the optical interaction with the quantum emitter [24, 55].

The second part of the thesis (Chapter 7-8) investigates the so-called radiative Auger process using single semiconductor quantum dots [78–80]. The radiative Auger process arises from Coulomb interactions between tightly confined carriers inside the dot [78, 79] together with symmetry breaking on a length scale smaller than the dot size [81]. In a radiative Auger process, single carriers are promoted to higher energy states within the quantum dot [21]. Due to energy conservation, the emitted photon is red-shifted, compared to the elastically scattered photons.

Though radiative Auger effects are rather weak, they are still part of the emission spectrum [21]. The measurements performed in this part are a combination of classical spectroscopy measurements and quantum optics measurements. We show that the Auger emission lines are also optical transitions that can be driven with a laser [22]. This corresponds to exciting the quantum dot with a red-detuned laser together with a carrier deexcitation. When optically addressing the radiative Auger transition, the emission (absorption) of the quantum dot can significantly be changed and a carrier can actively be promoted to a higher shell. This is a first step towards coherent control of the orbital degree of freedom of the Auger carrier [23].

In general, the thesis is written such that it can be read without the background theory part. This means the important equations from the theory chapter can also be found throughout the thesis. Furthermore, details on the measurement setup and finite-element simulations are also merged with the experimental chapters so that the theory chapter can focus on the important physics and fabrication background. The thesis is structured as follows.

**Chapter 2, “Background theory and device fabrication”**, introduces all relevant formalisms that are found throughout the thesis. The semiconductor background of the quantum dot is briefly summarised, including confinement, energy eigenstates, diode structure, and charge control. This is followed by the comparison of the optical excitation schemes. The different quantum dot excitons are collapsed into two-level problems with ground and excited states. A semi-classical description of the interaction between the laser and the two-level system is introduced, including dipole approximation and rotating wave approximation. Using the optical Bloch equations the difference between scanning the laser over the quantum dot resonance and the spectrally resolved emission is shown. The semi-classical optical model is extended by a mechanical coupling term and two fundamentally different mechanical frequency regimes are compared. Finally, the soft-mask fabrication of the devices is briefly discussed.

**Chapter 3, “Quantum-dot optomechanics in the unresolved-sideband regime”**, discusses the measurements performed on the first-generation mechanical devices, which are membrane-type cantilever resonators. The chapter starts with

a discussion of the different, low-frequency, mechanical modes with frequencies in the range of 0.5-19 MHz. These modes fall into the unresolved-sideband regime since the mechanical frequencies are much smaller than the optical decay rate. This is followed by a general optical and mechanical device characterisation. Using an electric-field antenna the mechanical resonator is actuated which increases the coupling effect to the quantum dot. With this, a series of resonant excitation measurements (time-averaged and time-resolved) are performed to investigate the quantum-dot-mechanical coupling. As a hallmark of this chapter, the coupling between the mechanical resonator and the quantum dot is measured only based on displacement fluctuations from Brownian motion. Finally, autocorrelation and time-trace measurements are compared in terms of the measurement imprecision noise.

**Chapter 4, “Mechanical damping in a quantum-dot optomechanical device”**, presents cavity-optomechanical measurements based on the same mechanical resonator as in Chapter 3. The optical cavity forms between the cantilever tip and the bottom of the under-etch. The optomechanical interaction is studied with a blue- and red-detuned laser. Exploiting optomechanical anti-damping, the effective mechanical damping is reduced by two orders of magnitude by going to the onset of the phonon-lasing regime. Finally, the optical cavity is used to precisely measure the damping associated with the applied gate voltage and above-band laser power.

**Chapter 5, “Quantum-dot optomechanics in the sideband regime”**, introduces the second-generation devices. The resonators in this chapter are used to transition to mechanical frequencies faster than the decay rate of the quantum dot. Compared to Chapter 3, the mechanical resonator is detached from the under-etched membrane, enabling high-frequency in-plane breathing modes. The chapter first focuses on basic optical and mechanical characterisation and then turns to Brownian motion measurements. Finally, using the electric-field antenna, a series of individual measurements are performed to better understand the optomechanical interaction. This includes the first observation of Brownian-motion acoustic sidebands and optomechanical wave-mixing. Although sidebands are observed, the mechanical frequencies are not larger than the quantum dot linewidth and hence, we call this frequency regime the sideband regime.

**Chapter 6, “Quantum-dot optomechanics in the resolved-sideband regime”**, presents the third-generation mechanical devices. The mechanical frequency at 1.5 GHz makes the transition from the sideband to the resolved-sideband regime. The chapter starts with in-depth mechanical simulations of the phononic-crystal resonator. This follows a qualification of the quantum dots including charge control, linewidth, lifetime, and single-photon purity measurements. Numerical simulations show that a different parameter set is needed for measuring the quantum-dot-mechanical interaction. After discussing measurement difficulties due to the high mechanical frequencies, Brownian-motion measurements are presented. Finally, the last part gives an extensive conclusion and outlook for all optomechanical measurements presented in this thesis.

**Chapter 7, “Radiative Auger process in the single-photon limit”**, makes the transition from the optomechanical experiments to the radiative Auger measurements. This chapter focuses on the emission produced during the radiative Auger process. First, the radiative Auger effect is introduced in detail as a consequence of Coulomb interactions and symmetry breaking. Second, a series of measurements

---

prove that the additionally observed emission lines are originating from the same emitter. Third, with the magnetic field dispersion of the emission lines, Auger transitions to p- and d-shells are identified. Last, single-carrier dynamics are extracted from a cross-correlation measurement.

**Chapter 8, “Optically driving the radiative Auger transition”**, turns from the emission to the excitation of the radiative Auger transition. In the strong driving limit of the fundamental quantum dot transition, an Autler-Townes splitting is observed in the radiative Auger emission. This follows a two-laser experiment in a  $\Lambda$ -configuration: a weak probe laser drives the quantum dot’s main transition while a strong pump laser scans over the radiative Auger transition. Due to quantum interference between different excitation paths, we observe an overall reduction in the emission (absorption) due to the formation of a dark state. This forms a coherent superposition of the Auger electron being in the s- and p-shells. The observations in this chapter have recently led to follow-up experiments by Yan et al. [23] showing the coherent control of the orbital state of an Auger hole.



---

## Background theory and device fabrication

---

## 2.1 A solid-state artificial atom

Single-photon sources are of great need for quantum information applications, especially when involving complex networks with multiple nodes connected to each other [8, 76]. Quantum emitters exist in different kinds, from cold atoms [82] and trapped ions [83, 84] to solid state-based emitters. The latter are studied intensively in recent years due to their versatility. Promising single-photon emitters in the solid state are two-dimensional (2D) materials [85–87], colour centres in diamond [88, 89], defects in silicon carbide [90, 91], quantum dots in nanowires [51, 92], and epitaxial semiconductor quantum dots. [14, 77, 93].

Ideal properties of quantum emitters are unity internal quantum efficiency, transform-limited linewidths, high single-photon purity and high indistinguishability, and finally, fast and bright single-photon emission [76, 94]. In recent years semiconductor quantum dots have proven to be ideal sources for coherent single photons [9, 11, 76, 95, 96]. Furthermore, the available semiconductor nanofabrication toolbox allows for engineering the mechanical environment of the dots [97]. Therefore, semiconductor quantum dots are ideal for studying the coupling between a quantum emitter and a mechanical resonator [20, 47, 50, 51, 54, 56, 98]. Note that recently also defect centres [41, 42], rare-earth emitters [43], and 2D-materials [44–46] have been investigated in this direction. The following paragraphs give a brief description of the confinement as well as the excitonic properties of quantum dots.

Semiconductor quantum dots are nanometre-sized structures embedded in a host crystal. They are epitaxially grown in a self-assembly process using molecular beam epitaxy. In this thesis, two different quantum dots are investigated, namely Stranski-Krastanow InAs quantum dots in GaAs [99–102] and droplet-etched GaAs quantum dots in AlGaAs [8, 66, 103]. The latter are exclusively studied during the radiative Auger measurements.

The quasi-zero-dimensional confinement of the quantum dot leads to quantised energy levels. For such a confined system, quantum effects become significant when the thermal energy is smaller than the quantisation energy. This is also captured by the thermal wavelength:

$$\lambda_{\text{dB}} = \frac{\hbar}{\sqrt{2m^*k_{\text{B}}T}}, \quad (2.1)$$

where  $m^*$  is the effective mass of the confined particle and  $T$  is the temperature. If the confinement scale is below the thermal wavelength, the system will be dominated by quantum effects. For a single electron in a quantum dot ( $m^* \approx 0.07m_e$ , see Chapter 7) at 4.2 K this translates into 3.7 nm. Since the quantum dot has a flat shape extending more than 20 nm in xy-direction and about 5 nm in z-direction [104], the system can be described by a two-dimensional quantum harmonic oscillator. Note that for GaAs quantum dots the size is usually larger, for more details see Ref. [66]. The Hamiltonian of the quantum harmonic oscillator is given by the momentum operator  $\hat{p}$  and the confinement potential  $V(\vec{x})$ :

$$\hat{H} = \frac{\hat{p}^2}{2m^*} + V(\vec{x}), \quad V(\vec{x}) = \frac{1}{2}m^*\omega^2\vec{x}^2, \quad (2.2)$$

where  $m^*$  is the effective mass inside the potential  $V(\vec{x})$ , and  $\omega$  is the angular fre-

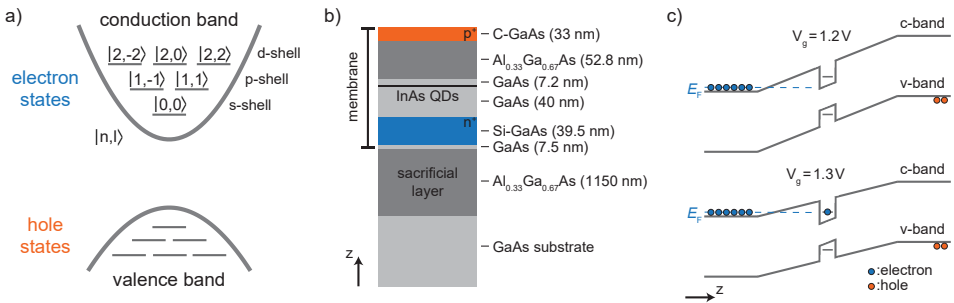


**Figure 2.1: Self-assembled semiconductor quantum dots.** (a) Eigenenergy spectrum obtained from solving the quantum harmonic oscillator. Each state can be filled with two electrons (holes) with anti-parallel spins. The radial quantum number,  $n$ , and the angular momentum quantum number,  $l$ , are displayed. (b) Heterostructure of the sample grown with molecular-beam epitaxy. The membrane is grown on top of a sacrificial layer and the quantum dots are tunnel coupled to the electron reservoir in the back gate. (c) Schematic bandstructure of the heterostructure diode. By applying a forward bias, the quantum dot can be filled with single electrons (bottom figure). Due to the thin diode of 180 nm there is a large electric-field gradient (in  $z$ -direction) and a high forward bias is needed to charge the quantum dot.

quency of the oscillator. The eigenenergies of the system can directly be obtained by analytically solving the time-independent Schrödinger equation:

$$\hat{H} |\Psi(\vec{x})\rangle = E |\Psi(\vec{x})\rangle, \quad (2.3)$$

where  $|\Psi(\vec{x})\rangle$  is the wavefunction of the confined particle. If an electric field is applied (along  $z$ -direction), a linear correction term is added to the potential. Consequently, the electron states shift to lower energies and the hole states shift to higher energies, known as the quantum-confined Stark effect [105–107]. The case of an applied magnetic field is studied in Chapter 7. The eigenenergies of the system are:

$$E_{n_x, n_y} = \hbar\omega_x \left( n_x + \frac{1}{2} \right) + \hbar\omega_y \left( n_y + \frac{1}{2} \right), \quad \text{with } n_{x,y} = 0, 1, 2, \dots \quad (2.4)$$

with  $n_x, n_y$  being the radial quantum numbers. Here, the radial symmetry is broken due to the  $x/y$ -asymmetry of the dot. For more details see Chapter 7. Following the nomenclature from atomic physics [108], the radial quantum number  $n = n_x + n_y$  gives rise to s-, p-, d-like energy shells ( $n = 1, 2, 3$ ) with in total  $n_x + n_y + 1 = n + 1$  (non-) degenerate states, see Fig. 2.1(a). Every state can be filled with two electrons (holes) with anti-parallel spin. This gives in total  $2(n + 1)$  charge carriers per shell.

To control how many electrons (holes) are filled into the dots, they are embedded in a doped-heterostructure diode. The diode not only allows quantum dot charge control (see below) but also stabilises the charge noise in the surrounding host material [66, 109]. Figure 2.1(b) shows the growth structure of the InAs quantum dot sample. The sample consists of a 180 nm thick membrane. [13] which includes the highly-doped gate layers. The membrane is later used to fabricate the mechanical resonator, see Chapter. 2.6. The quantum dots are capped with an AlAs monolayer to remove the



wetting layer states [102]. Furthermore, the quantum-dot layer is tunnel-coupled to the back gate by a 40 nm tunnel barrier. On top of the quantum dots, an AlGaAs blocking layer is grown which limits the current to a few nanoamps at the quantum dot operating bias voltage. The membrane is grown on top of a 1.15  $\mu\text{m}$  sacrificial layer which is selectively etched during the fabrication of the mechanical resonator, see Chapter 2.6.

Due to the highly-doped gate layers, the heterostructure diode has a strong in-built potential which can be lowered by applying a forward bias, see Fig. 2.1(c). This way, the conduction band electron states can be moved into the electron Fermi sea (back gate) and single electrons can tunnel into the quantum dot. The charge state of the quantum dot can therefore be controlled via the applied electric field. Due to the on-site Coulomb repulsion further electrons are hindered from tunnelling into the quantum dot, known as Coulomb blockade [110].

## 2.2 Optical excitation scheme

Two different excitation schemes are used throughout the thesis: above-band excitation and resonant excitation [102]. Figure 2.2 shows a schematic of the two excitation schemes. With above-band excitation a high-energy laser (780 or 830 nm) excites lots of charge carriers outside of the quantum dot (in bulk or in the wetting layer), see Fig. 2.2(a). These carriers then relax via phonon-assisted processes [111] into the lowest, non-occupied energy level of the quantum dot, followed by radiative recombination. This means that the emitted photons, also called photoluminescence, have a lower energy than the excitation laser. This technique allows the emission of all quantum dots within the collection spot to be observed at the same time. On the one hand, the excitation laser can be easily filtered out using a spectrometer, on the other hand, it is difficult to interact with only a single transition of a single dot. Therefore, this excitation technique is primarily used for initial quantum dot localisation and pre-characterisation.

With resonant excitation, a linearly-polarised narrow-bandwidth laser ( $\sim 300$  kHz) is tuned directly in resonance with the optical transition, see Fig. 2.2(b). This allows interacting directly with a specific excitonic transition of a single quantum dot (dependent on the applied bias voltage). The emitted photons, also called resonance fluorescence, are at the same wavelength as the excitation laser. Therefore, a cross-polarised microscope head is used to suppress the reflected excitation laser [112]. For more details on the measurement setup see Chapter 3.

The excitation laser creates bound electron-hole pairs, so-called excitons. The binding energy is given by Coulomb interaction between the two particles of opposite charge (for more details on Coulomb interactions see Chapter 7). Besides the optically created electron-hole pair, additional electrons (holes) can be charged into the quantum dot by tuning the bias voltage applied to the diode structure (see previous chapter). Figure 2.2(c) shows all excitons which can be resonantly addressed in a two-level description. For the neutral exciton,  $X^0$ , the ground state is empty and the excited state is a bound electron-hole pair. For the charged excitons (trions),  $X^{-(+)}$ , the ground state is a single electron (hole) and the excited state consists of two electrons and one hole (one electron and two holes). Throughout this thesis,

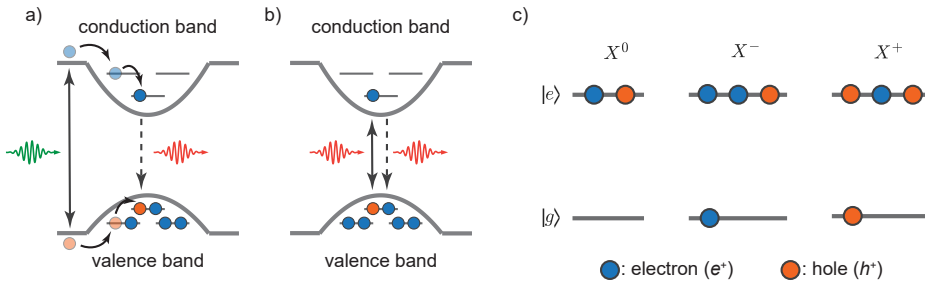


**Figure 2.2: Optical excitation of the quantum dot.** (a) With above-band excitation, carriers are excited outside of the dot (bulk or in the wetting layer). After phonon-assisted relaxation into the lowest, non-occupied energy state of the quantum dot, the carriers recombine by emitting a photon. The emitted photons, photoluminescence, are well separated in colour from the excitation laser. (b) A narrow-bandwidth laser is tuned in resonance with the dipole transition. The emitted photons, resonance fluorescence, are filtered from the excitation laser using polarisation optics. (c) The three excitons that can be addressed with a resonant laser in a two-level description: neutral exciton  $X^0$ , negative and positive trions  $X^-$  and  $X^+$ .

neutral excitons and negative trions are measured. For the optomechanical interaction, it does not matter, in principle, which exciton is chosen. However, radiative Auger transitions only exist for charged excitons (for more details see Chapter 7). When described as a simple two-level system (neglecting the fine-structure splitting and higher energy states) the three excitons presented above can be treated equally.

## 2.3 The optical two-level system

The following chapter gives a semi-classical description of a driven optical two-level system, following Refs. [108, 113, 114]. The description is used throughout the full thesis for charged and neutral excitons, as described in the previous chapter. In Chapter 5 and 6 the model is expanded by an optomechanical coupling parameter and in Chapter 8 it is expanded by a third level in a  $\Lambda$ -configuration and an additional driving laser.

The Hamiltonian of the optical two-level system is given by a quantum dot part and an interaction part:

$$\hat{H} = \hat{H}_{\text{QD}} + \hat{H}_{\text{int}}. \quad (2.5)$$

The quantum dot part of the Hamiltonian is described by two levels, see Fig. 2.3(a), a ground state  $|g\rangle$  with energy  $\hbar\omega_g$  and an excited state  $|e\rangle$  with energy  $\hbar\omega_e$ :

$$\hat{H}_{\text{QD}} = \hbar\omega_g |g\rangle \langle g| + \hbar\omega_e |e\rangle \langle e|. \quad (2.6)$$

We now set the ground state to zero energy by subtracting  $\hbar\omega_g$  from both states:

$$\hat{H}_{\text{QD}} = \hbar\omega_e |e\rangle \langle e| - \hbar\omega_g |e\rangle \langle e| = \hbar\omega_{ge} \hat{\sigma}_+ \hat{\sigma}_-, \quad (2.7)$$

where  $\omega_{ge} = \omega_e - \omega_g$  is the energy difference between excited and ground state, and  $\hat{\sigma}_+ = |e\rangle\langle g|$  and  $\hat{\sigma}_- = |g\rangle\langle e|$  are the raising and lowering operators with  $\hat{\sigma}_+\hat{\sigma}_- = |e\rangle\langle e|$ . The interaction of the quantum dot with the laser is described in the classical picture where the laser is given by a time-dependent electric field:

$$\mathcal{E}(t) = \mathcal{E}_1 \cos(\omega_1 t) = \frac{1}{2} \left( \mathcal{E}_1 e^{i\omega_1 t} + \mathcal{E}_1 e^{-i\omega_1 t} \right), \quad (2.8)$$

where  $\omega_1/2\pi$  is the laser frequency and  $\mathcal{E}_1$  the field amplitude. The interaction of the laser with the quantum dot can be treated perturbatively and is described with the dipole approximation [114]:

$$\hat{H}_{\text{int}} = -d \cdot \mathcal{E}(t), \quad (2.9)$$

where  $d$  is the dipole moment of the optical transition [115]. Assuming that the laser is linearly polarised along  $x$  (due to the microscope head [112]), Eq. 2.9 can be reformulated:

$$\hat{H}_{\text{int}} = -ex\mathcal{E}(t) = -(|e\rangle\langle g| + |g\rangle\langle e|) \mu_{ge} \mathcal{E}(t), \quad (2.10)$$

where  $\mu_{ge} = \mu_{eg}^* = e \langle e|x|g\rangle$  is the dipole matrix element for the x-polarised light. We now define the optical Rabi frequency as  $\Omega_R = |\mu_{ge}\mathcal{E}_1|/\hbar$ , which describes the interaction strength of the laser with the quantum dot. Note that  $\mathcal{E}_1$  scales quadratically with laser power and so does the Rabi frequency. The interaction part of the Hamiltonian is then given by:

$$\begin{aligned} \hat{H}_{\text{int}} &= -\frac{\hbar}{2} \Omega_R (|e\rangle\langle g| + |g\rangle\langle e|) \left( e^{i\omega_1 t} + e^{-i\omega_1 t} \right), \\ &= -\frac{\hbar}{2} \Omega_R (\hat{\sigma}_+ + \hat{\sigma}_-) \left( e^{i\omega_1 t} + e^{-i\omega_1 t} \right). \end{aligned} \quad (2.11)$$

In the Heisenberg picture, the transition operators  $\hat{\sigma}_+$  and  $\hat{\sigma}_-$  rotate with  $e^{\pm i\omega_{ge}t}$ . This leads to fast-varying terms  $e^{\pm i(\omega_{ge} + \omega_1)t}$  in Eq. 2.11, which are neglected via the rotating wave approximation [114]. The full Hamiltonian in matrix form reads as follows:

$$\hat{H} = \hat{H}_{\text{QD}} + \hat{H}_{\text{int}} = \frac{\hbar}{2} \begin{pmatrix} 0 & -\Omega_R e^{i\omega_1 t} \\ -\Omega_R e^{-i\omega_1 t} & 2\omega_{ge} \end{pmatrix}. \quad (2.12)$$

To get rid of the time dependence in the above-presented Hamiltonian we go into the rotating frame of the interacting laser. This is achieved by performing a unitary transformation:

$$\hat{U} = \begin{pmatrix} 1 & 0 \\ 0 & -e^{-i\omega_1 t} \end{pmatrix} \Rightarrow \hat{H}_{\text{rot}} = \frac{\hbar}{2} \begin{pmatrix} 0 & \Omega_R \\ \Omega_R & -2\Delta\omega_1 \end{pmatrix}, \quad (2.13)$$

where  $\Delta\omega_1/2\pi = (\omega_1 - \omega_{ge})/2\pi$  is the laser detuning from the excited state, see Fig. 2.3(a). We now solve the time-independent Schrödinger equation with the density matrix formalism. The density operator describes the quantum state of the system including pure and mixed states:

$$\hat{\rho} = \sum_{ij}^{nm} \rho_{ij} |\Psi_i\rangle\langle\Psi_j| = \rho_{gg} |g\rangle\langle g| + \rho_{eg} |e\rangle\langle g| + \rho_{ge} |g\rangle\langle e| + \rho_{ee} |e\rangle\langle e|, \quad (2.14)$$

where  $\rho_{ij}$  are the matrix elements of the density operator. The density matrix

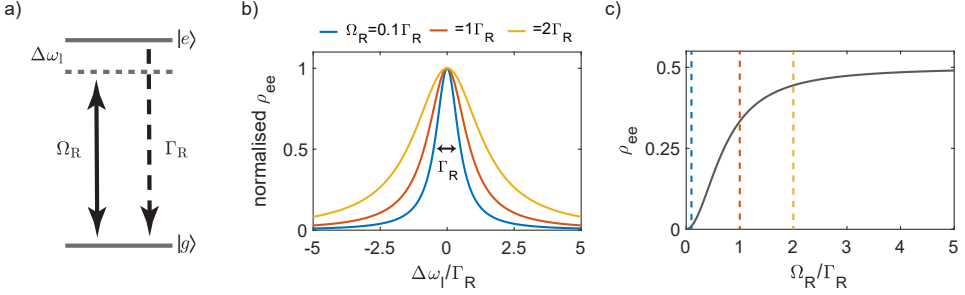


**Figure 2.3: Master-equation model of a two-level system.** (a) Level scheme of the optical two-level system. A near-resonant, coherent laser is driving the optical transition  $|g\rangle \leftrightarrow |e\rangle$  with a detuning of  $\Delta\omega_l$  from the excited state. The incoherent excited state decay is given by  $\Gamma_R$ . (b) Normalised excited-state population,  $\rho_{ee}$ , as a function of laser detuning and for different Rabi couplings. (c) On-resonance excited-state population, saturating above  $\Omega_R > \Gamma_R$ .

elements obey the following conditions:

$$\rho_{gg} + \rho_{ee} = 1, \quad \rho_{ge} = \rho_{eg}^*. \quad (2.15)$$

The time evolution of the system, including coherent and incoherent processes, is captured with the Lindblad master equation (von Neumann equation) [108]:

$$\frac{\partial}{\partial t} \hat{\rho} = -\frac{i}{\hbar} [\hat{H}_{\text{rot}}, \hat{\rho}] + \hat{\mathcal{L}}(\hat{\rho}), \quad (2.16)$$

$$\hat{\mathcal{L}}(\hat{\rho}) = \frac{1}{2} \left( 2L\hat{\rho}L^\dagger - \hat{\rho}L^\dagger L - L^\dagger L\hat{\rho} \right) \quad (2.17)$$

The first term in Eq. 2.16 captures the coherent part of the system, whereas the second term, the Lindblad operator, includes all incoherent processes via collapse operators. Here,  $L = \sqrt{\Gamma_R}|g\rangle\langle e| = \sqrt{\Gamma_R}\hat{\sigma}_-$  with  $\Gamma_R$  being the radiative decay rate, see Fig. 2.3(a). Note that pure dephasing of the excited state is neglected but could be added in the same ways as the radiative decay. The equations of motions of the density matrix elements, known as the optical Bloch equations, can then be solved for the steady-state  $\frac{\partial}{\partial t} \hat{\rho} = 0$ . This collapses the problem from a set of coupled differential equations to a set of coupled linear equations.

The quantum dot emission is proportional to the excited-state population which can be obtained from the steady-state solution of Eq. 2.16:

$$\langle \hat{\sigma}_+ \hat{\sigma}_- \rangle = \rho_{ee} = \frac{(\frac{1}{2}\Omega_R)^2}{\Delta\omega_l^2 + \frac{1}{2}\Omega_R^2 + (\frac{1}{2}\Gamma_R)^2}. \quad (2.18)$$

Figure 2.3(b) shows the excited state population in dependence on the laser detuning for low and high Rabi coupling. At low excitation power,  $\Omega_R \ll \Gamma_R$ , this corresponds to a Lorentzian lineshape with a FWHM given by  $\Gamma_R$ . At higher powers, the linewidth is power-broadened due to the additional Rabi term in the denominator of Eq. 2.18.

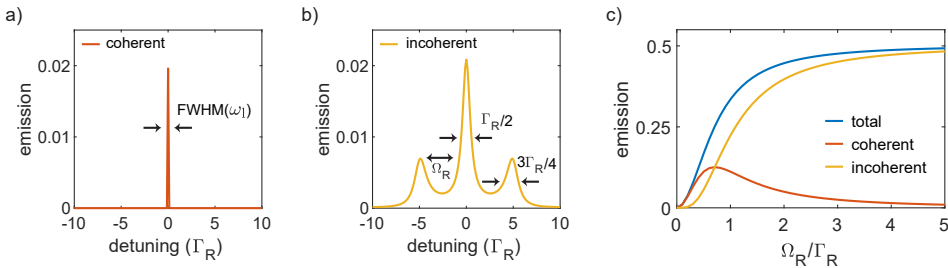


**Figure 2.4: Emission spectrum of an optical two-level system.** (a) Coherent and (b) incoherent part of the emission spectrum at  $\Omega_R = 5\Gamma_R$ . The coherent part is given by the elastically scattered laser whereas the incoherent emission is given by the spontaneous decay via  $\Gamma_R$ . (c) Total, coherent, and incoherent emission in dependence of the Rabi coupling.

Figure 2.3(c) shows the excited state population in dependence on the Rabi frequency. Due to the non-linear nature of the quantum emitter, the excited state population saturates at high powers: when  $\Omega_R \rightarrow \infty$  then  $\rho_{ee} \rightarrow 0.5$ .

Going into more detail, the emission of the quantum dot can be separated into two parts, a coherent and an incoherent part. The frequency-resolved emission can be obtained by performing a Fourier transformation on the first-order coherence function:

$$G^{(1)}(t, \tau) = \langle \hat{\sigma}_+(t) \hat{\sigma}_-(t + \tau) \rangle, \quad (2.19)$$

$$S(t, \omega) = \int_0^\infty G^{(1)}(t, \tau) e^{-i\omega\tau} d\tau. \quad (2.20)$$

The emission spectrum can be obtained analytically, however, we use an alternative approach by numerically simulating the spectrum using the Python quantum toolbox Qutip [116, 117]. The advantage of Qutip is that without a lot of effort, the emission spectrum can also be solved for a time-dependent Hamiltonian. Figure 2.4(a,b) shows the coherent and incoherent parts of the spectrally resolved emission and figure 2.4(c) shows the integrated coherent and incoherent emission in dependence on the Rabi frequency. At low powers,  $\Omega_R \ll \Gamma_R$ , the laser is coherently scattered and interacts only weakly with the quantum dot. The emission of the dot takes on the coherence of the laser and the excited state population stays low. At high powers,  $\Omega_R \gg \Gamma_R$ , the laser interacts strongly with the quantum dot. In quantum language, the strong interaction is described by the dressed-state picture. The emission is dominated by the incoherent part which is given by three peaks separated by the Rabi frequency  $\Omega_R$ , known as the Mollow triplet [118], see Fig. 2.4(b). The Mollow triplet was first observed in atomic sodium [119, 120] and later also with semiconductor quantum dots [1, 121]. Note that the total integrated emission (see Fig. 2.4(c)) follows the excited-state population from Eq. 2.18.

To summarise, we describe the optical two-level system using a semi-classical approach and obtain the quantum dot emission in dependence on laser detuning and laser power. The picture above describes the perfect, unperturbed optical emitter, however in nature, the quantum dot interacts with its environment. For example, the excited state can couple to lattice vibrations, i.e. phonons, which give rise to a

broad LA-phonon sideband [19, 122] surrounding the zero-phonon-line of the dot (see Chapter 7) as well as LO- and TO-phonon replica [21] (inelastic scattering). Phonons are also known to lead to pure dephasing of the excited state, a process which does not change the excited-state population, leading to a homogeneous broadening of the linewidth [123, 124]. In the description above, higher energy states (p-, and d-shell) are also neglected. As will be shown in Chapter 7, these higher energy states still play a role (0.1 to 2% of the emission) due to Coulomb interactions between the tightly confined carriers of the charged excitons. Furthermore, the quantum dot also interacts with its local charge and magnetic environment (nuclear spins), the major sources of inhomogeneous broadening [125]. This broadening is added to the model via a Lorentzian weighted jitter in the laser detuning.

## 2.4 Mechanical harmonic oscillator

The previous chapter focused on the optical description of the quantum dot. In the following two chapters, we focus on the interaction of the emitter with a single mode of a mechanical resonator (mechanical cavity), while in the end coming back to the impact on the quantum dot emission. The derivation of the mechanical system follows Refs. [29, 126, 127].

The complete three-dimensional motion of a mechanical mode can be described by the displacement function:

$$u(r, t) = x(t)|u(r)|, \quad (2.21)$$

where  $|u(r)|$  describes the normalised mode shape [128] and  $x(t)$  describes the time dependence of the motion. For simple resonators, for example a cantilever or a beam, the mode shape can be calculated analytically within the frame of the Euler-Bernoulli beam theory [127]. For more complex resonator design as presented in this thesis, the mode shape can be obtained by finite-element simulations. Since the mode shape is normalised  $|u(r)| = \frac{u(r)}{\max(|u(r)|)}$ , the function  $x(t)$  represents the displacement amplitude of the resonator. The time evolution of the resonator is then captured by a linear harmonic oscillator model [129, 130] with an effective mass  $m_{\text{eff}} = \int \rho \left( \frac{u(r)^2}{\max(|u(r)|^2)} \right) dr$ :

$$m_{\text{eff}} \frac{dx^2(t)}{dt^2} + m_{\text{eff}} \Gamma_m \frac{dx(t)}{dt} + m_{\text{eff}} \Omega_m^2 x(t) = F(t), \quad (2.22)$$

where  $\Omega_m/2\pi$  is the mechanical frequency,  $k = m_{\text{eff}} \Omega_m^2$  is the spring constant, and  $\Gamma_m$  the energy dissipation rate which relates to the mechanical quality by  $Q_m = \Omega_m/\Gamma_m$ .

High mechanical quality is advantageous since it increases the mechanical noise amplitude in the power spectrum and also the intensity of acoustic sidebands. The mechanical quality is composed of many individual damping mechanisms: medium damping due to the collision with gas molecules [131], clamping loss to the surrounding substrate (also called radiation loss) [132], and intrinsic damping:

$$\frac{1}{Q_m} = \frac{1}{Q_{\text{medium}}} + \frac{1}{Q_{\text{clamping}}} + \frac{1}{Q_{\text{intrinsic}}} + \dots \quad (2.23)$$

Intrinsic damping describes all material-related losses in bulk and at the surface of the mechanical resonator. This includes friction losses from material imperfections [133]

and fundamental losses such as thermoelastic [134–136] and phonon-phonon damping (Akhiezer damping) [137].

It is often not straightforward to pinpoint the dominant damping mechanism, especially for complex material platforms and complex resonator designs such as the ones presented in this thesis. Nevertheless, clamping losses can be studied with finite-element simulations, see Chapter 4. Furthermore, Chapter 4 makes an attempt to quantify some of the losses, namely, gas damping and measurement-based losses.

A figure of merit of mechanical resonators coupled to a thermal bath is the  $Q_m \cdot f_m$  product. It stands for how well the mechanical resonator can be decoupled from the thermal environment:  $Q_m \cdot f_m$  must be bigger than  $\frac{k_B T}{h}$  to perform at least one coherent oscillation. More precisely, the number of coherent oscillations in the presence of thermal decoherence is given by:

$$\frac{\Omega_m}{n_{\text{phon}} \Gamma_m} = Q_m \cdot f_m \times \left( \frac{h}{k_B T} \right). \quad (2.24)$$

In contrast to the classical picture (see Eq. 2.27), quantum mechanics describes the mechanical oscillator with quantised displacement and momentum [29]:

$$\hat{x} = x_{\text{zpf}} (\hat{b} + \hat{b}^\dagger), \quad (2.25)$$

$$\hat{p} = -im_{\text{eff}} \Omega_m x_{\text{zpf}} (\hat{b} - \hat{b}^\dagger), \quad (2.26)$$

where  $x_{\text{zpf}}$  is the zero-point motion of the resonator and  $\hat{b}^\dagger$  and  $\hat{b}$  are the phonon creation and annihilation operators. The following Hamiltonian is obtained by quantum mechanical treatment of the mechanical harmonic oscillator:

$$\hat{H}_{\text{mech}} = \hbar \Omega_m (\hat{b}^\dagger \hat{b} + 1/2), \quad (2.27)$$

where the mechanical quantum,  $\hbar \Omega_m$ , is described by the phonon. The mean phonon number is given by  $\langle n_{\text{phon}} \rangle = \hat{b}^\dagger \hat{b}$  which obeys the Bose-Einstein statistics. For  $k_B T \gg \hbar \Omega_m$  the occupation can be simplified to  $\langle n_{\text{phon}} \rangle = \frac{k_B T}{\hbar \Omega_m}$ .

To estimate the exciton-phonon coupling strength, the vacuum fluctuation and thermal motion of the resonator need to be determined. The vacuum fluctuation of the mechanical resonator is given for  $\langle n_{\text{phon}} \rangle = 0$ . Furthermore, the mean energy of the mechanical resonator is given by the equipartition theorem [29, 98]:

$$\langle E \rangle = k_B T = m_{\text{eff}} \Omega_m^2 x_{\text{zpf}}^2. \quad (2.28)$$

By equating Eq. 2.27 and 2.28 the zero-point motion is obtained:

$$x_{\text{zpf}} = \sqrt{\frac{\hbar}{2m_{\text{eff}} \Omega_m}}. \quad (2.29)$$

The thermal motion (Brownian motion) [127] of the resonator can be described by the mean-square random variation of the displacement. In other words, the effective spring is fluctuating randomly about the mean position due to temperature:

$$\frac{1}{2} m_{\text{eff}} \Omega_m^2 \langle x^2 \rangle = \frac{1}{2} k_B T. \quad (2.30)$$

Since the zero-point motion is given by half the energy of a single-phonon, the thermal displacement scales with  $\sqrt{2n_{\text{phon}}}$  in relation to the vacuum fluctuation:

$$x_{\text{th}} = \langle x^2 \rangle^{1/2} = x_{\text{zpf}} \sqrt{\frac{2k_{\text{B}}T}{\hbar\Omega_{\text{m}}}} = x_{\text{zpf}} \sqrt{2n_{\text{phon}}}. \quad (2.31)$$

## 2.5 An optical two-level system coupled to a mechanical resonator

The exciton-phonon coupling rate is described in the dispersive regime where the excited state of the two-level system is shifted linearly in energy due to the displacement of the mechanical resonator. This energy shift is due to deformation potential coupling, meaning that displacement creates strain, strain changes the local bandgap of semiconductor material, which in turn shifts the quantum dot transition energy. Deformation potential couplings for hydrostatic and shear strain of GaAs [20, 98] are  $a = -8.33 \text{ eV}$  and  $b = -1.7 \text{ eV}$  [138, 139]:

$$\delta E = a(\epsilon_{xx} + \epsilon_{yy} + \epsilon_{zz}) - \frac{b}{2}(\epsilon_{xx} + \epsilon_{yy} - 2\epsilon_{zz}). \quad (2.32)$$

The strain profile is obtained from finite-element simulations and normalised using thermomechanical calibration [128]. In this way, the vacuum exciton-phonon coupling strength can directly be obtained from Eq. 2.32 via:

$$g_{\text{ep}} = \frac{\partial \omega}{\partial x} x_{\text{zpf}} = \frac{\delta E}{\hbar}. \quad (2.33)$$

The thermal coupling strength, which is the angular frequency shift of the dot for  $\langle n_{\text{phon}} \rangle > 1$ , is then  $g_{\text{th}} = g_{\text{ep}} \sqrt{2n_{\text{phon}}}$  [140]. If expressed in terms of the coupling per single-phonon,  $g_{\text{th}}$  scales with  $\sqrt{n_{\text{phon}}}$ .

The backaction of the interacting system is given by the strain created by the exciton inside the quantum dot [55]. Together with the mechanical motion, this creates a time-dependent backaction force on the mechanical resonator [29]. For a laser at a fixed frequency, the mechanical motion modulates the excited state population (and thus the strain created by the exciton) with a specific phase delay. Dependent on whether the quantum emitter is driven red or blue detuned, the corresponding phase delay leads to optomechanical damping (anti-Stokes scattering) and anti-damping (Stokes scattering), respectively [29].

The full Hamiltonian of the coupled system consists of the bare quantum dot term (see previous chapter), the bare mechanical term, and the optomechanical coupling term:

$$\hat{H} = \hat{H}_{\text{QD}} + \hat{H}_{\text{mech}} + \hat{H}_{\text{coupl}} \quad (2.34)$$

$$\hat{H} = \hbar\omega \hat{\sigma}_+ \hat{\sigma}_- + \hbar\Omega_{\text{m}} \left( \hat{b}^\dagger \hat{b} + 1/2 \right) + \hbar g_{\text{ep}} \hat{\sigma}_+ \hat{\sigma}_- \left( \hat{b}^\dagger + \hat{b} \right), \quad (2.35)$$

with  $(\hat{b}^\dagger + \hat{b}) = \hat{x}/x_{\text{zpf}}$ . If the phonon occupation is high,  $\langle n_{\text{phon}} \rangle \gg 1$ , the coupling term can be expressed classically:  $\hat{H}_{\text{coupl}} = \hbar \frac{g_{\text{ep}}}{x_{\text{zpf}}} x_{\text{th}} \hat{\sigma}_+ \hat{\sigma}_- = \hbar g_{\text{th}} \hat{\sigma}_+ \hat{\sigma}_-$ . This expression is used throughout the thesis.



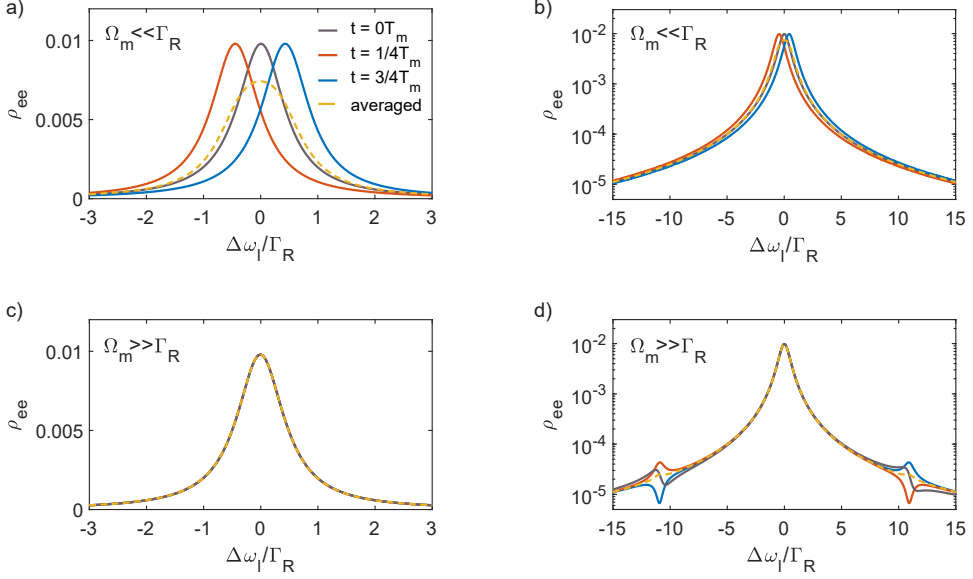


**Figure 2.5: Numerical simulations of the exciton-phonon coupling. (a,b)** Effect of the low-frequency optomechanical coupling in linear- and log-scale. The mechanical motion periodically shifts the exciton frequency. Time-averaging the frequency modulation (yellow-dashed line) results in a broadened linewidth. **(c,d)** Effect of the high-frequency optomechanical coupling in linear- and log-scale. The frequency modulation is much faster than the decay rate of the dot. Instead of a broadened linewidth, side peaks at  $\pm\Omega_m$  are observed. These side peaks show a time modulation due to effective-Rabi-frequency matching with the mechanical frequency. For (a)-(d) the frequency modulation of the excited state is  $g_{th}/2\pi = 60$  MHz. For more details on the simulations see Chapter 5.

The coupling between the quantum emitter and the mechanical resonator is studied in depth in Chapters 3 to 6. There are two distinct regimes where the coupling manifests itself in a different effect on the emission of the quantum emitter, see Fig. 2.5. For mechanical frequencies much slower than the quantum dot's excited state decay rate,  $\Omega_m \ll \Gamma_R$  (unresolved-sideband regime), the coupling leads to a frequency shift of the quantum dot resonance, see Fig. 2.5(a,b). Time-averaged, this results in a broadened linewidth. On the contrary, for mechanical frequencies much faster than the quantum dot's excited state decay rate,  $\Omega_m \gg \Gamma_R$  (resolved-sideband regime), the resonance of the dot does not shift at all, see Fig. 2.5(c). However, the coupling gives rise to acoustic sidebands, separated from the quantum dot resonance by the mechanical frequency, see Fig. 2.5(d). Interestingly, these sidebands also show a time modulation. The two regimes show a significant difference in the quantitative effect of the coupling. More precisely, for low frequencies, the effect on the emitted photons is solely given by the coupling rate, independent of the mechanical frequency. However, for the high-frequency regime, the sideband intensity is given by the coupling rate normalised to the mechanical frequency. In this thesis, we make an attempt to un-

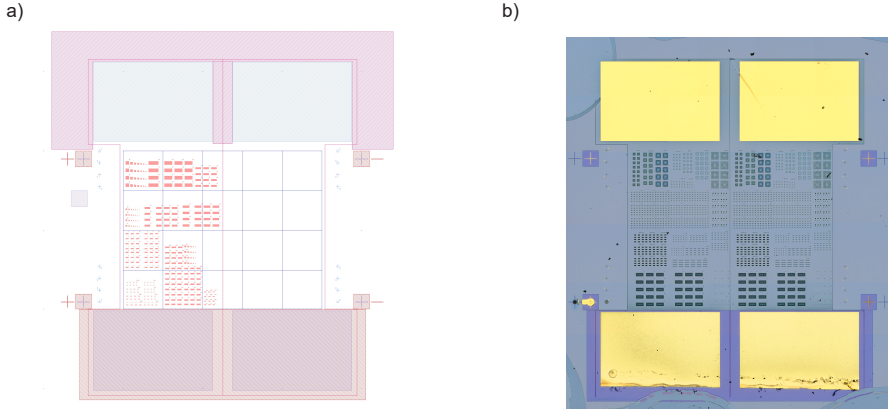


**Figure 2.6: Fabrication of the sample.** (a) Mask file including all fabrication-relevant steps from the markers to the contacts and the mesa, to the mechanical structures. (b) Optical image of the fabricated sample. The sample consists of two copies of the same mechanical structures, each with separate gates for individual charge control. Contact pads are  $1.5 \times 1 \text{ mm}^2$ .

derstand this interaction in-depth, such that the coupling can be exploited to control the mechanical state of the resonator via the optical interaction with the quantum emitter.

## 2.6 Fabrication of the mechanical resonators

As shown in Fig. 2.1(b), the optomechanical sample (wafer number #15027) consists of a 180 nm thick membrane grown on top of a  $1.15 \mu\text{m}$  AlGaAs sacrificial layer. As previously described, the membrane contains highly-doped gate layers for quantum dot charge control. The quantum dots are embedded in the centre of the membrane ( $z = 0$ ). The advantage of this position is that first, the dots couple strongly to mechanical in-plane bending and breathing modes (see Chapter 3-6) and second, the dots also couple strongly to TE-light modes confined within the membrane. The following gives a brief description of the fabrication process.

The wafer material is cleaved into  $4 \times 4 \text{ mm}^2$  pieces parallel to the small-flat of the wafer. This is crucial since the mechanical properties of GaAs are anisotropic and the fabrication axis needs to match the finite-element simulation axis ([110]). Then, the mesa structure is etched, followed by evaporating the contacts: Ni/Ge/Au/Ni/Au for the back contact (which is annealed to form an ohmic contact) and Cr/Au for the top contact.

The mechanical structures are then fabricated by means of electron-beam lithography. A soft mask is spin-coated on the sample and after baking, the mechanical structures are written with the electron beam. After development, the structures are dry-etched (inductively-coupled plasma reactive ion etching) into the membrane. The residual resist is removed and the structures are under-etched by selective-etching of

the sacrificial layer in a wet-etch process (hydrofluoric acid). To avoid a collapse of the structures, a final critical-point drying step is performed. More details on the fabrication process can be found in Ref. [97].

Finally, after the full fabrication process, the sample is glued on a Ti-sample holder and the contacts are connected (by hand) to a PCB using copper wires and silver epoxy. For more details on this step see Chapter 5.9. Figure 2.6 shows the full mask file compared to the fabricated structures.

The wafer material used in this thesis is grown by Sven Scholz and Julian Ritzmann in the group around Arne Ludwig and Andreas D. Wieck at the Lehrstuhl für Angewandte Festkörperphysik at the Ruhr-Universität Bochum (Germany). The fabrication of the mechanical structures is performed by Ying Wang in the group around Leonardo Midolo and Peter Lodahl at the Niels Bohr Institute in Copenhagen (Denmark).

---

**Quantum-dot optomechanics in the  
unresolved-sideband regime**

---

### 3.1 Introduction

Coupling a single-photon emitter to a mechanical resonator is of fundamental interest for applications involving the heralded emission or absorption of a single phonon. Semiconductor quantum dots have excellent optical properties and can be integrated into various mechanical resonators. However, to date, mechanical resonators hosting optically active quantum dots lack the scalability to gigahertz mechanical frequencies (the resolved-sideband regime). In our experiments, self-assembled InAs quantum dots are coupled to the in-plane mechanical motion of a 180 nm thick membrane resonator. The resonator holds three mechanical modes in the megahertz regime with high mechanical quality factors,  $Q_m > 2 \times 10^4$ . We probe the Brownian motion with the single photons emitted by the quantum emitter and observe a high exciton-phonon coupling rate,  $g_{ep}/2\pi \approx 100$  kHz. The membrane resonator design presented here, together with the nanofabrication toolbox, allows for translation to the resolved-sideband regime (see Chapter 6).

Optomechanical systems find numerous applications from precision sensing [141–144] to laser cooling [27] and microwave-to-optics conversion [145]. The choice of the mechanical and optical system thereby depends on the scope of the application. On the one hand, cavity optomechanical systems have found great success in many areas from macroscopical resonators for gravitational wave sensing [146] to microscopical systems probing the quantum nature of sound [36]. On the other hand, quantum dot optomechanical systems have recently shown significant advances by coupling to engineered mechanical resonators [20, 47–57, 68, 69] and surface acoustic waves [50, 58–65]. The main advantage of using a quantum dot as the optical part of the coupled hybrid system is the non-linear nature of the quantum emitter, enabling the deterministic generation of single phonons [72]. Additionally, the quantum dot is an excellent single-photon emitter [8, 22, 76] and can serve as a host for a single-spin [147].

So far, optomechanical interaction without additional mechanical driving has only been demonstrated once using quantum dots embedded in a trumpet resonator [20]. Although these measurements present a step towards single-phonon generation (absorption), the necessary scaling to higher frequencies is not straightforward with these systems. Additionally, the system lacks a diode structure for quantum dot charge stabilisation resulting in reduced sensitivity to mechanical noise.

In the following chapter, we present a membrane resonator with high-quality in-plane mechanical modes, coupling to numerous quantum dots. A mechanical frequency in the MHz regime (doppler regime) allows us to study the dispersive coupling between the macroscopic mechanical resonator and the microscopic quantum dots in detail. We resolve the Brownian motion of the mechanical modes by recording the emitted single photons with a Hanbury Brown-Twiss setup and single-photon detectors. The mechanical noise is recorded as a function of excitation power and laser detuning and shows the fundamental characteristics of a single-photon emitter coupled to a mechanical resonator.

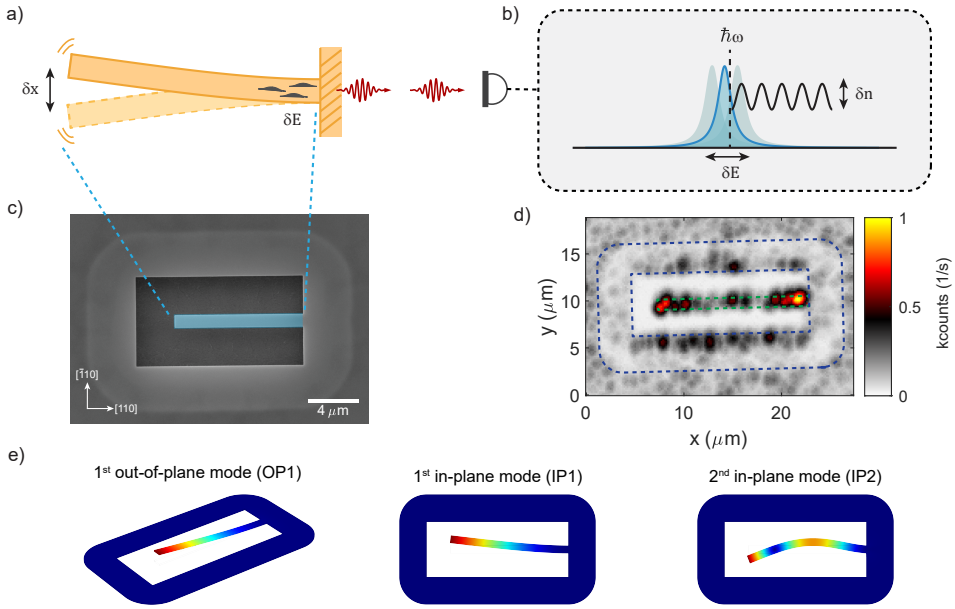


**Figure 3.1: Optomechanical coupling of a quantum dot and a mechanical resonator.** (a) Schematics of quantum dots coupled to a cantilever-type mechanical resonator. A displacement  $\delta x$  creates strain  $\delta \epsilon$  which changes the local bandgap  $\delta E$ . (b) The quantum dot's resonance frequency is shifted accordingly to the change in band gap which is then mapped onto the statistics of the emitted photons by a detuned laser. (c) Mechanical system: scanning electron microscope image of a membrane cantilever surrounded by the remaining under-etched membrane. (d) Optical system: a photoluminescence map of the cantilever reveals multiple quantum dots distributed over the full mechanical resonator. The cantilever is highlighted in green and the under-etched membrane in blue. (e) Normal bending modes of the cantilever with the major displacement either out-of-plane (OP1) or in-plane (IP1 and IP2).

## 3.2 A quantum dot coupled to a mechanical resonator

The material platform is a 180 nm thick membrane (see Chapter 2), hosting a GaAs p-i-n diode structure for charge control of the embedded InAs quantum dots [13]. The mechanical system is a cantilever-type resonator of  $15 \times 1 \mu\text{m}^2$ , fabricated with electron-beam lithography [97], Fig. 3.1(c). The quantum dots are embedded in the centre of the membrane (in z-direction) and can be found over the full area of the cantilever, highlighted in green in Fig. 3.1(d). An advantage of placing the quantum dots in the middle of the membrane is that they couple strongly to in-plane mechanical modes. These modes enable higher mechanical frequencies than out-of-plane modes (here 6-fold) for a given resonator size. We observe three mechanical bending modes: one out-of-plane mode (OP1) at 0.5 MHz, and two in-plane modes (IP1 and IP2) at 3.1 and 19.1 MHz, Fig. 3.1(e). A mechanical displacement  $\delta x$  of the cantilever tip creates strain at the cantilever clamp, shifting the quantum dot energy

by  $\delta E$  due to deformation potential couplings [98], see Fig. 3.1(a). The quantum dot energy shift can then be imprinted on the statistics of the emitted single photons by a detuned probe laser [20], Fig. 3.1(b). The resulting interaction is governed by the non-linear nature of the quantum emitter [62] as described by the interaction term in the following Hamiltonian [98]:

$$\hat{H} = \hbar\omega\hat{\sigma}_+\hat{\sigma}_- + \hbar\Omega_m(\hat{b}^\dagger\hat{b} + 1/2) + \hbar g_{\text{ep}}\hat{\sigma}_+\hat{\sigma}_-(\hat{b}^\dagger + \hat{b}), \quad (3.1)$$

where  $\omega/2\pi$  and  $\Omega_m/2\pi$  are the quantum dot and mechanical frequencies,  $\hat{b}^\dagger$  and  $\hat{b}$  are the mechanical creation and annihilation operators,  $\hat{\sigma}_+\hat{\sigma}_- = |e\rangle\langle e|$  is the Pauli operator acting on the optical two-level system, and  $g_{\text{ep}} = \frac{\partial\omega}{\partial x} \cdot x_{\text{zpf}}$  is the vacuum optomechanical coupling strength. Compared to cavity optomechanical systems, the exciton-phonon coupling cannot be scaled with excitation power and is solely given by the intrinsic strain coupling of the quantum dot. Thus, careful selection of the mechanical resonator design is an important prerequisite.

### 3.3 Quantum dot localisation and mechanical mode profile

We begin by locating the quantum dots on the mechanical resonator. The largest strain and thus the highest coupling of the quantum dots to the mechanical motion is at the clamping position of the cantilever. A photoluminescence map is taken where we record a full photoluminescence spectrum for every position on the mechanical resonator. The scanning is performed using a set of piezo steppers and scanners. Figure 3.2(b) represents the counts of the brightest quantum dot found at each position.

Since the intrinsic exciton-phonon coupling is not visible in photoluminescence, a mechanical drive is installed. An electric-field antenna [148], consisting of an sma cable with removed isolation, is mounted about 0.5 cm above the sample surface. The electric field radiated by the antenna couples to the in-built electric field of the membrane diode. Thus, the cantilever can be actuated by applying a microwave signal to the antenna at the resonance frequency of the mechanical resonator. The microwave applied to the antenna is generated using an arbitrary waveform generator. This way of mechanical driving is less invasive than for example thermal driving. It also does not rely on the precise positioning of the antenna with respect to the mechanical resonator and thus, many mechanical resonators can be probed with the same setup.

After locating the cantilever clamping position, we perform a cantilever displacement sweep from 0 to 35 nm, driving the first in-plane mechanical mode IP1, Fig. 3.2(a). Due to the optomechanical interaction, the quantum dot linewidth becomes broadened. The level of broadening is thereby given by the exciton-phonon coupling strength. Figure 3.2(a) shows several quantum dots with different coupling strengths at the cantilever clamping position. Because IP1 has a strain node in the centre of the cantilever (y-direction) and since the laser spot covers the full cantilever width, we can also see dots with close-to-zero coupling to the mechanical displacement. The quantum dots presented throughout the following chapters are labelled in Fig. 3.2(a).

Since the antenna driving is not affected by the position of the cantilever, we

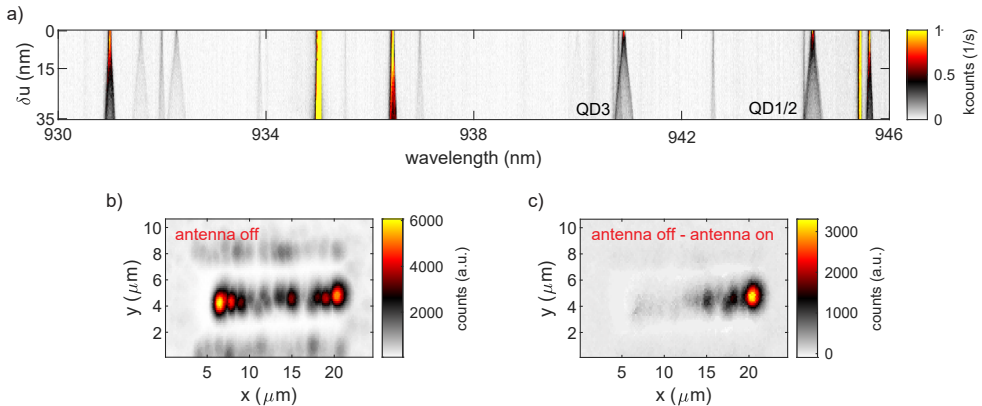


**Figure 3.2: Quantum dot localisation on the mechanical resonator and strain profile.** (a) Spectrally resolved photoluminescence at the cantilever clamping position as a function of mechanical displacement of the first in-plane mode IP1. Several quantum dots can be seen, each with a different coupling strength to the mechanical motion. (b) Photoluminescence map of the cantilever. For each position, a spectrum is taken and the count rate of the brightest quantum dot is selected. (c) Same as in (b) but for each position two spectra are taken, with the mechanical drive on and off. Each pixel is then given by the difference between the two spectra which represents the coupling strength and the local strain profile probed by the quantum dots.

can also perform a photoluminescence map with the antenna drive turned on. Subtracting a spectrum with antenna-drive on from a spectrum with antenna-drive off reveals the quantum dot coupling strength (highest reduction in signal). In other words, we use the quantum dot emission to probe the strain profile of the driven mechanical mode. Figure 3.2(c) shows the measured profile for the first in-plane mechanical mode, with the highest strain coupling at the cantilever clamp. Note that here we probe the absolute value of the strain and thus we cannot differentiate between strain coupling with opposite signs.

### 3.4 Mechanically modulated resonance fluorescence

Exploiting resonant excitation, a clear difference between the mechanical drive turned on and off is visible. In Fig. 3.3(a) the resonant linewidth scan of the negatively charged exciton  $X^{1-}$  shows a broadening of  $2\delta E/\hbar = 8.06$  GHz, due to mechanical driving of IP1. The data is fitted using a model including a sinusoidal modulation of the quantum dot resonance (see Chapter 3.6). The magnitude of the broadening (together with the vacuum exciton-phonon coupling rate) gives the displacement of the driven cantilever mode, which is  $\delta x = 1.28$  nm. Note that the maximum displacement achieved when driving IP1 is  $\delta x_{\max} = 34$  nm, see Fig. 3.2.

An important figure of merit is the mechanical quality factor of the membrane resonator. Compared to the previous trumpet resonator [20], the surface-to-volume



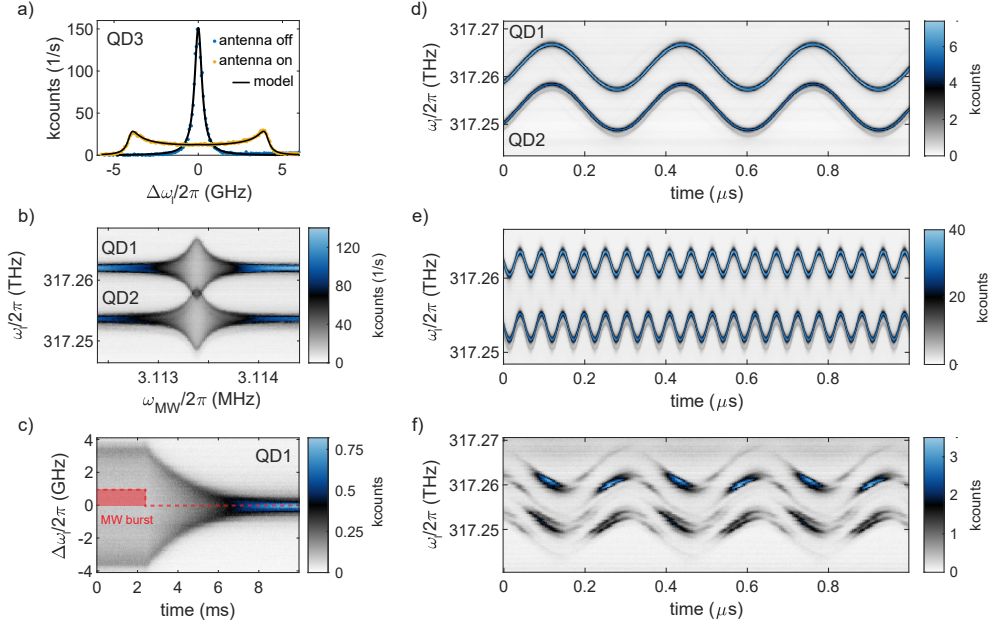


**Figure 3.3: Quantum dot resonance fluorescence modulated by the mechanical driving of the cantilever.** (a) Resonant linewidth scan of the quantum dot with the mechanical drive turned on and off. (b) Time-averaged resonance fluorescence as a function of mechanical drive frequency. The extracted FWHM results in a mechanical quality factor of  $Q_m = 2.2 \times 10^4$ . (c) Ring-down measurement of the cantilever driven by a 15 ms microwave burst pulse with 50% duty cycle. The lifetime of 2.2 ms matches well with the measured quality factor in (b). (d,e) Time-resolved resonance fluorescence of the first and second in-plane modes, the two quantum dots are modulated in phase with respect to each other. (f) Time-resolved measurement in a magnetic field of 1.1 T (Voigt geometry), both quantum dots split each into four allowed optical transitions. The signal recovering points at 317.26 THz and 317.25 THz are due to ineffective spin-pumping. (a-d,f) correspond to the first in-plane mode IP1 and (e) corresponds to the second in-plane mode IP2.

ratio of the cantilever is three times larger, making the system more prone to surface losses [133]. Moreover, the highly doped gate layers and the applied diode bias can add additional losses.

We probe the mechanical quality factor of IP1 in two different ways. First, we perform a mechanical resonance frequency scan, Fig. 3.3(b). Second, the mechanical lifetime is measured by actuating the cantilever with a burst pulse and monitoring the ring-down time, Fig. 3.3(c). In both cases, we record the resonance fluorescence emitted by the quantum dot and we perform a two-dimensional model fit, see Fig. 3.5. The extracted FWHM and lifetime are 141.5 Hz and 2.25 ms (for more details see Chapter 3.6). Both result in a mechanical quality factor of  $Q_m = 2.2 \times 10^4$ . Compared to the first-order bending mode of the previous trumpet resonators [20], this constitutes an increase in mechanical quality of a factor of 10, besides the already 6-fold increase in mechanical frequency.

The mechanical quality of IP2 is extracted from a ring-down measurement, which yields  $\tau_m = 0.376$  ms and  $Q_m = 2.2 \times 10^4$ . OP1 shows a quality of  $Q_m = 1.5 \times 10^4$  obtained from a quantum dot independent measurement, see Fig. 3.12. The mechanical properties in dependence on the applied bias voltage are studied in detail in [Supplementary note III](#).

We continue with time-resolved measurements while actuating the cantilever with the electric field antenna and extracting the phase relation of each quantum dot with respect to the mechanical drive (displacement). This allows the relative geometrical position of the individual quantum dots to be located. We record the resonance fluorescence in a histogram mode while sweeping the laser frequency. Figure 3.3(d,e) shows the modulated emission of QD1 and QD2 while driving the two in-plane modes IP1 and IP2, respectively. Each horizontal data line represents one measurement step where a histogram is recorded for 20 s. The full phase relation between mechanical response and applied microwave field is shown in Fig. 3.4. We observe that QD1 and QD2 react in phase with the mechanical driving for both IP1 and IP2. The same applies to QD3. This means that all three dots are located on the same half (in y-direction) and close to the clamp of the cantilever (less than  $2.8 \mu\text{m}$ , see [Supplementary note II](#)). This matches well with the position obtained from the photoluminescence map.

The dynamics in the time-resolved measurements become especially visible when a magnetic field is applied. Figure 3.3(f) shows the same setting as in Fig. 3.3(d) except that a magnetic field,  $B = 1.1$  T, is applied orthogonal to the growth axis (Voigt geometry). Note that the magnetic field adds additional phase noise to the measurement. Whether the noise is added via the antenna driving or via a mechanical resonance fluctuation needs further investigation. The two quantum dots each split into four optically allowed transitions, see Fig. 3.6. The measurement is performed in the centre of the  $X^{1-}$  charge plateau, thus, without mechanical driving the quantum dot emission vanishes due to effective spin pumping into a dark state [149]. However, with mechanical driving bright recovery spots appear, see Fig. 3.3(f).

For each measurement (horizontal line) the laser is fixed, however, the mechanical driving moves the optical transitions in and out of resonance with the laser. Thus, the spin is pumped back and forth between the two spin states every mechanical period and the emission is recovered. We support our argumentation with a numerical rate equation simulation, for more details see Chapter 3.7.

## 3.5 Amplitude and phase of the quantum dot modulation

The quantum dot resonance is sinusoidally modulated with a frequency given by the mechanical mode and an amplitude given by the exciton-phonon coupling together with the mechanical displacement. If a resonance scan is performed, the modulation becomes time-averaged which leads to a broadening of the linewidth, as sketched in Fig. 3.4(a). Figure 3.4(b) and (c) show the selected quantum dots from Fig. 3.2(a). The negatively charged  $X^{1-}$  plateau is scanned by tuning the applied bias voltage and sweeping the excitation laser. The emitted single-photons are monitored with single-photon detectors. The plateau scans are shown without (left) and with (right)

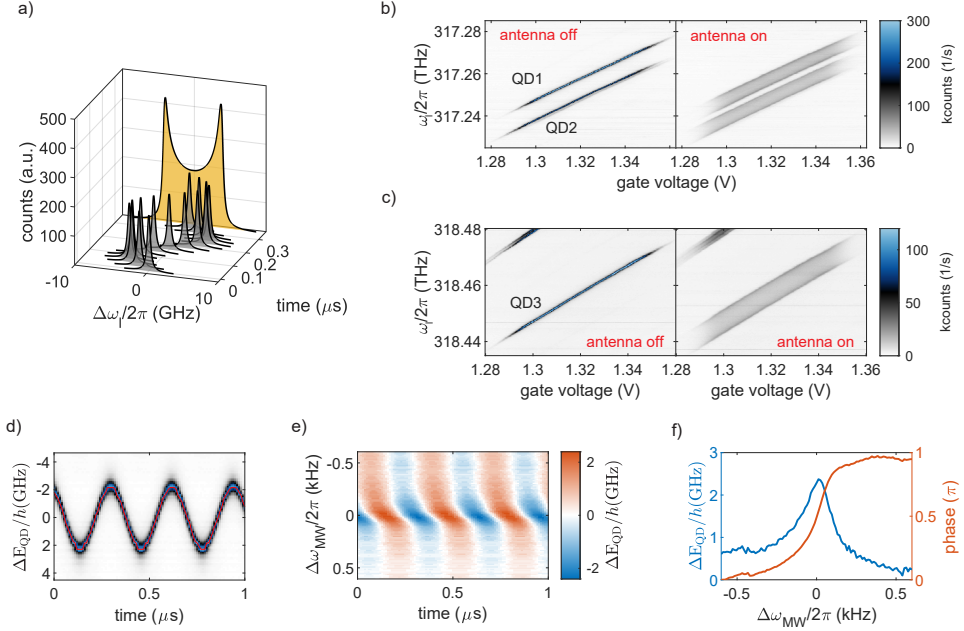


**Figure 3.4: Mechanical modulation of the quantum dot and phase measurement.** (a) Model of the sinusoidal frequency shift of the quantum dot. Shown is one oscillation period of the mechanical resonator, where each time step can be represented by a frequency-shifted Lorentzian. Time-averaged, a broadened linewidth is observed, as shown in yellow. (b,c) Resonant charge-plateau scan of the negatively charged exciton  $X^{1-}$  without (left) and with (right) mechanical driving. The broadening of the linewidth can be observed over the full plateau width. (d-f) Time-resolved measurement of the modulated quantum dot to extract the phase relation with respect to the mechanical driving. The quantum dot frequency shift is measured as a function of microwave detuning (e) from which the phase response can be extracted, shown in (f).

mechanical driving. Over the full range of the plateau, the mechanical frequency changes only slightly. Thus, the mechanical driving is always on resonance and a uniform broadening is observed. Since the exciton-phonon coupling is given by the strain-mediated bandgap shift, the plateau edges are not affected by the mechanical driving.

As discussed in the previous chapter, the sinusoidal quantum dot modulation can be probed in a time-resolved measurement. While driving the mechanical motion with the electric field antenna, the emitted single photons are collected in a histogram mode. For this, the time tagging module is synchronised to a trigger signal from the arbitrary waveform generator. Figure 3.4(d) shows a time-resolved measurement of QD3 while mechanical driving of IP1. Each horizontal line represents a histogram recorded for 20 s for a fixed laser frequency. Since the time tagger is synchronised with the waveform generator, the phase response of the mechanical displacement with respect to the drive can be measured. To determine the exact phase response for a fixed mechanical driving frequency, the quantum dot frequency is extracted for each

histogram time step, highlighted in red in Fig. 3.4(d). The time-resolved measurement is then repeated while scanning the applied microwave over the mechanical resonance.

The extracted quantum dot frequency shift as a function of mechanical driving frequency and time is shown in Fig. 3.4(e). A clear shift of the phase response can be observed around the mechanical resonance. As a last step, each of the extracted time-resolved quantum dot frequency shifts is fitted with a sine function to extract precise amplitude and phase values, which can be seen in Fig. 3.4(f). The phase undergoes the expected shift of  $\pi$  around the mechanical resonance. Note that the resonance scan deviates from the data shown in the previous chapter since these measurements were performed after swapping the sample to another cryostat. Nevertheless, with the method described above the phase response of all three dots with respect to the mechanical driving of IP1 and IP2 is extracted.

## 3.6 Model for quantum dot resonance modulation

Here, we describe the model which is used to fit the data in Fig. 3.3. We assume a Lorentzian quantum dot line shape:

$$L(\omega_1) = \frac{1}{2}\Gamma' \left( \frac{\frac{1}{2}\Gamma'}{(\omega_1 - \omega_0)^2 + (\frac{1}{2}\Gamma')^2} \right), \quad (3.2)$$

where  $\omega_1/2\pi$  is the laser frequency and  $\omega_0/2\pi$  is the quantum dot resonance frequency, and  $\Gamma'/2\pi$  is the inhomogeneously broadened quantum dot linewidth (FWHM). Although there is residual charge noise in our system (the linewidth is about a factor of two above the transform limit), the Lorentzian is still a good approximation, as can be seen in Fig. 3.3. Since the mechanical drive is still in the linear regime, we assume a sinusoidal modulation of quantum dot resonance frequency with a specific amplitude:

$$\omega_0(t) = \delta E/\hbar \cdot \sin(\Omega_m t), \quad (3.3)$$

where  $\Omega_m/2\pi$  is the mechanical frequency and  $\delta E$  is the quantum dot energy shift (due to the strain coupling to the mechanical resonator). Last, we integrate Eq. 3.2 and 3.3 for one mechanical period to obtain the quantum dot resonance broadening  $S(\omega_1)$  [98], which is then fitted to the data:

$$S(\omega_1) = \int_0^{2\pi/\Omega_m} L(\omega_1, t) dt. \quad (3.4)$$

Here we assume that the linewidth broadening is independent of the mechanical frequency. As shown in Chapter. 2.5, this model breaks down when the mechanical frequency approaches the quantum dot decay rate. For Fig. 3.3(a) we first fit the quantum dot resonance without mechanical driving to extract the quantum dot linewidth  $\Gamma'/2\pi$  and the quantum dot resonance  $\omega_0/2\pi$ . These parameters are then fixed when fitting the model to the data with mechanical drive turned on. The model given by Eq. 3.4 fits very well and allows the extraction of precise quantum dot energy shift  $\delta E$ .

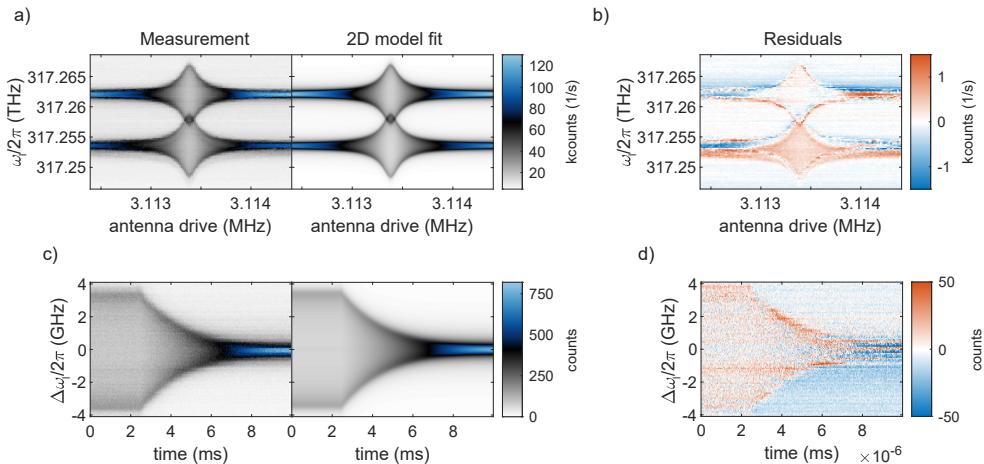


**Figure 3.5: Two-dimensional model fit.** (a,c) Comparison of the 2D model fit and the measured data. The model includes a sinusoidal modulation of the quantum dot resonance together with an amplitude modulation of either the square root of a Lorentzian (a) or an exponential decay (c). (b,d) The residuals of the fits.

For the two-dimensional measurement fits, used for extracting the mechanical quality factor, additional amplitude modulation is added to the model. In the case of the mechanical resonance scan, the amplitude in Eq. 3.3 is modulated with a square root of a Lorentzian:

$$\omega_0(t, \omega_{MW}) = \delta E/\hbar \cdot \sqrt{L(\omega_{MW})} \cdot \sin(\Omega_m t), \quad (3.5)$$

where  $L(\omega_{MW})$  is given by Eq. 3.2. The strain experienced by the quantum dots is linearly proportional to the displacement of the cantilever. Thus, the quantum dot energy shift shows a linear dependence on the mechanical amplitude and hence, the square root dependence to the mechanical drive in Eq. 3.5. In the case of the ring-down measurement, the amplitude in Eq. 3.3 is first fixed for a given driving time  $t' < t'_0$  and then modulated with an exponential decay:

$$\omega_0(t, t') = \delta E/\hbar \cdot e^{-t'/\tau_m} \cdot \sin(\Omega_m t), \quad \text{for } t' > t'_0, \quad (3.6)$$

where  $\tau_m$  is given by the mechanical lifetime. Note that the microwave burst pulse applied to the electric field antenna during this experiment is set long enough for the mechanical amplitude to reach a steady state. For both, mechanical resonance sweep and ring-down measurement, we integrate using Eq. 3.4 and perform a two-dimensional model fit using least-square minimisation. We first fit the model to an initial measurement with mechanical driving turned off to extract quantum dot related parameters and finally fit the full model. Figure 3.5(a) to (d) show the model fits compared to the data, as well as the two-dimensional residuals. The model fits exceptionally well with the data and allows extracting the mechanical lifetime, which is used to derive the mechanical quality factor.

### 3.7 Time-resolved measurement in a magnetic field

Fig. 3.6(a) shows the negatively charged excitons of QD1 and QD2 in an in-plane magnetic field (Voigt geometry) of  $B = 1.1$  T. Each quantum dot splits into four equally allowed transitions according to the level structure shown in Fig. 3.6(e). All transitions are linearly polarised, where the highest and lowest energy transitions (vertical transitions) have orthogonal polarisation to the inner two transitions (diagonal transitions). The excitation and emission strengths thereby depend on the alignment of the quantum dot with respect to the polarisation in the excitation and collection arm of the microscope head. Thus, the signal strength of the different transitions varies from dot to dot. Here, QD1 shows brighter signals on the vertical transitions than the diagonal transitions and QD2 shows about the same intensity for the four transitions, see Fig. 3.6(a). In the centre of the plateau, the quantum dot emission vanishes due to spin-pumping into a dark state. Here, the spin pumping fidelity is close to unity. At the plateau edges, spin-pumping is ineffective due to co-tunnelling of the quantum dot electron with an electron from the Fermi-sea in the back contact.

When the mechanical drive is turned on, spin-pumping in the plateau centre becomes ineffective. This can be seen by the recovered intensity in the time-resolved measurement shown in Fig. 3.6(b), which is the same data as in Fig. 3.3. Each horizontal line represents one measurement, recorded in a histogram mode. The mechanical driving moves the different transitions in and out of resonance with the fixed laser. Two of the four transitions pump the spin to the spin-up state  $|\uparrow\rangle$  (labelled green in Fig. 3.6(e)) and the other two transitions pump the spin to the spin-down state  $|\downarrow\rangle$  (labelled red in Fig. 3.6(e)). Whenever two transitions associated with opposite spin-pumping are moved in and out of resonance within one mechanical period, the spin is pumped back and forth between the two states and the intensity is recovered.

We confirm our observations with a numerical rate equation model in which QD1 and QD2 are represented by individual four-level systems. First, we define the time-modulated quantum dot energies of all transitions:

$$E(t) = E_0 + \delta E \cdot \sin(\Omega_m t) \quad (3.7)$$

$$E_{ij}(t) = E(t) \pm 1/2(g_e \pm g_h)B\mu_B, \quad i = \{1, 2\}, j = \{3, 4\}, \quad (3.8)$$

where  $g_e$  and  $g_h$  are the electron and hole g-factors,  $B$  is the magnetic field, and  $\mu_B$  is the Bohr magneton. Note that we assume fixed g-factors for the full mechanical oscillation period [47]. We further define detuning dependent driving rates [149] for the four optical transitions:

$$R_{ij}(t) = \frac{\Omega_{ij}^2}{\Gamma_R \left( \frac{4(\omega_1 - E_{ij}(t)/\hbar)^2}{\Gamma_R^2} + 1 \right)}, \quad i = \{1, 2\}, j = \{3, 4\}, \quad (3.9)$$

where  $\Omega_{ij}/2\pi$  is the Rabi frequency of the optical transitions,  $\omega_1 - E_{ij}(t)/\hbar$  is the time dependent laser detuning (in angular frequency), and  $\Gamma_R$  is the excited state decay rate. The latter is independent of the laser detuning and is obtained from a lifetime measurement,  $\Gamma_R/2\pi = 224$  MHz, shown in Fig. 3.10. Note that the spin-relaxation rate  $\kappa$  between the two ground states is assumed to be smaller than the mechanical frequency. Finally, using all rates described above we can model the dynamical system by a set of coupled rate equations:

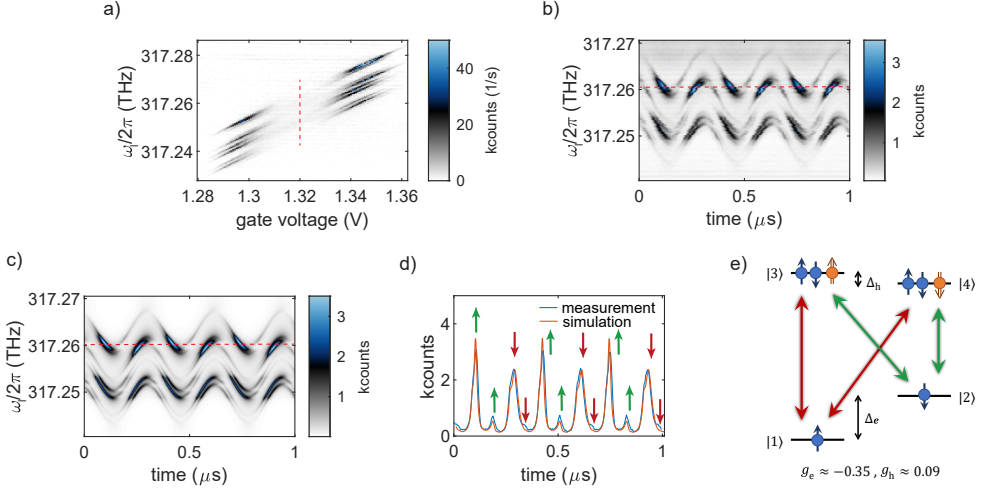


**Figure 3.6: Time-resolved resonance fluorescence in a magnetic field.** (a) Charge plateau scan of QD1 and QD2 at  $B = 1.1$  T. Each quantum dot splits according to the level scheme in (e), having four equally allowed optical transitions. The vanishing intensity in the plateau centre is due to spin-pumping. (b) Time-resolved measurement which is also shown in Fig. 3.3. The measurement is performed in the plateau centre, highlighted in red in (a). (c) Numerical rate-equation simulation of the two independent four-level systems, matching well with the experiment. (d) Line-cut comparison between measurement and model. Colored arrows represent the pumping of transitions with the same spin-state in the final state. It can be seen that spin pumping is reversed every mechanical period and thus the intensity is recovered.

$$\begin{aligned}
 \dot{n}_1 &= +R_{13}(t)(n_3 - n_1) + R_{14}(t)(n_4 - n_1) + \Gamma_R(n_3 + n_4) + \kappa(n_2 - n_1) \\
 \dot{n}_2 &= +R_{23}(t)(n_3 - n_2) + R_{24}(t)(n_4 - n_2) + \Gamma_R(n_3 + n_4) + \kappa(n_1 - n_2) \\
 \dot{n}_3 &= -R_{13}(t)(n_3 - n_1) - R_{23}(t)(n_3 - n_2) - 2\Gamma_R n_3 \\
 \dot{n}_4 &= -R_{14}(t)(n_4 - n_1) - R_{24}(t)(n_4 - n_2) - 2\Gamma_R n_4.
 \end{aligned} \tag{3.10}$$

The numerical simulation begins with an equal population in the two spin ground states  $n_1(0) = n_2(0) = 0.5$  and zero population in the excited states  $n_3(0) = n_4(0) = 0$ . The simulation is then evolved for 10 mechanical oscillations ( $\sim 3\mu\text{s}$ ) to reach a time-averaged steady state, followed by the final simulation, shown in Fig. 3.6(c). Here, we assume that the quantum dot count rate is proportional to the sum of the excited state populations and we normalise the simulation to the count rate of the measurement. The initial 10 mechanical oscillations are cut out since they would not be representative for the measurement. The simulation fits very well with the measured data and features not only the bright recovering spots but also all other weak-intensity changes in the background.

In Fig. 3.6(d) linecuts from the measurement and the simulation are compared. The red and green coloured arrows represent pumping of optical transitions associated with the same final spin state. Whenever a transition with the opposite final spin



state than the previous one is brought into resonance, the quantum dot intensity recovers due to spin-pumping. Contrary, when two transitions with the same final spin state are brought into resonance after each other, the intensity reduces for the second transition, since the spin is already pumped into the dark state. Thus, our measurement shows that the spin is pumped back and forth between the two states due to the mechanical driving and spin pumping becomes ineffective. Since we do not see any recovering spots between the upper and lower pair of four transitions, we can confirm that we measure two individual quantum dots which just by chance are very close to each other in emission frequency. Moreover, since we only see recovering spots between the upper two and lower two transitions of each dot, we can assign the measured g-factors to the correct charge carriers. Furthermore, from the polarisation of the transitions, we know that the electron and hole g-factors need to have opposite signs, thus  $g_e \approx -0.35$  and  $g_h \approx 0.09$ .

### 3.8 Brownian-motion measurement with single quantum dots

As the final hallmark of our experiments, we perform a Brownian-motion measurement, which presents the first step towards creating and absorbing a single phonon via the quantum dot. Since in the current system the mechanical frequency is smaller than the lifetime of the quantum dot ( $\Omega_m \ll \Gamma_R$ ), the optomechanical interaction can be probed by a slightly detuned laser ( $\Delta\omega_1/2\pi \approx 0.3 \times \text{FWHM}$ ), see Fig. 3.8. The challenging part thereby is that a weak but fast modulation is probed with low bandwidth – the mechanical frequency is up to two orders of magnitude faster than the single-photon count rate. Still, if enough single-photon clicks are recorded, the mechanical noise can be resolved.

The Brownian motion is either measured by recording a time trace or by performing an autocorrelation measurement and subsequent Fourier transformation. The time trace, however, shows a high level of measurement imprecision noise  $S_{\text{nn}}^{\text{imp}} = 0.8 \times 10^{-5} \text{ Hz}^{-1}$ , dominated by the shot noise of the low photon count rate, see Fig. 3.9. In the autocorrelation measurement, the shot noise is diluted during the averaging process due to a missing phase relation. As a consequence, the measurement imprecision noise reduces exponentially with integration time down to  $S_{\text{nn}}^{\text{imp}} = 8.5 \times 10^{-9} \text{ Hz}^{-1}$ , for more details see 3.10.

The autocorrelation measurement is performed at a Rabi frequency of  $\Omega_R = 0.6\Gamma_R$ , corresponding to 200 nW excitation power, and laser detuning of  $\Delta\omega_1/2\pi = 180 \text{ MHz}$ . Quantum dot lifetime and power curve are shown in [Supplementary note I](#). The autocorrelation is recorded for five hours while taking care of the spectral fluctuation [150] by performing a resonance scan every two minutes, see [Supplementary note I](#). At short time delays, the single-photon emitter shows an anti-bunching with a high single-photon purity of 96.3%, shown in Fig. 3.7(a). The remaining  $g^{(2)}(0)$  is given by the non-perfect laser suppression, mainly due to scattering at the cantilever edges. At longer time delays, the Brownian motion of the mechanical resonator is resolved. Fig. 3.7(b) shows the noise from the two in-plane modes IP1 and IP2, fitted with a double sine function (together with an exponential function for blinking [125]).

The photon noise power spectrum is related to the autocorrelation by the



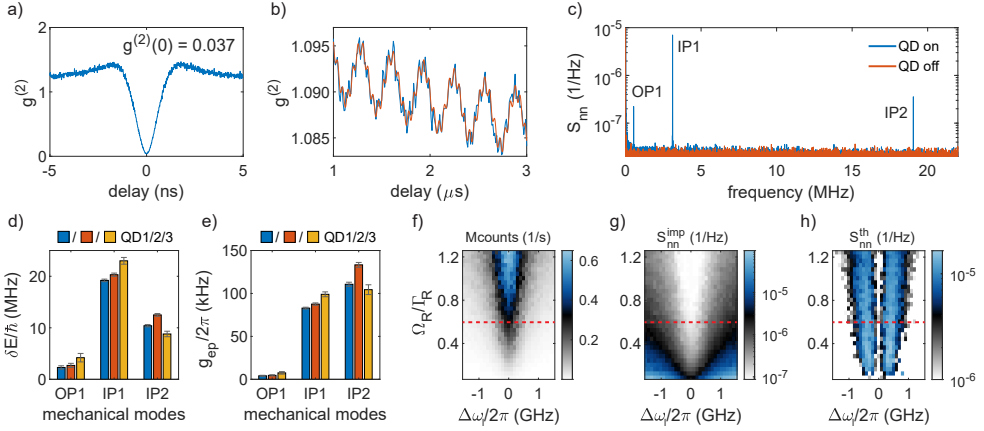


**Figure 3.7: Brownian motion resolved in the statistics of the emitted single photons.** (a) Auto correlation measurement showing the single-photon emission of the quantum dot. (b) Large time delays in the autocorrelation reveal oscillations from the Brownian motion of the mechanical resonator, here IP1 and IP2. (c) Photon-noise power spectrum obtained by a Fourier transformation of the autocorrelation measurement. The clearly distinct peaks are stemming from the thermal noise of the mechanical modes shown in Fig. 3.1(e). (d) Quantum dot resonance shift of the three mechanical modes obtained by the integrated noise spectrum together with the measured quantum dot linewidth. (e) Estimated optomechanical coupling rate  $g_{ep}$ . (f) Quantum dot count rate, (g) measurement imprecision noise, and (h) thermal noise of the first in-plane mode IP1 as a function of excitation power and laser detuning. The single-photon emitter starts to saturate above  $\Omega_R = \Gamma_R$  and the linewidth increases due to power broadening. Consequently, the imprecision noise improves initially but then also starts to saturate. In contrast, the thermal noise is highest at low powers and small detunings. Measurements shown in (a-e) are performed at  $\Omega_R = 0.6\Gamma_R$ , red-dashed line.

Wiener–Khinchin theorem and can be obtained by performing a Fourier transform [20], shown in Fig. 3.7(c). The noise power is obtained from an autocorrelation with a maximum time delay of  $t_{del} = \pm 3$  ms and a binning of  $t_{bin} = 10$  ns, [Supplementary note I](#). Thus, all three mechanical modes are well resolved. To confirm that the measured noise arises solely from quantum dot optomechanical interaction, a reference measurement is performed with the quantum dot tuned out of resonance. As can be seen, the noise power remains flat throughout the full spectrum. By integrating the thermal noise for each mechanical mode, the quantum dot resonance shift due to Brownian motion is obtained, which is shown in Fig. 3.7(d). Here, we assume that the optomechanical damping is much smaller than the intrinsic mechanical damping (less than 2%). Thus, although single phonons are created, the effect of the optomechanical damping on the mechanical mode temperature can be neglected.

We estimate the vacuum exciton-phonon coupling rate with the measured quantum dot resonance shift together with parameters for effective mass  $m_{eff}$  and zero-point-motion  $x_{zpf}$ . The parameters are obtained from finite-element simulations, shown in [Supplementary note II](#). As expected, the quantum dots couple well to the two in-plane mechanical modes IP1 and IP2, see Fig. 3.7(e). The out-of-plane mode OP1

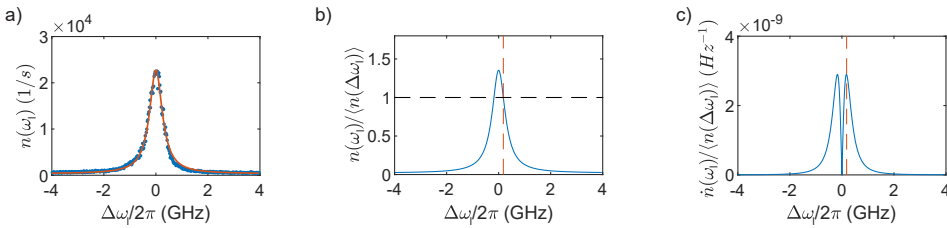


**Figure 3.8: Quantum dot resonance shift estimation via the measured linewidth.** (a) Quantum dot linewidth scan, (b) normalised count rate, and (c) derivative of the normalised count rate as a function of laser detuning. The laser detuning of the Brownian-motion measurement is highlighted in orange ( $\Delta\omega_1/2\pi = 180$  MHz).

only shows residual coupling. More details on the coupling rate estimation will be discussed in Chapter 3.9.

Going one step further, the thermal-mechanical noise of IP1 and the measurement imprecision noise are probed in dependence of excitation power and laser detuning, Fig. 3.7(f-h). Here, the main difference compared to other optomechanical systems becomes visible. As an optical two-level system, the quantum dot starts to saturate above  $\Omega_R = \Gamma_R$ . Consequently, the measurement imprecision noise (dominated by shot noise) improves initially but then starts saturating. The thermal noise, on the contrary, is mainly given by the intrinsic exciton-phonon coupling,  $g_{ep}$ , and cannot be increased with excitation power (which can be done with cavity-optomechanical systems). Moreover, the thermal noise is proportional to the derivative of the quantum dot's count rate and therefore is maximal at low powers in the absence of power broadening. The measurements in Fig. 3.7(f-h) are performed in the same way as in Fig. 3.7(c) but with an integration time of 1 min per autocorrelation measurement. Therefore, the imprecision noise would improve further by increasing the integration time.

### 3.9 Estimation of the exciton-phonon coupling rate

A mechanical displacement  $\delta x$  creates strain  $\delta\epsilon$ , which shifts the quantum dot energy  $\delta E$  due to deformation potential couplings. This energy shift  $\delta E$  (quantum dot resonance shift) is mapped to the statistics of the emitted single-photons by the detuned laser. The noise in the emission of the quantum dot is then captured in the autocorrelation measurement and the corresponding noise power spectrum. By integrating the thermal noise peaks in the normalised photon noise spectrum  $\int S_{nn}(f)df$ , we obtain the measured noise in the percentage of the normalised photon count rate. This normalised count-rate fluctuation can then be converted to a quantum dot resonance fluctuation by comparing it to the derivative of the quantum dot count rate as a function of laser detuning, which is obtained as follows. First, the quantum dot count rate is measured as a function of laser detuning  $n(\omega_1)$  and is fitted with a Lorentzian, which is shown in Fig. 3.8(a). The linewidth scan takes about two minutes, thus, it includes all quantum dot related noise within this time scale. Slower noise processes,

e.g. spectral fluctuation, are filtered out by the locking of the quantum dot resonance. The measurement is repeated three times for statistical error estimation. Second, the quantum dot emission is normalised to the count rate during the autocorrelation measurement. The normalised count rate  $n(\omega_1)/\langle n(\Delta\omega_1) \rangle$ , shown in Fig. 3.8(b), is obtained with parameters from the linewidth fit. Last, we take the derivative of the normalised quantum dot count rate  $\dot{n}(\omega_1)/\langle n(\Delta\omega_1) \rangle$ , shown in Fig. 3.8(c). Since we work with a fixed laser detuning (highlighted in orange), the measured amplitude fluctuation can be converted to a quantum dot frequency fluctuation [20]:

$$\delta E/\hbar = \frac{\sqrt{\int S_{\text{nn}}(f)df}}{\dot{n}(\omega_1)/\langle n(\Delta\omega_1) \rangle}. \quad (3.11)$$

The frequency shift due to Brownian motion at liquid helium temperature is then converted to the vacuum coupling rate using zero-point motion  $x_{\text{zpf}}$  and thermal motion  $x_{\text{th}}$  obtained from finite-element simulations:

$$g_{\text{ep}} = \frac{\partial\omega}{\partial x} \cdot x_{\text{zpf}} = \frac{\delta E/\hbar}{x_{\text{th}}} \cdot x_{\text{zpf}}. \quad (3.12)$$

### 3.10 Time-trace and autocorrelation measurements

The photon-noise power spectral density can be obtained via a Fourier transformation of a time-trace or autocorrelation measurement. In the case of the time trace, we record the emitted single photons on a single detector for 60 s and then relock the laser frequency to the quantum dot resonance. The actual time spent recording 60 s of single photons takes much longer (about 5 min) due to the time spent transferring data from the time tagger to the computer. In total, 300 individual time traces of each 60 s are recorded, which gives 5 hours of emitted single photons. Three example time traces are shown Fig. 3.9(a). The high ratio of up to two orders of magnitude between the count rate of 250 kHz and the mechanical frequency of up to 20 MHz becomes visible. The collected single photons are post-processed to time traces of length  $t_{\text{int}} = 6$  ms with a time binning of  $t_{\text{bin}} = 10$  ns. Note that this post-processing takes about 2-3 hours on a standard desktop computer. A Fourier transformation is performed on each time trace (normalised to the average counts per binning  $\langle n_{\text{bin}} \rangle$ ) with subsequent averaging:

$$S_{\text{nn}}(f) = 2\text{FFT} \left[ \frac{n(t)}{\langle n_{\text{bin}} \rangle} \right]^2 \frac{t_{\text{bin}}^2}{t_{\text{int}}}. \quad (3.13)$$

The noise power spectrum obtained from the time trace as a function of averaging time,  $t_{\text{aver}}$ , is shown in Fig. 3.9(b). Since we time-average after performing the Fourier transformation, a high measurement imprecision noise of  $S_{\text{nn}}^{\text{imp}} = 0.8 \times 10^{-5} \text{ Hz}^{-1}$  is observed (given by the shot noise of the low photon count rate:  $S_{\text{nn}}^{\text{shot-noise}} = 2/\langle n \rangle$ ). The slight variations between the measurements in Fig. 3.9(b) arise from the uncertainty of the count rate normalisation.

In the autocorrelation measurement, the emitted single photons are sent to a 50:50 fibre beam splitter and recorded with two individual detectors (Hanbury Brown-Twiss setup). Thus, the count rate per detector is reduced by a factor of two compared to

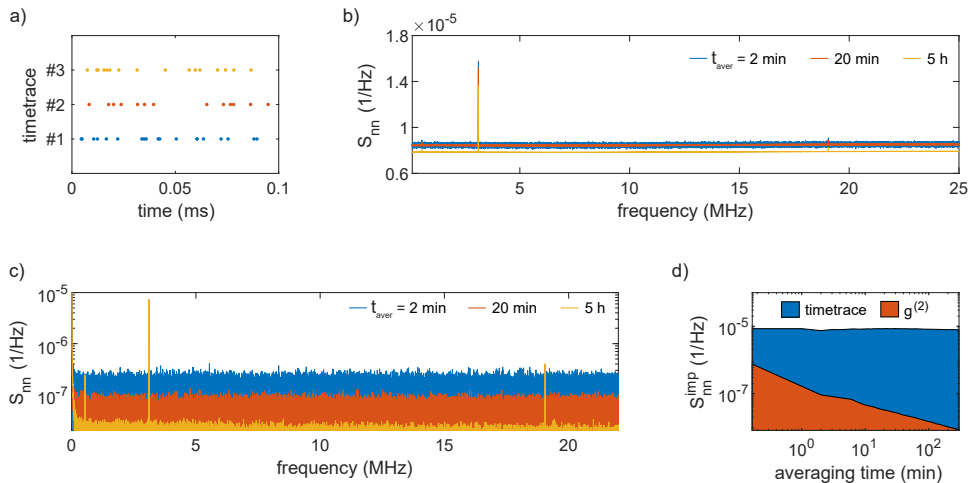


**Figure 3.9: Noise performance of the time-trace and autocorrelation measurement.** (a) Single-photon clicks detected during three different time traces. (b) Fourier transformation of the time trace ( $t_{\text{int}} = 6$  ms,  $t_{\text{bin}} = 10$  ns) shows a high measurement imprecision noise of about  $0.8 \times 10^{-5}$  Hz $^{-1}$  given by the shot noise of the low count rate in (a). Every individual time trace (of length  $t_{\text{int}}$ ) ends up with about the same shot noise, which is passed on during the averaging process. Thus, the imprecision noise does not reduce when increasing the averaging time,  $t_{\text{aver}}$ , see (d). (c) Fourier transformation of the autocorrelation ( $t_{\text{del}} = \pm 3$  ms,  $t_{\text{bin}} = 10$  ns) recorded for different averaging times. Since the shot noise is averaged in the autocorrelation before transformation, the imprecision noise goes down with averaging time. The obvious difference compared to the time trace is visible in (d) where the autocorrelation outperforms the time trace even with only 1 s of averaging time.

the time-trace measurement. Although this decreases the signal-to-shot-noise ratio, the shot noise is averaged out during the autocorrelation measurement due to the missing phase relation. We collect coincidence clicks for 5 hours and relock the laser frequency to the quantum dot resonance every 2 min. Since we only transfer the coincidence counts from the time tagger to the computer (and not all single photon clicks), the transfer only takes about 1 s which reduces the measurement time by a lot. We perform a Fourier transformation of the normalised autocorrelation measurement with a time delay of  $t_{\text{del}} = \pm 3$  ms and a binning of  $t_{\text{bin}} = 10$  ns:

$$S_{\text{nn}}(f) = 2\text{FFT} \left[ g^{(2)}(\tau) \right] t_{\text{bin}}. \quad (3.14)$$

The noise power spectrum as a function of averaging time is shown in Fig. 3.9(c). In terms of measurement imprecision noise, the autocorrelation outperforms the time trace already with an averaging time of only 1 s. Figure 3.9(d) shows that the imprecision noise is diluted by the averaging process, down to  $S_{\text{nn}}^{\text{imp}} = 8.5 \times 10^{-9}$  Hz $^{-1}$  (corresponding to  $S_{\text{nn}}^{\text{shot-noise}} = 2/(\sqrt{t_{\text{aver}}/t_{\text{del}}})\langle n \rangle$ ). In summary, the main advantages of the autocorrelation measurement compared to the time trace are: a several times shorter measurement time (due to the lower data stream between time tagger and

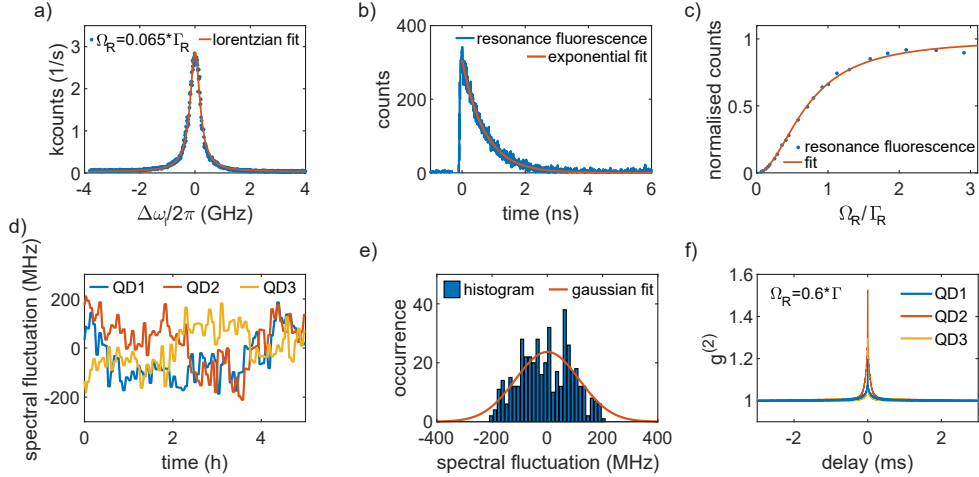
measurement computer), almost no postprocessing needed, live-view of the recorded autocorrelation and corresponding noise spectrum, and a much lower measurement imprecision noise.

### 3.11 Conclusion

The mechanical membrane resonator shown here is a step towards more scalable quantum-dot optomechanical systems. We show that the electron-hole pair created inside the quantum dot couples strongly with the macroscopic motion of the in-plane mechanical modes. Although the quantum dots are embedded in a thin membrane only 90 nm away from the surface, they still show bright signals and narrow optical linewidths, resulting in a high sensitivity to optomechanical interaction. Due to the introduced diode heterostructure, the charge noise in the system is highly reduced compared to the trumpet resonators [20], further increasing the mechanical sensitivity. More importantly, the high mechanical quality factor is proof that the doped gate layers do not have a significant impact on the mechanical properties. However, there is still room for improvement. Especially when going to the resolved sideband regime, it is crucial to further increase the exciton-phonon coupling rate and reduce the mechanical losses to a minimum. Methods from the mechanical toolbox for improvement are readily available [151]. Embedding the mechanical resonator in a phononic shield [152–154] will not only improve the mechanical properties but also further confine the mechanical mode, increasing the exciton-phonon coupling strength. We estimate that by improving the resonator design and by reducing the mechanical mode volume by a factor of three, the exciton-phonon coupling strength  $g_{\text{ep}}/2\pi$  can be increased to the MHz regime.

A limiting factor in our system is the intrinsic excited state lifetime of the quantum dot, giving an optical decay rate of  $1/\tau = 2\pi \times 224$  MHz. Although strong coupling seems out of reach ( $g_{\text{ep}} \ll \Gamma_{\text{R}}$ ), the coupling can be increased further, eventually enabling optomechanical induced transparency and slow light [155, 156]. Moreover, since several quantum dots can be coupled to the same resonator, see Fig. 3.1(d), the mutual coupling of two (or more) dots to the same mechanical resonator can be studied. The frequency tuning capability of the optical emitters of more than 50 times the linewidth (30 GHz) is another advantage for measurement schemes involving more than one optomechanical system, as for example, optomechanical teleportation [70] or entanglement [157].

### 3.12 Supplementary note I: Quantum dot characterisation



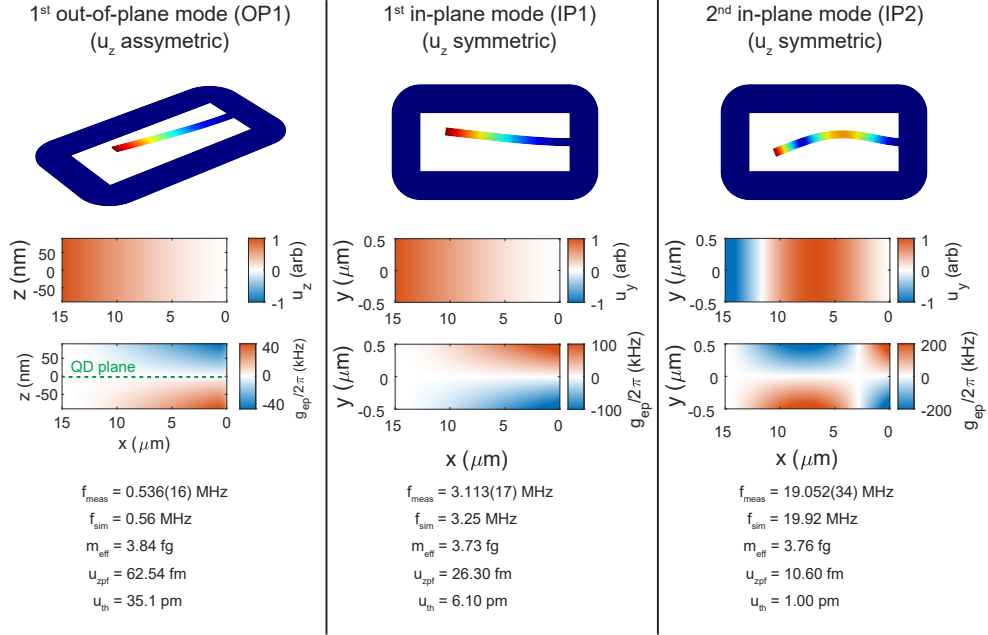
**Figure 3.10: Quantum dot characterisation.** (a) Resonant linewidth scan of QD1 much below saturation power to prevent power broadening. The Lorentzian fit gives a linewidth  $\text{FWHM} = 435$  MHz. (b) Lifetime measurement of QD1 using ps-pulse excitation.  $\tau = 711$  ps is obtained by a single-exponential fit. (c) Resonant power dependence for calibration of the Rabi frequency  $\Omega_R$ . (d) Spectral fluctuation of the quantum dot resonance during the Brownian-motion measurement. A fluctuation with a FWHM of about 115 MHz is measured, shown in (e). (f) Autocorrelation measurement used for the estimation of the exciton-phonon coupling rate. The bunching close to zero delay is partially due to charge noise but also due to the onset of Rabi oscillations.

Fig. 3.10 shows the characteristics of QD1: (a) quantum dot linewidth, (b) excited-state lifetime, (c) power saturation curve, (d) and (e) spectral fluctuation, and (f) long-time-delay autocorrelation. These measurements are repeated for all three quantum dots. The linewidth scan is performed at very low excitation powers to avoid power broadening, here,  $\Omega_R = 0.065\Gamma_R$ . The extracted linewidth is  $\text{FWHM} = 435$  MHz, which is 1.9 times the Fourier limit  $1/(2\pi\tau)$ . The latter is obtained from a lifetime measurement performed with ps-pulses from a mode-locked laser. The measurement shows a single exponential decay with a time constant of  $\tau = 711$  ps. Here, we assume the same excited-state lifetime for QD1 and QD2 since the ps-pulses are too broad to individually excite the two dots. The linewidth of QD2 and QD3 are 490 and 410 MHz, respectively. The lifetime of QD3 is  $\tau = 916$  ps. Note that the linewidth during the autocorrelation measurements is already slightly power broadened to  $\text{FWHM} \approx 600$  MHz. The quantum dot emission measured as a function of excitation power shows the behaviour of an optical two-level system with saturation above  $\Omega_R = \Gamma_R$ :

$$\rho_{ee} = \frac{\frac{1}{2}\Omega_R^2}{\frac{1}{2}\Gamma_R^2 + \Omega_R^2}, \quad \Omega_R^2 \propto P_{\text{laser}}, \quad (3.15)$$

where  $\rho_{ee}$  is the excited state population (see Chapter 1),  $\Omega_R$  the Rabi frequency, and  $\Gamma_R$  is the excited state decay rate. Note that if  $\Omega_R \rightarrow \infty$  using continuous wave excitation, the excited state population is maximised to  $\rho_{ee} = 0.5$ . Every data point in the power measurement presents the peak intensity of a linewidth scan. The measured data together with Eq. 3.15 is used to convert the excitation power to the Rabi frequency  $\Omega_R$ . This calibration measurement is repeated whenever the optical setup is changed, the quantum dot position is changed, or the cryostat is refilled with liquid helium. As described previously, spectral fluctuation is corrected during the Brownian-motion measurement by tracking the resonance frequency every two minutes. During the tracking of the quantum dot resonance, the autocorrelation measurement is paused. We assume a Gaussian fluctuation which shows a FWHM of 115 MHz. This shows the importance of the tracking technique: the small but finite detuning of the probing laser of 180 MHz is in the same order of magnitude and is essential for a precise measure of the exciton-phonon coupling rate. For a correct estimation of the exciton-phonon coupling, it is also important to perform a correct normalisation of the autocorrelation measurement. Therefore, the autocorrelation is recorded for long time delays up to  $3 \mu\text{s}$  where we normalise the coincidence counts to one. The bunching peak at short time delays is partially due to the onset of Rabi oscillations and partially due to blinking. Note that the measurement is very sensitive to charge noise since it is recorded with a detuned laser. For more details on the noise performance of the dots see Chapter 5.15.

### 3.13 Supplementary note II: Finite-element simulations



**Figure 3.11: Finite-element simulations.** Displacement profile  $u$ , exciton-phonon coupling rate  $g_{\text{ep}}$ , effective mass  $m_{\text{eff}}$ , and zero-point motion  $x_{\text{zpf}}$  for the first out-of-plane, first in-plane and second in-plane modes. The effective mass and subsequently the zero-point motion are obtained by thermomechanical calibration. The exciton-phonon coupling rate is then estimated using deformation potential couplings.

The mechanical resonator is designed using Comsol Multiphysics, where the equations of motion are solved for a pre-defined mesh. The size of the mesh units is optimised by performing a convergence test. The outcomes of the simulations are shown in Fig. 3.11. [100] material parameters of GaAs are used together with an in-plane rotated coordinate system to align the x-axis of the design to [110], which is the x-axis of our wafer material. Eigenmode studies with fixed boundary conditions are performed to find the eigenfrequencies, displacement and strain profiles of the resonator. Using thermomechanical calibration [128], effective mass  $m_{\text{eff}}$  and zero-point motion  $x_{\text{zpf}}$  [29] are obtained:

$$m_{\text{eff}} = \int \rho \left( \frac{|u(x, y, z)|^2}{\max(|u(x, y, z)|^2)} \right) dV \quad (3.16)$$

$$x_{\text{zpf}} = \sqrt{\frac{\hbar}{2m_{\text{eff}}\Omega_{\text{m}}}}, \quad (3.17)$$



where  $\rho$  is the material density of GaAs, and  $|u(x, y, z)|$  is the norm of the displacement vector. The Brownian motion is then given by the equipartition theorem [98]:

$$x_{\text{th}} = x_{\text{zpf}} \sqrt{\frac{2k_{\text{B}}T}{\hbar\Omega_{\text{m}}}}, \quad (3.18)$$

where  $T$  is the phonon-bath temperature and  $k_{\text{B}}$  is the Boltzmann constant. The strain profile obtained in Comsol is also normalised via thermomechanical calibration and is used to estimate the quantum dot energy shift via deformation potential couplings for hydrostatic and shear strain of GaAs [20, 98],  $a = -8.33$  eV and  $b = -1.7$  eV [138, 139]:

$$\delta E = a(\epsilon_{xx} + \epsilon_{yy} + \epsilon_{zz}) - \frac{b}{2}(\epsilon_{xx} + \epsilon_{yy} - 2\epsilon_{zz}). \quad (3.19)$$

Finally, we estimate the vacuum exciton-phonon coupling rate using the zero-point motion:

$$g_{\text{ep}} = \frac{\partial \omega}{\partial x} x_{\text{zpf}} = \frac{\delta E}{\hbar}. \quad (3.20)$$

### 3.14 Supplementary note III: Electric-field antenna characterisation

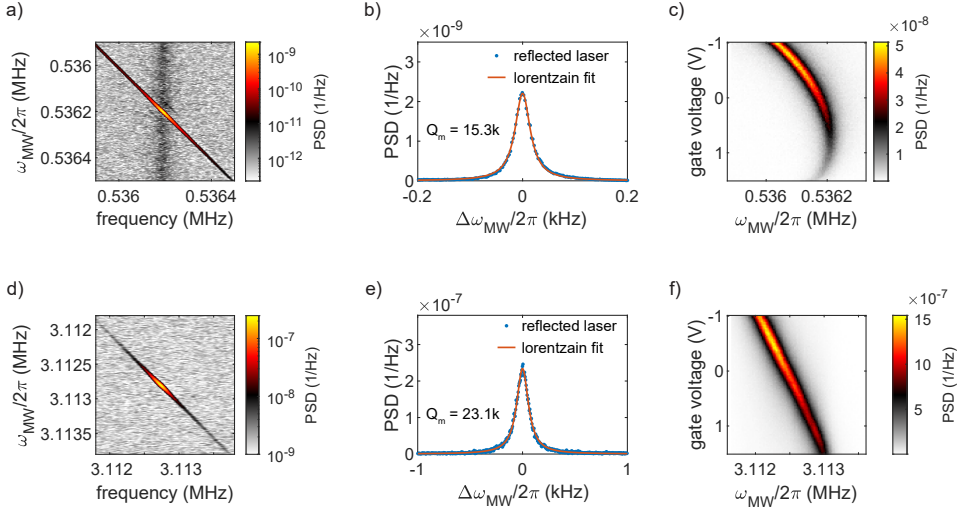


**Figure 3.12: Characterisation of the antenna driving as a function of the applied bias voltage.** (a,d) Measurement of the mechanical frequency at 0 V bias of OP1 and IP1 by positioning the laser spot at the tip of the cantilever. The reflected laser light is detected, amplified and send to a spectrum analyzer and for each microwave frequency a spectrum is recorded. (b,e) The diagonal cuts in (a,d) result in mechanical resonance scans with quality factors of  $1.5 \times 10^4$  and  $2.3 \times 10^4$ , respectively. (c,f) Mechanical resonance scans as a function of applied gate voltage. A clear shift of the mechanical frequency from 0 V to the quantum dot gate voltage of 1.32 V is observed. Additionally, a dependence of the mechanical amplitude on the applied bias is observed.

The mechanical driving is characterised by focusing the laser spot at the cantilever tip, where the displacement is maximal. The reflection of the laser is changed by the cantilever displacement, which is monitored with a fast photodiode and a spectrum analyzer. Note that only OP1 and IP1 give a strong enough change in reflection to be recorded with this method. A mechanical resonance scan is performed at a gate voltage of 0 V (where the QDs are not active) by sweeping the applied antenna microwave frequency while recording the noise power. In Fig. 3.12(a) and (d) each horizontal line represents one spectrum recorded with the spectrum analyzer while driving OP1 and IP1, respectively. As a function of applied microwave frequency, a strong noise peak due to mechanical driving can be observed. The weak background in the centre of Fig. 3.12(a) is the Brownian motion of the mechanical mode, which is highly amplified once the driving frequency is resonant.

Fig. 3.12(b) and (e) show diagonal cuts of the data presented in Fig. 3.12(a) and (d). The two mechanical modes show a Lorentzian mode profile with quality factors (FWHM) of  $1.5 \times 10^3$  (35 Hz) and  $2.3 \times 10^3$  (135 Hz). Figures 3.12(c) and (f) show the mechanical resonance scan as a function of applied diode bias for the two

mechanical modes. Both, OP1 and IP1, show a reduced mechanical amplitude for forward bias. We speculate that this is due to the reduced electric field within the p-i-n diode when forward bias is applied. The frequency dependence with respect to the applied bias behaves differently for the two mechanical modes. For OP1 there is a quadratic-like and for IP1 a linear dependence. However, for a detailed analysis, further investigations are needed.

### 3.15 Supplementary note IV: Measurement setup

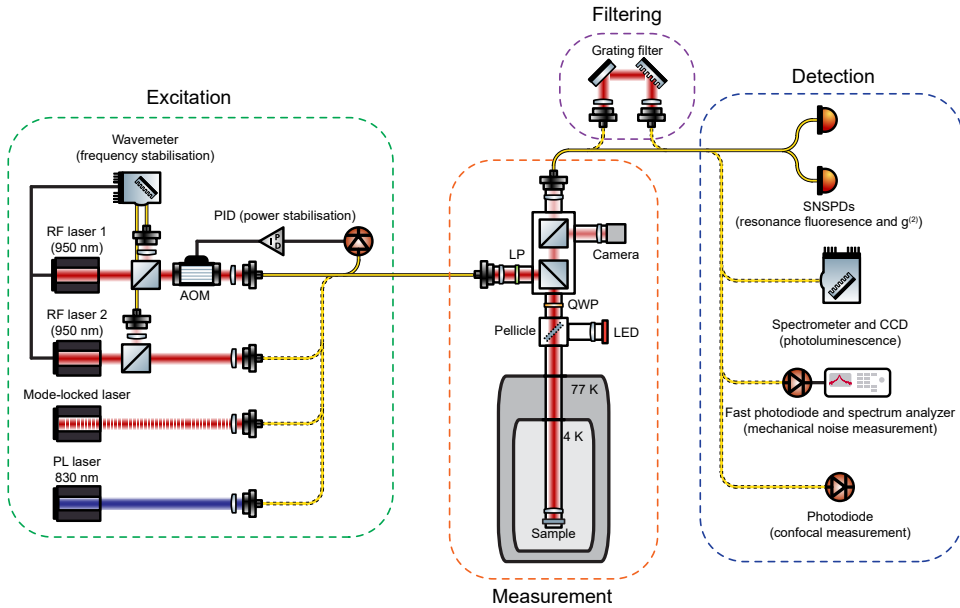


**Figure 3.13: Simplified optical setup.** Excitation: four different lasers are used for the various measurements including two frequency stabilised resonant (RF) lasers, a mode-locked laser for pulsed excitation, and an above band (PL) laser. A double-pass acoustic-optic-modulator (AOM) setup is used for power stabilisation and power control. Measurement: the sample is held at 4.2K in a He-bath cryostat. A cross-polarisation scheme is used for suppressing the reflected laser light. An LED and a camera are installed for imaging the sample surface with a field of view of about  $10 \mu\text{m}$ . Filtering and detection: dependent on the measurement, the collected quantum dot emission is sent to either single photon detectors (SNSPDs), a spectrometer, a spectrum analyzer, or just a photodiode.

The sample is mounted on a set of x/y/z-piezo steppers (Attocube, ANPx101 & ANPz101) and an x-y-scanner (Attocube, ANSxy100lr) in a home-built vacuum-tube microscope with an optical  $\text{NA} = 0.65$ . The tube is pump-flushed several times with helium gas before final pumping to  $4 \times 10^{-6}$  mbar with subsequent filling of 0.2 mbar helium exchange gas (final pressure of  $\approx 2.8 \times 10^{-3}$  mbar at 4.2 K). The gas pressure is chosen such that gas damping is negligible, which we find below 1 mbar at room temperature, see Chapter 4.9. The tube is precooled in liquid nitrogen (77 K) for 2 hours and finally moved into a helium bath cryostat (Cryovac) at 4.2 K. Note that our cryostat also holds a 3 T in-plane (9 T out-of-plane) superconducting magnet (Cryovac) and a liquid nitrogen shell to reduce liquid helium consumption. The mechanical quality factor of OP1 at different temperatures is:  $Q_m^{300\text{K}} = 1.3 \times 10^3$ ,  $Q_m^{77\text{K}} = 3.8 \times 10^3$ , and  $Q_m^{4\text{K}} = 1.5 \times 10^4$ . The improvement at low temperatures is typically connected with reduced intrinsic losses. For example, the coefficient of linear expansion is lower at cold temperatures which reduces thermoelastic damping, see Refs. [136, 151].

The quantum dot membrane sample bias voltage is controlled with a digital-to-analogue converter (Basel Precision Instruments, DAC SP 927) and the microwave signal applied to the electric field antenna is generated with an arbitrary waveform generator (Keithley, 3390). The main optical components of the setup are shown in Fig 3.13. The optical excitation part of the setup consists of three different lasers: a diode laser at 830 nm for photoluminescence excitation (PicoQuant, LDH-D-C-830), a mode-locked laser for quantum dot lifetime measurements (Coherent, Mira 900-D), and two tunable diode lasers at 950 nm for resonant excitation (Toptica, DL pro). The resonant lasers are frequency stabilised using a wavemeter (HighFinesse) and power stabilised using a double-pass acousto-optic modulator setup (Gooch and Housego, AOM 3200-1113 & AODR 1200AF-AINA-2.5 HCR) with a home-built PID-controller. All lasers are fibre-coupled (Thorlabs, SM-780HP) and sent to the cross-polarised optical microscope head. At the heart of the microscope head, there are two polarising beam splitters [112]. Together with a linear polariser and a quarter-waveplate, a laser suppression of  $10^{-6}$  is achieved. An LED (Thorlabs, M940D2), a camera (Allied Vision, Guppy), and a removable pellicle beamsplitter (Thorlabs, BP145B2) are installed for imaging of the sample surface, giving a field-of-view of around  $10\ \mu\text{m}$ . The collected quantum dot emission is then fibre coupled and sent to the detection setup. Dependent on the measurement, we chose between single-photon detectors (Single Quantum, Eos) connected to a time tagging module (Swabian Instruments, Time Tagger Ultra), a Peltier-cooled CCD connected to a spectrometer (Teledyne Princeton Instruments, Blaze 100HRX & Acton SP2500i with 300, 1200, and 1500 grooves/mm), a fast photodiode connected to an electronic spectrum analyzer (Rohde&Schwarz, FPL1007), or a photodiode connected to an IV-converter (Stanford Research Systems, SR570) and a multimeter (Keithley, 2000).

---

**Mechanical damping in a quantum-dot  
optomechanical device**

---

## 4.1 Introduction

Mechanical resonators find a wide range of applications; from precision sensing at the atomic level [158] to macroscopic sensing of gravitational waves [146]. For the majority of applications, it is important to reduce the mechanical damping mechanisms (mechanical losses), to a minimum. Therefore, mechanical losses have been studied extensively in the past decades for various types of resonators [127, 131, 135, 159, 160]. Some of the main mechanical losses are identified to be either due to radiation to the surrounding substrate or poor surface quality [127, 161] (including surface roughness, surface impurities, surface oxidation, etc.).

Classifying the damping mechanisms is not always straightforward. This has recently been a challenge in quantum dot optomechanical devices [20]. These devices are made of a layer of self-assembled quantum dots and a heterostructure diode with highly doped gate layers for quantum dot charge control [66, 109]. Moreover, measuring mechanical losses via the quantum dot mechanical coupling is challenging because of the single-photon nature of the optical two-level system. The photon count rate can be several orders of magnitude lower than the mechanical frequency. Thus, resolving the mechanical linewidth (mechanical damping rate), can take up to hours of measurement time [20, 55].

In the following chapters, we introduce a Fabry–Pérot-like optical cavity in a quantum-dot optomechanical device. We leverage the cavity-optomechanical interaction to probe the mechanical damping associated with the quantum dot mechanical device. Thanks to the classical optical resonator, the measurement time of the mechanical damping rate is in the order of a few seconds. Additionally, we make use of the optomechanical interaction rate, scaling with  $\sqrt{\bar{n}_{\text{cav}}}$ , to greatly increase our sensitivity by reducing the effective mechanical damping by two orders of magnitude [162, 163]. This is achieved by blue-detuned driving of the optical cavity. The optical power is chosen in such a way that the mechanical amplitude is close to the phonon lasing threshold, where the effective mechanical damping approaches zero [29]. Thus, the system is highly susceptible to any changes in the mechanical properties of the resonator. We implement a two-laser pump-probe scheme in which we first stabilise the system close to phonon lasing and then introduce a weak perturbation. Damping rates due to either applying an electric field to the semiconductor diode [109] or due to photoluminescence excitation of the quantum dots [102] are measured. The first part of this chapter will focus on the cavity-optomechanical method to implement the increased sensitivity, followed by the second part, which will focus on the additional damping added by the perturbations.

## 4.2 Optomechanical device

The hybrid system consists of a  $15 \times 1 \times 0.18 \mu\text{m}^3$  GaAs cantilever which is selectively under-etched [97], see Fig. 4.1(a). The cantilever hosts self-assembled InAs quantum dots [102] and a doped p-i-n diode for quantum dot charge control. An optical cavity of length  $l_{\text{cav}} = 970 \text{ nm}$  forms between the cantilever and the substrate, where the optomechanical coupling is highest at the cantilever tip. The mechanical out-of-plane (asymmetric) bending of the cantilever results in a displacement of the top mirror of the Fabry–Pérot cavity and shifts the cavity resonance by  $\partial\omega_{\text{cav}}/\partial x = 270 \cdot 2\pi$

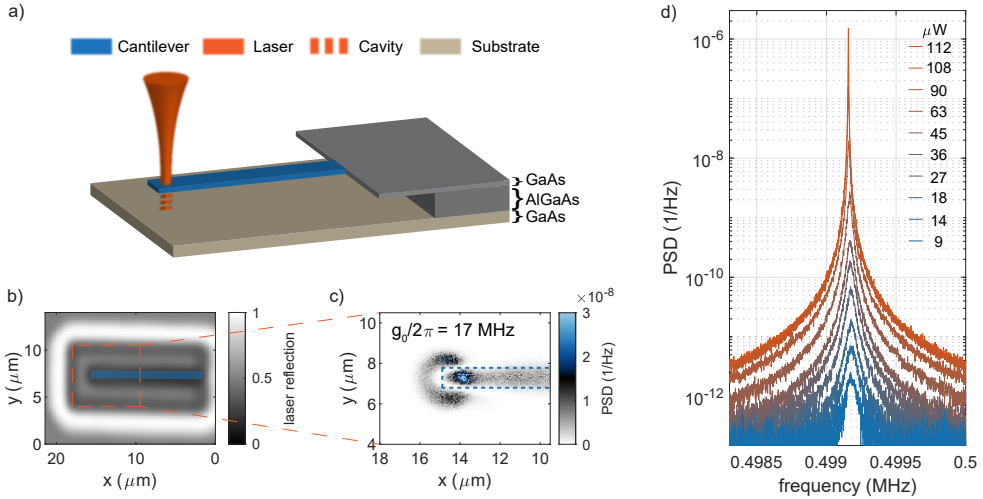


**Figure 4.1: Fabry–Pérot optomechanical cavity.** (a) An optical cavity of 970 nm forms between the cantilever tip and the substrate. The first-order bending mode of the cantilever couples to the optical cavity with a rate of  $g_0/2\pi = 17$  MHz. (b) Confocal laser reflection scan of the  $15 \times 1 \mu\text{m}^2$  cantilever (highlighted in blue). The bright frame surrounding the cantilever is the under-etched membrane remaining from the isotropic AlGaAs etching process. (c) Mechanical noise power spectrum map of the cantilever in (b) at low probe laser powers. (d) Power spectral density of the first-order bending mode with increasing probe laser power at 945 nm (blue detuned).

GHZ/nm. For more details on the coupling-rate estimation, see Chapter 4.4. Although the optical quality of the cavity is poor,  $Q_o \approx 10$ , the single-photon optomechanical coupling rate is very strong,  $g_0/2\pi \approx 17$  MHz. Thus, only small pump powers,  $10 \mu\text{W}$  at 910 nm, are required to bring the system to the phonon lasing regime [164].

Figure 4.1(b) shows a confocal map of the cantilever structure where the reflected laser is recorded with a photodiode. The cantilever, highlighted in blue, is surrounded by the remaining under-etched membrane. A weak probe laser close to the cavity resonance ( $\Delta\omega_1^{\text{probe}} = \omega_1^{\text{probe}} - \omega_{\text{cav}} > 0$ ,  $\Gamma_{\text{om}} < 0$ ) is focused at the tip of the cantilever and the reflected signal is recorded using a fast photodiode (Thorlabs SM05PD1A & Femto DHPCA-100) and an electronic spectrum analyzer (R&S FPL1007). Figure 4.1(c) shows the power spectrum of the mechanical mode mapped out as a function of the laser position on the cantilever tip. The highest response of the optomechanical cavity is obtained in the centre at the tip of the cantilever. Due to the classical nature of the optical cavity, the optomechanical interaction can be scaled by the (square root) intra-cavity photon number,  $g = g_0\sqrt{n_{\text{cav}}}$  [29]. As a consequence, the response of the probe laser scales with power [27], see Fig. 4.1(d). Two effects are visible in the power spectrum. First, a higher probe power increases the absolute mechanical noise on the photodiode and results in a higher signal-to-noise ratio. Second, a higher optomechanical interaction increases the mechanical amplitude, which results in a stronger noise peak in the power spectrum.



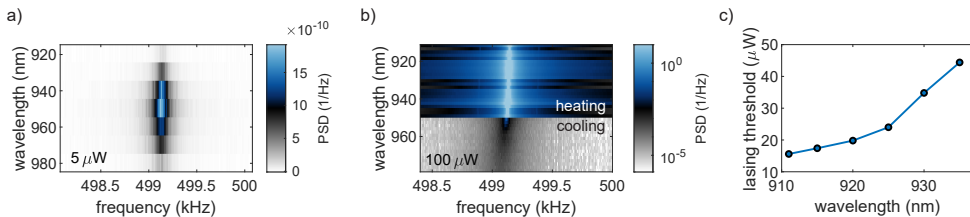


**Figure 4.2: Characterisation of the optomechanical cavity.** (a) Mechanical power spectrum as a function of probe-laser wavelength at low powers. The measurement sensitivity depends on the cavity detuning and the collection efficiency of our setup which is optimised at 950 nm. (b) Same as in (a) but with high probing powers. The optomechanical interaction switches from heating to cooling at the cavity resonance of 950 nm. (c) Threshold power to reach phonon lasing as a function of the pump-laser wavelength.

### 4.3 Optical cavity characterisation

The optomechanical cavity forms between the cantilever and the substrate after under-etching. The etching step is selective to the AlGaAs sacrificial layer, which has a thickness of  $1.15 \mu\text{m}$  (see Chapter 2). Since the etching is isotropic we can confirm by the remaining under-etched membrane of  $2.7 \mu\text{m}$  around the cantilever, that all AlGaAs below the cantilever was etched away. However, we see that the cavity length deviates slightly from the thickness of the sacrificial layer. This is because the  $15 \mu\text{m}$  long cantilever tends to bend upwards or downwards. This we observe by a changing focus when moving along the cantilever (y-direction).

Measuring the exact cavity length, however, is not straightforward, since our optical setup is not optimised for such a wide wavelength range. The setup is usually aligned on bulk around 950 nm with an outcoupling efficiency of the reflected laser of up to 60%. Nevertheless, we measure the mechanical noise power as a function of laser wavelength to estimate the cavity resonance at the cantilever tip. Fig. 4.2(a) and (b) show the power spectrum for the mechanical out-of-plane (asymmetric) bending mode at 5 and  $100 \mu\text{W}$  laser power, respectively.

At low powers, Fig. 4.2(a), the optomechanical interaction is negligibly small and no significant (anti)damping is induced. Thus, a potential resonance is found, however, this resonance is also influenced by the optical alignment and mechanical noise sensitivity of our setup. At high powers, Fig. 4.2(b), we leverage the optomechanical interaction to estimate the cavity resonance. For blue detuning, we introduce mechanical antidamping (heating). Here, the power is chosen such that for all detunings the optomechanical antidamping is large enough to introduce phonon lasing. For red detuning, the laser induces optomechanical damping, or cooling, which highly increases the mechanical linewidth. The transition from heating to cooling marks the resonance of the cavity [127], which we find around 950 nm. We double-check the resonance of the cavity at intermediate powers to make sure to not overlook any effect of cavity length dragging due to actual heating and expansion of the cantilever [165]. Note that if thermal expansion were happening, the optical resonance would not be much affected, since expansion of the mechanical resonator affects mainly the xy-plane and not the cavity length. Figure 4.2(c) shows the threshold power needed to reach the

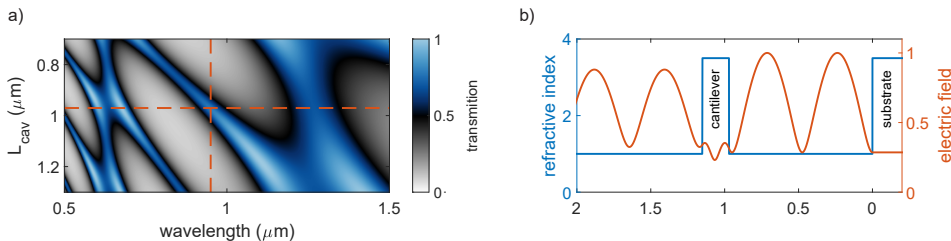


**Figure 4.3: Transfer matrix description of the optical cavity.** (a) Reflection of the optical cavity using a transfer matrix approach. The cavity resonance of  $\lambda = 950$  nm is satisfied with a cavity length of  $L_{\text{cav}} = 970$  nm, highlighted in red. (b) Normalised electric field showing a slight enhancement inside the cavity.

phonon lasing regime depending on the laser wavelength. The cavity resonance is very broad,  $\kappa \approx 28$  THz (90 nm, see Fig.4.3(a)), thus we also observe phonon lasing for large detunings.

## 4.4 Optomechanical coupling rate

In the following paragraphs, we describe the optical cavity using a transfer matrix approach, with  $n_{\text{GaAs}} = 3.5$ . The reflection of the cavity is simulated as a function of the cavity length and the laser wavelength, Fig. 4.3(a). When the laser is in resonance with the cavity, the reflection is reduced. We use these simulations to estimate the actual cavity length, which we do not know exactly due to the unknown bending of the cantilever. To obtain an optical resonance at 950 nm the cantilever needs to bend 180 nm downwards at the tip to reach a cavity length of 970 nm, which is reasonable given its length of 15  $\mu\text{m}$ . The electric field of such an optical mode is shown in Fig. 4.3(b), where the field is slightly amplified inside the cavity.

The transfer matrix simulations can also be used to estimate the single-photon optomechanical coupling rate  $g_0 = (\partial\omega_{\text{cav}}/\partial x) \cdot x_{\text{zpf}}$ . From the slope of the optical mode in Fig. 4.3(a) we obtain  $\partial\omega_{\text{cav}}/\partial x = 270 \cdot 2\pi$  GHz/nm. Together with the zero-point motion,  $x_{\text{zpf}} = 62.54 \times 10^{-15}$  m, obtained from finite element simulations, we estimate  $g_0/2\pi = 17$  MHz. A similar value is obtained when using the standard Fabry-Pérot optomechanical cavity equation,  $g_0/2\pi = (\omega_{\text{cav}}/L_{\text{cav}}) \cdot x_{\text{zpf}} = 20$  MHz [127].

## 4.5 Pump-probe optomechanical experiments

To avoid the effect of the probe power on the mechanical sensitivity, we introduce a two-laser pump-probe experiment, see Fig. 4.4(a). The setup consists of a weak probe laser of  $P_{\text{probe}} = 5 \mu\text{W}$  at 945 nm and a variable pump laser at 910 nm, where we observe the lowest phonon lasing threshold of  $P_{\text{pump}} = 10 \mu\text{W}$  (see Fig. 4.2). The frequencies of the lasers are stabilised with a wavemeter and the power of the pump laser is stabilised using a double-pass acousto-optic modulator (AOM) setup together with a home-built PID-loop [21, 22]. The circularly polarized lasers are focused on

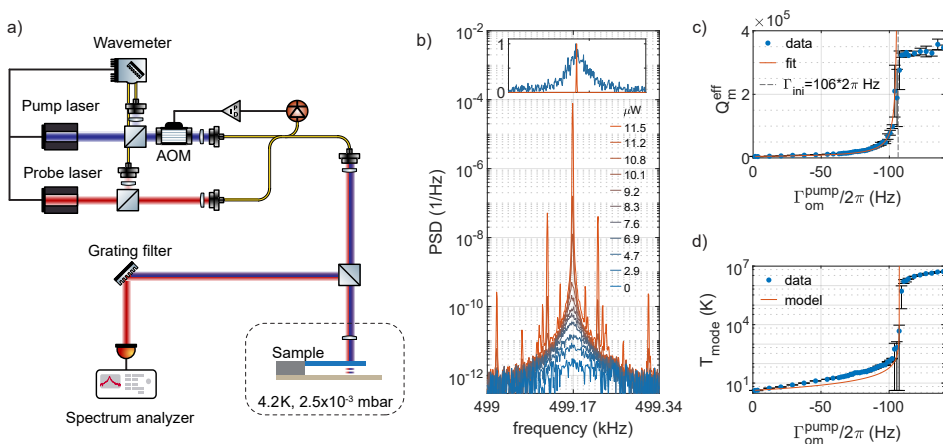


**Figure 4.4: Two laser experiments and dynamical instability.** (a) Schematic of the two-laser experiment with a probe laser close to resonance and a blue detuned pump laser. A grating filter (FWHM 150 GHz) is implemented to filter out the pump and monitor the reflected probe on a spectrum analyzer. (b) Power spectrum as a function of pump laser power. Already at low pump powers phonon lasing can be observed. The inset at the top shows the highly reduced mechanical linewidth (more than two orders of magnitude) above the phonon lasing threshold. (c) Effective mechanical quality factor versus optomechanically induced antidamping. We observe an increase of two orders of magnitude, from  $Q_m^{\text{ini}} = 5.8 \times 10^3$  to  $Q_m^{\text{eff}} = 3.5 \times 10^5$ . (d) Mechanical mode temperature obtained from integrating the power spectral density. Once the optomechanically induced damping overcomes the intrinsic loss rate,  $-\Gamma_{\text{om}}^{\text{pump}} > \Gamma_{\text{ini}}$ , the effective mechanical loss rate goes towards zero and phonon lasing is observed.

the cantilever tip using a polarizing microscope [125]. This design allows up to 60 % of the reflected laser signal to be collected when focusing on bulk material. Finally, a 150 GHz-bandwidth grating-based filter is introduced to separate the probe from the pump laser. The sample is held in a helium-bath cryostat [8] at 4.2 K and at  $\approx 2.5 \times 10^{-3}$  mbar helium exchange gas.

Figure 4.4(b) shows the power spectrum measured by the reflected probe laser as a function of the pump-laser power. Now, the mechanical noise sensitivity stays constant (as can be seen by the flat noise power away from the mechanical resonance) and we only probe the effect on the mechanical amplitude. Note that the additional peaks around the mechanical resonance have been observed also in other systems [166], however, their origin is still unclear. The inset in Fig. 4.4(b) shows the normalised power spectrum at a pump power of 2.9 and 11.5  $\mu\text{W}$ . Since the pump laser is blue detuned, the optomechanically induced interaction leads to antidamping [162],  $\Gamma_{\text{om}}^{\text{pump}} < 0$ . The mechanical quality factor ( $Q_m^{\text{eff}}$ ) and the damping are modified accordingly [29]:

$$Q_m^{\text{eff}} = \frac{\Omega_m}{\Gamma_{\text{ini}} + \Gamma_{\text{om}}^{\text{pump}}}, \quad (4.1)$$

$$\Gamma_{\text{ini}} = \Gamma_{\text{int}} + \Gamma_{\text{om}}^{\text{probe}}, \quad (4.2)$$

where  $\Gamma_{\text{ini}}$  is the initial effective damping (at  $P_{\text{pump}} = 0$ ) given by the intrinsic mechanical damping  $\Gamma_{\text{int}}$  [127] and the residual damping added by the probe laser  $\Gamma_{\text{om}}^{\text{probe}}$ . Figure 4.4(c) shows the extracted effective mechanical quality factor  $Q_{\text{m}}^{\text{eff}}$  as a function of pump-laser power. By fitting Eq. 4.1 to the data we convert the optical pump power to the optomechanical interaction rate. Here, we assume that  $\Gamma_{\text{om}}^{\text{pump}} \propto \bar{n}_{\text{cav}}$  and  $\bar{n}_{\text{cav}} \propto P_{\text{pump}}$  [29]. The introduced antidamping increases the phonon number which increases the mechanical mode temperature and amplitude. Once the effective mechanical damping goes towards zero, any additionally added energy is converted into mechanical displacement. However, when the displacement becomes very large, the optomechanical cavity is no longer effective [167]. Therefore, the effective mechanical quality clamps [167] at  $Q_{\text{m}}^{\text{eff}} = 3.5 \times 10^5$ .

By integrating the power spectrum, the mechanical mode temperature is extracted [127], as shown in Fig. 4.4(d). Here we assume that the initial mode temperature at  $P_{\text{pump}} = 0$  is approximately equal to the bath temperature. The prominent increase in mode temperature at zero effective mechanical damping is a clear feature of dynamical instability or also called phonon lasing [164, 167]. We use the fit parameters from Fig. 4.3(c) and plot the expected mode temperature [29]:

$$T_{\text{mode}} = T_{\text{ini}} \frac{\Gamma_{\text{ini}}}{\Gamma_{\text{ini}} + \Gamma_{\text{om}}^{\text{pump}}}. \quad (4.3)$$

The mode temperature is slightly underestimated at large mechanical amplitudes since we do not integrate the higher-order noise peaks.

## 4.6 Mechanical damping measurements

In the following measurements, we use the two-laser experiment to sensitively probe the mechanical losses associated by either applying a voltage to the semiconductor diode, Fig. 4.5(a), or by using a 830 nm laser for photoluminescence (PL) excitation, Fig. 4.5(d). The measurement is performed as follows. First, the mechanical quality factor is measured with the weak probe laser. Second, the effective mechanical loss rate is reduced by two orders of magnitude from  $\Gamma_{\text{ini}}/2\pi = 106 \text{ Hz}$  to  $\Gamma_0/2\pi \approx 3 \text{ Hz}$  (corresponding to  $Q_{\text{eff}} \approx 1.8 \times 10^5$ ). In this regime, the mechanical resonator is placed at the onset of phonon lasing where the system is stable enough to still create reproducible data. Last, the system is perturbed by sweeping the gate voltage and PL laser power. The corresponding damping rates are extracted via a measurement of the effective mechanical quality factor [29]:

$$\Gamma_{\text{Vg/PL}} = \frac{\Omega_{\text{m}}}{Q_{\text{eff}}} - \Gamma_0, \quad (4.4)$$

$$\Gamma_0 = \Gamma_{\text{ini}} + \Gamma_{\text{om}}^{\text{pump}}. \quad (4.5)$$

Here, we assume that the optomechanical interaction is not significantly influenced by the mechanical perturbation added to the system. Figures 4.5(b) and (e) show the raw data of the mechanical loss measurements, where the shift of the mechanical frequency is highlighted by the dashed line. The corresponding extracted loss rates are shown in Fig. 4.5(c) and (f).

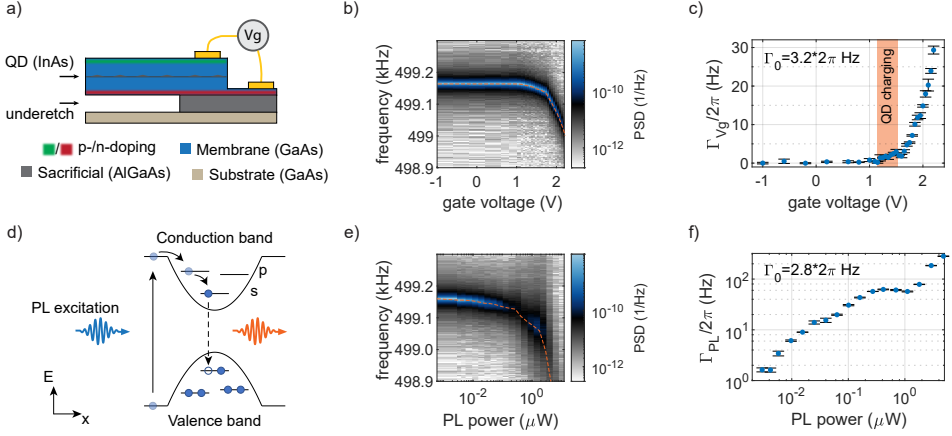


**Figure 4.5: Measurement of mechanical damping due to gate voltage and photoluminescence excitation.** (a) 180 nm thick membrane structure hosting a semiconductor diode and self-assembled quantum dots. By applying a DC voltage to the p- and n-doped gate layers the quantum dot charge state is controlled. (b) Optical excitation scheme of the quantum dot. Electrons are excited from the valence to the conduction band outside the quantum dot. After relaxation to the lowest energy state inside the dot, the electron recombines with a hole from the valence band, emitting a photon. (c,d) Mechanical power spectrum as a function of applied gate voltage and excitation laser power. (e,f) Mechanical damping rate extracted from (c,d), where  $\Gamma_0 = \Gamma_{\text{ini}} + \Gamma_{\text{om}}^{\text{pump}}$ .

When sweeping the gate voltage applied to the semiconductor diode, Fig. 4.5(c), no additional damping is added in the range of  $-1$  to  $1$  V, where the diode leakage current stays below  $20$  nA (below one electron flowing through the cantilever per mechanical oscillation period, see [Supplementary note II](#)). In the region of  $1.15$  to  $1.5$  V, single charge carriers tunnel into the quantum dots and at the same time the leakage current starts to increase. We observe a slight increase of the damping rate to about  $\Gamma_{V_g}/2\pi = 3$  Hz. Above the diode turn-on voltage of  $1.6$  V (see [Supplementary note II](#)), a current starts flowing through the membrane-cantilever, creating an additional mechanical dissipation channel. We conclude that the additional damping is not due to a change in the electric field but due to the current created by the applied voltage.

The  $830$  nm laser creates additional damping already at low excitation powers, see Fig. 4.5(f). Above  $1 \mu\text{W}$  of laser power, the added loss even exceeds the intrinsic mechanical damping. Similar to the gate voltage, the  $830$  nm laser excites a large number of electrons and holes which leads to additional damping. This is a problem for optomechanical experiments based on photoluminescence excitation. For several reasons we assume that the interaction of the  $830$  nm laser with the optical cavity is negligible: (i) the laser is far detuned from the cavity resonance, (ii) the laser is still blue-detuned which should lead to antidamping, and (iii) the focus is far from optimal since we use chromatic optical elements centred around  $950$  nm. Note that this measurement is performed at  $V_g = 0$  V.

## 4.7 Conclusion

In the damping measurements, the change in mechanical frequency (change in spring constant since  $k = m_{\text{eff}}\Omega_{\text{m}}^2$ ) is very small, below 0.2%. Therefore, we assume that the decreasing mechanical quality originates from additional dissipation rather than a change in material properties. In both cases, when either a current starts flowing or electrons are excited, free charge carriers are created. We speculate that these charge carriers increase the mechanical damping rate by electron-phonon scattering [168, 169]. Our measurements show that the damping added by the leakage current at the quantum dot bias voltage limits the achievable mechanical quality to  $\Omega_{\text{m}}/\Gamma_{\text{Vg}} = 1.7 \times 10^5$ . So far, this has not been an obstacle for the current mechanical resonator, which is mainly limited by the intrinsic mechanical quality. However, it might become important for low intrinsic loss quantum dot optomechanical devices involving soft clamping [170, 171] or dissipation dilution [172, 173]. On the contrary, photoluminescence excitation presents a significant issue for quantum dot optomechanical experiments. The usual excitation power in our setup necessary to measure quantum dot photoluminescence is around 0.1-1  $\mu\text{W}$  at which the mechanical damping rate is almost doubled. However, this issue can be overcome by using resonant quantum dot excitation [20].

With the cavity-optomechanical method presented here, we are able to increase our sensitivity to mechanical damping by two orders of magnitude. This enables precise measurements of mechanical perturbations, even if the induced damping is much smaller than the intrinsic mechanical linewidth. However, the increase in sensitivity (and working close to phonon lasing) automatically brings the challenge of a very susceptible system which we solve by careful stabilisation of the pump laser power. The mechanical stability (sensitivity) of our device could be further improved by using an injection locking scheme [167, 174].

## 4.8 Supplementary note I: Optomechanical cooling

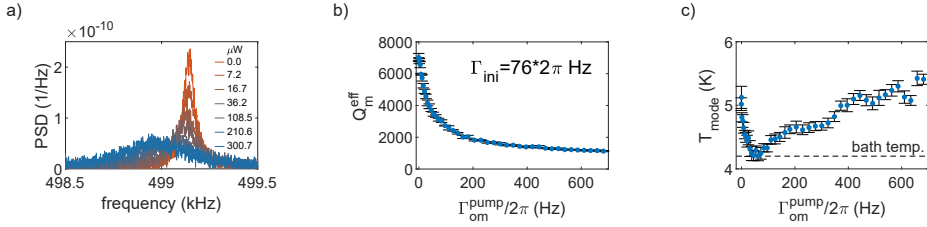


**Figure 4.6: Optomechanical cooling.** (a) Optomechanical interaction with a red-detuned pump laser, where  $\Delta\omega_1^{\text{pump}} < 0$  and  $\Gamma_{\text{om}}^{\text{pump}} > 0$ . (b) The effective mechanical quality factor is reduced due to the additional mechanical damping introduced by the optomechanical interaction. (c) Mechanical mode temperature extracted from (a), since the optomechanical system is in the Doppler regime, cooling below bath temperature, 4.2 K, is not possible.

In chapter 4.5, we describe the optomechanical interaction in the blue detuned case. Here, we will present the effect of a red-detuned pump laser. The induced optomechanical interaction introduces additional damping  $\Gamma_{\text{om}} > 0$ . Red detuning the laser can also be understood as a cavity-enhanced anti-Stokes scattering rate of the laser, whereas the Stokes scattering rate is suppressed. This creates an imbalance between the two rates which reduces the number of phonons of the mechanical oscillator, resulting in effective cooling of the mechanical mode [175]. However, since we are in the Doppler regime ( $\Omega_m \ll \kappa$ ) and our optical cavity is very broad, the lowest phonon number achievable with the optomechanical interaction is much above room temperature, given by  $\bar{n}_{\text{min}} = \kappa/4\Omega_m$  [127].

Figure 4.6(a) shows the mechanical noise power for a red-detuned pump laser at 980 nm. The introduced optomechanical damping increases the mechanical linewidth, Fig. 4.6(b). The measurement is performed in the same way as in Chapter 4.5 by using a weak probe and a strong pump laser. The initial power of the probe laser is increased so that we start at a slightly elevated mechanical mode temperature. At low pump powers, the red-detuned laser cools the mechanical resonator back to the bath temperature, Fig. 4.6(c). When increasing the optomechanical damping further, the linewidth keeps broadening, however, the cooling is ineffective. This can be observed by a slow but steady increase in the mode temperature due to actual heating of the mechanical resonator.

## 4.9 Supplementary note II: Device characterisation and clamping loss

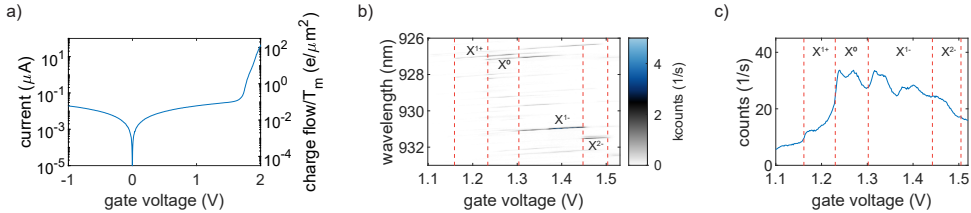


**Figure 4.7: Electrical and optical device characterisation.** (a) Voltage-current properties of the heterostructure diode. The current is converted to a charge flow per unit area and per mechanical period, plotted on the right y-axis. (b) Photoluminescence of a single quantum dot as a function of applied diode gate voltage. The individual exciton regions are highlighted in red. (c) Ensemble photoluminescence of about five quantum dots, showing a similar gate voltage dependence as in (b).

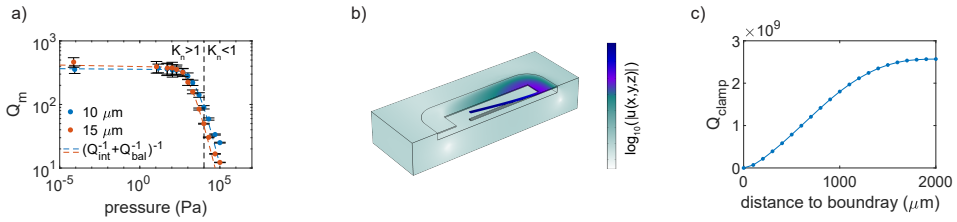
Figure 4.7(a) shows the current-voltage measurement of the semiconductor diode, with a diode turn-on voltage of 1.6 V. The leakage current below the diode turn-on remains below 35 nA. With the diode area of 4 mm<sup>2</sup> and assuming a homogeneous current flow, the current is converted to a charge flow per unit area and per mechanical oscillation. Figure 4.7(b) shows the photoluminescence of a single quantum dot located on the cantilever. The exciton charging voltage is found between 1.15 - 1.5 V. Individual excitons are highlighted in red, from the single positively charged exciton X<sup>1+</sup> to the double negatively charged exciton, X<sup>2-</sup>. Ensemble photoluminescence recorded on bulk material shows a charging behaviour similar to that of the single quantum dot, Fig. 4.7(c). The collected counts are averaged over the full wavelength range of 920-940 nm.

Figure 4.8(a) shows the mechanical quality factor of a 10 and 15 μm<sup>2</sup> long cantilever. The measurement is performed at room temperature in dependence on the helium-gas pressure inside the measurement chamber. The dashed line indicates the transition from the fluidic to the ballistic regime. The transition is defined by the Knudsen number,  $K_n = 1$ , which is given by the ratio of the mean free path of the gas and the representative physical length scale of the mechanical resonator (cantilever width [127]). The dashed lines show the sum of the intrinsic quality,  $Q_{\text{int}}$ , and the gas damping in the ballistic regime,  $Q_{\text{bal}}$ . The latter is a linear function of the gas pressure  $p$  and is fitted using a free fit parameter,  $Q_{\text{bal}}^{-1} = c_1 p$  [127]:

$$Q_m^{-1} = Q_{\text{int}}^{-1} + c_1 p. \quad (4.6)$$

Note that in the fluidic regime,  $K_n < 1$ , where the dimension of the mechanical resonator is greater than the mean free path of the gas, the mechanical quality starts to deviate from the ballistic damping. The pressure that was finally selected for cooling down the measurement chamber is 20 Pa which gives a final pressure of 0.28 Pa at 4.2 K.





**Figure 4.8: Mechanical device characterisation.** (a) Mechanical quality factor in dependence of pressure (gas damping), for a 10 and 15  $\mu\text{m}$  cantilever. (b) Displacement norm of a finite element simulation with a mirror symmetry in the  $xz$ -plane. Here, the distance from the cantilever to the boundary in each direction is 5  $\mu\text{m}$ . (c) Simulated mechanical quality of the finite element simulation in dependence on the distance from the cantilever to the boundary layers.

In Chapter 4.5 we observe that the intrinsic mechanical damping is relatively high, compared to standard cantilever devices [133]. A major source could be surface friction losses [127], due to the high surface-to-volume ratio [161] [176]. Clamping losses are usually at low levels in long and thin cantilevers, which we estimate here  $Q_{\text{clamp}} \approx 2 \times 10^9$ , assuming a semi-infinite elastic substrate [127]. A similar behaviour is observed in finite element simulations; see Fig. 4.8(b) and (c). We apply a lossy (low-reflecting) boundary condition to all four side walls and the bottom. The mechanical quality initially increases as a function of the distance between the cantilever and the boundary layers and in the end, converges towards  $Q_{\text{clamp}} \approx 2.6 \times 10^9$ . Note that in this simulation no material loss is added.

---

**Quantum-dot optomechanics in the sideband  
regime**

---

## 5.1 Introduction

Quantum dot optomechanics in the unresolved-sideband regime was shown in Chapter 3, with mechanical frequencies as high as 19 MHz. In this regime, the coupling between the two systems is measured by detuning the laser from the quantum dot resonance such that the derivative of the count rate (with respect to the laser detuning) is maximised. With this, highest mechanical noise sensitivity is achieved and the mechanical modulation of the quantum dot transition energy is imprinted on the emission count rate. From another perspective, the interaction of the laser with the quantum dot, more specifically the Rabi frequency and the excited-state population, are also modulated (however with a slight delay). This, in turn, gives a time-dependent back-action force on the mechanical system, since the presence of an exciton in the quantum dot leads to strain [55].

This chapter presents an optimised mechanical resonator design and gives a first insight into quantum dot optomechanics in the regime where the mechanical frequency is larger than the quantum dot decay rate. The mechanical resonator is designed such that there is a series of mechanical modes with frequencies lower ( $\Omega_m/2\pi < 150$  MHz) and higher than the excited-state decay rate ( $\Omega_m/2\pi > 150$  MHz). This allows us to study the coupling of the hybrid system in both frequency regimes with the same device. An additional feature compared to the cantilever structure is that the new design also hosts in-plane breathing modes (longitudinal modes) [177]. These modes have a higher spring constant and thus also a higher vibrational frequency compared to in-plane bending modes (lateral modes), see Fig 5.1 and Tab.5.1. This allows a larger resonator size at high mechanical frequencies which facilitates quantum dot localisation.

Chapter 5.2-5.4 will focus on the general optical and mechanical device characterisation, Chapter 5.5-5.6 on the detection of Brownian motion using the coupling between the two systems, and Chapter 5.7.1-5.7.7 on the modulation of the quantum dot resonance by additional mechanical actuation using a classical but coherent drive. Note that from now on the quantum dot frequency shift at 4.2 K,  $\delta E/\hbar$  (see Chapter 3), is replaced by the thermal coupling rate  $g_{\text{th}}$ .

## 5.2 Optimised mechanical resonator design

The mechanical resonator is similar to the cantilever shown in Fig. 3.1: both resonators consist of a beam of roughly equal dimensions. Here, a simple yet highly effective change is made to the design which is that the resonator is detached from the surrounding under-etched substrate [151, 178]. This is achieved by freely suspending the beam using four 200 nm wide and 2.8  $\mu\text{m}$  long tethers. Though this minimises the contact with the under-etched substrate, there is still a finite coupling, especially for higher-order in-plane bending modes.

A major advantage of this resonator design is that longitudinal breathing modes can be observed. With the cantilever resonator, these modes hybridised with the under-etched substrate, resulting in a highly increased mode volume and a highly reduced mechanical quality factor and thus they were not observed in the experiments. With the optimised design, these in-plane breathing modes are observed, even up to the 3rd-order.

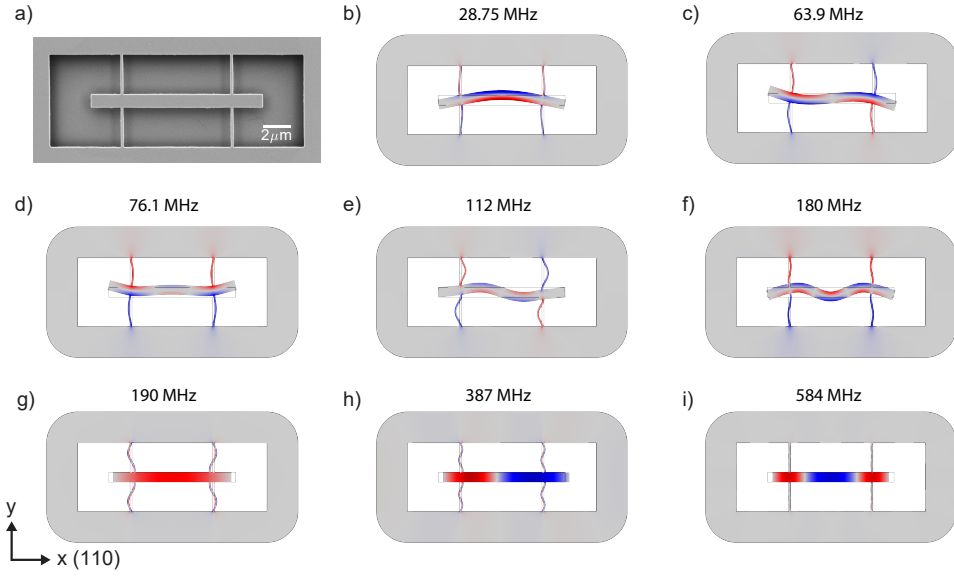


**Figure 5.1: Finite-element simulations of the mechanical resonator.** (a) Scanning electron microscope image of the suspended beam resonator. (b-i) Mode profile (shown as displacement) and quantum-dot mechanical coupling profile (normalised colour scale) of all modes which are observed in the experiments. The resonance frequencies obtained from the measurements are displayed for every mode. (b-f) 1st- to 5th-order in-plane (symmetric/even) bending modes, showing a clear asymmetry in the coupling profile. Quantum dots need to be displaced from  $y = 0$  to couple to these modes. (g-i) 1st- to 3rd-order in-plane breathing modes showing a very homogenous coupling profile. This facilitates quantum-dot-mechanical coupling and limits the search for a good quantum dot to a single geometrical axis (x-axis).

The design of the freely suspended beam is optimised using finite-element simulations (COMSOL Multiphysics, see Fig. 5.1(b-i)). The resonator is optimised for two different beam lengths:  $12\ \mu\text{m}$  which is shown in the following chapters, and  $25\ \mu\text{m}$  which is shown in [Supplementary note VI](#). The width of the beam is also optimised such that the outcoupling of the emission of the quantum dots is maximised, see Chapter 6. Fig. 5.1(a) shows a scanning electron microscope image of the  $12\ \mu\text{m}$  long freely suspended beam. The length and position of the tethers are also optimised. First, the distance from the resonator to the substrate is chosen to be roughly similar to the one of the cantilever resonator ( $3\ \mu\text{m}$ ). This is several times larger than the focus spot diameter and thus not only locating the resonator in y-direction is facilitated (see Fig. 5.3) but also the laser suppression is improved. Second, a fine adjustment of the tether length is done by minimising the mode volume and the leakage to the under-etched substrate as well as the tether deformation. The fine adjustment becomes increasingly important for higher mode numbers. Going one step further, also the tether attachment position is optimised by minimising the loss to the substrate. Especially for the 3rd-order in plane mode, this plays an important role – if optimised

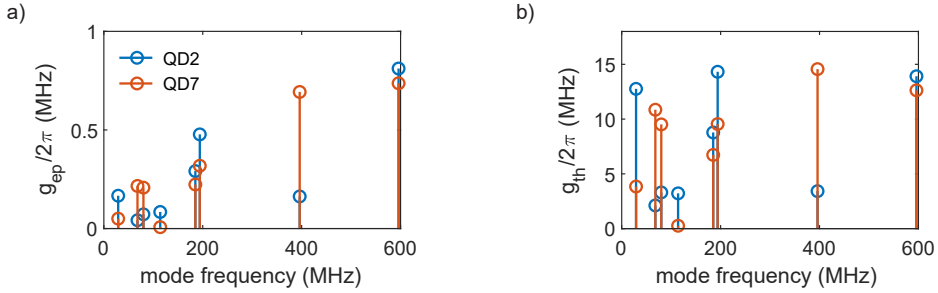


**Figure 5.2: QD-mechanical coupling rate.** Finite-element simulations are used to estimate the exciton-phonon coupling rate. For this, the effective mass,  $m_{\text{eff}}$ , and mechanical vacuum fluctuation,  $x_{\text{zpf}}$ , are obtained via thermomechanical calibration. (a) Estimated vacuum exciton-phonon coupling rate,  $g_{\text{ep}}$ , of the measured quantum dots, for each mechanical mode shown in Fig. 5.1. (b) Thermal exciton-phonon coupling rate,  $g_{\text{th}}$ , for the same modes as shown in (a).

correctly, the displacement profile shows a node at the attachment position and thus leakage to the substrate is highly minimised [178], see Fig. 5.1(i).

Besides the optimisation of the displacement profile, we are also highly interested in the exciton-phonon coupling profile, shown by the colour scale in Fig. 5.1. The coupling rate is estimated via the zero-point motion and effective mass of the individual modes. For more details see Chapter 3.13. As can be seen in Fig. 5.1(b-f), the in-plane bending modes all show an odd y-symmetry with a node in the beam centre. Thus, to observe quantum dot mechanical coupling the dots need to be located away from the centre of the beam. The more the quantum dot is displaced from the y-axis the higher the coupling rate, since strain is maximised at the sidewalls of the beam. This places a constraint on finding a quantum dot with a high coupling rate for these modes. This limitation is highly relaxed when working with an in-plane breathing mode, see Fig. 5.1(g-i). The coupling profile is highly homogenous in y-direction and the quantum dots found in the laser spot roughly all show the same coupling strength (see Fig. 5.10). Therefore, for locating a quantum dot with a high coupling rate, only the x-position needs to be considered. This is straightforward due to the relatively large resonator size in the x-direction, which is about 12 times the laser spot diameter (see also Fig. 5.4). Note that due to the large size mismatch in all three dimensions,  $l \approx 12 \times w \approx 65 \times h$ , there is no hybridisation of the mechanical modes.

Figure 5.2 shows the estimated vacuum and thermal exciton-phonon coupling rates,  $g_{\text{ep}}$  and  $g_{\text{th}}$  (see Chapter 2), evaluated at two different positions on the mechanical resonator [54]: QD2 is located in the centre of the resonator slightly displaced from  $y = 0$ , and QD7 is located close to the tether attachment also displaced from  $y = 0$ . Therefore, both quantum dots show individual coupling strengths for the mechanical modes. Interestingly, although the vacuum coupling rate increases for higher mechanical modes, the thermal coupling rate stays roughly constant. The reason is the decreasing phonon number (at bath temperature) for increasing mechanical frequency. Thus, the higher the mechanical frequency the higher the vacuum

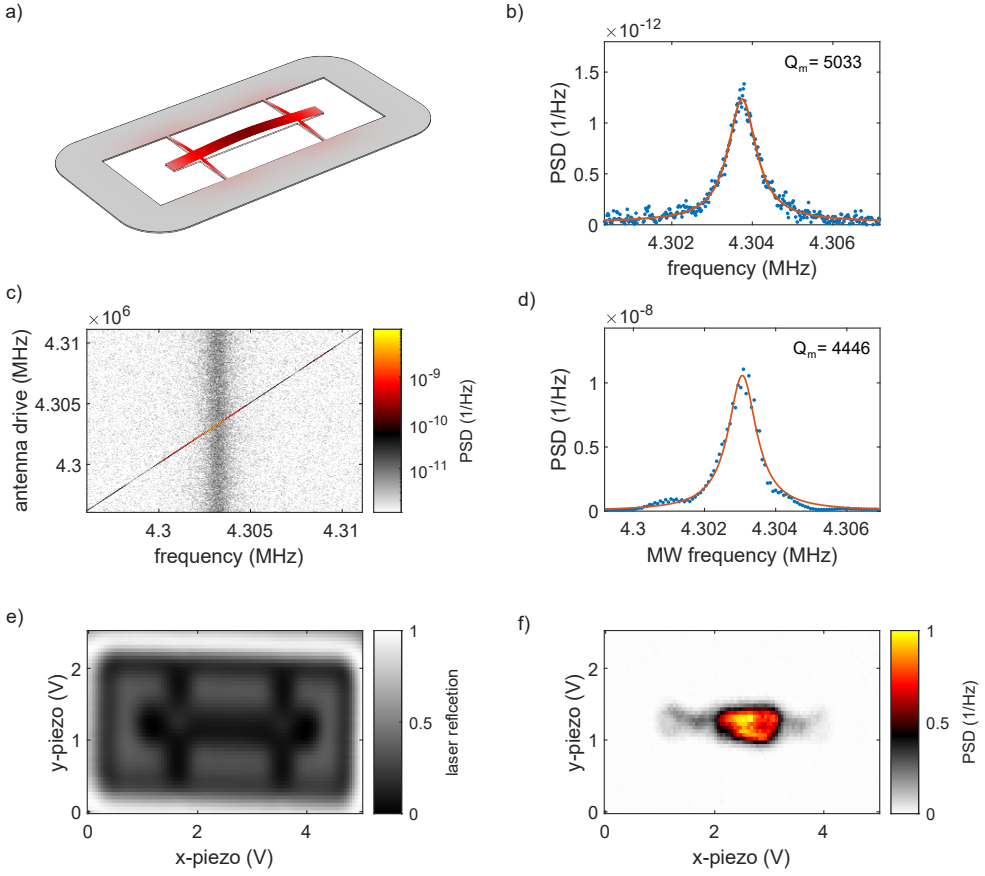


**Figure 5.3: Out-of-plane bending mode characterisation.** (a) Mechanical mode profile (shown as displacement) and z-displacement (shown in colour) of the 1st-order out-of-plane (asymmetric/odd) mechanical mode which is used to pre-characterise the mechanical resonator. (b) Brownian-motion mechanical quality factor,  $Q_m$ , measured via the cavity between the beam and the substrate. (c) Electric-field-antenna actuation of the mechanical mode: the applied microwave frequency (y-axis) is swept through the mechanical resonance while the power spectrum is recorded (x-axis/colour scale). (d) The diagonal cut of (c) shows the driven mode spectrum with a similar mechanical quality factor as in (b). (e,f) Confocal and mechanical mode profile scans of the resonator: the microscope head is operated in the bright-field mode and the intensity (e) and the noise power (f) of the reflected laser are recorded.

optomechanical coupling rate must be for observing optomechanical coupling (given by Brownian motion). Simulation parameters for eigenfrequency, effective mass, zero-point motion, thermal motion, spring constant, and phonon number can be found in Tab. 5.1 in [Supplementary note II](#).

### 5.3 Mechanical pre-characterisation

For an initial mechanical device characterisation we make use of the under-etch cavity, presented in Chapter 4. The freely suspended beam also has an out-of-plane bending mode with maximal displacement in the beam centre, see Fig. 5.3(a). Measuring the mechanical vibration via the under-etch cavity is much faster than using the single-quantum dot emission, therefore, it is a perfect tool to probe the mechanical quality factor before turning to extensive single-quantum dot measurements. Fig. 5.3(b) shows the noise power from a reflected laser, measured with a fast photodiode and a spectrum analyser (for more details see Chapter 4). The Brownian motion noise peak of the out-of-plane bending mode at  $\Omega_m/2\pi \approx 4.3$  MHz shows a mechanical quality factor of  $Q_m = 5000$ . This is lower than what was measured for the cantilever (shown in Fig. 3.3). We speculate that this is due to the different mechanical resonator designs and the different mode shapes. Note that the out-of-plane mechanical quality factor of the 25  $\mu\text{m}$  beam is comparable to the ones of the cantilever, see [Supplementary note VI](#).

The mechanical quality factor can also be measured by driving the resonator with the electric-field antenna, shown in Fig. 5.3(c,d). For this measurement, the frequency applied to the electric-field antenna is swept through the mechanical resonance (y-axis) while for every frequency step, a noise power spectrum is recorded (x-axis and colour scale). The constant signal independent of the mechanical drive in Fig. 5.3(c) is the thermal motion of the resonator. The narrow diagonal feature is the signal from the coherent drive. A linecut of the drive is presented in Fig. 5.3(d), with a mechanical quality factor similar to the Brownian-motion measurement.

By driving the mechanical mode at the resonance frequency, the motion is highly increased which we can use to image the displacement profile of the mechanical mode. For this, the reflected laser power and the mechanical noise power are recorded simultaneously as a function of the laser position on the mechanical resonator (using the x-y-piezo scanner, see [Supplementary note I](#)). The reflected laser power is shown in Fig. 5.3(e) and the noise power is shown in Fig. 5.3(f). Although the recorded mechanical noise power is influenced by the collection efficiency of the reflected laser (which depends on the laser position on the mechanical resonator), a similar mode profile as in the simulation is observed. Since the electric-field antenna is much larger than the mechanical resonator and since the antenna is installed far away from the resonator, we assume that moving the sample around does not affect the driving efficiency.

With the measurement presented above we identify resonators with high mechanical quality factor and continue with the quantum dot characterisation, presented in the following chapter

### 5.4 Quantum dot characterisation

The first step for single-quantum-dot measurements is locating suitable dots on the mechanical resonator. A similar measurement as the one presented in the previous chapter is performed by recording the quantum dot photoluminescence as a function of the position. The gate voltage is set to 1.37 V, which corresponds to the emission of the negative trion transition. Due to the high quantum dot density of more than

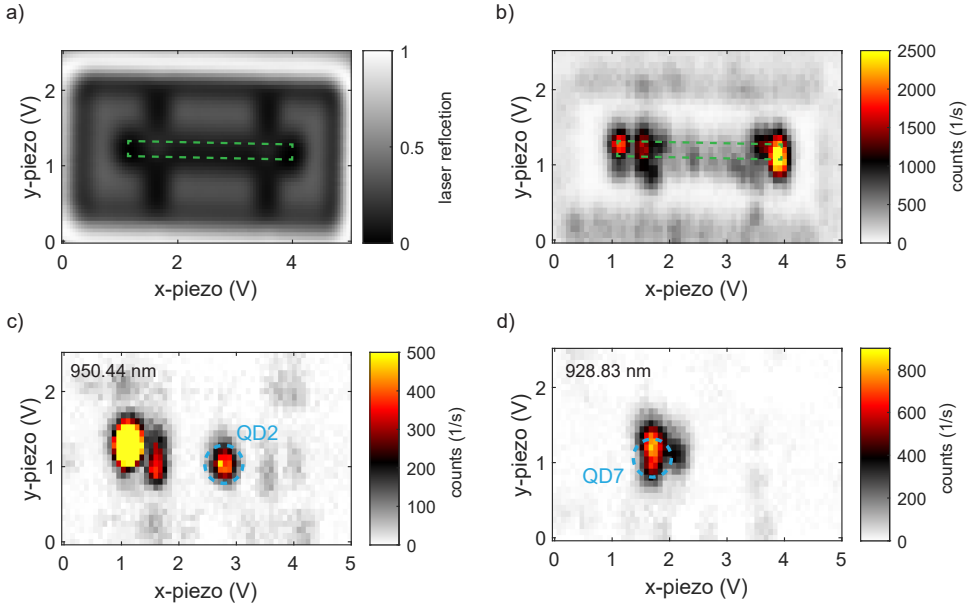


**Figure 5.4: Photoluminescence characterisation of the mechanical resonator (a)** Confocal scan of the mechanical resonator. **(b)** Photoluminescence map of the same mechanical resonator as shown in (a). Photoluminescence spectra are recorded while an xy-piezo scanner moves that sample around the laser spot. For each data point, the maximum intensity peak of each spectrum is shown. Several quantum dots can be found distributed over the full resonator. **(c,d)** Single-wavelength evaluation of the photoluminescence map at 950.44 nm (QD2) and 938.83 nm (QD7). The QD luminescence is well localised (highlighted in blue) and no strong waveguiding is observed.

ten dots per  $\mu\text{m}^2$ , plenty can be found on the mechanical resonator, see Fig. 5.4(a,b). Note that this becomes even more important when further reducing the resonator size as in Chapter 6. In general, the emission collection is higher on the resonator and the under-etched substrate due to the additional reflection from the hollow space below the structure. Furthermore, as mentioned before, the width of the beam is optimised to maximise the outcoupling to the top (see Chapter 6.9). We also observe that at the two ends of the beam, there is a further enhancement, however, this does not directly translate to what we see with resonant excitation and further investigations are needed.

In the measurement shown in Fig. 5.4(b) for every data point a full emission spectrum is recorded of which the maximum intensity is shown. Though this gives a rough estimate of the general quantum dot distribution, this type of evaluation is not enough to locate individual dots. Therefore, the recorded spectra are evaluated for single wavelengths. Figure 5.4(c,d) shows the emission evaluated for QD2 at 950.44 nm and for QD7 at 928.83 nm. The emission of an individual quantum dot is well localised, at least in the x-direction, which allows quantum dots to be selected with different coupling strengths to the individual mechanical modes (see Fig. 5.2).



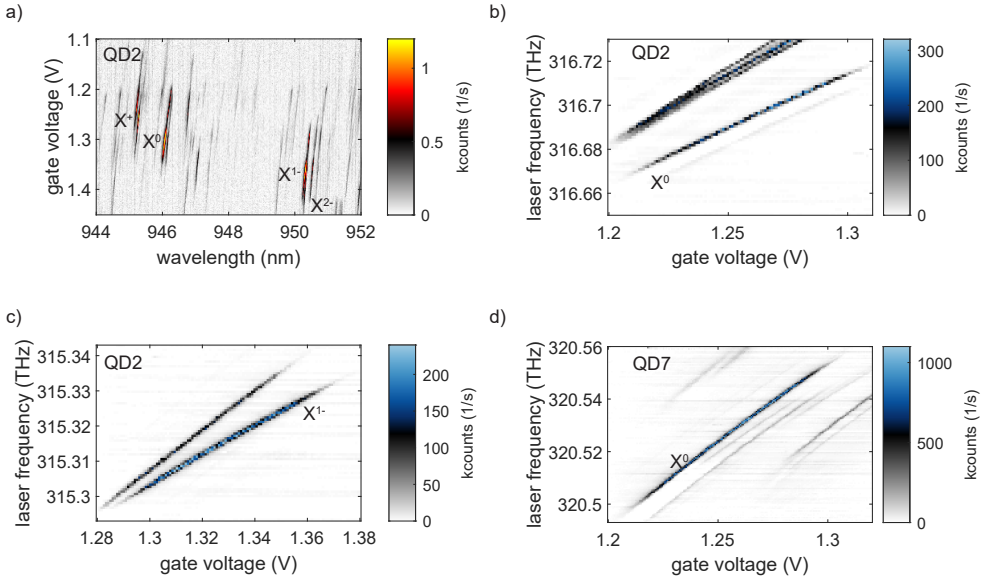


**Figure 5.5: Quantum dot charge plateau characterisation.** (a) Voltage scan of the quantum dot's photoluminescence: by applying a gate voltage, the quantum dot's charge state can be changed from the positive trion,  $X^+$ , to the negative trion,  $X^{1-}$ . (b-d) Resonance fluorescence charge plateau scans of neutral and charged excitons of QD2 and QD7. Excitons from multiple quantum dots can be observed due to the high quantum dot density. The measurements are performed in a way such that for each laser frequency the full gate voltage range is scanned and the QD emission is recorded using single-photon detectors.

All the following measurements on the freely suspended beam are based on the two quantum dots presented here.

A major challenge with structures with small footprints is the gate functionality. The membrane resonators rely on good conductance of the doped gate layers at the top and the bottom of the membrane. For the suspended beam, the smallest connection to the surrounding membrane and to the electrical contacts are the 200 nm-wide tethers. The four tethers combined result in good conductance to the surrounding membrane and there is no degradation of the gate quality on the mechanical resonator. Fig. 5.5 shows a photoluminescence scan of QD2 as a function of applied bias voltage revealing the transitions of the charge plateaus from  $X^+$  to  $X^{2-}$ . The wavelength separation between the neutral exciton,  $X^0$ , and the trion,  $X^{1-}$ , is approximately 4 nm, a typical value for InAs quantum dots [109].

Besides quantum dot charge control, also the semiconductor noise depends on the diode quality. This can be probed with resonant quantum dot excitation. For the cantilever resonator, the inhomogeneously broadened linewidth was a factor of two larger than the transform limit, see Fig. 3.10. Here, this ratio is slightly higher with a linewidth approximately three times larger than the transform limit (see [Supplementary note III](#)). To what extent the inhomogeneous broadening is limited by the tether width or fabrication imperfections requires further investigation.

Figure 5.5 (b-d) shows the resonant charge plateaus of the exciton and trion of QD2 and QD7. The excitation power is chosen close to saturation such that  $\Omega_R \approx \Gamma_R$ , which corresponds to roughly 200 nW of laser power reaching the sample. The measurement is performed in a way that first the laser spot position is optimised using the photoluminescence signal and second, laser frequency and gate voltage are swept while recording the emission with a single-photon detector. Even though the laser suppression becomes worse for small mechanical structures, it is still stable enough so that when tuning the laser in a range of more than 100 GHz, the change in laser suppression is negligibly small. However, the laser suppression also depends highly on the excitation power and worsens when the power increases due to the emission saturation of the quantum dot.

Correlating the emission intensities of non-resonant and resonant excitation it can be seen that QD7 shows an increased count rate compared to QD2, about a factor of three with resonant excitation. This might be an effect of the lateral quantum dot position and the beam width optimisation. However, there is no significant reduction of the radiative lifetime and thus the higher count rate is not due to Purcell enhancement but due to a better collection efficiency for QD7. In addition, we also observe a better excitation efficiency for QD7 (lower power needed to reach a specific Rabi frequency).

## 5.5 Master-equation simulations of the exciton-phonon coupling

In Chapter 3, it was shown that measuring the Brownian motion can be very time-consuming, especially if non-optimal measurement parameters, i.e., excitation power and laser detuning, are used. Therefore, this chapter focuses on modelling the interaction between the mechanical resonator and the single-photon emitter such that optimal parameters can be estimated prior to the measurement. The method used to describe the hybrid system follows the approach in Ref. [61, 62].

Theoretically describing an isolated two-level system driven by a single close-to-resonance laser is relatively straightforward using the Lindblad master equation approach. However, modelling a quantum dot coupled to a mechanical resonator whose displacement fluctuations are coupled to a thermal bath is not so simple. Furthermore, estimating the impact of the optical interaction with the dot on the mechanical resonator requires a quantum mechanical description of the phononic states. Although this has been described in Ref. [179, 180], we follow a simpler approach of describing the hybrid system with a classical coherent mechanical drive [61, 62].

We start by describing the quantum dot by a driven optical two-level system with a semi-classical approach. For more details see Chapter 2. The coupling between the mechanical and the optical system is then added by a term which includes the modulation of the quantum dot transition energy based on the thermal exciton-phonon coupling strength and the mechanical frequency. When going to the rotating frame of the interacting laser, the Hamiltonian looks as follows:

$$\hat{H} = \frac{\hbar}{2} \left[ \Omega_R (\hat{\sigma}_+ + \hat{\sigma}_-) + 2 (g_{\text{th}} \sin(\Omega_{\text{m}} t) - \Delta\omega_1) \hat{\sigma}_+ \hat{\sigma}_- \right], \quad (5.1)$$

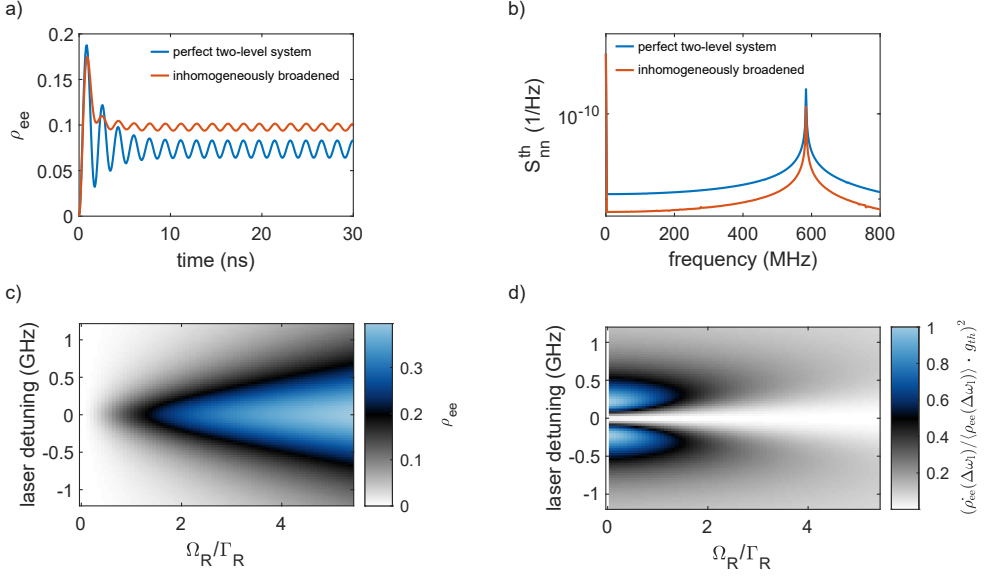


**Figure 5.6: Numerical master equation simulations of the optomechanical interaction.** (a) Excited-state population (for a detuned laser) as a function of time using the time-dependent Hamiltonian shown in Eq. 5.1. The simulations are performed over 200 mechanical oscillations. At short times ( $< 10$  ns) large changes in population due to Rabi-oscillations can be observed. At large times, the noise is given by the mechanical modulation of the quantum dot energy. (b) Fast Fourier transform of the data shown in (a). The transformation is performed without Rabi oscillations by skipping the first 50 mechanical oscillations. (c,d) Numerical simulations in dependence of laser detuning and Rabi frequency,  $\Omega_R$  ( $\propto \sqrt{\text{laser power}}$ ). The excited-state population in (c) is the average population at later time in (a). The expected amplitude noise in the quantum dot emission, only given by the derivative of the quantum dot count rate, is shown in (d). For every simulation point, the normalised derivative of the quantum dot count rate with respect to the laser detuning,  $\dot{\rho}_{ee}(\Delta\omega_1)/\langle\rho_{ee}(\Delta\omega_1)\rangle$ , is multiplied by the quantum dot frequency modulation given by thermal motion,  $g_{th}$ .

where  $\Omega_R$  is the optical Rabi frequency,  $\Delta\omega_1/2\pi$  is the laser detuning from the quantum dot resonance,  $\Omega_m/2\pi$  the mechanical frequency, and  $g_{th}$  the thermal exciton-phonon coupling rate. The latter is obtained from the finite-element simulations presented in Chapter 5.2. The exciton-phonon coupling as described in the Hamiltonian above can also be understood as a sinusoidal time-dependent detuning between the laser and the quantum dot resonance. Finally, the incoherent excited-state decay rate is added via a Lindblad collapse operator,  $L = \sqrt{\Gamma_R}|g\rangle\langle e|$ , and the system evolution is described by a set of coupled differential master equations, see Chapter. 2

Since the Hamiltonian in Eq. 5.1 is time-dependent, there is no steady state and it is solved numerically. The numerical simulation is performed in total over 200 mechanical periods and an inhomogeneous broadening (estimated from the mea-

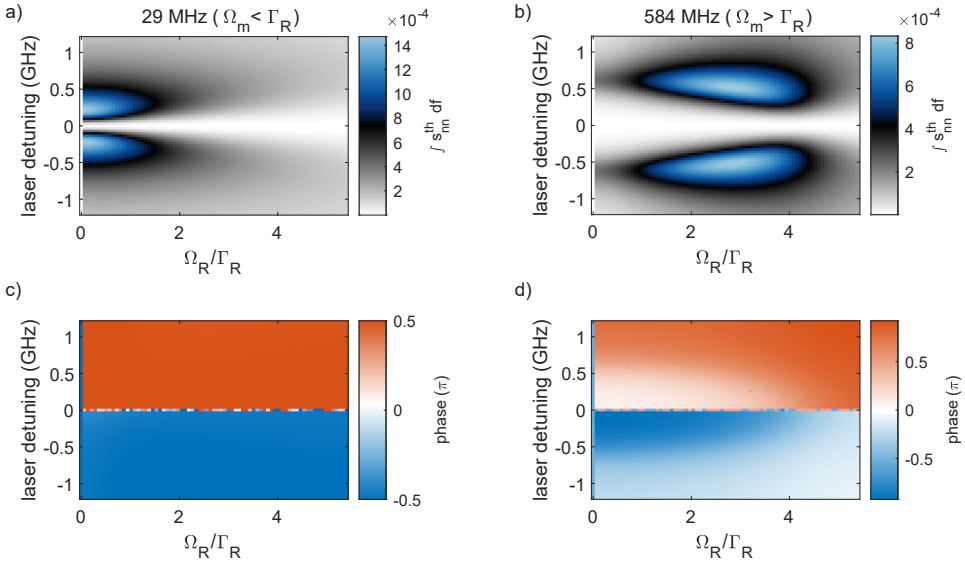


**Figure 5.7: Simulated mechanical noise for low- and high-frequency modes.** (a,b) Numerical simulations of the mechanical noise power for the 29 MHz ( $\Omega_m < \Gamma_R$ ) and 584 MHz ( $\Omega_m > \Gamma_R$ ) modes. The noise power is obtained by integration of the resonance peak in Fig. 5.6(b). (c,d) Extracted phase of the noise shown in (a, b). The noise profile of the low-frequency mode matches the expected noise given by the derivative of the quantum dot count rate, see Fig. 5.6(d). For the high-frequency mode, however, the magnitude and phase of the noise deviate strongly from the expectation of Fig. 5.6(d).

surements) is added with a Lorentzian weighted distribution of 300 MHz (FWHM). In general, we observe that inhomogeneous broadening is rather Lorentzian than Gaussian, hinting at an interaction with only a few charge traps [125]. The quantum dot emission rate is proportional to the excited-state population,  $\rho_{ee}$ , which is shown in Fig. 5.6(a) for an off-resonant laser. For times much larger than the Rabi oscillations, the excited-state population oscillates due to the time-dependent detuning between dot and laser, see Fig. 5.6(a). The numerical simulation is analysed for the time-averaged excited-state population and for the noise power from the mechanical interaction. The excited-state population is averaged over the last 100 mechanical oscillations, Fig. 5.6(c), and the noise power is obtained by a fast Fourier transformation (also of the last 100 mechanical oscillations), Fig. 5.6(b).

For mechanical frequencies that are much lower than the excited-state decay rate (unresolved-sideband regime) the noise which is imprinted on the quantum dot emission depends on the derivative of the linewidth, see Chapter 3. Therefore we take the derivative of the excited-state population as a function of laser detuning, which corresponds to the expected noise power in the unresolved-sideband regime. This is shown in Fig. 5.6(d).

To continue, we compare the expected noise power between the cases where the mechanical frequency is slower and faster than the excited-state decay rate. The

numerical simulations are performed for the 1st-order bending mode at 29 MHz and for the 3rd-order breathing mode at 584 MHz. The thermal exciton-phonon coupling rates are taken from the finite-element simulations, see Fig. 5.2. The power and the phase of the noise are extracted, shown in Fig. 5.7. As expected, for the low-frequency mechanical mode, the highest noise sensitivity is at low excitation power and small detunings. In fact, the sensitivity in Fig. 5.7(a) matches remarkably well with the expectation from the derivative analysis of the linewidth in Fig. 5.6(d). Note that Fig. 5.7(a) is the noise power of the normalised excited-state population, see Chapter 3. Thus, the noise sensitivity is highest at low power, however, the emission count rate is also low (increasing the measurement time).

When comparing the noise sensitivity of the high-frequency to the low-frequency mechanical mode, a significant difference is visible, Fig. 5.7(b). The highest noise sensitivity is now at elevated excitation power and at a detuning which does not directly correspond to the maximum slope of the quantum dot count rate (see Fig. 5.6(d)). The phase also shows a significant difference. There are not one but three transitions of  $\pi$ , see Fig. 5.7(c,d).

To summarise, this comparison shows that the noise sensitivity is not the same for mechanical frequencies slower and faster than the decay rate. Consequently, different laser powers and detunings need to be chosen as in the previous measurements with the cantilever resonator. Further discussion on this topic will follow in Chapter 6.

## 5.6 Brownian-motion measurement

The Brownian-motion measurement is performed in the same way as in Chapter 3, however, with an optimised parameter set, chosen from the analysis in the previous chapter. The autocorrelation measurement is performed at  $\Omega_R \approx 3\Gamma_R$  and with a laser detuning of  $\Delta\omega_l/2\pi = 300$  MHz. Since this corresponds to a relatively high excitation power where the quantum dot emission is close to saturation, laser suppression is difficult. Therefore, it is even more important to automatically suppress the laser during the course of the measurement. Nevertheless, there is still a finite leakage of the laser which increases the  $g^{(2)}(0)$ , as can be seen in Fig. 5.8(a). Note that at low laser powers a  $g^{(2)}(0) = 0.03$  is obtained, see [Supplementary note III](#).

A zoom-in of the autocorrelation measurement (at large time delays) reveals multiple oscillations with different coupling strengths, Fig. 5.8(b). As in Chapter 3, a Fourier transformation is performed to obtain the noise power spectrum, which is shown in Fig. 5.8(c,d) for QD2 and QD7, respectively. In total eight noise peaks are observed, corresponding to the mechanical modes presented in Fig. 5.1. The height of the noise peaks depends not only on the exciton-phonon coupling strength but also on the mechanical quality factor, or more precisely the frequency width in the noise spectrum. Thus, the coupling strengths of the modes cannot be compared by just judging from the intensity of the individual noise peaks. Since the noise does not directly depend on the derivative of the linewidth, it is not straightforward to directly convert the observed noise to a coupling rate, especially for the high-frequency modes. Nevertheless, we can compare the measured noise to the noise obtained from the numerical simulations, for which we use the expected coupling rates from the

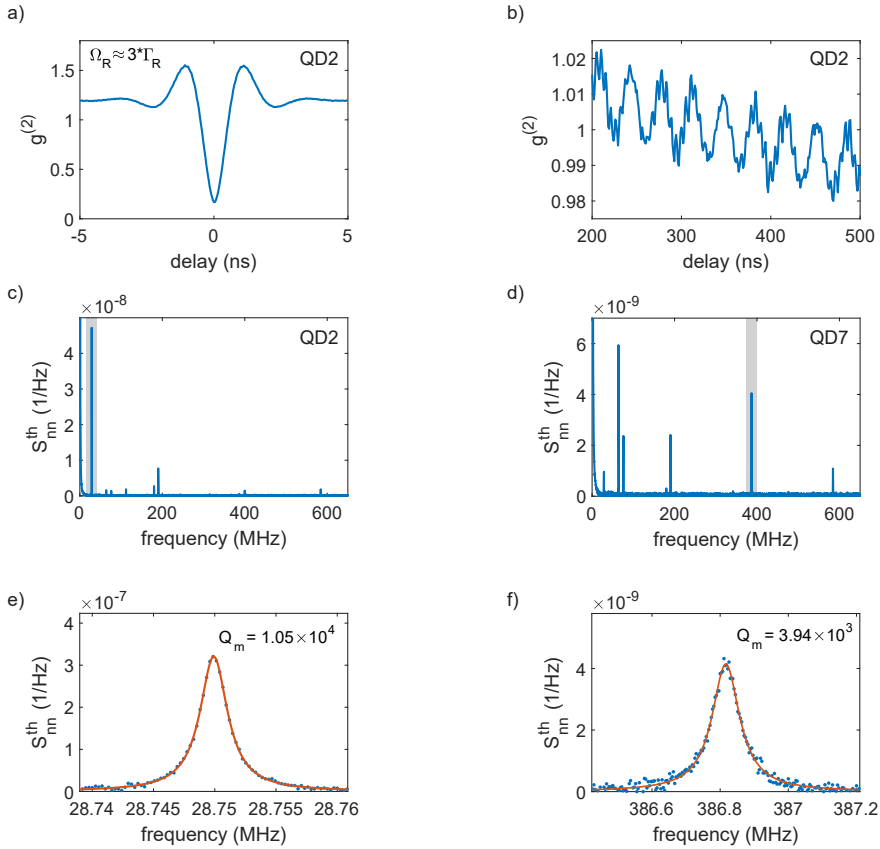


**Figure 5.8: Brownian-motion measurement with a single quantum dot.** (a,b) Brownian motion autocorrelation measurement of QD2 with a Rabi frequency of  $\Omega_R \approx 3\Gamma_R$  and a laser detuning of  $\Delta\omega_1/2\pi = 300$  MHz, which is  $1/3$  of the quantum dot linewidth at the corresponding laser power. (c,d) Power spectrum of the autocorrelation measurement showing multiple noise peaks from, in total, eight mechanical modes. The strengths of the individual noise peaks depend not only on the mechanical quality factor but also on the quantum dot position and the mechanical mode shape (see Fig. 5.1 and Fig. 5.4). (e,f) Zoom-in of the power spectrum (grey shaded area in (c, d)) revealing the Lorentzian lineshape of the mechanical modes. Mechanical quality factors of  $1.05 \times 10^4$  and  $3.94 \times 10^3$  are obtained for the 1st-order in-plane bending and 1st-order in-plane breathing modes, respectively. The mechanical quality factors of the remaining modes can be found in Tab. 5.1.

finite-element simulations. Focusing on the 587 MHz mechanical mode, we obtain an integrated noise power of about  $6 \times 10^{-4}$  which is comparable to the noise expected from Fig. 5.7(b), considering the power and detuning parameters from the measurement. Also for all other modes, we see a similar (same order of magnitude) noise power in the measurement as we would expect from the simulations and thus, the coupling rates should be comparable to the ones presented in Fig. 5.2.

The mechanical quality factors can directly be obtained from the noise power spec-

trum. Two examples are shown in Fig. 5.8(e,f), and the extracted quality factors are listed in Tab. 5.1. For the bending modes, the mechanical quality factor reduces from an initial  $Q_m = 1.05 \times 10^4$  for the 1st-order mode down to  $Q_m = 8.1 \times 10^2$  for the 5th-order mode. This corresponds to a decrease of more than an order of magnitude which we attribute to the leakage to the surrounding under-etched substrate (see Chapter 5.2) as well as an increase of intrinsic losses. A similar effect is observed for the breathing modes where the quality factor reduces from  $3.8 \times 10^3$  to  $2.0 \times 10^3$ . More importantly, the 3rd-order breathing mode does not show any sign of an increased mechanical quality factor due to a reduced clamping loss [151, 177]. Therefore, the degradation of the mechanical quality factor for higher frequency modes is strongly influenced by an increase in intrinsic losses.

So far, the single-quantum dot noise measurements are based on the displacement obtained from Brownian motion. The following chapters will focus on quantum dot optomechanics under driving of the mechanical modes using the electric-field antenna.

## 5.7 Mechanical actuation

Controlling the state of the mechanical resonator via the optical interaction with the quantum dot is one of the big pictures of this work. The Brownian-motion measurement presents a first step in this direction. However, the interaction between the quantum emitter and the mechanical resonator is rather complex due to the non-linear nature of the quantum dot. The following subchapters present a collection of individual measurements where the resonator displacement is enhanced by a classical, yet coherent, drive. These experiments help to better understand the interaction of the coupled hybrid system. The magnitude of quantum dot resonance modulation at a specific driving power will be referred to as  $g_{\text{th}}^{\text{drive}}$ .

### 5.7.1 Plateau broadening

The exciton-phonon coupling is based on deformation potential [24] (see Chapter 2 and 3). Therefore, the neutral exciton and the charged trion should be equally affected. To investigate this, resonant charge plateau maps are performed for both, the exciton and the trion of the same quantum dot. In addition, the transition frequency shift due to the quantum dot mechanical coupling is highly enhanced by driving the mechanical 1st-order bending mode. Assuming that the mechanical amplitude stays the same when going from the exciton to the trion gate voltage (for more details see Chapter 3.14), there should be an equally strong linewidth broadening for both of them.

Figure 5.9(a,b) shows the exciton and trion charge plateaus of QD2 measured with resonant excitation. The measurement is performed in the following way: first, the laser is frequency locked and the gate voltage is scanned while recording the emission with a single-photon detector, and second, this process is repeated for all laser frequencies. Note that the single-photon clicks are counted with a time tagger which is operated in the network-time-tagger mode where the single-photon tags are forwarded to the experimental computer for evaluation. With his method, the delay due

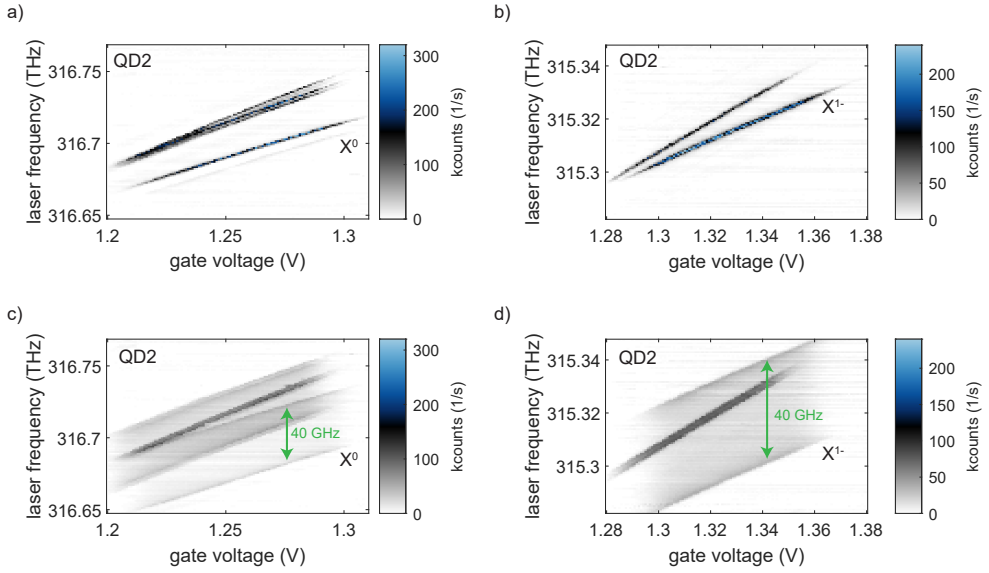


**Figure 5.9: Charge-plateau broadening due to mechanical quantum dot resonance modulation.** (a,b) Resonant charge plateau scans of the neutral exciton,  $X^0$ , and charged exciton,  $X^{1-}$ , of QD2 as a function of laser frequency and gate voltage. Additional plateaus can be seen which originate from different quantum dots. (c,d) Broadening of the quantum dot resonance under strong driving of the 1st-order in-plane bending mode at 29 MHz. As expected from deformation potential coupling, both excitons show the same amount of broadening of  $2g_{th}^{drive}/2\pi = 40$  GHz, highlighted in green.

to the communication with the time tagger is highly minimised, resulting in short measurement times.

Once the electric-field antenna is turned on, the quantum dot linewidth broadens, with a linear dependence on the field amplitude (applied voltage). As expected, both, exciton and trion, show the same charge plateau broadening, Fig. 5.9(c,d). Since for these experiments, an in-plane bending mode is mechanically driven, the additional quantum dots in Fig. 5.9(c,d) show different coupling strengths due to a different y-position on the resonator (for more details see the following chapter).

### 5.7.2 Phase response to individual modes

The in-plane bending and in-plane breathing modes show a fundamentally different coupling profile, see Fig. 5.10(a,b). All bending modes show an odd y-symmetry of the coupling profile, with compressive stress on one side, tensile stress on the other side, and zero stress in the centre of the beam. Consequently, dots with different y-positions can show different coupling strengths. Furthermore, quantum dots with different signs of coupling can be found if the dots are located on opposite sides of the beam.

Figure 5.10 shows a time-resolved measurement of the neutral exciton of QD2. Every horizontal row corresponds to a single measurement where the laser is locked



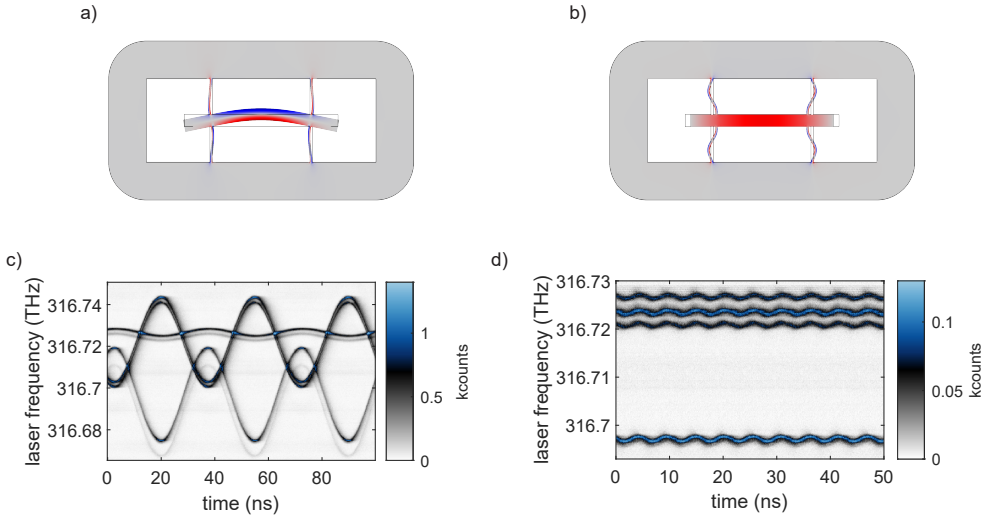


**Figure 5.10: Time resolved mechanical driving of breathing and bending modes.** (c,d) Time-resolved resonance fluorescence of the neutral excitons of three different quantum dots (see Fig. 5.9(a)) under mechanical driving of the 1st-order in-plane bending (a,c) and in-plane breathing (b,d) mode. In-plane bending modes have an odd  $y$ -axis symmetry of the coupling profile which is visible by the two  $\pi$ -out-of-phase excitons in (c). In contrast, in-plane breathing modes show an even symmetry along  $y$ , therefore, all quantum dots are modulated in phase with respect to the mechanical driving. Further, due to the homogeneous coupling profile of the breathing mode all quantum dots show the same amount of modulation.

at a specific frequency and the quantum dot emission is recorded in a histogram mode, for which the time tagger is synchronised to the driving field. By repeating the histogram measurements for a series of laser frequencies, the time-resolved resonance shift of the quantum dot is made visible. Besides QD2 (lowest two emission lines), there are two more quantum dots visible in Fig. 5.10(c). The three dots do not all react in phase to the mechanical displacement. Thus we infer that they are located on opposite sides of the beam (in  $y$ -direction). Also, they show individual coupling strengths which are again determined by the dot position. QD2 shows the highest frequency shift, hinting that it is located furthest from the centre ( $y = 0$ ) of the resonator. Note that each exciton shows two emission lines due to the fine-structure splitting [66].

In contrast to the bending modes, the breathing modes all show a homogenous coupling profile with an even  $y$ -symmetry [177]. This is also reflected in the time-resolved measurement in Fig. 5.10(d), which shows the same dots as in Fig. 5.10(c). All three dots are now synchronised in time and show the same amount of frequency shift. We conclude that the high-frequency modes are breathing modes (and not higher-order bending modes). This is also supported by the change in mechanical quality factor when going from the 5th to the 6th mode that we observe.

The reduced frequency shift when driving the breathing mode compared to the

bending mode is not due to a reduced coupling strength (see Fig 5.2) but due to less efficient mechanical driving. For the mechanical modes above 150 MHz the AC-voltage is not applied with the arbitrary waveform generator (see Chapter 3) but with an RF-source (National instruments, FSW-0020) in combination with an amplifier (Mini-circuits, ZFL-2500VH+). For better actuation, the shield of the antenna is disconnected from the RF-source so that the electric field forms between the antenna and the sample ground, resulting in a magnitude higher mechanical amplitude.

### 5.7.3 Quantum dot lifetime

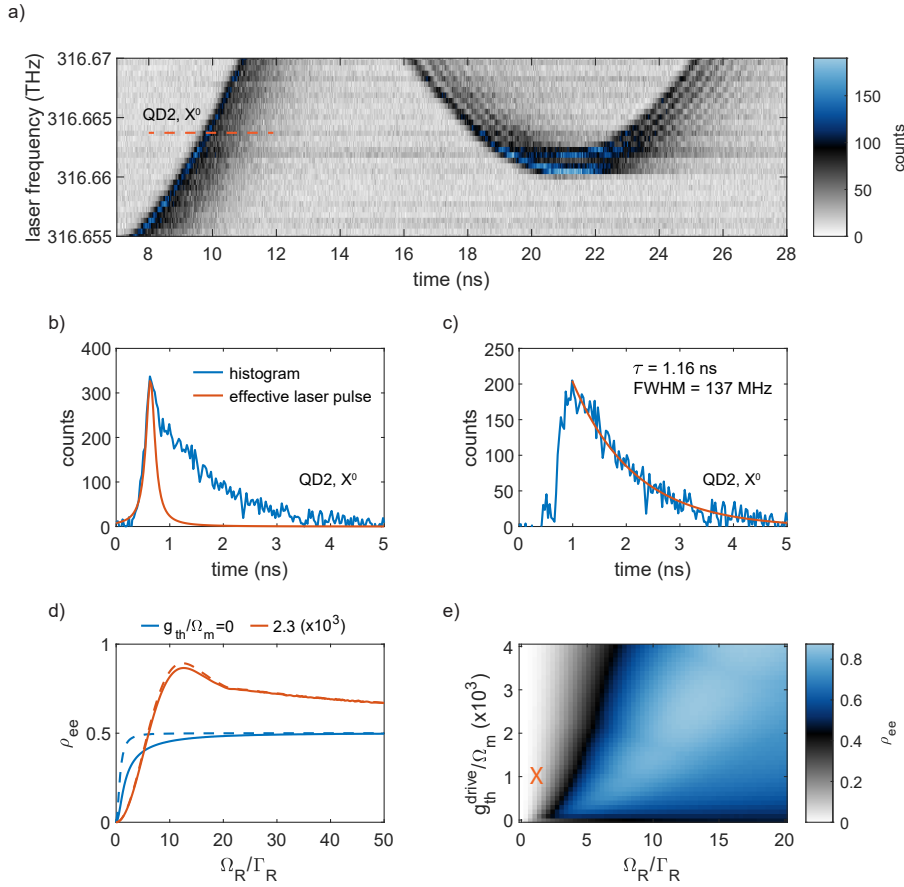
The current wafer material has a high quantum dot density ( $10 \mu\text{m}^{-2}$ ) and as a consequence, there are additional quantum dots close to QD2 and QD7, see Fig. 5.5. The issue with close-by quantum dots is that it is not possible to individually excite them with a mode-locked laser due to the large optical bandwidth of the short pulses. Thus, the lifetime of the dots cannot easily be determined individually. In the following paragraphs, we leverage the optomechanical interaction to create an effective-pulsed measurement which enables individual lifetime measurements, even of close-by quantum dots.

Figure 5.11(a) shows a time-resolved measurement of QD2 (same as in the previous chapter) with strong mechanical driving. The frequency shift of the quantum dot is 30 GHz. The two emission lines are a zoom-in of the sinusoidal quantum dot resonance shift, where the left one corresponds to QD2. For each experiment (horizontal row), the laser is at a fixed frequency and the mechanical motion moves the quantum dot in and out of resonance.

When the mechanical displacement becomes very large, the quantum dot moves very fast through the laser which creates an effective pulsed excitation of FWHM = 200 ps, see Fig. 5.11(b). This leads to a shadowing effect in the time-resolved measurement due to spontaneous emission, shown in the line cut in Fig. 5.11(b). The response of the effective laser pulse is shown in red, followed by the spontaneous radiative decay of the dot. After subtracting the pulse response, a single exponential function is used to extract the excited-state lifetime of  $\tau = 1.16$  ns. Note that we find a similar lifetime for QD7, see [Supplementary note III](#).

The very fast interaction with the laser is even stronger visible with the second emission line in Fig. 5.11(a). This quantum dot has a relatively small fine-structure splitting of 1 GHz and both emission lines move through the laser within the lifetime of the dot. Thus, the fine-structure splitting manifests itself in a time-dependent quantum beating. At the maximum displacement point (21 ns) the quantum dot spends more time in resonance with the laser than the lifetime of the dot and therefore the fine-structure splitting can be observed.

The measurement presented above resembles a rapid adiabatic passage-type experiment where the population can be inverted in a regime independent of the excitation power [181, 182]. In such an experiment, a chirped pulse is used to excite the quantum dot. Here, the time-dependent detuning between the laser and the quantum dot creates an effective chirp. In the frame of the quantum dot, the laser moves quickly through resonance either from blue to red or vice-versa. The magnitude of the effective chirp thereby depends on the mechanical amplitude and the sign of the effective chirp depends on the movement direction.



**Figure 5.11: Quantum dot lifetime measurement using strong mechanical driving.** (a) Time resolved resonance fluorescence of the neutral exciton ( $X^0$ ) of QD2 under strong mechanical driving ( $2g_{th}^{drive}/2\pi \approx 60$  GHz) of the 29 MHz mechanical mode. Due to the strong driving, the quantum dot resonance is accompanied by a spontaneous emission tail. (b) Line-cut of (a) corresponding to a single experiment where the laser is at a fixed frequency and the QD moves fastly through the laser by mechanical driving. This leads to an effective pulsed excitation of 200 ps duration. (c) After subtraction of the effective pulse response, the lifetime is extracted via a single-exponential fit. (d) Numerical simulation of the excited-state population for zero mechanical drive (blue) and a drive amplitude comparable to the measurement (orange). Dashed lines are without and solid lines with inhomogeneous broadening. (e) Numerical simulation in dependence of both, excitation power and mechanical drive amplitude.

Figure 5.11(a) shows numerical simulations of the excited-state population with the mechanical drive off and on. The simulations are performed over ten mechanical oscillations and the highest excited-state population during the effective pulse is extracted. Without mechanical driving, the quantum dot interacts with a CW-laser and the highest population is given by  $\rho_{ee} = 0.5$ . In contrast, with mechanical driving,

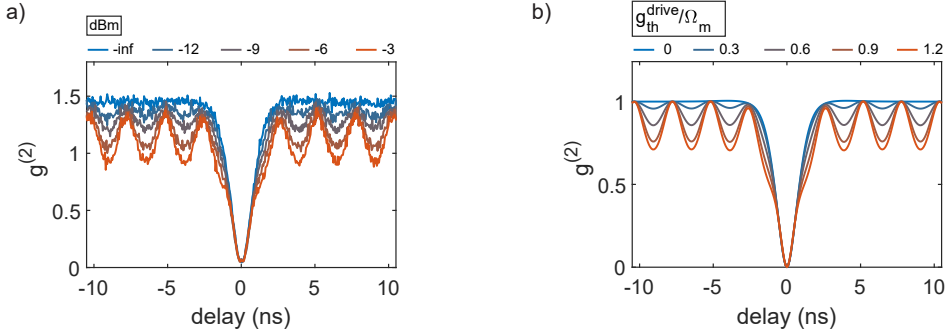


**Figure 5.12: Resonant autocorrelation measurement with fast mechanical modulation.** (a) Resonant autocorrelation measurement of QD7 with increasing driving strength of the 2nd-order in-plane breathing mode. Due to the fast mechanical driving at 387 MHz ( $\Omega_m = 2.6\Gamma_R$ ) the autocorrelation shows a modulation even in the anti-bunching region. (b) Numerical simulation of the 2nd-order coherence function, using the Hamiltonian in Eq. 5.1, with increasing modulation amplitude of the quantum dot resonance. The simulation matches well with the experiment.

the population can go above 0.5. Figure 5.11(e) shows the excited-state population in dependence on both, the optical power and the mechanical driving amplitude. The higher the modulation, the more power is needed to reach the maximum population. The highest excited-state population that is obtained from the simulations is  $\rho_{ee} = 0.87$ , which is limited by the finite effective pulse length. For very large optical powers, the population goes back towards the steady-state population, since the linewidth is power broadened, highly increasing the effective pulse width. Whether in the experiment enough CW-laser power can be reached to invert the population remains an open question. With the current experimental parameters  $\rho_{ee} = 0.05$ , highlighted in orange in Fig. 5.11(e).

#### 5.7.4 Autocorrelation measurement

Since all in-plane breathing modes have a higher mechanical frequency than the excited-state decay rate, there should also be an effect on the anti-bunching in the autocorrelation measurement, especially with additional mechanical driving. This is investigated with the 2nd-order breathing mode at 387 MHz which is more than twice as large as the excited-state decay rate. We cannot drive the 3rd-order breathing mode efficiently enough for performing this measurement (partially due to the high spring constant and partially due to the mode shape).

Figure 5.12(a) shows a series of resonant autocorrelation measurements at low excitation powers and with increasing mechanical driving amplitude. Also here, the laser is automatically suppressed every minute and the quantum dot resonance is locked to the laser frequency using the applied gate voltage. The normalisation of the autocorrelation is performed via the average count rate on the detectors, for more details see Chapter 7.7. The bunching to  $g^{(2)}(\tau) = 1.45$  is due to blinking with a corresponding

on-off ratio [183] of 69%. For all measurements, the single-photon purity remains at a high level of 94%.

The mechanical driving results in a periodic modulation of the emission count rate, which is reflected in the autocorrelation measurement. The mechanical modulation in the autocorrelation is given by a cosine function (with a  $\pi$  phase) with respect to zero delays. On the contrary, Rabi oscillations are described by a sinusoidal function (for more information see Fig. 6.9). Due to the short mechanical period of 2.6 ns the anti-bunching broadens for high mechanical amplitudes, however, at very short delays (below 0.8 ns), the anti-bunching seems not to be influenced.

We support our observations with a numerical simulation of the second-order coherence function:

$$g^{(2)}(t, \tau) = \frac{\langle \hat{\sigma}_+(t)\hat{\sigma}_+(t+\tau)\hat{\sigma}_-(t+\tau)\hat{\sigma}_-(t) \rangle}{\langle \hat{\sigma}_+(t)\hat{\sigma}_-(t) \rangle^2}. \quad (5.2)$$

Using the Hamiltonian from Eq. 5.1, the correlation function is simulated using the Python quantum toolbox Qutip [116, 117]. The correlation function is time-averaged over 20 mechanical oscillation periods, similar to what is described in Chapter 5.5. The inhomogeneous broadening is included by assuming a Lorentzian weighted laser detuning. Figure 5.12(b) shows numerical simulations of the second-order coherence function with increasing mechanical driving amplitude. Measurement and simulation match well, including all details discussed above.

### 5.7.5 Resonant linewidth scan

In Chapter 5.5 it was shown that there is a fundamental difference between the interaction of the quantum dot with low- and high-frequency mechanical modes. Here, this relationship is explored further by performing resonant linewidth scans while increasing the mechanical driving amplitude. As already shown in Chapter 5.7.1, when the mechanical frequency is lower than the excited-state decay rate of the dot, the quantum dot transition energy shift is a linear function of the displacement which, time-averaged, results in a broadened linewidth. Fig. 5.13(a) shows in more detail the linewidth broadening when driving the 1st-order bending mode at 29 MHz. The laser detuning (x-axis) is normalised to the mechanical frequency. The measurement is performed at low excitation power such that power broadening of the linewidth is absent (FWHM = 450 MHz). Since the electric-field antenna heats the sample, especially for high frequencies, there are a lot of drifts during the linewidth measurement. To overcome this issue, every line scan is composed of 20 individual fast line scans where in between the laser is automatically suppressed and the quantum dot resonance is locked to the laser frequency. In addition, instead of scanning the laser, the gate voltage is scanned (and converted to frequency using the slope from the charge plateau) which speeds up the measurement 10-fold.

A similar measurement as in Fig 5.13(a) is also shown in Chapter 3, where the broadened lineshape is fitted with a model which describes a time-averaged sinusoidal modulation of the Lorentzian lineshape. Here, the measurement is overlaid with a numerical simulation of the Hamiltonian in Eq. 5.1. The simulations are performed in the same way as in Chapter 5.5, solving for the time-averaged excited-state population as a function of laser detuning. Also here, the inhomogeneous broadening is

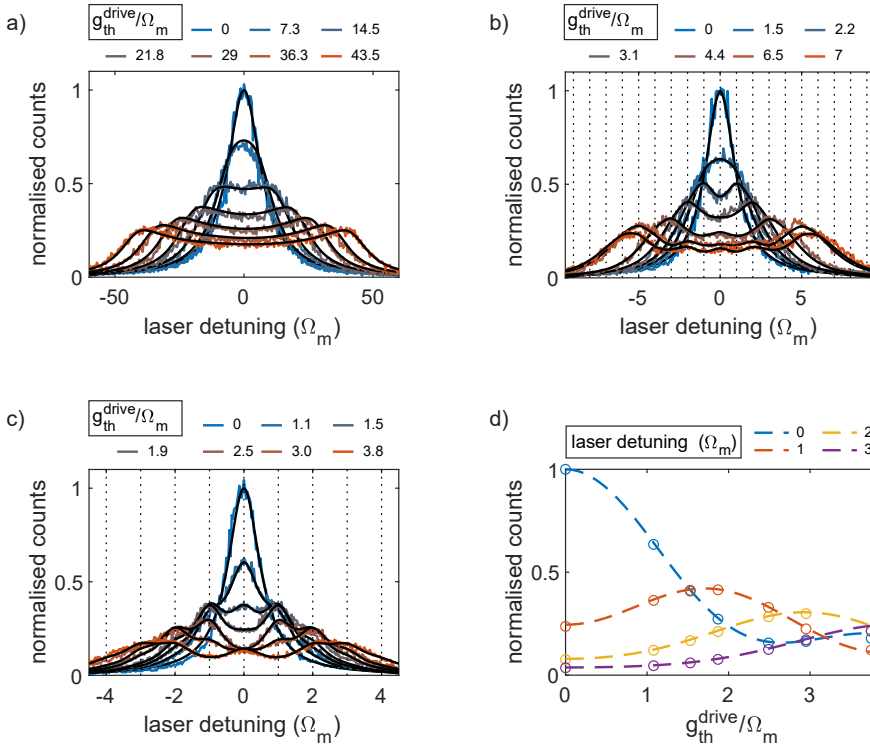


**Figure 5.13: Resonant linewidth broadening due to fast mechanical driving.** (a-c) Resonant linewidth scans of the neutral exciton of QD7 at low excitation powers ( $\Omega_R \ll \Gamma_R$ ) under mechanical driving at: (a) 29 MHz ( $\Omega_m = 0.2\Gamma_R$ ), (b) 190 MHz ( $\Omega_m = 1.3\Gamma_R$ ), and (c) 387 MHz ( $\Omega_m = 2.6\Gamma_R$ ). Black curves are numerical simulations using Eq. 5.1 where we solve for the excited-state population. The simulations include a homogeneous linewidth of 150 MHz and an inhomogeneous linewidth broadening of 300 MHz, resulting in an effective linewidth of 450 MHz. There is a clear difference between mechanical modes which are slower and faster than the quantum dot decay rate. For the modes faster than the quantum dot decay rate we observe an increased intensity at laser detunings of multiples of the mechanical frequency. (d) Intensity comparison of the measurement (circles) shown in (c) and the numerical simulations (dashed line) for integer detunings of  $\Omega_m$ .

an important part of the simulations. As expected from previous measurements, the data match very well with the simulations.

The interaction of the quantum dot with a driven mechanical mode which is faster than the excited-state decay rate is shown in Fig 5.13(b,c) for the 1st- and 2nd-order in-plane breathing modes, respectively. The quantum dot transition frequency shift is not a linear function of the displacement anymore and an increased intensity at laser detunings of multiples of the mechanical frequency is observed. This is especially prominent in the 387 MHz experiments where for the first four mechanical amplitudes the intensity bunches at a laser detuning of  $\pm\Omega_m/2$ . For a resonance mod-

ulation larger than  $g_{\text{th}}^{\text{drive}} > 2.5\Omega_m$  the intensity bunches at a detuning of  $\pm 2\Omega_m$  and  $\pm 3\Omega_m$ . Similar behaviour is observed for driving the 190 MHz mode, however, the mechanical frequency is too small in relation to the quantum dot linewidth and the increased-intensity peaks are washed out. Note that without inhomogeneous broadening, fully-resolved peaks appear at multiple detunings of  $\pm\Omega_m$ .

Finally, the emission intensity at detunings of integer values of  $\Omega_m$  is extracted in dependence of the mechanical driving, Fig. 5.13(d), which matches well to the expectation from the numerical simulations.

With the measurements shown in Fig. 5.13(c), it seems as if sidebands are created due to the strong mechanical driving, however, the count rates present the fully integrated emission spectrum. It will be shown in Chapter 5.7.7 that at the mechanical driving powers used here, many actual sidebands are already visible in the emission spectrum.

## 5.7.6 Time-resolved measurement

The measurements and simulations presented in the previous chapter are time-averaged. Time-resolved measurements can give more insight into the mechanism behind the appearing increased intensity at multiple detunings of  $\Omega_m$ . However, there is only a certain range of mechanical frequencies for which both, frequency-resolved and time-resolved modulation, can be measured. The quantum dot lifetime ( $\tau$ ) is the fundamental limit meaning that first, the mechanical frequency needs to be higher than the Fourier limit of the linewidth,  $\Omega_m/(2\pi) > 1/(2\pi\tau)$ , and second, the mechanical period needs to be longer than the lifetime,  $(2\pi)/\Omega_m > \tau$ . The additional factor of  $2\pi$  from the conversion of the lifetime to the decay rate enables a range of frequencies,  $1/\tau < \Omega_m < (2\pi)/\tau$ , for which both modulations can be observed. Here,  $150 < \Omega_m/(2\pi) < 930$  MHz which includes all breathing modes of the suspended beam resonator. The lower limit is in fact washed out due to the inhomogeneous broadening. The following measurements present time-resolved resonance fluorescence using the exact same parameters as in the previous chapter.

The heating effect of the electric-field antenna has a much stronger impact on the time-resolved than on the time-averaged measurements. Due to the heating, there is a time-dependent frequency shift of the mechanical resonator. Though it is relatively small, it imprints a phase instability on the measurements. This means that the measurement needs to be performed much faster than the quantum dot drift (also due to heating) and the phase drift, which is less than 1 min. Therefore, the measurement is repeated 120 times with an integration time of 0.25 s per single histogram. After determining the phase of each measurement an averaging is performed which gives a total integration of 30 s for each histogram (horizontal data row in Fig. 5.14). The issue is that with 0.25 s integration per single measurement, for the 2nd-order breathing mode, there is an average photon click of  $1.3 \times 10^{-5}$  per mechanical oscillation on the detectors. Thus, precisely determining the phase of each measurement requires additional data stitching and averaging, for more details see [Supplementary note IV](#).

Figure 5.14(a,c,e) shows the time-resolved resonance fluorescence under strong driving of the three mechanical modes which are also presented in the previous section. Figure 5.14(b,d,f) shows the same numerical simulations as in Fig. 5.13, however not



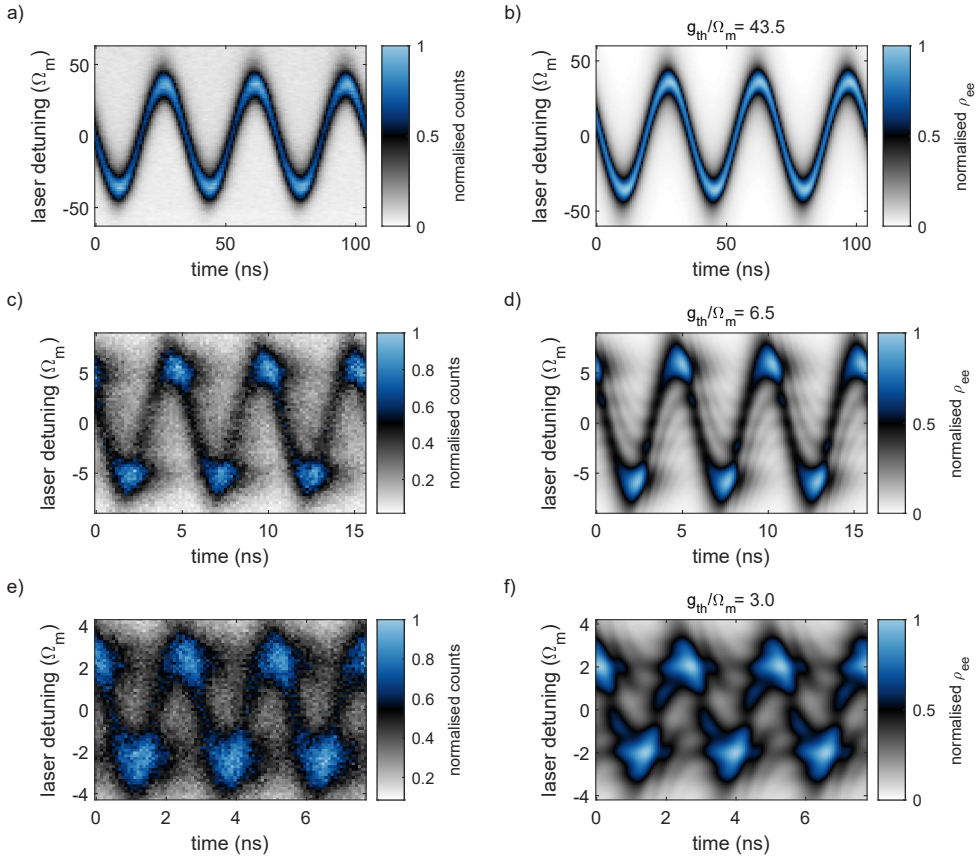


**Figure 5.14: Time-resolved resonance fluorescence with fast mechanical driving.** (a,c,e) Low-power ( $\Omega_R \ll \Gamma_R$ ) time-resolved resonance fluorescence as a function of laser detuning with mechanical driving of the same three mechanical modes as shown in Fig. 5.13: (a) 29 MHz, (b) 190 MHz, and (c) 387 MHz. For each frequency, three mechanical periods are shown. For mechanical modes slower than the quantum dot decay rate  $\Gamma_R$  (see (a)), a sinusoidal quantum dot resonance modulation is observed. When the mechanical mode is faster than  $\Gamma_R$  (see (c,e)), there is a time modulation of the increased intensity observed in Fig. 5.13(b, c). The delayed response of  $\rho_{ee}$  to the mechanical modulation manifests in a phase delay, especially visible for high frequencies. In addition, there is a blurring effect due to the short mechanical period which is only a factor of two larger than the excited-state lifetime:  $T_m \approx 2\tau$ . (b,d,f) Numerical simulations (without time averaging as in Fig. 5.13), matching well with the measurements shown on the left-hand side. A full set of data with various driving amplitudes is shown in [Supplementary note IV](#).

time-averaged. For the 1st-order bending mode at 29 MHz, which is much slower than the decay rate of the dot, a sinusoidal modulation of the quantum dot resonance is measured. The same is observed in the numerical simulations.

A clear difference is observable when driving at frequencies higher than the decay rate of the dot, Fig. 5.14(c-f). The increased intensity at multiples of  $\pm\Omega_m$  shows a



sinusoidal-like time modulation with a region in between the increased-intensity peaks where the interaction with the dot is highly reduced. More importantly, there is a phase delay in the time modulation of the increased intensity (due to the delayed response of the dot), which increases for higher frequencies. The numerical simulations are matching well with the data. Note, without inhomogeneous broadening, also here clearly resolved peaks would be observable at multiple detunings of  $\pm\Omega_m$ .

### 5.7.7 Emission spectrum

In the previous two chapters, an increased intensity at detunings of multiples of the mechanical frequency is observed. However, for these measurements, the count rate on the detector represents the fully integrated emission spectrum. Here, we investigate to what extent this increased intensity corresponds to optomechanical sidebands by resolving the emission spectrum using a narrow optical filter.

A standard piezo-tunable Fabry-Pérot etalon with 8.5 MHz FWHM is installed free-space. The quality of the etalon is poor with a transmission efficiency of 10% (5% fibre-to-fibre) and large frequency drifts. When measuring at low excitation powers, the etalon and the spectral fluctuation of the dot are locked to the fixed laser and the measurement is averaged over many individual runs, for more details see [Supplementary note V](#).

To test the etalon, the quantum dot emission is measured with increasing excitation power, Fig. 5.15(a). Although the etalon has a suppression of four orders of magnitude, at low powers, the background level (of the normalised emission) is at  $2 \times 10^{-3}$ , due to the broad incoherent emission of the dot and the LA-phonon sideband. At high excitation powers, the laser interacts strongly with the two-level system and the Mollow-triplet appears [4, 5, 118]. The higher the power the lower the coherently scattered laser and the higher the incoherent emission of the Mollow-triplet. As expected, the separation of the Mollow peaks increases linearly with the Rabi-frequency. The measurements presented in Fig. 5.15(a) match well with the numerical simulations of the emission spectrum which are shown in Fig. 5.15(c).

The emission spectrum with additional weak mechanical driving of the first two breathing modes is shown in Fig. 5.15(b). The excitation power is chosen around saturation ( $\Omega_R \approx \Gamma_R$ ) so that the coherent emission still dominates and the total emission count rate is not too low. A series of sidebands shows up. Also here, the measurements match well with the numerical simulations shown in Fig. 5.15(d).

The numerical simulations in Fig. 5.15(c,d) are performed using the Hamiltonian from Eq. 5.1. The time-dependent emission spectrum is obtained by solving the first-order coherence function using the quantum toolbox Qutip [116, 117] and by performing a Fourier transformation of the coherence function:

$$G^{(1)}(t, \tau) = \langle \hat{\sigma}_+(t) \hat{\sigma}_-(t + \tau) \rangle, \quad (5.3)$$

$$S(t, \omega) = \int_0^\infty G^{(1)}(t, \tau) e^{-i\omega\tau} d\tau.$$

Finally, the emission spectrum is time-averaged over 20 mechanical periods and a Lorentzian filter function is applied. The inhomogeneous broadening is included in the same way as for the second-order coherence function in Chapter 5.7.4.

When the mechanical drive is turned on, the quantum dot resonance is modulated

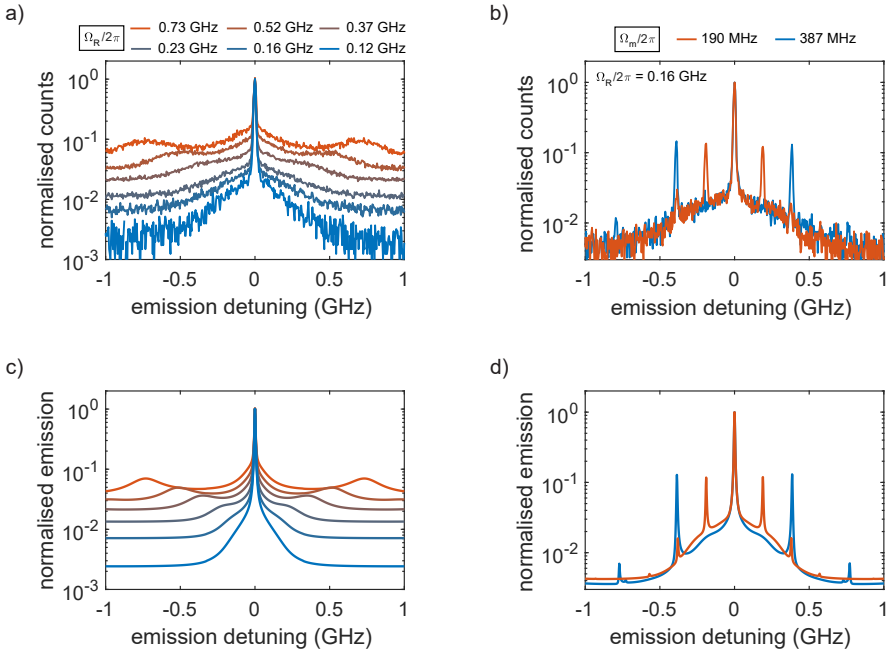


**Figure 5.15: Emission spectrum of an optical two-level system.** (a) Emission spectrum of QD7 using the etalon from Fig. 5.24(b). The spectra are offset by 0.01 in y-direction for better visibility. Due to stability reasons, every data set corresponds to 20 individual scans, see [Supplementary note V](#). At low excitation powers the spectrum is dominated by the coherently scattered laser, whereas at high power spontaneous emission starts to dominate and we observe the Mollow triplet. (b) QD7 emission spectrum at medium excitation powers ( $\Omega_R \approx \Gamma_R$ ) while driving the in-plane mechanical breathing modes at 190 and 387 MHz. The side peaks at  $\pm \Omega_m$  are due to the interaction of the fixed laser and the mechanical modulation of the quantum dot resonance. (c,d) Numerical simulations using the same parameters as in the experiments in (a, b). The simulations include an inhomogeneous broadening of 300 MHz.

in time with respect to the fixed laser. As shown in Fig. 5.16(a,b) this leads to a series of sidebands at integer detunings of the mechanical frequency. In the classical picture, the quantum dot sees a detuning-modulated electric field [184]. This results in a time-modulated excited-state population. In frequency space, this corresponds to a carrier signal surrounded by side peaks which will be imprinted on the emission of the quantum dot. The conversion of the CW-laser (at a fixed frequency) to an amplitude-modulated emission requires energy, which does not come from the dot itself but from the mechanical drive (via the QD-mechanical coupling). Overall, the quantum dot converts light from a single frequency to a series of frequencies using the energy from the mechanical drive, which is a very similar description to a classical electro-optic modulator. The description above does not include the lifetime of the dot which means that even for frequencies much slower than the decay rate of the dot, sideband should appear. This is exactly what we observe even for the 29 MHz

mode (thanks to the narrow filter).

In quantum language, light is not described by a field but by photons. The quantum dot is inherently non-linear and absorbs and emits single photons. This means that the emitted photon is, compared to the input photon, frequency shifted by  $\pm\Omega_m$ . As for the classical picture, the quantum dot cannot do this on its own and additional energy is required from the quantised mechanical field. The mechanical quantum – the phonon – is defined as  $\hbar\Omega_m$ . In this picture, a photon emission in the blue sideband corresponds to the absorption of a phonon and the emission in the red sideband corresponds to the emission of a phonon [62]. Also with this description, sidebands can be observed in the emission spectrum even for  $\Omega_m < \Gamma_R$ .

In our model, the mechanical part is described classically (see Eq. 5.1). Still, the quantum effects in the measurements (single-phonon absorption/emission) are described well by the model. This is in analogy to the classical description of the optical driving field (see Chapter 2). Our optical simulations reproduce the anti-bunching, although this is an effect of the quantumness of the light. This is possible since the non-linear optical two-level system renders the classical input to a quantum output. Therefore we argue that it is enough to model quantum effects (optical and mechanical), with a classical drive as long as the emitter is modelled quantum mechanically. Of course, this model breaks down for low phonon numbers and for backaction effects on the mechanical resonator.

Figure 5.16(a,b) shows the emission at low excitation powers with mechanical driving of the first two breathing modes at 190 and 387 MHz, respectively. For these measurements, we exploit the poor quality of the etalon such that a  $\text{FSR}_{-9\text{dB}} = 2.9$  GHz is obtained, see [Supplementary note V](#). The higher the mechanical driving amplitude, the more sidebands are visible. The width of the coherently scattered laser peak, as well as the sideband width, is given by the bandwidth of the spectral filter (8.5 MHz) which is much broader than the spectral properties of the laser ( $\approx 300$  kHz). The antenna driving powers used here ( $g_{\text{th}}^{\text{drive}}/\Omega_m < 1$ ) are substantially less than in Chapter 5.7.5.

In general, the intensities of the sidebands depend on the ratio of quantum dot modulation and mechanical frequency [185],  $g_{\text{th}}/\Omega_m$ , which is sometimes referred to as the modulation index [64, 65]. This also counts for the resolved-sideband regime, where the single-phonon scattering Rabi frequency ( $\Delta\omega_1 = \pm\Omega_m$ ) is given by  $\Omega'_R = g_{\text{th}}\Omega_R/\Omega_m$  [64, 180]. The normalised coupling strength is relatively simple to understand: to maximise the absolute intensity of the first sideband (assuming no inhomogeneous broadening), the resonance shift of the quantum dot needs to be  $\sim \Omega_m$ , thus  $g_{\text{th}}/\Omega_m = 1$ . This intensity behaviour is also captured by the Bessel function of 1st kind [61]. This means that if the mechanical frequency is doubled, the thermal coupling rate should also be doubled to observe the same sideband intensity. Since the phonon occupation also decreases when going to higher frequencies, the vacuum coupling rate actually needs to be more than doubled. This is rather challenging as can be seen in the finite-element simulations in Chapter 5.2. This shows the importance of careful design optimisation, especially for GHz mechanical resonators.

Resolving the sidebands in the emission spectrum does not necessarily mean that the system is in the resolved-sideband regime. The definition of the resolved-sideband regime is that the mechanical frequency must be (much) larger than the decay rate of the optical system. Though this is enough for cavity optomechanical systems, for

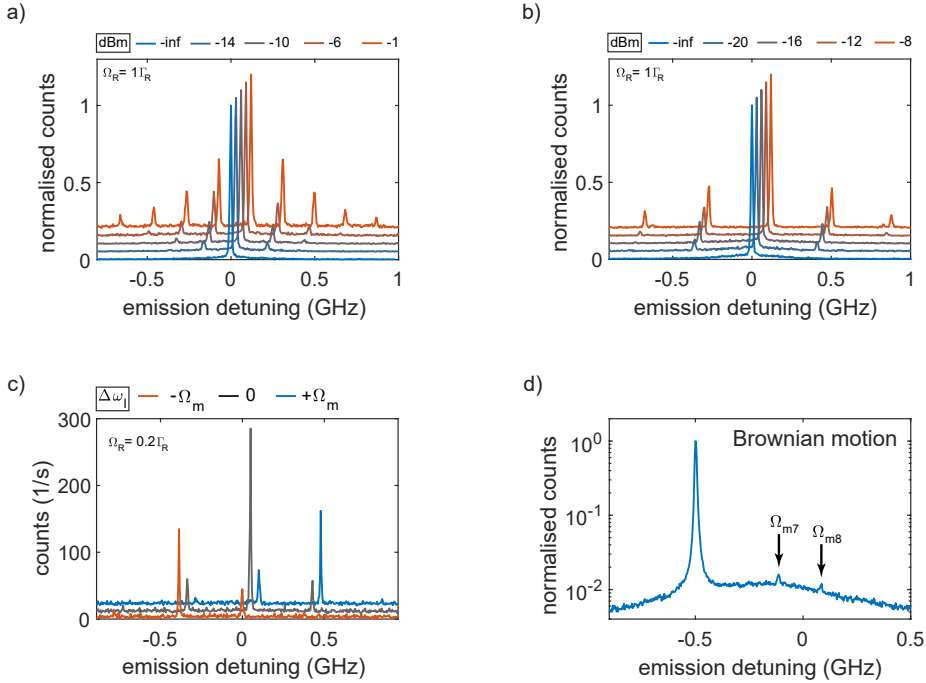


**Figure 5.16: Mechanically modulated emission spectrum of a single quantum dot.** (a,b) Emission spectrum of QD2 with medium excitation powers,  $\Omega_R \approx \Gamma_R$ , in dependence of the mechanical driving amplitude at (a) 190 MHz and (b) 387 MHz. The spectra are offset in x- and y-direction for better visibility. The spectrum is dominated by the coherently scattered laser, which is resonant with the quantum dot transition. A series of emission side peaks can be observed at multiple detunings of  $\pm\Omega_m$ . (c) Mechanically modulated emission spectrum at low optical excitation powers,  $\Omega_R \approx 0.2\Gamma_R$  and laser detunings of 0 and  $\pm\Omega_m$ , respectively. Due to the narrow optical linewidth,  $\approx 500$  MHz, and the low mechanical driving amplitude, the emission spectrum is highly asymmetric when the laser is detuned. (d) Brownian-motion measurement of the acoustic sidebands with a laser detuning of  $\Delta_l = -0.5$  GHz. Acoustic sidebands of the 2nd- and 3rd-order in-plane breathing modes can be seen.

a quantum dot optomechanical system, where the inhomogeneous broadening plays a big role, an additional definition is needed: the mechanical frequency also needs to be (much) larger than the inhomogeneously broadened linewidth. This means that the laser can be tuned to either the red or blue sideband with a negligible interaction with the main resonance. This is especially important for optomechanical cooling experiments. Here, the mechanical frequencies of the first two breathing modes are still smaller than the measured linewidth of 450 MHz.

Figure 5.16(c) shows the emission for blue- and red-detuned optical driving at  $\Delta\omega_1/2\pi = \pm\Omega_m/2\pi$ . The optical power is chosen such that the linewidth does not show power broadening. Therefore, the detuned emission spectra are highly asymmetric. For the first time, we also observe acoustic sidebands even without mechanical

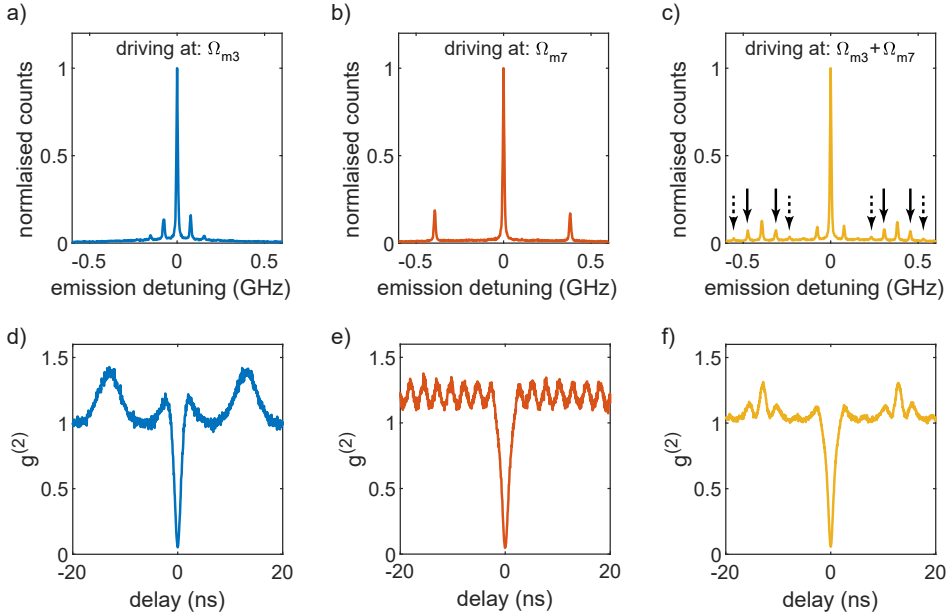


**Figure 5.17: Optomechanical wave mixing.** (a,b) Acoustic sidebands of the 3rd-order bending and the 2nd-order breathing modes, labeled as  $\Omega_{m3}$  and  $\Omega_{m7}$ , respectively. (c) Emission spectrum when driving both modes simultaneously. Additional sidebands due to optomechanical wave-mixing appear at  $\pm\Omega_{m7} \pm (2)\Omega_{m3}$ . (d-f) Autocorrelation measurements of the exact same conditions as in (a-c),  $g^{(2)}(0)$  remains below 6%. When driving both mechanical modes, additional time modulation due to mixed frequencies appears.

driving, see Fig. 5.16(d). In this experiment, we are mainly limited by the quality of our measurement method. The broad background is partially due to finite incoherent scattering and partially due to the LA-phonon sideband, spanning over many free spectral ranges. Note that during all the measurements presented above the laser suppression is below 2% of the total emission.

The final measurements of this chapter present a wave-mixing type experiment. Without going into much detail, the quantum dot performs a wave mixing of a laser photon and the coherent fields of two different mechanical modes [62]. Figure 5.17(a,b) shows the emission spectrum of the quantum dot when driving the 3rd and 7th mechanical modes separately. Sidebands at  $\pm\Omega_{m3}$  and  $\pm\Omega_{m7}$  appear due to the absorption and emission of phonons of the two modes. When driving both mechanical modes simultaneously, see Fig. 5.17(c), additional peaks at  $\pm\Omega_{m7} \pm \Omega_{m3}$  show up due to optomechanical wave-mixing [62]. The driving of the two mechanical modes is achieved by frequency mixing a carrier signal of  $(\Omega_{m7} - \Omega_{m3})/2 + \Omega_{m3}$  with a modulation signal of  $(\Omega_{m7} - \Omega_{m3})/2$ . The signal is then amplified and sent to the electric field antenna.

To argue that one photon interacts with multiple phonons at a time, it is important to show single-photon emission even with strong mechanical driving. Figure 5.17(d-f) shows autocorrelation measurements of the exact same measurement configuration as

in Figure 5.17(a-c), where the coincidence counts are normalised using the detector count rates. For all measurements,  $g^{(2)}(0)$  remains below 6 %. Also here, additional frequency components appear in the time modulation when both mechanical modes are driven at the same time.

## 5.8 Conclusion

The optimised resonator design of the freely suspended beam enables the observation of up to eight mechanical modes in a frequency range of tens of MHz to hundreds of MHz. This frequency range is ideal to study the difference in the exciton-phonon coupling between mechanical modes which are slower and faster than the excited-state decay rate of the quantum dot. It is observed that the optimal detuning and excitation power, in terms of noise sensitivity, are not the same in these two regimes. The linewidth scans with mechanical driving also show significantly different behaviour in the two regimes, from a basic linewidth broadening to an increased intensity at integer laser detunings of the mechanical frequency. On the contrary, the emission spectrum does not show a substantial difference between the two regimes unless the laser is also detuned to the blue or red sideband. More importantly, for reaching the resolved-sideband regime, it is not enough that the mechanical frequency is faster than the decay rate of the dot, but it also needs to be (much) larger than the inhomogeneously broadened linewidth.

Due to the reduced phonon population, the higher the mechanical frequency, the higher needs to be the vacuum exciton-phonon coupling rate to observe the same amount of interaction (at 4.2 K). Reaching a higher-coupling rate is important for experiments such as optomechanical cooling where the sideband-scattering rate is the limiting factor for the temperature that can be reached. For the suspended beam resonator the sideband scattering rate at low excitation powers is still lower than the mechanical loss rate to the substrate. Thus the resonator design needs to be modified further to reach higher mechanical frequencies with higher exciton-phonon coupling rates.

Nevertheless, the suspended beam is a good testbed since it not only has a wide range of mechanical frequencies but also since the mechanical modes can still be actuated well with the electric field antenna. Furthermore, the quantum dot localisation on the mechanical resonator is straightforward, and also the general optical excitation works well with a high level of laser suppression.

## 5.9 Supplementary note I: Electric-field antenna and sample setup

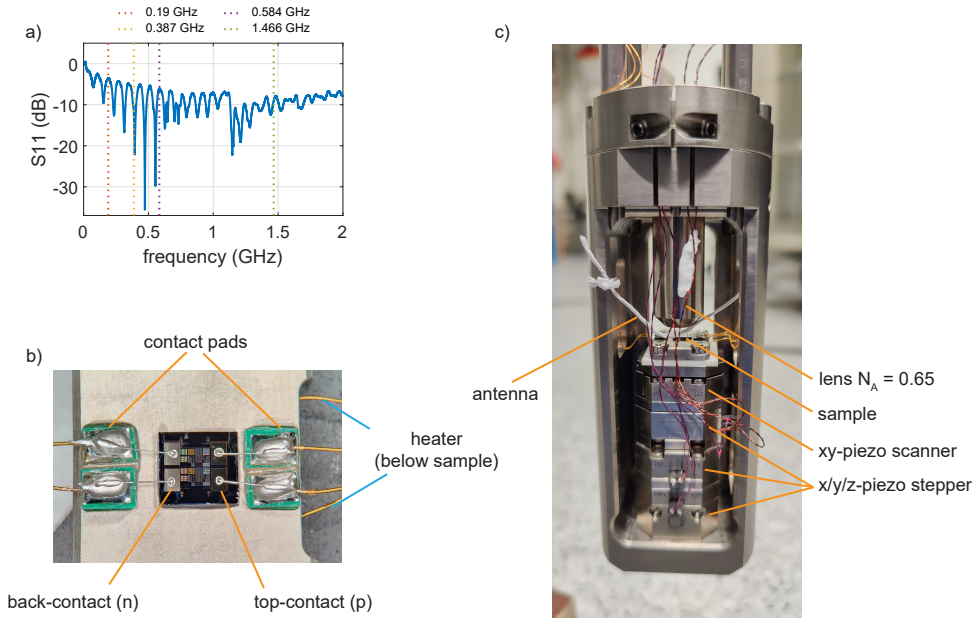


**Figure 5.18: Electric-field antenna characterisation and sample setup.** (a) Reflection spectrum measurement of the electric-field antenna using a vector network analyzer. A series of resonances can be observed, however, the antenna is not optimised for any of the mechanical modes. (b) Top view of the sample holder. The sample is glued on the sample holder using a non-conductive two-component epoxy. The top- and back-contact are connected by hand to the contact pads using a copper wire and a conductive epoxy. Below the sample holder, a resistive heater is installed, which is used during the warmup of the sample to avoid condensation on the sample. (c) Cage setup including a focusing lens with a working distance of about 2 mm ( $N_A = 0.65$ ), xy-piezo scanners (Attocube, ANSxy100std), x/y/z-piezo steppers (Attocube, ANPx101 & ANPz101), and the electric-field antenna consisting of a  $\approx 8$  cm unisolated coaxial cable wrapped in Teflon tape. For further details on the measurements setup see Chapter 3.15.

For many of the presented experiments, the electric field antenna is indispensable. Though it is a very simple scheme, it is yet very effective. The antenna consists of a coaxial cable (LakeShore, CC-SC-25) where the isolation is removed at the end of the cable for about 8 cm. The antenna is installed approximately with 5 mm distance to the sample surface, see Fig. 5.18(c). The orientation is chosen such that there is a  $45^\circ$  angle between the antenna and the sample design axis such that a force acts in both, x- and y-direction. The advantage of this antenna design is a broad field distribution and that all resonators can be actuated at the same time. Furthermore, we assume that the sample position relative to the antenna (within  $\pm 100 \mu\text{m}$ ) does not have an

impact on the actuation efficiency. The dependence of the mechanical amplitude on the applied AC-voltage is linear (see. Fig. 3.2) and we do not see any improvement by additional combination with a DC offset [56, 186].

To briefly characterise the antenna, a reflection spectrum is recorded using a vector network analyzer (Keysight, N5230A PNA-L), Fig. 5.18(a). The frequencies of the breathing modes (as well as the ones of the resonator of Chapter 6) are highlighted. Though there are a few resonances where power is efficiently radiated, none of the mechanical modes coincides with them. The radiation efficiency of the antenna varies slightly for the individual modes. We assume that this is negligible for the actuation efficiency of the mechanical modes. The more important factor is the mechanical mode profile. It is clear that a left-right mechanical bending mode (as for the cantilever), can be much better actuated as the 3rd-order breathing mode of the suspended beam.

Figure 5.18(b) shows the sample top-view. The sample is glued to the sample holder using non-conductive two-component epoxy (UHU, endfest 300). The evaporated contacts are  $1 \times 1.5$  mm in size and are connected to the contact pads by hand, using a copper wire and a conductive epoxy (EPO-TEK, E4110). The sample is then mounted in a cage on top of a piezo stack, see Fig. 5.18(c). For more details on the measurement setup see Chapter 3.15.



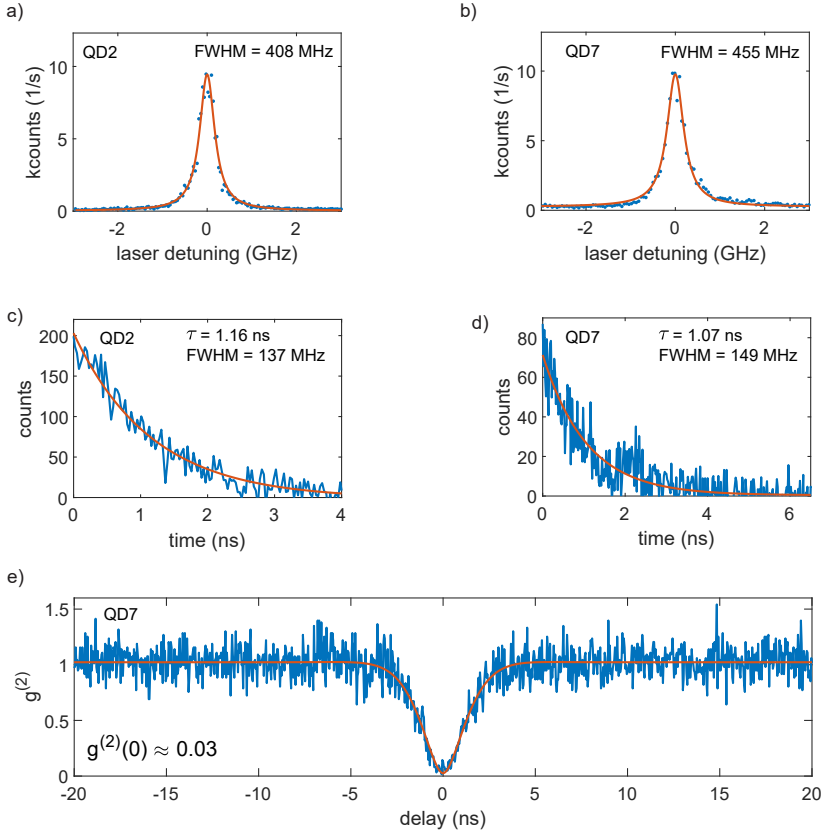
## 5.10 Supplementary note II: Mechanical parameters

Table 5.1 shows the full set of parameters extracted from the Brownian-motion measurements and the finite-element simulations. For more details on the finite-element simulations see Chapter 5.2 and 3.13.

**Table 5.1: Measurement and simulation parameters of the mechanical modes.** The first two rows show the measured mechanical resonances,  $\Omega_m^{\text{meas}}$ , and mechanical quality factor,  $Q_m^{\text{meas}}$ . The remaining rows show parameters for mechanical eigenfrequency,  $\Omega_m^{\text{sim}}$ , effective mass,  $m_{\text{eff}}$ , spring constant,  $k$ , vacuum fluctuation,  $x_{\text{zpf}}$ , thermal displacement at 4.2 K,  $x_{\text{th}}$ , and thermal phonon occupation,  $n_{\text{phon}}$ , obtained from finite-element simulations (COMSOL Multiphysics).

	1	2	3	4	5	6	7	8
$\Omega_m^{\text{meas}}/2\pi$ (MHz)	28.7	63.9	76.1	112	180	190	387	584
$Q_m^{\text{meas}}$	10500	11100	1600	2700	815	3800	3900	2000
$\Omega_m^{\text{sim}}/2\pi$ (MHz)	29	68	80	114	185	194	396	596
$m_{\text{eff}}$ ( $10^{-15}$ kg)	4.8	1.6	2.0	5.0	5.2	6.2	5.7	5.6
$k$ ( $10^3$ N/m)	0.16	0.30	0.52	2.5	6.9	9.2	35	78
$x_{\text{zpf}}$ ( $10^{-15}$ m)	7.7	8.7	7.0	3.8	2.9	2.6	1.9	1.6
$x_{\text{th}}$ ( $10^{-13}$ m)	5.9	4.3	3.2	1.4	0.9	0.8	0.4	0.3
$n_{\text{phon}}$	3050	1370	1150	781	486	460	226	150

## 5.11 Supplementary note III: Quantum dot characterisation



**Figure 5.19: Quantum dot characterisation.** (a,b) Resonant linewidth scans of QD2 and QD7 with corresponding minimal linewidths of 408 and 455 MHz, respectively. The linewidth is fitted with a Lorentzian function. (c,d) Lifetime measurements of QD2 and QD7 as described in Fig. 5.11. The corresponding transformation limits for the quantum dot linewidths are given by  $1/2\pi\tau = 137$  and 149 MHz, respectively. (e) Low power auto-correlation showing high level of anti-bunching with  $g^{(2)}(0) \approx 0.03$ . The fit curve is given by Eq. 5.4. For this measurement, every minute the laser is automatically suppressed and the quantum dot resonance is locked to the laser frequency using the gate voltage.

The inhomogeneous broadening of the quantum dot emission can be probed by a low-power resonant linewidth scan, where power broadening is absent. Figure 5.19(a,b) shows linewidth scans at 1 nW excitation power ( $\Omega_R \ll \Gamma_R$ ) for QD2 and QD7. Both dots show a similar linewidth of 408 and 455 MHz, extracted with a Lorentzian fit. For an ensemble of charge traps, a Gaussian or Voigt profile would be expected. Due to the low excitation power, the laser suppression is at a high level. Note that if the

laser suppression is not optimised, Fano lineshapes are often observed. The measurements are performed on the neutral exciton.

The lifetime of the two dots is extracted as described in Chapter 5.7.3. the decay is fitted with a single exponential curve and the lifetime is extracted  $\tau_{\text{QD2}} = 1.16$  ns and  $\tau_{\text{QD7}} = 1.07$  ns, see Fig. 5.19(c,d). The corresponding Fourier limit of the linewidth is  $\text{FWHM}_{\text{QD2}} = 137$  MHz and  $\text{FWHM}_{\text{QD7}} = 149$  MHz. Therefore, the measured linewidths of QD2 and QD7 are a factor of 2.98 and 3.05 above the Fourier limit. As discussed in the main chapters, this reduces the noise sensitivity and also leads to a reduced frequency resolution.

Figure 5.19(e) shows a low-power resonant autocorrelation measurement. The counts are split 50:50 with a fibre-base beamsplitter and sent to individual single-photon detectors. A high single-photon purity of 97% is obtained, mainly also due to the automated laser suppression which is performed every minute. The autocorrelation is fitted with the standard autocorrelation function of a two-level system [183]:

$$g_{\text{TLS}}^{(2)}(\tau) = 1 - \exp\left(\frac{1}{4}(3\Gamma_{\text{R}} + 2\gamma^*)\tau\right) \cdot \left(\cos(\lambda\tau) + \frac{3\Gamma_{\text{R}} + 2\gamma^*}{4\lambda} + \sin(\lambda\tau)\right), \quad (5.4)$$

$$\lambda = \sqrt{\Omega_{\text{R}}^2 - \frac{1}{16}(\Gamma_{\text{R}} - 2\gamma^*)^2}, \quad (5.5)$$

where  $\Gamma_{\text{R}}$  is the spontaneous decay rate,  $\Omega_{\text{R}}$  the Rabi frequency of the optical drive, and  $\gamma^*$  the pure dephasing rate of the excited state.

## 5.12 Supplementary note IV: Time-resolved measurements

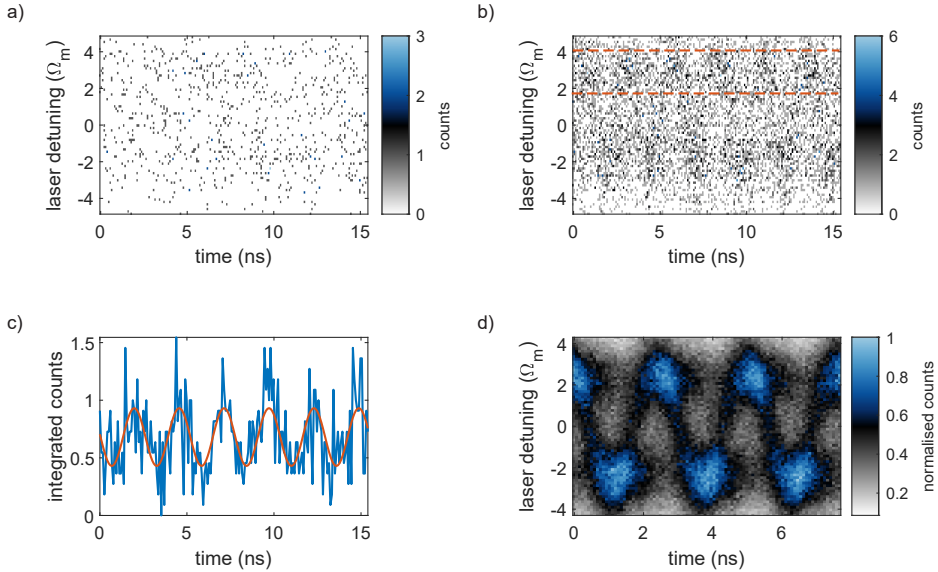


**Figure 5.20: Time resolved measurement method.** (a) Single time-histogram of the 387 MHz mechanical mode. Due to the high mechanical frequency and the low count rate on the detector of  $\approx 1$  kHz, the modulation is highly undersampled and no modulation is visible. (b) Due to the time synchronisation of the time tagger and the microwave source we can fold back the data of a 150 ns measurement so that we obtain an average over 10 times 15 ns of the histogram. Consequently, time dynamics become visible. (c) Average over the orange highlighted region in (b) fitted with a sine function to obtain phase information. This phase information is used in (d) to average over 100 individual measurement runs.

In Chapter 5.7.6 time-resolved resonant linewidth measurements are shown for various mechanical frequencies. In the following, it is explained how the data is analysed to produce the final 2D-color plots. As already mention in Chapter 5.7.6 the mechanical frequency is almost four orders of magnitude higher than the single-photon count rate on our detectors. Furthermore, due to the large drifts in the experiments, spectral wandering and heating from the electric field antenna, the measurement time for a single run needs to be below 1 min. This means that for a single histogram (horizontal data row in Fig. 5.20(a)) the integration time is only 0.25s. Thus, the histogram is recorded with a time axis of 154 ns which is folded back to a range of 15 ns to obtain an effective averaging of ten, see Fig. 5.20(b). Now a slight count rate modulation can already be observed. Note that the folding back is only possible by introducing a time binning which is an exact multiple of the applied mechanical drive. The measurement is repeated over 120 times and averaged again. For this averaging, the phase of each individual measurement needs to be determined. Otherwise, due to the phase drift in the measurements, the outcome would be completely washed out. To extract the

phase, the orange-highlighted region in Fig. 5.20(b) is averaged in  $y$ -direction and fitted with a sine function, see Fig. 5.20(c). this phase information is then used for the final averaging process, shown in Fig. 5.20(d).

The following three figures, Fig. 5.21, 5.22, and 5.21, present the full data and simulation set for three different mechanical driving amplitudes for the mechanical modes already presented in Chapter 5.7.6.

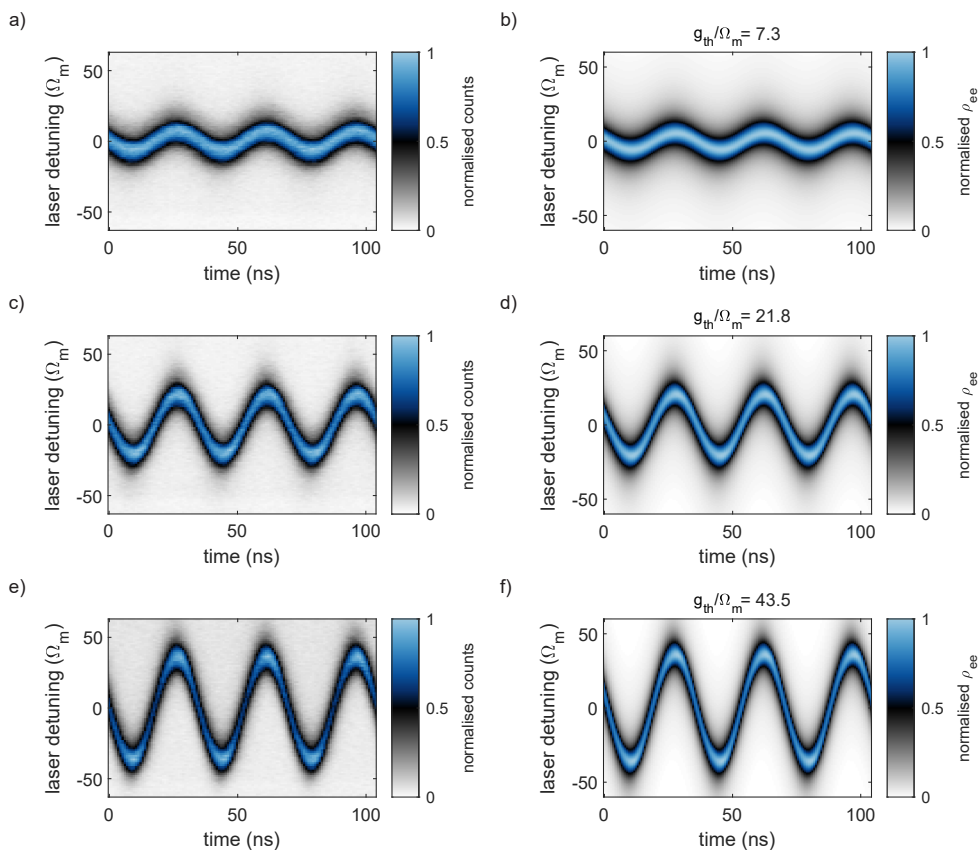


**Figure 5.21: Time resolved measurement set of the 1st-order in-plane bending mode.** Comparison of the time resolve measurement and the numerical simulation for different mechanical driving amplitudes at 29 MHz: (a,c,e) measurement, and (b,d,f) simulation.

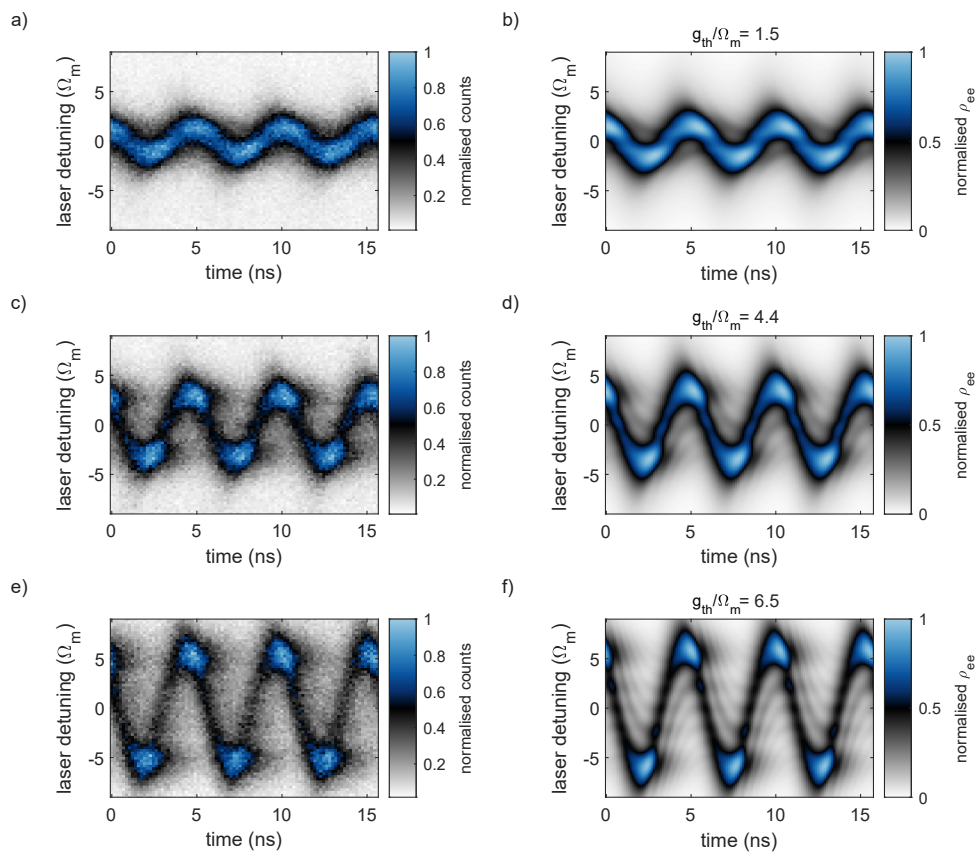


**Figure 5.22: Time resolved measurement set of the 1st-order in-plane breathing mode.** Comparison of the time resolve measurement and the numerical simulation for different mechanical driving amplitudes at 190 MHz: (a,c,e) measurement, and (b,d,f) simulation.

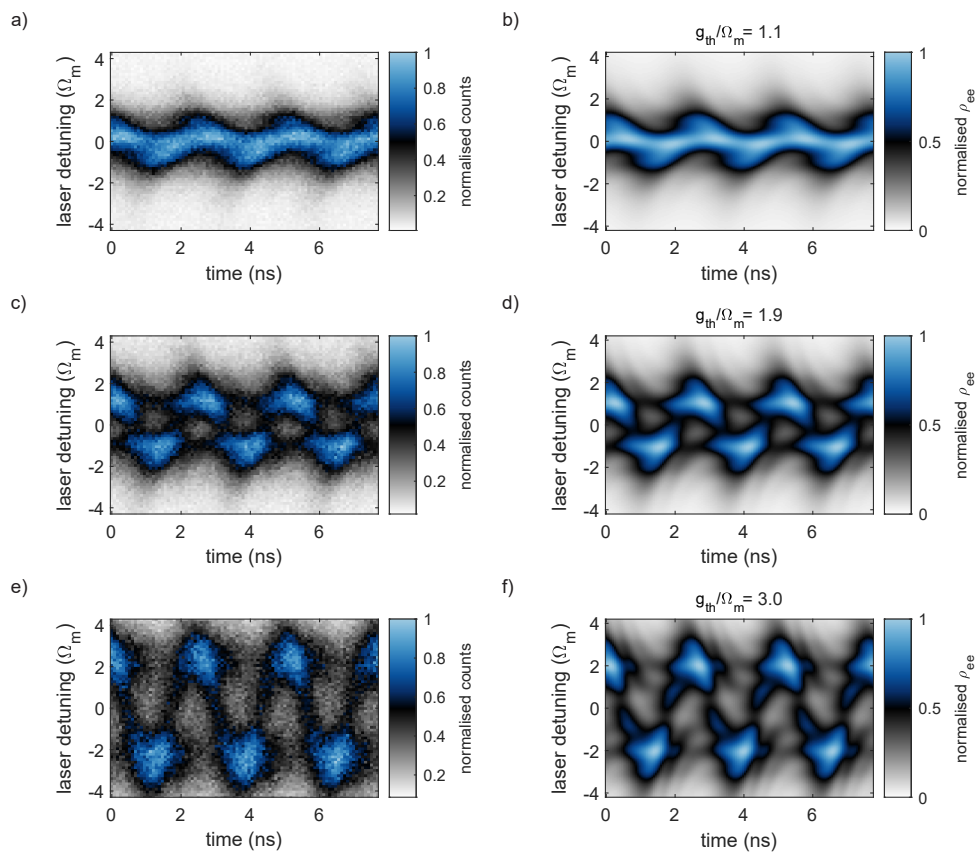


**Figure 5.23: Time resolved measurement set of the 2nd-order in-plane breathing mode.** Comparison of the time resolve measurement and the numerical simulation for different mechanical driving amplitudes at 387 MHz: **(a,c,e)** measurement, and **(b,d,f)** simulation.



## 5.13 Supplementary note V: Emission spectrum measurements

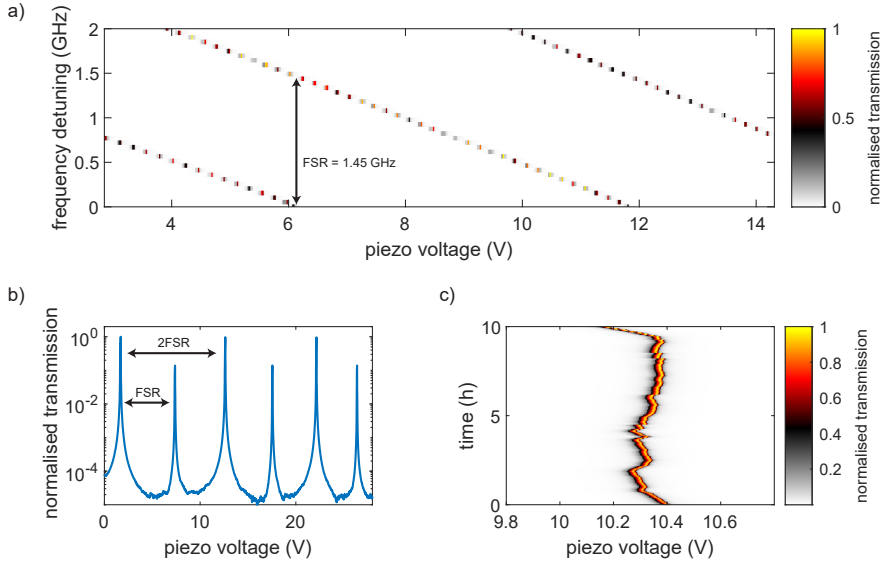


**Figure 5.24: Piezo-tunable Fabry-Pérot etalon.** (a) Record of the etalon transmission (Thorlabs, SA200-8B) while sweeping the voltage applied to the cavity piezo-element as well as the laser frequency. The etalon has a natural free spectral range of  $\text{FSR} = 1.45 \text{ GHz}$  and a Finesse of  $\mathcal{F} = 170$  which corresponds to a transmission window of  $\Delta_\nu = 8.5 \text{ MHz}$ . (b) The etalon is set up free-space and coupled back into a fibre. For some experiments, we leverage the low quality of the etalon to reduce the transmission of every second transmission peak by an order of magnitude, which gives an effective  $\text{FSR}_{-9\text{dB}} = 2.9 \text{ GHz}$ . (c) Stability of the etalon over time, with a mean drift of  $0.06 \Delta_\nu/\text{min}$  and a maximum drift of  $0.4 \Delta_\nu/\text{min}$ .

The emission spectra in Chapter 5.7.7 are performed with a standard piezo tunable confocal Fabry-Pérot etalon (Thorlabs, SA200-8B). The etalon is set up in free space with two mirrors for each, in and out-coupling. During the alignment process, it is made sure that the beam is perfectly parallel to the cavity to maximise the transmission as well as minimise the etalon transmission width. The alignment is performed optically by continuously scanning the cavity around the resonance using an arbitrary waveform generator and imaging the mode profile on a camera. The etalon transmission at resonance is 10% (same as in specifications). The transmission is limited by the etalon quality (which can also be seen by the poor lateral profile of the optical modes).

Fig. 5.24(a) shows the transmission scan of the etalon in dependence of the applied piezo voltage (Basel Precision Instruments, DAC SP 927 & Attocube, ANC300) and the laser frequency. Three optical modes with a transmission width of  $\Delta_\nu = 8.5 \text{ MHz}$  are shown separated by a confocal free-spectral range of  $\text{FSR} = 1.45 \text{ GHz}$ . Due to the overlap of the FSR with the higher order side peaks of the  $387 \text{ MHz}$  mechanical

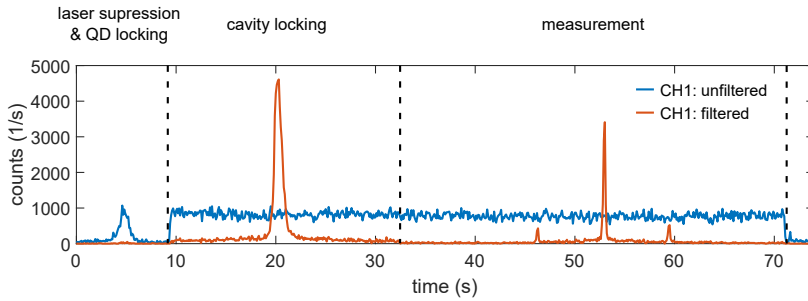


**Figure 5.25: Emission spectrum measurement method.** Measurement method for the emission spectrum of the quantum dot using the Fabry-Pérot etalon (see Fig. 5.16): automatic laser suppression (channel 1), locking the quantum dot resonance to the laser frequency (channel 1), locking of the etalon transmission window to the laser frequency (channel 2), and measurement (channel 2). For high measurement quality, the full sequence needs to be several times faster than the etalon drift as well as the quantum dot resonance drift.

mode, we exploit the poor quality of the etalon to obtain an effective free spectral range of  $\text{FSR}_{-9\text{dB}} = 2.9 \text{ GHz}$ . Since the etalon is a confocal filter, every second mode is a higher-order mode. The alignment can be changed such that the transmission efficiency of the higher-order modes is reduced 10-fold, see Fig. 5.24(b).

Besides the low transmission, the etalon also shows a very unstable resonance condition. Figure 5.24(c) shows the drift of the cavity resonance over the course of ten hours. The mean drift of the etalon is  $0.06 \Delta_v/\text{min}$  and the maximal drift observed is  $0.4 \Delta_v/\text{min}$ . Thus the experiments need to be performed faster than the drift (faster than a minute). However, since the count rate is low, due to the low excitation to omit power broadening, the measurement needs to be repeated many times to achieve a satisfying signal-to-noise ratio.

Figure 5.25 shows a time stream of a single quantum dot emission measurement. The collected emission is sent to a 20:80 fibre beam splitter. The stronger fibre output is connected to the etalon whereas the weaker arm is directly connected to the single-photon detectors. The measurement is performed as follows. First, the unfiltered channel is used to correct for spectral fluctuation by locking the quantum dot to the fixed laser using the applied gate voltage. Second, using the filtered channel, the cavity resonance drift is corrected by locking it also to the laser frequency. Finally, the mechanical drive is turned on and the cavity is slowly scanned and the filtered emission is recorded. The full sequence takes about a minute, see Fig. 5.25, and is averaged over 20 individual scans. Though the technique described above enables a clean emission spectrum to be recorded, the stability of the etalon could be optimised using a temperature stabiliser.

## 5.14 Supplementary note VI: 25 $\mu\text{m}$ mechanical resonator

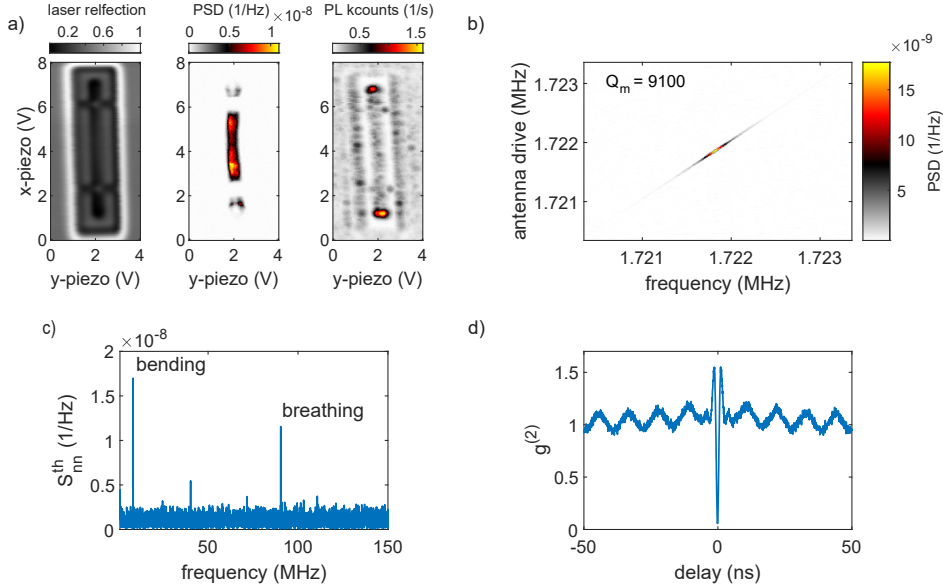


**Figure 5.26:** 25  $\mu\text{m}$  freely-suspended beam. (a) Laser reflection, mechanical mode shape of the out-of-plane bending mode, and photoluminescence map of a  $25 \times 0.96 \mu\text{m}^2$  beam. (b) Mechanical quality factor measurement by driving the resonator with the electric-field antenna and recording the power spectrum on a spectrum analyzer. (c) Resonant power spectral density of a single quantum dot which is located in the centre of the resonator. The 1st-order in-plane bending and breathing modes are labelled. (d) Resonant autocorrelation while driving the breathing mode at low amplitude.

A larger version of the freely suspended beam is also measured in the same way as described in the main chapters. The resonator length is 25  $\mu\text{m}$  which facilitates the search for quantum dots on the mechanical resonator, see Fig. 5.26(a). We observe that the mechanical quality factor of the 1st-order out-of-plane bending mode is higher than the one of the 12  $\mu\text{m}$  resonator,  $Q_m = 9.1 \times 10^3$  (see Fig. 5.26(b)). We attribute this to a better mode profile with less leakage to the surrounding under-etched substrate. We observe the same mechanical in-plane bending and breathing modes as for the smaller resonator. Since the resonator is about twice the size of the smaller one, the mechanical frequencies are also shifted down by a factor of two. A noise power spectrum of a single quantum dot measurement in the centre of the beam is shown in Fig. 5.26(c). Furthermore, the autocorrelation of the same dot under mechanical driving of the  $\approx 100$  MHz mode is shown in Fig. 5.26(d). Note that there was also a 6  $\mu\text{m}$  long resonator fabricated, however, it was not possible to observe any mechanical modes, most likely due to a too-high coupling to the surrounding under-etched substrate.

## 5.15 Supplementary note VII: A comment on charge and spin noise

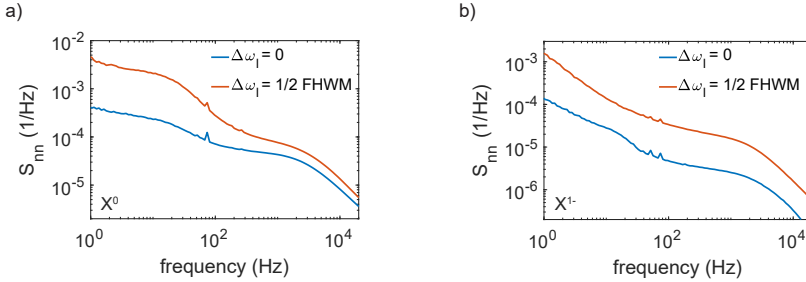


**Figure 5.27: Charge and spin noise measurement.** (a,b) Power spectrum measurements of the neutral exciton,  $X^0$ , and the charged exciton,  $X^{1-}$ , of QD2. For both excitons, the measurement is performed on resonance with the quantum dot (blue) and detuned by half a linewidth (orange). Besides a  $1/f$  noise, charge noise is present by the low-frequency noise ( $1 - 10^2$  Hz), whereas spin noise is present at high frequencies ( $10^2 - 10^4$  Hz). The power spectrum is obtained from a fast Fourier transform of a time trace measurement.

The inhomogeneous broadening of the quantum dot resonance leads to an increased linewidth of a factor of  $\sim 3$ . Previously it was seen that this broadening is not just due to charge noise but also to a large extent due to spin noise [125]. Therefore, a low-frequency noise measurement is performed on the exciton and trion of QD2, Fig. 5.27(a,b). The measurement is performed in the same way as in Ref. [125] by recording a time trace of the quantum dot emission on resonance with the dot and also half a linewidth detuned (blue detuned). According to Ref. [125] the slow noise ( $1 - 10^2$  Hz) is given by charge noise and the fast noise ( $10^2 - 10^4$  Hz) is given by spin noise. This is also reflected in our experiments. The high-frequency noise increases for the trion where the ground state is given by a single-electron spin (whereas the ground state of the exciton is empty). Further, when detuning the laser, the low-frequency noise increases for both, exciton and trion, which would correspond to charge noise. Although both excitons show different amounts of noise, the inhomogeneous broadening is about the same (as also observed in Ref. [125]). To summarise, we observe that both, spin and charge noise are present, however, for quantification further investigation is needed. Note that the weak peaks around 50-80 Hz come from noise in the instrumental setup (ground loops).



---

**Quantum-dot optomechanics in the  
resolved-sideband regime**

---

## 6.1 Introduction

Coupling a single-photon emitter to a mechanical resonator is of high interest, especially at high mechanical frequencies, i.e., GHz frequencies, where motional sidebands can be observed. These mechanical sidebands can be used to deterministically create or annihilate single-phonons which can be used, for example, to cool a mechanical resonator to its motional ground state [24, 27, 187]. Similar to cavity optomechanics, phonons can be created in a heralded manner [72, 188] and stored in a mechanical resonator mode [189, 190] for much longer than the quantum dot lifetime due to the long lifetime of the mechanical vibration (here  $2\pi/\Gamma_m = 1.41 \mu\text{s}$ , see Chapter 6.6).

So far, quantum-dot optomechanics in the resolved-sideband regime has only been observed with additional mechanical driving of the resonator. Though this makes a lot of measurements much less time-consuming (see Chapter 5), it also overshadows the true coherent interaction between the quantum dot and the mechanical resonator, which is necessary, for example, to observe cooling of a mechanical mode.

As shown in the previous chapter, the interaction between the two systems based on Brownian motion (especially in the resolved-sideband regime) is not yet fully understood. The observations from the previous chapter suggest that there is a fundamental difference in the interaction between the two systems if the mechanical frequency is slower or faster than the quantum dot decay rate. Here, the beam resonator design is optimised further to push the mechanical frequency far into the resolved-sideband regime. This chapter presents a combination of simulations and optomechanical measurements to investigate if first, a mechanical resonator with sufficient quality can be achieved, second, if quantum dots can be located on the resonator and excited resonantly, and third, if exciton-phonon coupling can be observed without additional mechanical driving.

## 6.2 Finite-element simulations

For both – cantilever and suspended beam resonators – the coupling to the surrounding under-etched membrane is a limiting factor for high-frequency mechanical modes. Furthermore, suspended beam resonators smaller than  $12 \mu\text{m}$  showed no high-frequency mechanical modes due to the strong coupling to the surrounding membrane. Therefore, a phononic-crystal structure is introduced to decouple the mechanical resonator from the surrounding substrate [152–154].

Figure 6.1(a) shows the mechanical displacement profile of the  $\sim 1.5 \times 1 \mu\text{m}^2$  resonator, embedded in a phononic-crystal structure. The design of the mechanical resonator is inspired by the devices used in the cavity-optomechanics community [27]. Note that the width of the phononic-crystal beam is exactly the same as for the suspended beam from the previous chapter. The mode of interest is the fundamental in-plane (longitudinal) breathing mode at 1.466 GHz. The high mechanical frequency puts us far into the resolved-sideband regime: the mechanical frequency is not only higher than the decay rate of the dot, here  $\Omega_m = 10\Gamma_R$ , but also larger than the inhomogeneously broadened linewidth, here  $\Omega_m = 3\text{FWHM}$ . The high confinement of the mechanical mode shown in Fig. 6.1(a) is due to a gap in the density of states of the phononic-crystal structure. As a consequence, a mode volume

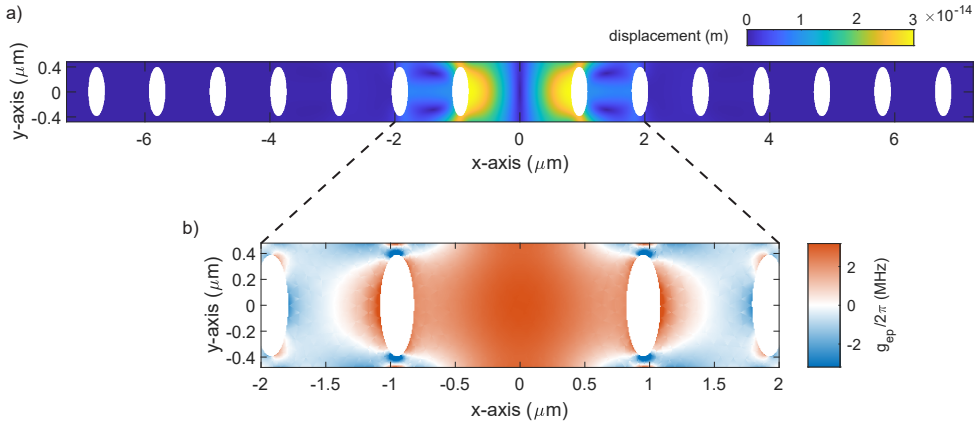


**Figure 6.1: Finite-element simulations of the phononic-crystal beam.** (a) Displacement profile of the mechanical in-plane breathing mode ( $z$ -symmetric/even) at  $\Omega_m = 1.466$  GHz, where most of the displacement is in  $x$ -direction (along  $[110]$ ). The width of the beam is 960 nm, the height is 180 nm (including the diode structure), and the phononic shield consists of seven equally-spaced etched ellipses (see Fig. 6.2). The mechanical mode is highly confined, resulting in a mechanical mode volume as small as  $3 \times 10^{-3} \lambda^3$  (with  $\lambda = 3.6 \mu\text{m}$ ). (b) Vacuum exciton-phonon coupling rate (at  $z = 0$ ) obtained from thermomechanical calibration. As for the resonator in Chapter 5, the in-plane breathing mode shows a highly homogeneous coupling profile in the centre of the resonator where we expect a maximum coupling of  $g_{\text{ep}}/2\pi = 3.2$  MHz.

$V_m = \int \frac{|u(x,y,z)|^2}{\max(|u(x,y,z)|^2)} dV$  as small as  $3 \times 10^{-3} \lambda^3$  is achieved [65]. This is substantially smaller than the mode volume of recent quantum-dot surface-acoustic-wave cavities [64, 65], showing the large potential of the membrane-type resonator.

The in-plane breathing mode is selected due to the homogeneous displacement and strain profile. Figure 6.1(b) shows the vacuum exciton-phonon coupling profile (which is directly related to the strain profile, see Chapter 3) of the fundamental breathing mode. The profile shows a very homogeneous distribution, especially along the  $y$ -axis. A maximum coupling of  $g_{\text{ep}}/2\pi = 3.2$  MHz is achieved if the quantum dot is located exactly in the centre of the resonator. This is comparable, also slightly higher, than what was recently observed with surface acoustic wave cavities [64, 65].

The displacement profile, as well as the coupling profile, are extracted from finite-element simulations. The displacement profile is integrated to obtain the effective mass,  $m_{\text{eff}} = 7.4 \times 10^{-16}$  kg, which is used to estimate the spring constant,  $k = 63 \times 10^3$  N/m, the zero-point motion,  $x_{\text{zpf}} = 2.7 \times 10^{-15}$  m, and the exciton-phonon coupling rate,  $g_{\text{ep}}/2\pi$ . Compared to the previous resonators, here, the thermal phonon population has reduced another three-fold to  $n_{\text{phon}} = 58$ . The thermal displacement is  $x_{\text{th}} = 3.0 \times 10^{-14}$  m and the thermal coupling rate is  $g_{\text{th}}/2\pi = 34.5$  MHz.

Figure 6.2(a) shows the unit cell of the phononic crystal [152–154], consisting of an ellipse airhole with a size of  $w_e = 270$  nm and  $h_e = 775$  nm. The lattice constant is  $l = 970$  nm. The nanostructuring of the unit-cell leads to modulation of the mass and when periodic conditions are applied, a gap opens up in the band diagram



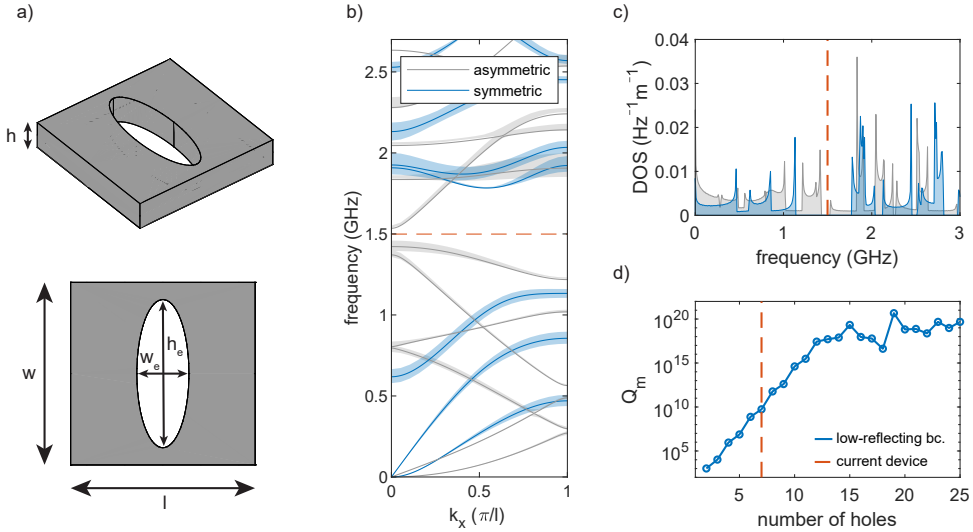


**Figure 6.2: Phononic bandgap simulations.** (a) Side-view and top-view of the geometrical unit cell of the structure shown in Fig. 6.1 with length scales of:  $l = 970$  (lattice constant),  $w = 960$ ,  $h = 180$ ,  $h_e = 775$ , and  $w_e = 270$  nm. (b) Band diagram of the phononic-shield unit cell. The simulation is performed twice, for mechanical modes with  $z$ -asymmetry (grey) and  $z$ -symmetry (blue). Additionally, band broadening due to fabrication imperfections is studied (shaded area around the bands) by introducing size fluctuations of the air-hole by up to  $\pm 20$  nm in both directions. The mechanical mode at  $\Omega_m/2\pi = 1.466$  GHz is highlighted in orange. (c) Phonon density of states (DOS) obtained from integration of the band diagram in (a), normalised to the unit-cell length. (d) Mechanical quality study in dependence of the number of etched holes. The loss in the study is given by two low-reflecting boundaries at the clamping edges of the phononic-crystal beam (left and right edges). The quality factor increases rapidly and flattens above 12 holes. The current device with seven holes is highlighted in orange.

(similar to a diatomic chain), see Fig. 6.2(b). The mechanical mode frequency is highlighted in orange. The band diagram is obtained from an eigenmode study where periodic conditions are applied in  $x$ -direction and the  $k$ -vector is swept in the range of  $k_x = [0, \pi/l]$  (irreducible Brillouin zone in the reciprocal lattice). The simulations are performed for in-plane (even/symmetric) and out-of-plane (odd/asymmetric) modes. The phononic gap for in-plane modes is very large,  $0.65$  GHz  $\approx 45\%$  of  $f_m$ , whereas the one for out-of-plane modes is rather small,  $0.11$  GHz  $\approx 7\%$  of  $f_m$ . The latter can have an impact on the confinement of the mechanical mode if there are fabrication imperfections which introduce a hybridisation of in- and out-of-plane modes. As an estimate of the bandgap dependence on fabrication imperfections, an additional study is performed where the ellipse parameters are swept by  $\pm 20$  nm. We assume that the ellipse etching is the major source of fabrication imperfection (compared to the lattice constant and the beam width). The effect of fabrication imperfections is a broadening of the acoustic bands, shown by the shaded areas in Fig. 6.2, whereas the centre of the gap is not much affected. Therefore, the current device should be

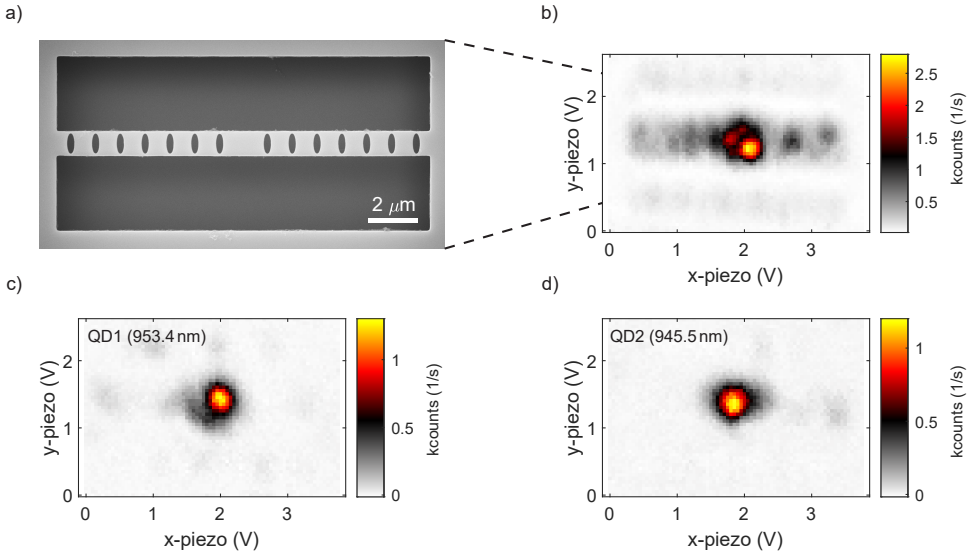


**Figure 6.3: Photoluminescence map of the optomechanical device.** (a) Scanning electron microscope image of the phononic-crystal beam. The residues which are visible around the beam are remainings of the photoresist after the etching step. (b) Photoluminescence map of the phononic-crystal beam, showing a bright luminescence from many dots at the location of the mechanical resonator. (c,d) Single-wavelength evaluation of the photoluminescence map at 953.4 nm (QD1) and 945.5 nm (QD2). The emission of both quantum dots is well localised without any apparent waveguiding.

relatively robust and we assume that the fabrication imperfections which we observe in the SEM pictures are negligible (see Fig. 6.3(a)). Figure 6.2(c) shows the density of states (DOS) normalised to the unit-cell length [75], obtained from an integration of the band diagram. Close to the bandgap edges a high increase is observed, described by the Van Hove singularity [191].

The de-coupling of the mechanical resonator from the substrate depends on the number of shield elements. Figure 6.2(d) shows a study of the mechanical quality (limited by clamping loss) in dependence on the number of etched airholes. Due to the exponential decay of the displacement profile, already three air holes result in strong suppression of the leakage to the substrate. To be on the safe side, also considering potential fabrication imperfections, seven air holes are chosen for the current device. Note that axis orientation plays a crucial role in the resonator described above. For a rotation of  $\pm 45^\circ$  (from [110] to [100]/[010]) and keeping the design the same, the mechanical mode would not exist anymore.

## 6.3 Optical device characterisation

Two very important factors of mechanical resonators with feature sizes in the nanometre regime are the localisation of a quantum dot on the resonator and the local semi-

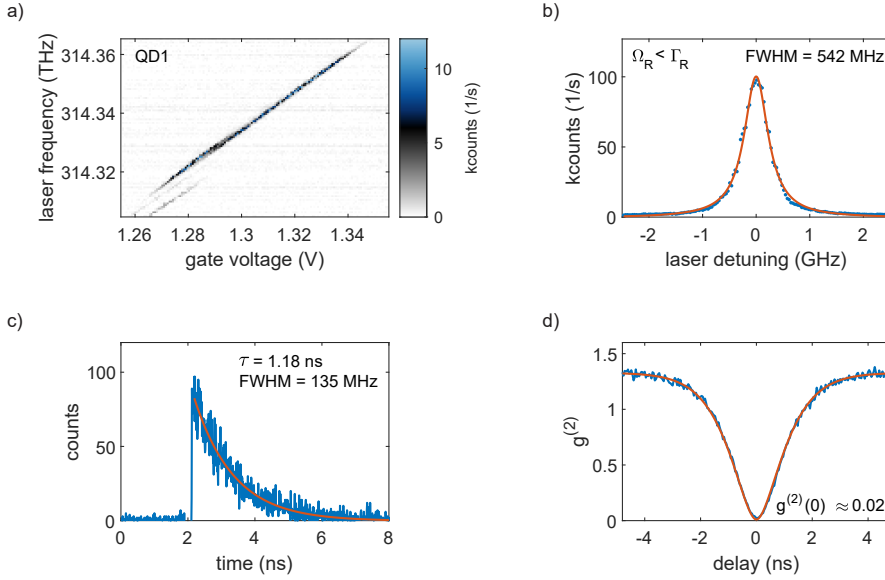


**Figure 6.4: Quantum dot characterisation.** (a) Resonant charge plateau scan of the single-negatively charged exciton,  $X^{1-}$ , of QD1. The doped gate layers still work well and there is no issue with charging the quantum dots, although the smallest connection of the phononic-crystal beam is only 90 nm in width. (b) Low-power resonant linewidth scan in the centre of the plateau shown in (a). There is a slightly larger inhomogeneous broadening than for the previous mechanical resonators (see Chapter 3 and 5), though the lineshape remains close to a Lorentzian. (c) Lifetime measurement of QD1. There is no evidence of Purcell enhancement and thus our optical optimisation does not affect the intrinsic linewidth. The measurement is performed using picosecond pulses from a mode-locked laser. (d) Low-power autocorrelation measurement showing a high level of single-photon purity of 98%, even though the laser suppression on small structures is usually challenging. The fit function is given by Eq. 5.4

conductor diode quality. Quantum dot localisation was found to be a major issue with previous mechanical resonator designs (not shown in this Thesis). Often, quantum dots were much brighter on the phononic shield compared to the resonator and due to optical waveguiding via straight connections, it was impossible to precisely locate individual dots. We overcome these issues via careful design optimisation. We optimise the mechanical resonator dimensions for maximum outcoupling to the top, see [Supplementary note II](#). Furthermore, we avoid straight connections from the centre position on the resonator to the surrounding phononic shield which suppresses optical waveguiding, see Fig. 6.3(a).

The result of the optical optimisation can be seen in the photoluminescent map in Fig. 6.3(b). The quantum dots on the phononic-crystal beam are brighter than on the bulk but more importantly, the dots on the mechanical resonator itself are even brighter and the emission is well localised. The same is observed when evaluating the photoluminescence map for single wavelengths, at 953.4 nm for QD1 and 945.5 nm,

see Fig. 6.3(c,d). There is some slight waveguiding of the luminescence but at a negligible level and the quantum dot position on the resonator can be well determined. Note that some of the dots show an increased level of optical waveguiding due to the non-centred location on the resonator.

The quality of the diode structure depends on how well the doped gate layers conduct through the narrow connections in the phononic-crystal structure. The smallest connection is as thin as 80-90 nm. The quality of the gates is probed via resonance fluorescence. We not only observe a good tunability of the charge plateau, see Fig. 6.4(a), but also narrow optical linewidths, see Fig. 6.4(b). For excitation powers much below saturation, the minimal linewidth is  $\approx 540$  MHz. Although there is an enhancement in collection counts (compared to the dots on the suspended beam), there is no significant change in the quantum dot lifetime with  $\tau = 1.18$  ns, see Fig. 6.4. Therefore, there is no effect of Purcell enhancement (which would broaden the linewidth), and there is slightly more semiconductor noise on this structure with  $\text{FWHM} = 4\Gamma_{\text{R}}$ . Here, the lifetime is measured with a mode-locked laser (ps-pulses).

The performance of the laser suppression is worse than on the resonators presented in Chapter 3 and 5. We observe a lower suppression level as well as large drifts on a timescale of tens of seconds. At low powers, it is still possible to compensate for these drifts, however, at high powers, laser suppression becomes an inevitable problem, see Chapter 6.5. Furthermore, laser suppression depends highly on the laser spot position and sometimes it is worth sacrificing count rates for better laser suppression by changing the laser position with single piezo steps.

Figure 6.4(d) shows a low-power autocorrelation measurement of QD1 fitted by Eq. 5.4. The high single-photon purity of 98% ( $g^{(2)}(0) = 0.02$ ) is proof of a high level of laser suppression at the corresponding laser power.

## 6.4 Numerical master-equation simulations

The mechanical frequency of the phononic-crystal beam of 1.466 GHz is three times higher than of the suspended beam (2nd-order breathing mode). Therefore, numerical master-equation simulations of the mechanical noise sensitivity are performed in the same way as in Chapter 5.5 but with three times higher Rabi frequencies. For the simulations, the thermal quantum dot resonance modulation,  $g_{\text{th}}$ , is taken from the finite-element simulations in Chapter 6.2. Figure 6.5(a) shows the average excited-state population in dependence on Rabi frequency and laser detuning. The inhomogeneous broadening is included as described previously, which leads to faster dampening of the Rabi oscillations (broadening in frequency space, see [Supplementary note I](#)) and a lower excited-state population.

Figure 6.5(b) shows the noise sensitivity of the 1.466 GHz mode. Now the difference compared to the derivative of the quantum dot linewidth is more obvious as in Fig. 5.7. In dependence on the laser detuning, the sensitivity is highest, whenever the effective Rabi frequency matches the mechanical frequency:

$$\Omega_{\text{eff}} = \sqrt{\Omega_{\text{R}}^2 + \Delta\omega_1^2} \stackrel{!}{=} \Omega_{\text{m}}, \quad (6.1)$$

where  $\Omega_{\text{R}}$  is the bare Rabi frequency,  $\Delta\omega_1/2\pi$  the laser detuning, and  $\Omega_{\text{m}}/2\pi$  the mechanical frequency. The condition of Eq. 6.1 is shown in orange in Fig. 6.5(b).

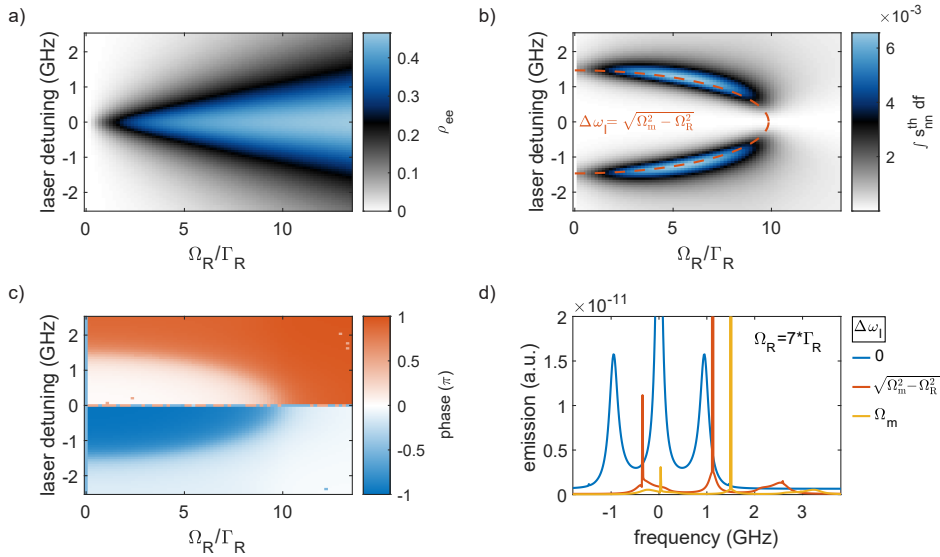


**Figure 6.5: Numerical master equation simulations in the resolved-sideband regime.** (a-c) Numerical master equation simulation using the Hamiltonian in Eq. 5.1 evaluated for (a) the mean excited-state population, (b) the noise power, and (c) the corresponding phase. The noise profile is intriguingly different compared to mechanical frequencies much lower than the quantum dot decay rate, see Chapter 5.5 Fig. 5.7. The observation of the mechanical noise in the quantum dot count rate is most efficient whenever the effective Rabi frequency,  $\Omega_R^{\text{eff}}$ , is equal to the mechanical frequency (highlighted in orange). The corresponding phase shows a similar behaviour with a  $\pi$ -phase shift not only at zero laser detuning but also at detunings when  $\Omega_R^{\text{eff}} = \Omega_m$ . (d) Numerical simulations of the emission spectrum at different detunings show that at the optimal detuning not only the noise in the count rate is enhanced but also the sideband intensity (see (b)).

Strikingly, there is a low-power low-detuning regime where the sensitivity to low-frequency modes would be very high but there would not be any signal from the 1.466 GHz mode.

Figure 6.5(c) shows the extracted phase of the noise in Fig. 6.5(b). Overall, there are three transitions of  $\pi$ . First, when the laser is in resonance with the dot,  $\Delta\omega_1/2\pi = 0$ . Second, when the laser detuning satisfies Eq. 6.1. This shows that there is not only an increased sensitivity at  $\Omega_R^{\text{eff}} = \Omega_m$  but in fact, some sort of a transition.

In addition to the excited-state population, numerical simulations of the emission spectrum are performed in the same way as described in Chapter 5.7.7 but without applying a filter function. Figure 6.5(d) shows three emission spectra with the same Rabi frequency but different laser detunings. We assume that although the interaction is modelled with a classical mechanical drive, the model is a good estimate for the interaction since the mechanical linewidth is three orders of magnitude smaller than the optical linewidth. If the laser is in resonance with the quantum dot, the sideband intensity is about  $5 \times 10^{-4}$  of the normalised emission (independent of excitation power), see Fig. 6.5(b). In the detuned case, one would assume that when the laser

is detuned by  $\Delta\omega_1 = \Omega_m$ , the emission into the sideband should be highest. Whereas this is true for low excitation power, at high powers, the numerical simulations show that the sideband intensity is maximal when the laser detuning satisfies Eq. 6.1. The normalised intensity of the sidebands in the detuned case is  $1.8 \times 10^{-2}$  for  $\Delta\omega_1 = \sqrt{\Omega_m^2 + \Omega_R^2}$  and  $6 \times 10^{-3}$  for  $\Delta\omega_1 = \Omega_m$ . Note that the inhomogeneous broadening affects the sideband intensity mainly at low powers. At high powers, the quantum dot is less affected by the inhomogeneous broadening due to power broadening. Thus, without inhomogeneous broadening, the noise sensitivity would be maximal at low Rabi frequencies.

To summarise, for measuring optomechanical interaction in the GHz-regime, based on Brownian motion, high excitation powers and very specific laser detunings are needed. The mechanism behind the increased sensitivity at the condition of Eq. 6.1 is not yet fully understood. One explanation could be that in the dressed state picture, the splitting between the two states matches the mechanical frequency. Another explanation could be bandwidth matching – the mechanical modulation of the excited-state population works best if it matches the excited-state modulation of the driving laser.

## 6.5 High-power resonant excitation

As discussed in the previous chapter, high excitation powers are needed to observe quantum dot mechanical interaction at high mechanical frequencies. This, however, is an issue for the phononic-crystal resonator. Figure 6.6(a,b) shows resonant linewidth scans of QD1 and QD2 at an optical Rabi frequency of  $\Omega_R \approx 8\Gamma_R$ . Besides the power broadened linewidth of FWHM  $\approx 2$  GHz, there is an increased background, especially for QD2.

The contribution of the unsuppressed laser is measured by turning the gate voltage to zero, highlighted by the orange shaded area. The unsuppressed laser contributes about 50 % to the background (for both dots). The remaining 50% of the background is likely due to phonon-assisted excitation of the same dot. We exclude phonon-assisted excitation of close-by quantum dots by introducing a 150 GHz grating filter before the detectors.

The almost five times higher background for QD2 compared to QD1 is due to a lower excitation efficiency. To reach the same Rabi frequency for QD2 as for QD1, about five times higher laser power is used. The quantum dot emission saturates but the unsuppressed laser increases linearly with laser power. Therefore, the relative background changes for the same amount as the increased laser power. The relative background plays an even bigger role in detuned measurements. The optimal detuning for a Brownian-motion measurement (see Fig. 6.5) is here 1 GHz. For QD1 this still gives an acceptable signal-to-background ratio of 3.2:1. In contrast, for QD2 the signal-to-background ratio is 0.5:1 which makes autocorrelation measurements very challenging (at these high excitation powers).

The laser suppression is not only at a high level but also very unstable. Thus, automatic laser suppression is an important part of our measurements. Figure 6.6(c) shows two individual time traces of a typical autocorrelation measurement. First, the laser is automatically suppressed. Second, spectral wandering is corrected by

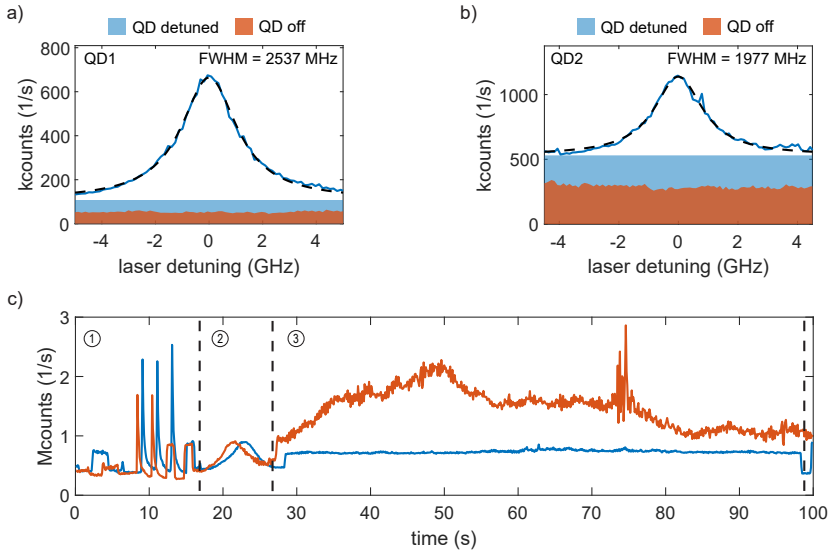


**Figure 6.6: High-power resonant-excitation.** (a,b) High power,  $\Omega_R \approx 8\Gamma_m$ , resonant linewidth scans of QD1 and QD2. Due to the high power, the laser suppression is not optimal, highlighted by the orange shaded area. In addition, when the laser is detuned from the quantum dot resonance, additional emission is observed likely from phonon sideband excitation of close-by quantum dots (highlighted in blue). For QD2, an almost five times higher laser power is needed to reach the same Rabi coupling and thus the background increases. (c) Two individual time traces of an autocorrelation measurement at high power: (1) automatic laser suppression, (2) locking the quantum dot transition to the laser frequency, and (3) detuned autocorrelation measurement for 60 s. At these high excitation powers, the laser suppression level is not only far from optimum but also highly unstable (see orange curve). This leads to an increased  $g^{(2)}(0)$ , see Fig. 6.7(b).

locking the quantum dot to the laser frequency. Third, the laser is detuned and the autocorrelation measurement is performed for 1 min. These three steps are repeated until enough photon statistics are recorded, usually up to five hours. As can be seen in Fig. 6.6(c), even with automatic laser suppression, large drifts can occur during the measurement. This is a result of an unstable laser spot position due to vibrational noise from the environment and also due to pressure changes in the helium recovery line. All sensitive measurements are therefore carried out during the night and during weekends.

## 6.6 Brownian-motion measurement

The Brownian-motion noise-power measurements presented in the following chapter are performed on QD1. The measurements are performed in the same way as in Chapter 5.6 by doing a Fourier transformation of an autocorrelation measurement. To confirm that the mechanical noise peak can only be measured when fulfilling Eq. 6.1,

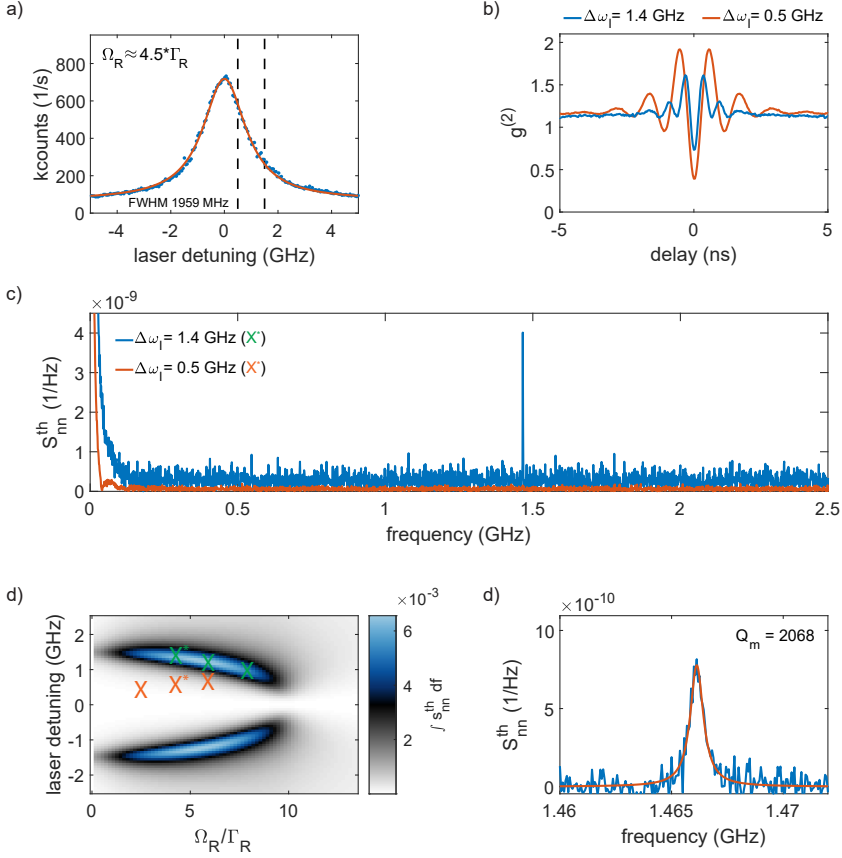


**Figure 6.7: High-power Brownian-motion autocorrelation measurement.** (a) Linewidth scan of QD7 with  $\Omega_R \approx 4.5\Gamma_R$ . Two detunings are highlighted for which each an autocorrelation measurement is performed,  $\Delta\omega_1/2\pi = 0.5$  GHz and  $\Delta\omega_1/2\pi = 1.4$  GHz. The larger detuning is chosen such that the effective Rabi frequency,  $\Omega_R^{\text{eff}}$ , is equal to the mechanical frequency,  $\Omega_m$ . (b) Autocorrelation measurements at the detunings highlighted in (a). Both measurements show a  $g^{(2)}(0)$  much higher than at low powers due to the unsuppressed laser. (c) Fourier transformation of the autocorrelation measurements. Although the measurement at smaller detuning has a higher count rate and thus a lower noise floor in the power spectrum, the mechanical noise peak is only visible for the higher detuning measurement, where  $\Omega_R^{\text{eff}} = \Omega_m$ . (d) The power spectrum measurement is performed for six different combinations of Rabi frequencies and laser detunings. Whenever the optimal detuning condition is matched, the mechanical noise peak is observed (highlighted in green), otherwise, the noise peak is not observed (highlighted in orange). The measurements from (c) are labelled with a \*. (e) The mechanical quality factor is extracted from the power spectrum via a Lorentzian fit,  $Q_m = 2 \times 10^3$ .

the autocorrelation measurement is performed for different laser detunings.

Figure 6.7(a) shows a resonant linewidth scan of QD1 at  $\Omega_R \approx 4.5\Gamma_R$ . The detunings where the autocorrelation measurements are performed are highlighted: 0.5



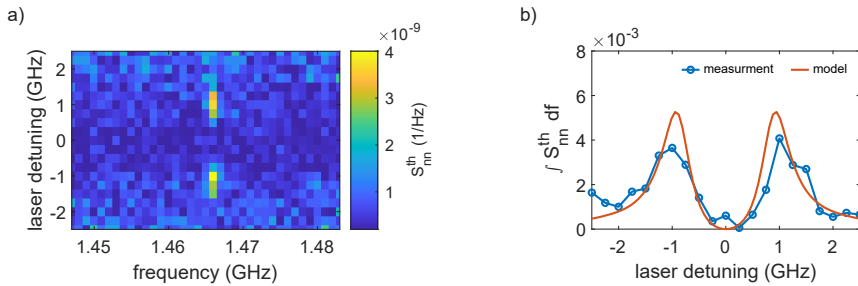


**Figure 6.8: Detuning series of the noise power spectrum.** (a) Power spectrum measured in dependence of the laser detuning. The Rabi frequency of  $\Omega_R = 8\Gamma_R$  ( $1\ \mu\text{W}$  optical power) is chosen such that at the optimum detuning, here  $\pm 1$  GHz, the count rate is not too low. Nevertheless, at large detunings, the count rate increases the noise floor, highly reducing the signal-to-noise ratio in the power spectrum. (b) Integrated noise power around the mechanical resonance in (a) overlaid with the corresponding line-cut from the numerical simulation in Fig. 6.5(d). This comparison shows that in the measurements the exciton-phonon coupling rate is slightly lower than the coupling rate obtained from the finite-element simulations,  $g_{ep}/2\pi = 3.2$  MHz.

and 1.4 GHz. The first one represents the highest noise sensitivity expected by the derivative of the count rate (see Chapter 5.5) and the latter one is the optimal detuning satisfying Eq. 6.1. The corresponding autocorrelation measurements are shown in Fig. 6.7(b). The higher the laser detuning the bigger the effect of the unsuppressed laser, which manifests itself in a reduced single-photon purity (increased  $g^{(2)}(0)$ ). Note that for a signal-to-background of 1:1 we estimate a  $g^{(2)}(0) = 0.75$  (assuming a negligible correlation between quantum dot photons and laser photons) which is comparable to what is observed in the measurements. This confirms the observations of the numerical simulations.

Figure 6.7(c) shows the noise power spectra of the autocorrelation measurements from Fig. 6.7(b). For more details on the Fourier transformation see [Supplementary note I](#). The mechanical noise peak of the in-plane breathing mode is only visible for the larger detuning measurement, even though there is a much higher count rate and a lower measurement imprecision noise (noise floor) for the laser detuning of 0.5 GHz. Overall, six autocorrelation measurements are performed, each with an individual combination of laser power and laser detuning, see Fig. 6.7(d). When the combination of laser power and laser detuning is set according to Eq. 6.1, the mechanical noise peak is observed (highlighted in green in Fig. 6.7(d)). If Eq. 6.1 is not fulfilled, the mechanical noise peak is not observed (highlighted in orange in Fig. 6.7(d)).

Figure 6.7(d) shows a zoom-in of the power spectral density. A mechanical quality of  $Q_m = 2 \times 10^3$  is extracted from the measurement via a Lorentzian fit. Compared to the highest mechanical mode of the suspended beam resonator, the mechanical frequency increased by a factor of 2.5 while the mechanical quality stayed the same. Furthermore, only one mechanical mode is observed although there are many more mechanical modes, however, outside the phononic bandgap. Therefore we conclude that the mechanical mode at 1.466 GHz is well confined by the phononic shield. The

remaining mechanical damping is most likely due to intrinsic material losses.

Finally, to quantify the observed mechanical coupling, a laser detuning series of the noise power measurement is performed, see Fig. 6.8(a). Each noise power (horizontal data row) represents the Fourier transform of a 1 h autocorrelation measurement. Also for this measurement, every minute the laser is automatically suppressed and spectral wandering is corrected (see Chapter 6.5). As expected from the simulations in Fig. 6.5, the noise peaks appear for a laser detuning of  $\pm 1$  GHz. Note that at large detunings the count rate reduces which increases the noise floor. Fig. 6.8(b) shows the integrated noise power overlayed with the results from the numerical simulations. Both show a comparable noise power, meaning the actual exciton-phonon coupling rate is only slightly smaller than the one obtained from the finite-element simulations,  $g_{\text{ep}}/2\pi = 3.2$  MHz. However, for direct extraction of the coupling rate from the measurements, the mechanical displacement would need to be calibrated, which is not possible with the current setup.

## 6.7 Conclusion and future directions

Measuring the coupling of a single-photon emitter to a mechanical resonator in the GHz regime is not trivial. In the unresolved-sideband regime, the parameter space of laser power and detuning is independent of the mechanical frequency. In contrast, in the resolved-sideband regime, the effective Rabi frequency must be matched to the mechanical frequency. More specifically, high excitation powers are required, which in turn result in a high level of unsuppressed laser. Without additional mechanical driving, this puts an upper limit on the observable mechanical frequency, since at some point, the signal-to-background simply becomes too high.

Due to the mechanical and optical optimisation of the GHz-resonator it is straightforward to locate a dot on the mechanical resonator which shows a large coupling rate to the mechanical displacement. Thanks to the phononic crystal, the mechanical mode at 1.466 GHz is well isolated from all other modes and shows a high mechanical quality. Consequently, a high exciton-phonon coupling rate is obtained, which might be enough to observe optomechanical sidebands even without mechanical driving. The high  $Q \cdot f$  product of  $2.9 \times 10^{12}$  is proof of the low phase noise which enables 34 mechanical oscillations before coherence is lost to the bath. Furthermore, for the sideband scattering rate (see Chapter 5.7.7) to exceed the mechanical dissipation rate, the (on-resonance) Rabi frequency only needs to be  $\Omega_{\text{R}} > \Omega_{\text{m}}\Gamma_{\text{m}}/g_{\text{th}} = 0.2\Gamma_{\text{R}}$  (taking  $g_{\text{th}}$  from finite-element simulations). Nevertheless, the mechanical quality factor related to intrinsic losses could be improved further by introducing a surface passivation treatment [192–194].

Future directions for design improvements could be to increase the exciton-phonon coupling rate by optimising the mechanical-coupling profile. A tapering of the air holes might reduce the areas of enhanced strain around the first air hole. This would not only improve the strain in the centre of the resonator but also the mechanical quality due to soft clamping [170]. Another approach could be to use a resonator with the same x- and y-dimensions. Such a resonator would have a degenerate x/y-breathing mode which would increase the coupling strength about two-fold. We want to emphasise that it is important to improve  $g_{\text{ep}}/\Omega_{\text{m}}$  rather than  $g_{\text{ep}}$ . We estimate

for the current resonator that with a five to ten-fold increase in the coupling rate, cooling of the mechanical resonator [24] and transparency due to coherent population oscillations would be within reach [195, 196]. As proposed in Ref. [197] the coupled hybrid system could then be used to create a single-photon router or an all-optical Kerr switch. In terms of the inhomogeneous broadening in our system, the InAs quantum dots could be replaced by the droplet-etched GaAs quantum dots where recently lifetime-limited linewidths were observed [66]. Whether this would actually increase the sensitivity to mechanical noise remains an open question since these dots have a relatively large natural linewidth of around 600 MHz.

For on-chip applications, such as quantum transduction [198], the mechanical resonator could be combined with a photonic-crystal cavity [71] and an optical or mechanical waveguide [72–75, 199]. It was already shown that the membrane platform used in this work is highly suitable for on-chip applications [9, 13, 200–203]. If additional mechanical actuation is still needed, the electric field antenna can be converted to an on-chip antenna, highly increasing the coupling efficiency to the mechanical resonator [56, 186, 202]. Another option could be to integrate a piezo-optomechanical transducer [145, 204]. Overall, the three mechanical resonators (cantilever, suspended beam, and phononic-crystal beam) show that the membrane design has a large potential for a wide range of applications.

The measurements on the GHz resonator show that the phononic shield is working properly, otherwise many more mechanical modes would be observed. In future, the shield could not only be used to confine mechanical modes but also to reduce phonon-assisted relaxation processes of the quantum dot electron spin. By tuning the Zeeman energy of the dot into resonance with the phononic gap, single-phonon-assisted relaxation processes could be highly reduced. However, these effects mainly limit the  $T_1$  time at high magnetic fields [205–207] and a phononic band gap at tens of GHz would be needed. This means that the mechanical structures need to be much smaller which might eventually be limited by the fabrication process. Furthermore, the current sample has a characteristic spin  $T_1$  time of few  $\mu s$ , which suggests that the spin lifetime is currently limited by other factors (for example co-tunnelling).

Finally, we propose to prove that single phonons are emitted and absorbed by measuring the single-photon nature of the Stokes and anti-Stokes sidebands [188] with a Hanbury Brown-Twiss setup.

## 6.8 Supplementary note I: From autocorrelation to power spectral density

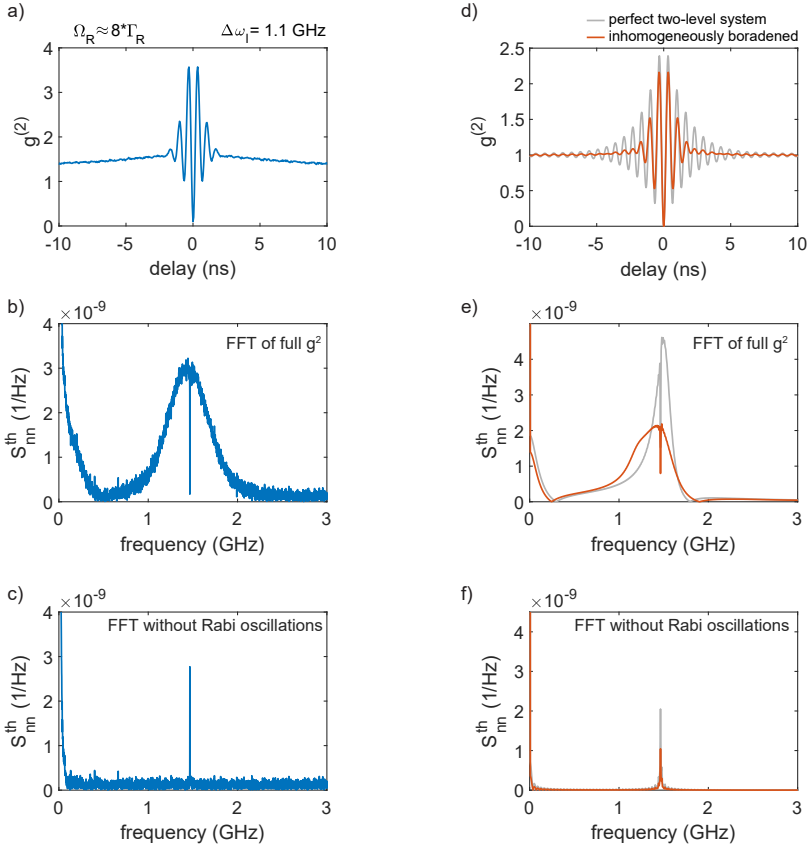


**Figure 6.9: Fast Fourier transformation method.** (a) Autocorrelation measurement at  $\Omega_R = 8\Gamma_R$  and optimum detuning. (b) Fast Fourier transformation of the full autocorrelation. The broad feature comes from the Rabi oscillations and the narrow feature is from the mechanical modulation. Since there is a  $\pi$ -phase shift between them, the mechanical modulation appears as a dip in the broad Rabi feature. (c) Fast Fourier transformation without Rabi oscillations, showing the true mechanical noise peak. (d-f) Numerical simulations of the second-order coherence function without and with inhomogeneous broadening. The Fourier transformations with and without Rabi oscillations show the same behaviour as in (b, c).

The following paragraphs explain how the Fourier transform of the autocorrelation is performed and compares the results to numerical simulations of the second-order coherence function. Figure 6.9(a) shows an autocorrelation measurement after background correction. For this, we assume that there is a negligible correlation between the quantum dot photons and the laser photons. This means that the unsuppressed

laser results in a flat background in the autocorrelation. This might be true at high powers when the incoherent part dominates the quantum dot emission. However, at low powers (coherent-scattering regime), the unsuppressed laser together with the quantum dot signal can lead to photon bunching in the autocorrelation measurement (close to zero delays) and the above assumption is not valid anymore. In Chapter 6.6 the autocorrelation is shown as measured, however, for obtaining the true noise power, the background is corrected [5]. The numerical simulation of the second-order coherence function (Eq. 5.2), Fig. 6.9(b), shows that the inhomogeneous broadening not only changes the Rabi frequency but also leads to a fast damping of the Rabi oscillations.

Figure 6.9(b-f) shows the comparison between a Fourier transformation with and without Rabi oscillations for measurement and simulation. The Rabi oscillations can be described with a damped cosine function whereas the mechanical noise is described by a damped cosine with a  $\pi$ -phase shift. Due to the  $\pi$ -phase shift between the two, the mechanical noise appears as a sharp dip in a broad Rabi peak. This is also observed in the numerical simulations. To obtain the true mechanical noise peak, the Fourier transformation is performed without Rabi oscillations. The broad Rabi feature disappears and the mechanical noise peak appears on a flat noise floor. Since the Rabi oscillations dampen much faster than the mechanical oscillations ( $Q_m \approx 2000 \times Q_{\text{Rabi}}$ ), the procedure described above does not influence the mechanical noise power significantly.

## 6.9 Supplementary note II: A comment on optical device optimisation

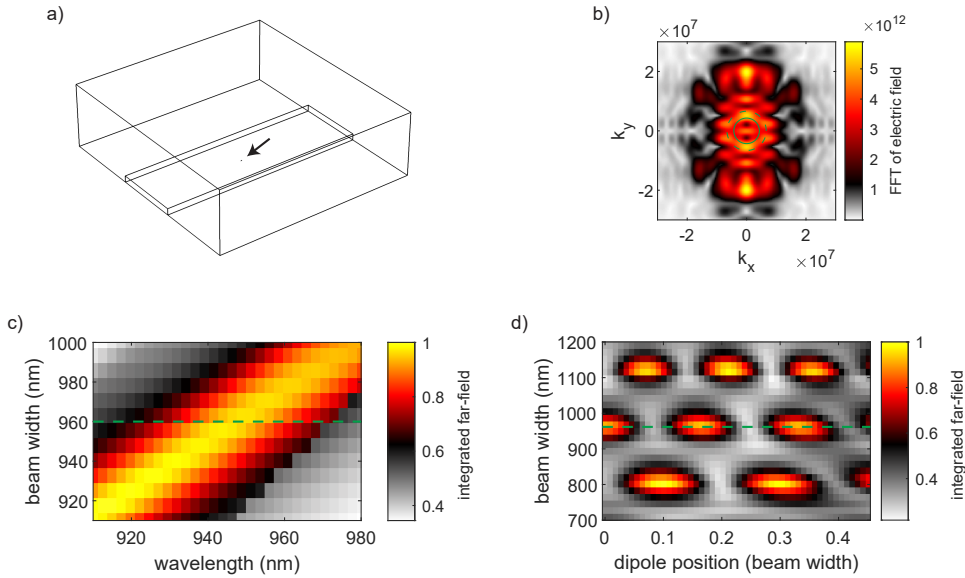


**Figure 6.10: Far-field simulations.** (a) Geometrical structure of the finite-element simulation where the beam is surrounded by an airbox. The simulation is performed with a  $z$ -symmetry for the electric field (TE mode). A scattering-boundary condition is applied to all four sidewalls and the top surface. An electric dipole (20 nm, along  $x$ -axis) is placed in the centre of the beam and a frequency-domain study is performed. (b) Far-field obtained from a Fourier transformation of the electric field in real space (evaluated just above the beam). The light-line ( $|k| < \omega/c$ ) is highlighted by the dashed green line and the lens collection ( $|k| < N_A\omega/c$ ) is highlighted by the solid green line. (c) Integrated far-field ( $|k| < N_A\omega/c$ ) in dependence of the wavelength and the beam width. The structure is optimised for an optical wavelength of 945 nm (quantum dot emission wavelength), for which we find a maximum in collection for a beam width of around 960 nm. This can be understood by a standing wave being formed between the two horizontal sidewalls of the beam, which boosts the emission to the top. (d) Integrated far-field at a wavelength of 945 nm in dependence of the dipole position (in  $y$ -direction) and the beam width. The simulation shows that independent of the dipole position, for a given wavelength there is a certain beam width which results in a reduced collection, for example, 816-915 nm and 1020-1100 nm.

In the photoluminescence maps of the cantilever resonator, we observe that there is an intensity dependence on the width of the beam. Therefore, far-field simulations are performed to optimise the outcoupling efficiency of the quantum dot emission. A short piece of the nanobeam is surrounded by an airbox and a 20 nm long electric dipole is placed in the beam centre, see Fig. 6.10(a). Scattering boundary conditions are applied to all sides and a  $z$ -symmetry for the electric field is applied to obtain TE-modes. Finite-element simulations are performed in the frequency domain to obtain

the electric field emitted from the dipole. The electric field is evaluated just above the beam and a two-dimensional Fourier transformation is performed, see Fig. 6.10(b). To obtain the lens collection, the far field is integrated for  $|k| < N_A \omega/c$ .

Figure 6.10(c) shows the integrated far-field in dependence on the beam width and the studied wavelength. For a dipole in the centre of the beam, an optimal beam diameter for an emission wavelength of around 945 nm (centre of ensemble emission of the current wafer) is found. To determine whether there is a dependence of the dipole position on beam width, an additional study is performed at 945 nm where the dipole position is swept from the centre to the edge of the beam, Fig. 6.10(d). As can be seen, the outcoupling to the top is optimised due to a standing wave that is formed inside the beam. Therefore, the beam width needs to be multiples of  $\lambda/2$ . Furthermore, in the region of 915 nm and 1020-1100 nm the outcoupling efficiency is reduced independent of the dipole position. Note that changing the emission wavelength does not change the outcome significantly and only leads to a slight shift in the optimal beam width. The optical quality of the standing-wave mode is probably not high and the enhancement observed in the simulations will not be observed at the same level in the experiment. Nevertheless, we observe that the optimisations described above have a significant impact on quantum dot localisation. Finally, for the phononic-crystal resonator also the y-length scale of the resonator matters. This can be seen by the very dark dots in the phononic shield compared to the bright dots on the resonator.

---

## Radiative Auger process in the single-photon limit

---

**The content of this chapter is adapted from:**

M. C. Löbl, C. Spinnler, A. Javadi, L. Zhai, G. N. Nguyen, J. Ritzmann, L. Midolo, P. Lodahl, A. D. Wieck, A. Ludwig, and R. J. Warburton,

“**Radiative Auger Process in the Single-Photon Limit**”, *Nature Nanotechnology* **15**, 558–562 (2020).



## 7.1 Introduction

In a multi-electron atom, an excited electron can decay by emitting a photon. Typically, the remaining electrons are left in their ground state. In a radiative Auger process, the leftover electrons are promoted to an excited state and a red-shifted photon is created due to energy conservation [78, 79, 208, 209]. In a quantum dot, radiative Auger is predicted for charged excitons [80]. Here, we report the observation of radiative Auger emission on trions in single quantum dots.

For a trion, a photon is created by electron-hole recombination, leaving behind a single electron in the conduction band s-shell. The radiative Auger process promotes this additional (Auger) electron to a higher shell of the quantum dot. We show that the radiative Auger effect is a powerful probe: the energy separation between the resonance fluorescence and the radiative Auger emission directly measures the single-particle splitting of the electronic states in the quantum dot with high precision. In semiconductors, these single-particle splittings are otherwise hard to access by optical means as particles are typically excited in pairs (as excitons). The radiative Auger transition is followed by a carrier relaxation of the Auger electron back to the ground state (s-shell). Going beyond the original theoretical proposals, we show how applying quantum optics techniques to the radiative Auger photons gives access to the single-electron dynamics, notably relaxation and tunnelling. This is also hard to access by optical means: even for quasi-resonant  $p$ -shell excitation, electron relaxation takes place in the presence of a hole, complicating the relaxation dynamics. We propose that the radiative Auger effect can be exploited in other semiconductor nanostructures and quantum emitters in the solid state for studying the energy level arrangement and the dynamics of single carriers.

Auger processes are a well-known phenomenon in atoms [210, 211]. Nonradiative Auger processes involving continuum states have been observed in several solid-state systems: quantum dots [212], two-dimensional materials [213], colour centers [214], and semiconductor lasers [215]. As originally predicted for atoms, an Auger process can also take place in connection with a radiative transition [78, 79]. The radiative Auger process has been observed in X-ray spectra [208, 209]. The so-called electron shake-off process has a similar physical origin [216]. At optical frequencies, the radiative Auger process has been described in ensembles of donors [217] and as a so-called shake-up process in the Fermi-sea (a many-particle effect) [218–220]. So far, the radiative Auger process has not been observed with a single-photon emitter or a few-electron configuration.

## 7.2 The radiative Auger process

We observe the radiative Auger process on two different systems: first, a self-assembled InGaAs quantum dot (QD) in GaAs grown in the Stranski-Krastanov mode [80] and second, a GaAs quantum dot in AlGaAs grown by infilling of droplet-etched nano-holes [221]. We resonantly excite the negative trion ( $X^{1-}$ ) of a dot with a narrow-bandwidth laser. In both quantum dot systems, the charge state of the dot is precisely controlled via Coulomb blockade [110]. We collect the emission of the dot and resolve it spectrally, as schematically shown in Fig. 7.1(a). Fig. 7.1(b) is the result of such a measurement for an InGaAs quantum dot. The main peak at photon

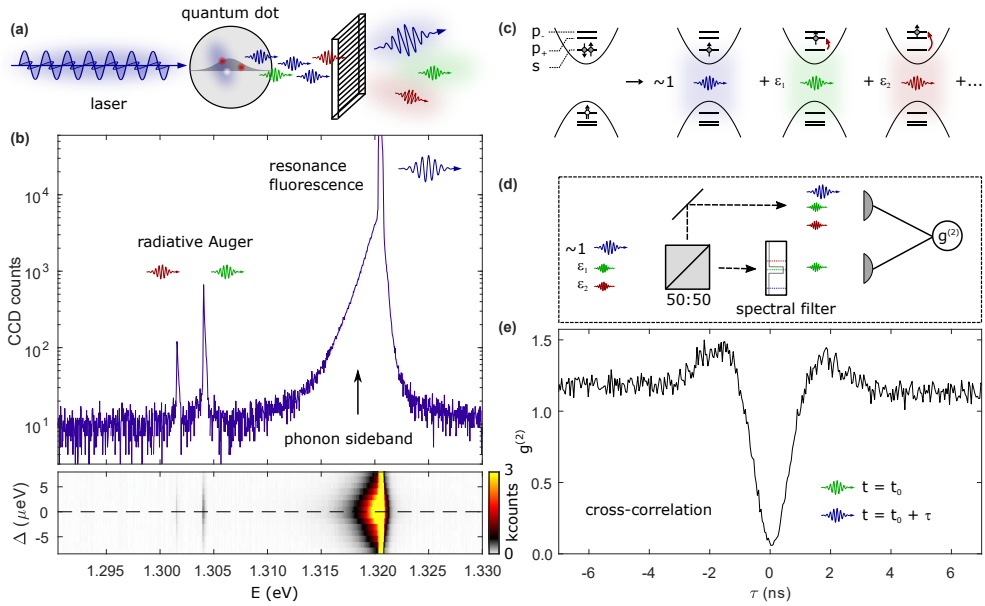


**Figure 7.1: Observation of a radiative Auger process on a single quantum dot.** (a) Schematic of the experimental setup: the quantum dot (QD) is resonantly excited with a narrow-bandwidth laser, and its emission is spectrally resolved. (b) Upper panel, emission spectrum of the negative trion ( $X^{1-}$ ) in an InGaAs quantum dot under resonant excitation ( $T = 4.2$  K). The strong peak at  $E \simeq 1.321$  eV is the resonance fluorescence, surrounded by a broad LA-phonon sideband. Red-shifted by  $\hbar\omega_0 \sim 18$  meV there are two additional emission lines, stemming from the radiative Auger process. Lower panel, the dot can be tuned in and out of the resonance with the laser by exploiting the dc Stark effect. The shown spectrum is measured at zero detuning,  $\Delta$ , between dot and laser (dashed line). Resonance fluorescence and radiative Auger are maximised when the laser is in resonance ( $\Delta = 0$ ). (c) Mechanism of the radiative Auger process: with a probability close to one, the trion recombination results in an emission of a resonant photon and leaves the remaining electron in the ground state ( $s$ -shell). With small probabilities  $|\epsilon_1|^2$  and  $|\epsilon_2|^2$ , the remaining electron is promoted into one of the  $p$ -shells, and the photon is consequently red-shifted. (d) Setup for the cross-correlation between the radiative Auger emission and the resonance fluorescence. The delay  $\tau$  corresponds to the duration between the arrival of a resonant photon on detector 2 after detecting an Auger photon on detector 1. (e) Cross-correlation measurement between the radiative Auger emission and the resonance fluorescence. The strong anti-bunching at zero time delay proves that both emission lines originate from the same emitter.

energy  $\sim 1.321$  eV is the resonance fluorescence of the trion. This spectrally narrow emission is accompanied by an LA-phonon sideband on the red (blue) side [222–224]. In addition, we observe two weak emission lines, red-shifted by  $\sim 18$  meV from the main fluorescence peak. In the following measurements, we show that these emission lines originate from a radiative Auger process as illustrated in Fig. 7.1(c): an electron and a hole recombine optically and with a small probability, the second electron is promoted to an excited state, the  $p$ -shell of the dot. In the case of resonance fluorescence, in contrast, the optical recombination of the trion leaves behind a single

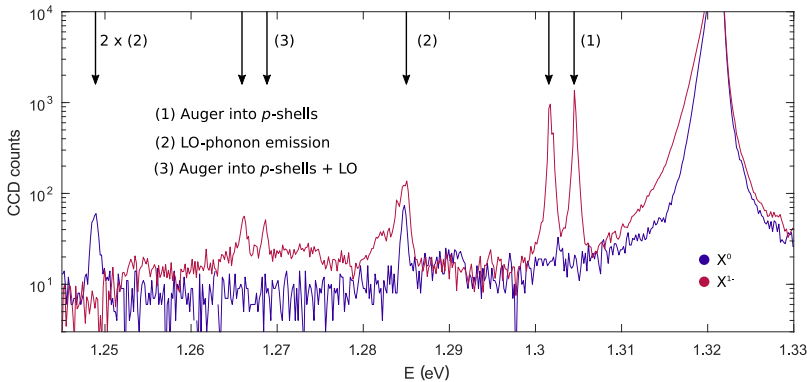


**Figure 7.2: Comparison of neutral and charged excitons.** Emission spectrum of the InGaAs quantum dot shown in Fig. 7.3(a). The  $s$ -to- $s$  transition of the quantum dot is resonantly excited. The emission is shown for the neutral exciton (blue) and the singly charged trion (red). For better comparability, the neutral exciton ( $X^0$ ) is shifted in energy such that its resonance fluorescence peak overlaps with the charged exciton ( $X^{1-}$ ). In both cases, the resonance fluorescence (at  $E \simeq 1.321$  eV) dominates. Emission at lower energies is caused by an energy transfer to either an LO-phonon or an additional carrier via the radiative Auger process. The radiative Auger process is only possible for the trion, not for the neutral exciton.

electron in the ground state ( $s$ -shell of the dot).

Several observations substantiate the interpretation that the two red-shifted lines originate from a radiative Auger process. First, the Auger lines disappear on removing the additional electron – they are absent in the emission spectrum of the neutral exciton,  $X^0$ , see Fig. 7.2. Second, the red-shifted emission lines only appear when the laser is in resonance with the quantum dot (Fig. 7.1(b)). Third, the time-resolved cross-correlation between the radiative Auger emission and the resonance fluorescence, Fig. 7.1(d,e), shows a pronounced anti-bunching at zero time delay. This measurement demonstrates that the different emission lines originate from the same dot. The emitter produces either a resonance-fluorescence photon or a radiative-Auger photon, but never two photons at the same time. Finally, to prove that the radiative Auger process leaves an electron in a higher shell, we measure the optical emission as a function of the magnetic field (Faraday geometry). The magnetic field dispersion of the radiative Auger emission is shown in Fig. 7.3(a,b) for an InGaAs dot and in Fig. 7.3(c,d) for a GaAs dot, respectively. At high magnetic fields, the two red-shifted emission lines, which are closest in energy to the resonance-fluorescence, have a dispersion of  $\pm \frac{1}{2} \hbar \omega_c$  (cyclotron frequency:  $\omega_c = \frac{eB}{m^*}$ , electron effective mass  $m^*$ ). This type of magnetic field dispersion shows that the emission is connected to an energy transfer to the  $p$ -shells. More generally, the strong magnetic field dispersion of the radiative Auger emission arises because the magnetic field creates additional orbital confinement, which leads to a strong magnetic field dependence of higher quantum dot shells [225–227]. The magnetic field dependence is important to distinguish radiative Auger emission from phonon-related features.

## 7.3 Magnetic field dependence

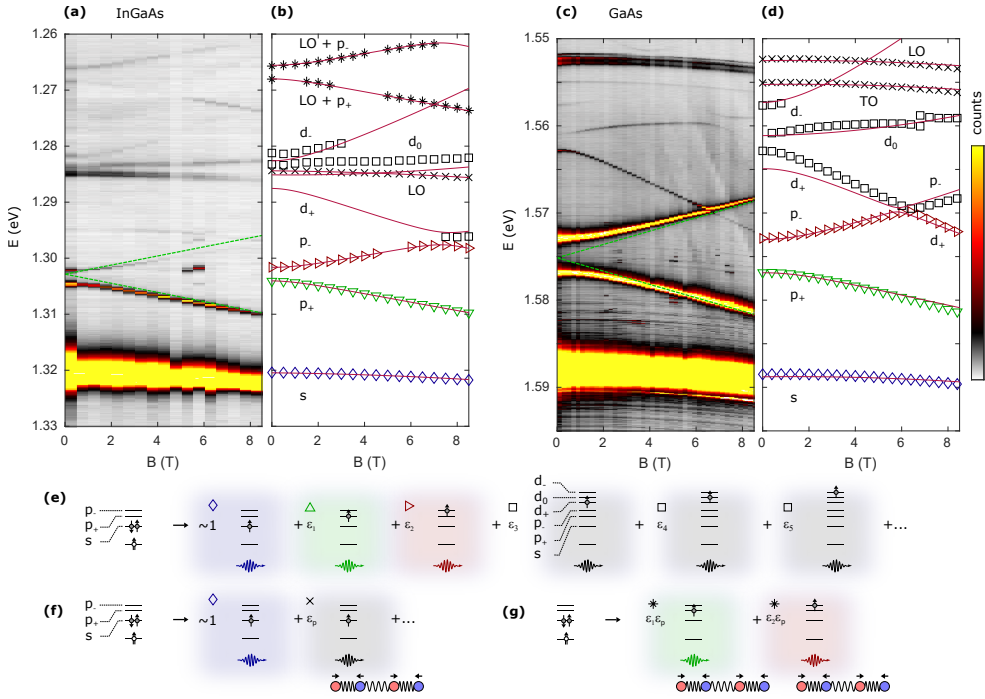


**Figure 7.3: Magnetic field dispersion of the radiative Auger emission.** (a) Emission spectrum under resonant excitation as a function of the magnetic field measured on an InGaAs quantum dot (QD). The two green lines indicate the radiative Auger emission where one electron is promoted into the  $p$ -shells. This emission follows a dispersion of  $\sim \pm \frac{1}{2} \hbar \omega_c$ , with  $m^* \simeq 0.071 m_e$  ( $s$ -to- $p$ -splitting:  $\hbar \omega_0 \simeq 17.7$  meV, further parameters in Tab. 7.1). (b) Magnetic field dispersion of the radiative Auger emission. The emission lines above the  $s$ -shell can be well described by the Fock-Darwin spectrum. The red lines represent a fit of our analytical model of the radiative Auger emission. (c) Radiative Auger emission as a function of the magnetic field measured on a GaAs quantum dot ( $m^* \simeq 0.076 m_e$ ,  $\hbar \omega_0 \simeq 13.8$  meV). (d) Magnetic field dispersion of the radiative Auger emission for the GaAs dot. (e) Schematics of the radiative Auger process involving both  $p$ - and  $d$ -shells. (f) Optical recombination involving the creation of an LO- or a TO-phonon. We note that this process is observed for the trion and the neutral exciton (see Fig. 7.4).  $|\epsilon_p|^2$  labels the probability for the process involving the LO phonon. (g) Schematics of the radiative Auger process involving both carrier excitation to the  $p$ -shell and the creation of a phonon.

The separation between resonance fluorescence and radiative Auger emission corresponds to the single-particle splittings. Thus, the radiative Auger emission allows for determining the single-particle spectrum of a quantum dot with high precision. At zero magnetic field ( $B = 0$  T), there is a splitting between the two  $p$ -shell-related Auger lines, revealing an asymmetry of the dot. This asymmetry lifts the four-fold degeneracy of the  $p$ -shells into two doublets at zero magnetic fields. For both types of quantum dots, we also observe radiative Auger emission at even lower energies, see

Fig. 7.3(a,c). These emission lines correspond to a radiative Auger process involving the  $d$ -shells (sketched in Fig. 7.3(e)). At high magnetic fields, the upper  $p$ -shell ( $p_-$ ) shows an anti-crossing with the lowest  $d$ -shell ( $d_+$ ). For the GaAs quantum dot, we even observe radiative Auger emission involving all three  $d$ -shells. For the InGaAs quantum dot, the  $d_+$ -shell is only visible in the radiative Auger emission when it is coupled to the  $p_-$ -shell. For both types of dots, we model the dispersion of the emission lines by the Fock-Darwin spectrum [226, 227] (details can be found in Chapter 7.4). The model assumes a harmonic confinement potential and matches well with the lower quantum dot shells, see Fig. 7.3(a,c). Differences between model and data (e.g. for the  $d$ -shells) reveal the deviation from a harmonic confinement potential towards higher single-particle energy.

For a rotationally symmetric confinement potential, angular momentum is a good quantum number such that promotion of the Auger electron to the  $d_0$ -shell is possible, but promotion to the other  $p$ - and  $d$ -shells is forbidden. In practice, we find that the radiative Auger involving the  $p$ -shells is relatively strong and that the intensity of these processes is not strongly dependent on the magnetic field. Besides, the  $p$ -shells are not degenerate at zero magnetic fields. These observations show that angular momentum is not a good quantum number. We do not observe Zeeman splittings in the radiative Auger lines, which shows that the processes are spin-conserving. Spin is a good quantum number; equivalently, spin-orbit interactions of the electron states are weak.

There are several additional red-shifted emission lines that are not related to electron shells or continuum states, see Fig. 7.3(a,b): An emission red-shifted by  $\sim 36$  meV (labelled LO in Fig. 7.3(b,d)) which corresponds to optical recombination along with the creation of an LO-phonon (sketched in Fig. 7.3(f)). The magnetic field dispersion is weak and follows the  $s$ -shell – no higher shells are involved. At lower photon energies, even the LO-phonon replica of the radiative Auger emission is visible (labelled LO +  $p_{\pm}$  in Fig. 7.3(b), schematic illustration in Fig. 7.3(g)). In this case, Auger carrier excitation into the  $p$ -shell and LO-phonon creation occur simultaneously with the optical recombination.

## 7.4 Modelling the magnetic field dispersion

The radiative Auger emission appears on resonantly exciting the trion. The final states after the optical recombination of the trion are single-particle states. Therefore, the separations between the different emission lines are precise single-particle splittings. Shown in Fig. 7.4(c,d) is the single-particle dispersion for the two dots also shown in Fig. 7.3. Fig. 7.4(a,b) is the magnetic field dispersion of the extracted single-particle splittings for two additional dots. At zero magnetic field, we measure an  $s$ -to- $p$ -splitting of 17.7 meV and 21.0 meV for the InGaAs dots; and 13.8 meV and 17.6 meV for the GaAs dots. Further parameters of the single-particle spectrum are obtained by fitting the data to a model which assumes states of an asymmetric harmonic confinement potential. The red lines in Fig. 7.4(b-e) represent the model that is developed in this section.

For a symmetric, two-dimensional harmonic confinement potential, the magnetic field dependence of the single-particle states forms the Fock-Darwin spec-

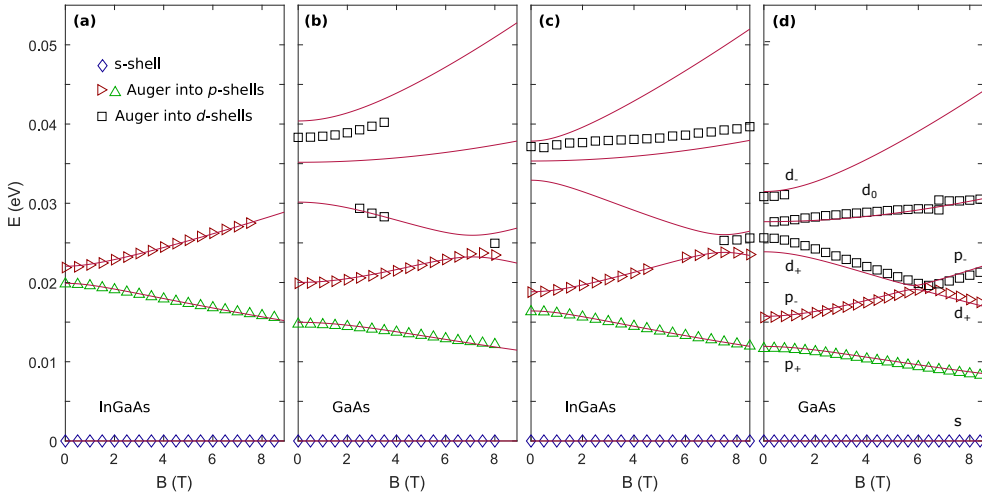


**Figure 7.4: Magnetic field dependence compared to an asymmetric Fock-Darwin model.** (a) Single-particle magnetic field dispersion for an additional InGaAs quantum dot. To obtain the single-particle splittings, the  $s$ -shell energy is subtracted from the energies of the radiative Auger lines. (b) Single-particle magnetic field dispersion for an additional GaAs quantum dot embedded in AlGaAs. (c) Single-particle splittings for the dot shown in Fig. 7.3(a). (d) Single-particle splittings for the dot shown in Fig. 7.3(c).

trum [226, 227]. The eigenenergies  $E_{n,l}$  depend on two quantum numbers, the radial quantum number,  $n$ , and the angular momentum quantum number,  $l$  [225]. In this model, the two  $p$ -shells are degenerate at zero magnetic fields. This is clearly not the case in our experiments. Thus, to describe the single-particle dispersions, we assume an asymmetric harmonic confinement potential of the form  $V(x, y) = \frac{1}{2}m_e^* \left( \omega_x^2 x^2 + \omega_y^2 y^2 \right)$ . When the radial symmetry is broken, angular momentum is no longer a good quantum number, and the eigenenergies are  $E_{n_x, n_y} = \hbar\omega_x \left( n_x + \frac{1}{2} \right) + \hbar\omega_y \left( n_y + \frac{1}{2} \right)$ , with the two quantum numbers  $n_x$  and  $n_y$  (also see Chaprt 2). The eigenenergies of such asymmetric harmonic confinement as a function of the magnetic field are given in Ref. [228].

The absolute energies of the emission lines correspond to the energy differences between the initial state ( $E_{\text{trion}}$ ) and the final states ( $E_f$ ). To fit the dispersions of the emission, we compute the energy of the initial trion state as the sum of its single-particle energies plus the corresponding Coulomb and exchange terms. For the Coulomb energy terms, we assume symmetric confinement as the corresponding energy terms can be easily computed analytically [102, 229, 230]. Coupling terms admixing higher shells are not considered in this estimation [229, 230].

At a magnetic field of  $B \simeq 8$  T, the  $p_-$ - and the  $d_+$ -shells anticross. This is not a feature of the energy spectrum of an asymmetric harmonic oscillator. The anti-crossing is included by a phenomenological coupling  $\Delta_{pd}$  between  $p_-$ - and  $d_+$ -shell. We speculate that the coupling between both shells arises due to the deviation from the harmonic confinement. When part of the energy is transferred to an LO-phonon,

**Table 7.1:** Fit results for the magnetic field dispersion shown in Fig. 7.4 and Fig. 7.3. The effective mass is given in units of the electron mass and difference energies  $\Delta_i$  are given in meV.

	$E_0$ (eV)	$m_e^*$	$g_h - g_e$	$\hbar\omega_0$ (meV)	$\Delta_p$	$\Delta_{pd}$	$\Delta_{LO}$	$\Delta_{TO}$
InGaAs								
Fig. 7.3(b)	1.3214	0.0712	1.505	17.67	1.26	1.12	36.1	–
Fig. 7.3(b)	1.3152	0.0762	1.968	20.98	1.08	–	–	–
GaAs								
Fig. 7.3(d)	1.5925	0.0757	1.135	13.84	1.90	0.25	36.3	33.5
Fig. 7.3(c)	1.5757	0.0737	1.1	17.59	2.61	1.37	36.5	–

the corresponding photon energy is given by,  $E_{\text{trion}} - E_f^s - \Delta_{LO}$ . Thus, the emission has the same weak magnetic field dependence as the resonance fluorescence ( $s$ -shell emission).

The results of the model fits are shown in Fig. 7.4 and Fig. 7.3. A list of definitions is given in Tab. 7.3 in [Supplementary note II](#), and the fit parameters are given in Tab. 7.1. For all measured dots, the strong magnetic field dispersion of the radiative Auger emission lines is well reproduced. In the case of the InGaAs quantum dot shown in Fig. 7.3(a), we fit the energies of the  $s$ -shell emission and the radiative Auger emission into both  $p$ -shells simultaneously. The coupling term  $\Delta_{pd}$  is included as a fit parameter. The exciton  $g$ -factor is measured independently by mapping out the charge plateau of the trion in a magnetic field. The fit reproduces the data very well and gives a good description of the radiative Auger excitation into some of the  $d$ -shells. The LO-phonon replica of the radiative Auger excitation into the  $p$ -shells is also excellently reproduced by the fit.

To fit the magnetic field dispersion of the InGaAs quantum dot shown in Fig. 7.4(a), we also make a simultaneous fit to the energies of the  $s$ -shell emission and the radiative Auger emission into both  $p$ -shells. The coupling term  $\Delta_{pd}$  is not included as there is no hint of an anticrossing with the  $d_+$ -shell. For the GaAs quantum dot shown in Fig. 7.3(c), we again fit the energies of the  $s$ -shell emission and the radiative Auger emission into both  $p$ -shells simultaneously. The coupling term  $\Delta_{pd}$  is included as a fit parameter. The exciton  $g$ -factor is measured independently and not fitted. For the GaAs quantum dot shown in Fig. 7.4(b), we also fit the energies of the  $s$ -shell emission and the radiative Auger emission into both  $p$ -shells simultaneously. The exciton  $g$ -factor is fixed to a value typical for GaAs dots. When observable, all phonon-related features are included in the fit with a single fit parameter for the phonon energy.

## 7.5 Time-dynamics of the radiative Auger process

We turn to the dynamics of the radiative Auger process, that is, the dynamics of the electron left in an excited state after a radiative Auger process. Detecting a photon from a radiative Auger process projects the Auger electron into one of the excited electron states. The dynamics of this single electron can be investigated by determining the time of subsequent emission events. The experiment involves measuring the  $g^{(2)}(\tau)$  correlation function with high precision in the delay  $\tau$ . We compare the



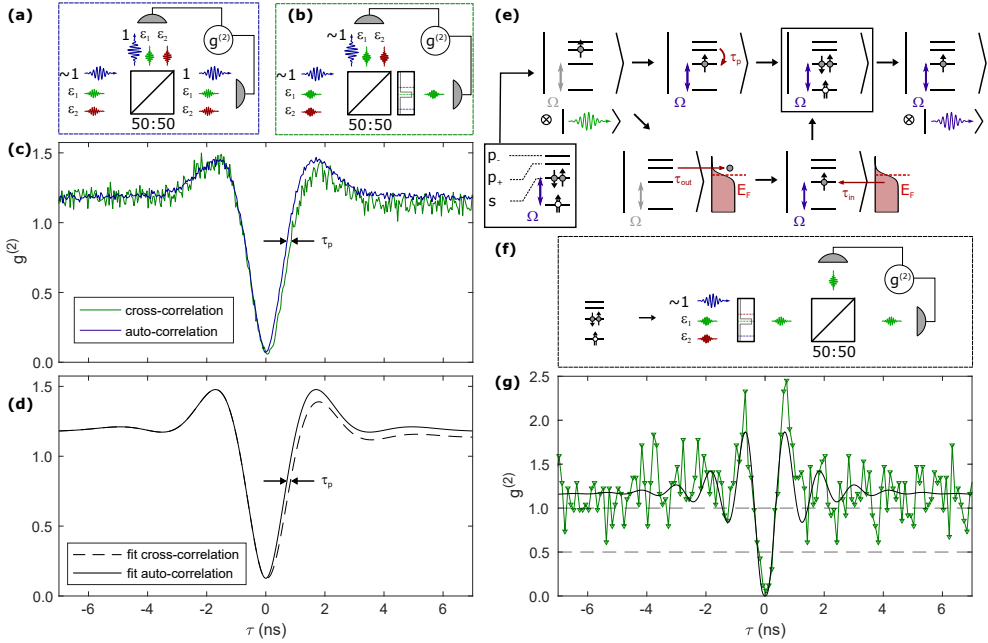


**Figure 7.5: Time-resolved correlation measurements.** (a) Schematic of the measurement to determine the auto-correlation of the resonance fluorescence from a quantum dot. The signal is split by a 50:50 beamsplitter; photon arrival times are recorded on two single-photon detectors ( $g^{(2)}$ -measurement). (b) Schematic of the cross-correlation measurement between resonance fluorescence and radiative Auger emission. The Auger emission is spectrally filtered to remove all resonant photons. (c) Cross-correlation between the resonance fluorescence and the radiative Auger emission (green), measured on the InGaAs quantum dot shown in Fig. 7.1. An auto-correlation of the resonance fluorescence (blue) is shown for comparison. (d) Fits to the auto- and cross-correlation measurements. (Parameters listed in Tab. 7.2) (e) Model for the dynamics connected to the radiative Auger process. After the radiative Auger excitation, the second electron occupies the  $p$ -shell of the quantum dot. When the electron occupies the  $p$ - rather than the  $s$ -shell, the Coulomb interactions are different, tuning the  $s$ -to- $s$  transition out of resonance with the laser. The dot cannot be re-excited until the electron has relaxed to the  $s$ -shell. There are two relaxation channels: a direct relaxation to the  $s$ -shell on a time scale  $\tau_p$ ; and ionisation of the quantum dot by tunnelling from the  $p$ -shell to the Fermi-reservoir ( $E_F$ , Fermi energy) of the back gate ( $\tau_{\text{out}}$ ) followed by slower tunnelling from the Fermi reservoir to the  $s$ -shell ( $\tau_{\text{in}}$ ). (f) Schematic setup for the auto-correlation measurement of the radiative Auger emission. The radiative Auger signal is split and sent to two single-photon detectors. (g) Auto-correlation of the radiative Auger process involving the lower energy  $p$ -shell.

auto-correlation of the resonance fluorescence (Fig. 7.5(a)) to the cross-correlation between the radiative Auger emission and the resonance fluorescence (Fig. 7.5(b)). This comparison provides immediate insight into the carrier relaxation mechanism following the radiative Auger process. The corresponding  $g^{(2)}$ -measurements are shown in Fig. 7.5(c).

The auto-correlation (blue curve) shows a very pronounced anti-bunching ( $g^{(2)} \ll$



1) at zero time delay, proving the single-photon nature of the resonance fluorescence. The anti-bunching is surrounded by a bunching ( $g^{(2)} > 1$ ) at a non-zero time delay. This effect is caused by the onset of Rabi oscillations under strong resonant driving. The cross-correlation (green curve) differs from the auto-correlation in two aspects: The  $g^{(2)}(\tau)$  is a slightly asymmetric function of  $\tau$  and has a time-offset towards positive  $\tau$ . We can explain these features (see fit in Fig. 7.5(d)) with the mechanism shown in Fig. 7.5(e): After the emission of a radiative Auger photon, the second electron is located in a higher shell. Before re-excitation of the trion can take place, this electron has to relax down to the  $s$ -shell – in contrast to the resonance fluorescence where re-excitation is immediately possible.

By comparing auto- and cross-correlation, we determine the relaxation time for an isolated electron to be  $\tau_p \simeq 85$  ps. The time scale of the electron relaxation is comparable to numbers reported for weak nonresonant excitation [231, 232]. The relaxation is probably caused by a multi-phonon emission process [111]. We stress the advantage of the present method: the radiative Auger process leaves only a single electron in a higher shell. In contrast to nonresonant excitation, all other carriers have disappeared and the relaxation of the electron can be investigated independently of other relaxation mechanisms.

The asymmetry of the cross-correlation measurement can be explained by ionisation of the quantum dot following the radiative Auger emission. In a higher shell, the electron has an enhanced tunnelling rate out of the quantum dot [233]. Following very fast relaxation down to the Fermi energy, tunnelling back into the  $s$ -shell of the dot takes about ten times longer, and the quantum dot is ionised for a finite time. We estimate the corresponding tunnelling times by modelling the auto- and cross-correlation measurements. The full model and the fit results are given in Chapter 7.6; the fits describe the experimental data well, see Fig. 7.5(d).

Finally, we perform the first auto-correlation measurement of the radiative Auger emission itself. For this measurement, the resonance fluorescence is filtered out with a grating basel filter (see schematic in Fig. 7.5(f)). To maximise the count rate of the weak radiative Auger emission, we use a higher excitation power (Rabi frequency) compared to the cross-correlation measurement. The auto-correlation measurement is shown in Fig. 7.5(g). At zero time delay, there is a clear anti-bunching in the  $g^{(2)}$ -measurement, which proves the single-photon nature of the emission connected to the radiative Auger process. At non-zero time delay, the onset of Rabi oscillations (of the  $s$ -to- $s$  transition) is visible as a photon bunching of the radiative Auger emission. Both features are well described by our model (see Chapter 7.6).

## 7.6 Cross-correlation theory

The  $g^{(2)}$ -measurements are modelled with the formalism introduced in Chapter 2 and using the level scheme shown in Fig. 7.6. There are four different states which are taken into account for our simulation: the ground state,  $|g\rangle$ , with a single electron in the quantum dot; the excited state,  $|e\rangle$ , a trion with two  $s$ -shell electrons; the state after radiative Auger emission,  $|p\rangle$ , where a single electron occupies the  $p$ -shell of the dot; and the ionised quantum dot state,  $|b\rangle$ , where the electron has tunnelled out. We

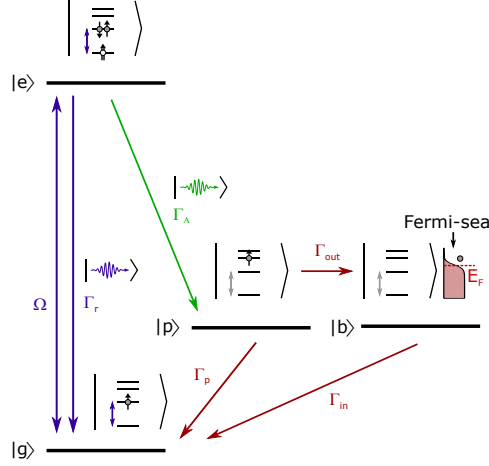


**Figure 7.6: Dynamics of the radiative Auger process.** Model used for the simulation of the auto-correlation measurement of the resonance fluorescence together with the cross-correlation between the resonance fluorescence and the radiative Auger emission.

simulate the system by assuming the following Hamiltonian in the rotating frame of the laser ( $\hbar = 1$ ):

$$\hat{H}_{\text{int}} = \frac{\Omega_R}{2} (|g\rangle \langle e| + |e\rangle \langle g|). \quad (7.1)$$

All decay channels are modelled following the scheme shown in Fig. 7.6. The Lindblad operator is:

$$\hat{\mathcal{L}} = \sqrt{\Gamma_R} |g\rangle \langle e| + \sqrt{\Gamma_A} |p\rangle \langle e| + \sqrt{\Gamma_p} |g\rangle \langle p| \quad (7.2)$$

$$+ \sqrt{\Gamma_{\text{out}}} |b\rangle \langle p| + \sqrt{\Gamma_{\text{in}}} |g\rangle \langle b|. \quad (7.3)$$

We compute the steady-state density matrix,  $\rho_s$ , and obtain the auto- and cross-correlation by using the Python quantum toolbox Qutip [116, 117]. The operator for the resonant decay is  $\hat{a} = |g\rangle \langle e|$ , and the operator for the radiative Auger decay is  $\hat{a}_A = |p\rangle \langle e|$ . Auto- and cross-correlations are computed numerically by applying the quantum regression theorem. The auto-correlation of the resonance fluorescence is given by:

$$g^{(2)}(\tau) = \frac{\langle \hat{a}^\dagger(t) \hat{a}^\dagger(t+\tau) \hat{a}(t+\tau) \hat{a}(t) \rangle}{\langle \hat{a}^\dagger(t) \hat{a}(t) \rangle^2}. \quad (7.4)$$

The cross-correlation is given by:

$$g^{(2)}(\tau) = \frac{\langle \hat{a}_A^\dagger(t) \hat{a}^\dagger(t+\tau) \hat{a}(t+\tau) \hat{a}_A(t) \rangle}{\langle \hat{a}^\dagger(t) \hat{a}(t) \rangle \langle \hat{a}_A^\dagger(t) \hat{a}_A(t) \rangle}. \quad (7.5)$$

The auto-correlation of the radiative Auger emission is:

$$g^{(2)}(\tau) = \frac{\langle \hat{a}_A^\dagger(t) \hat{a}_A^\dagger(t+\tau) \hat{a}_A(t+\tau) \hat{a}_A(t) \rangle}{\langle \hat{a}_A^\dagger(t) \hat{a}_A(t) \rangle^2}. \quad (7.6)$$

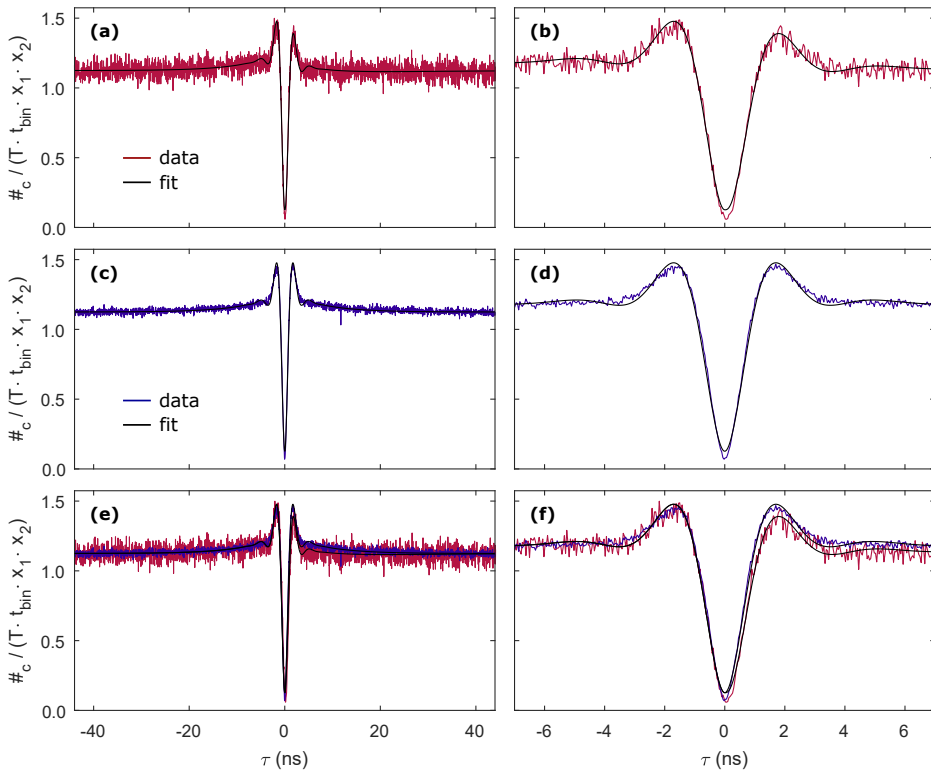


**Figure 7.7: Comparison of auto- and cross-correlation measurements.** Fits to the  $g^{(2)}$ -measurements shown in Fig. 7.5(c). Simultaneous fitting of Eqs. 8.3 and 8.4 to the corresponding auto- and cross-correlation data is performed. In the following sub-figures, the black lines correspond to the fit result. (a) Red line: cross-correlation measurement between resonance fluorescence and the radiative Auger emission where the second electron is transferred into the  $p_+$ -shell of the quantum dot. (b) Cross-correlation measurement from (a) on a shorter time scale. (c) Blue line: auto-correlation measurement of the resonance fluorescence. (d) Auto-correlation measurement from (c) on a shorter time scale. (e) Comparison of the auto- and the cross-correlation measurement together with the corresponding fits. (f) Comparison of the auto- and the cross-correlation measurement, plotted on a short time-scale.

We multiply the result of this simulation by  $1 + c_1 \cdot \exp(-|\tau|/t_{b1})$  to take into account a weak blinking on short time-scales [183]. The blinking might be caused by electron spin pumping enabled by a weak nuclear magnetic field [234]. Additionally, the model function is multiplied with a global prefactor  $c_0$ , which takes into account a weak blinking on long time scales of  $\sim 0.1$  ms, probably caused by charge noise. For the resonance fluorescence, a small fraction  $c_1$  of reflected laser in the resonant emission is taken into account via  $g^{(2)} \rightarrow g^{(2)} \cdot (1 - c_1) + c_1$ . We perform a simultaneous fit of this model to the auto-correlation of the resonance fluorescence and the cross-correlation between the resonance fluorescence and the radiative Auger emission. The result of this fit is shown in Fig. 7.7. The obtained fit parameters can be found in

Tab. 7.2. These parameters also give a good fit to the auto-correlation of the radiative Auger emission, which is shown in Fig. 7.5(g). For this, the fit parameters are kept the same, and only the Rabi frequency is increased ( $\Omega_R = 5.4$  GHz), taking into account that the auto-correlation of the radiative Auger emission has been measured at higher power. The following chapter explains in detail how the correlation data is obtained from the raw time clicks on our detectors.

**Table 7.2:** Parameters obtained from simultaneously fitting the auto- and cross-correlation measurements shown in Fig. 7.7. The radiative decay rate,  $\Gamma_R$ , is obtained from a separate lifetime measurement and is not included in the fit.  $\Gamma_A$  is estimated from the intensity ratio between radiative Auger emission and resonance fluorescence and is also not included in the fit. Decay rate units are in GHz.

$\Omega_R$ (GHz)	$\Gamma_R$	$\Gamma_A$	$\Gamma_p$	$\Gamma_{out}$	$\Gamma_{in}$	$t_{bl}$ (ns)	$c_0$	$c_1$	$c_l$
1.85	1.22	0.001	11.7	0.82	0.07	7.2	1.143	0.153	0.126

## 7.7 Evaluation of correlation measurements

All  $g^{(2)}$ -measurements are performed in a time-tagged, time-resolved mode. The arrival times of all photons are recorded over the full integration time,  $T$ , on two single-photon detectors. All data analysis is carried out post-measurement. We compute the cross-correlation ( $g^{(2)}$ ) between both signals by counting the coincidence events between the two detectors as a function of a time delay,  $\tau$ , between the signals.

Let  $x_1, x_2$  be the count rates on detectors 1 and 2, respectively. We divide the full integration time into time intervals of length,  $t_{bin}$ . The value for  $t_{bin}$  is chosen to be small enough such that the probability of a photon in the corresponding time-interval is very small:  $t_{bin} \cdot x_{1/2} \ll 1$ . For each detector, we determine the number of detection events for all time intervals. This number is either 0 for no photon or 1 for one photon since the probability of having more than one photon in an interval is negligibly small (for  $t_{bin} \cdot x_{1/2} \ll 1$ ). When there is one detection event on detector 1 in an interval at time  $t$  and another detection event on detector 2 in an interval at time  $t + \tau$ , we call it a coincidence event for time delay  $\tau$ . For different time delays, we count the number of coincidence events,  $\#_c$ , over the full integration time. The cross-correlation between both detectors is obtained by dividing  $\#_c(\tau)$  by its expectation value for the case of two uncorrelated detection channels:  $\langle \#_c \rangle = T \cdot t_{bin} \cdot x_1 \cdot x_2$ . This expression for  $\langle \#_c \rangle$  is obtained by the following consideration: the probability of finding a detection event in a certain time interval is  $t_{bin} \cdot x_1$  and  $t_{bin} \cdot x_2$ . If both detection channels are uncorrelated, the probability of finding a detection event for the first detector at time  $t$  and a detection event for the second detector in the time-interval at  $t + \tau$  is  $p_c = t_{bin}^2 \cdot x_1 \cdot x_2$ . For  $T \gg \tau$ , the probability density distribution of  $\#_c$  is thus a binomial distribution:

$$P(\#_c) = \binom{T/t_{bin}}{\#_c} \cdot (1 - p_c)^{T/t_{bin} - \#_c} \cdot p_c^{\#_c} \quad (7.7)$$

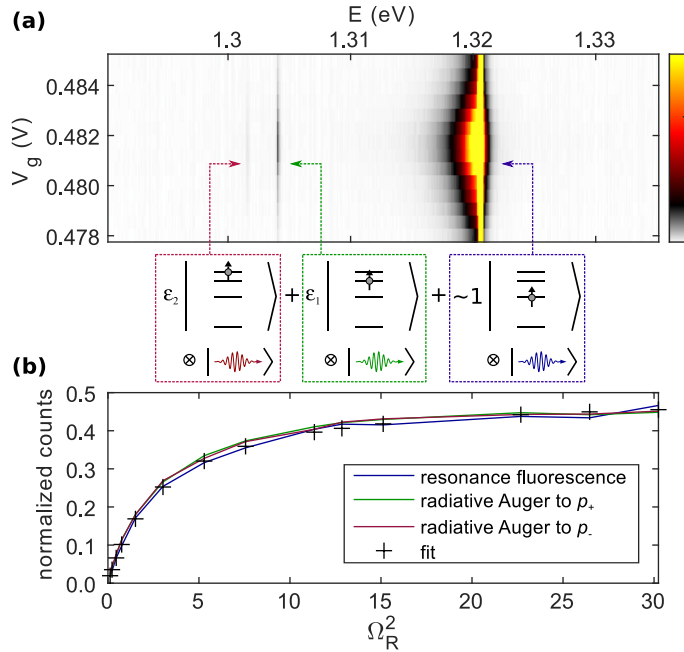


**Figure 7.8: Power dependence of the radiative Auger emission.** (a) Resonance fluorescence and radiative Auger emission. The excitation laser is fixed ( $E \simeq 1.321$  meV), and the quantum dot is swept through the resonance by tuning the gate voltage,  $V_g$ . (b) Dependence of resonance fluorescence and radiative Auger emission on the power of the resonant laser. For the power dependence, the laser is kept in resonance with the trion ( $X^{1-}$ ). When normalised, the resonance fluorescence and the radiative Auger emission intensity depend equally on the excitation power. Both are proportional to the trion occupation of a resonantly driven two-level system (Eq. 7.8).

The expectation value of this distribution is the corresponding normalisation factor:  
 $\langle \#_c \rangle = T \cdot t_{\text{bin}} \cdot x_1 \cdot x_2$ .

## 7.8 Power dependent excitation and radiative Auger linewidth

We measure the intensity of the radiative Auger emission as a function of resonant excitation power and laser detuning. This measurement is shown in Fig. 7.8. In a first measurement, we keep the narrow-band laser at a fixed frequency and sweep the detuning between trion transition and laser by applying a gate voltage,  $V_g$ . The gate voltage shifts the trion energy via the quantum-confined Stark effect. The intensity and the energy of the emission are recorded with a spectrometer. This measurement is shown in Fig. 7.8(a). When laser and trion energy are on resonance, there is a bright emission at  $\sim 1.321$  eV, the resonance fluorescence. This emission is spectrally asymmetric due to the LA-phonon sideband around the resonant peak. At lower energy,  $\sim 18$  meV below the resonance fluorescence, there is the emission corresponding

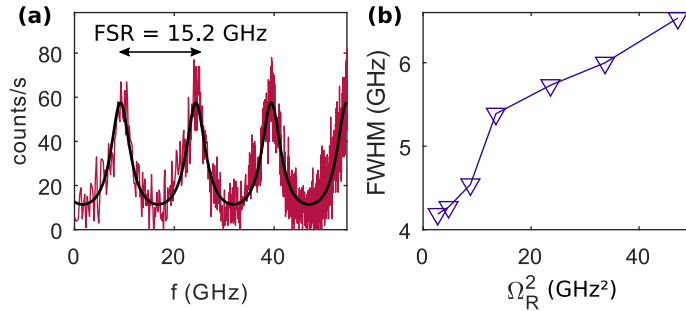


**Figure 7.9: Linewidth measurement of the radiative Auger emission.** (a) Radiative Auger emission at  $\Omega_R = 0.73$  GHz transmitted through a 0.41 GHz Fabry-Perot cavity. (b) Linewidth of the radiative Auger emission as a function of the resonant Rabi frequency.

to the radiative Auger excitation into the  $p$ -shells. This emission is strongest when also the resonance fluorescence is at its maximum, indicating that the intensity of the radiative Auger emission is proportional to the excited state population of the quantum dot. Our model of the radiative Auger process implies this proportionality since the process only takes place in the excited state (trion) of the dot.

To investigate this dependence further, we keep the laser on resonance with the trion and measure the emission intensities as a function of power. This measurement is shown in Fig. 7.8(b). The power dependence of the resonance fluorescence and the radiative Auger emission follows the power saturation curve of a two-level system very well. This result also confirms that the radiative Auger process is entirely related to the trion. Its rate is proportional to the trion occupation,  $\rho_{22}$ , under resonant excitation [235]:

$$\rho_{22} = \frac{1}{2} \frac{\Omega_R^2}{2\Gamma_R^2 + \Omega_R^2}. \quad (7.8)$$

We expect that the ratio of the radiative Auger and the resonance fluorescence intensities roughly reflects the ratio  $\Gamma_A/\Gamma_R$ . This way, we estimate the value for  $\Gamma_A$  to be on the order of  $\sim 1$  MHz.

Finally, we measure the linewidth of the radiative Auger emission. We pass the emission through a Fabry-Perot cavity (15.2 GHz free spectral range, 0.41 GHz linewidth) and sweep the cavity length. The result of this measurement on the  $p_+$ -emission is shown in Fig. 7.9(a). We determine the linewidth of the radiative Auger emission by fitting a multi-Lorentzian which is convoluted with the cavity linewidth. At low power, we measure a minimum linewidth of 4.19 GHz. For comparison, the lifetime limited linewidth is estimated by the decay rate of the  $p_+$ -state after the radiative Auger process:  $\frac{\Gamma_p}{2\pi} = 1.99$  GHz. We repeat the linewidth measurement for different excitation Rabi frequencies. This measurement is shown in Fig. 7.9(b) and shows a linear increase of the linewidth as a function of the excitation power. The reason for the additional contribution to the linewidth and its linear broadening with the excitation power requires further investigations.

## 7.9 Conclusion

The radiative Auger process takes place because the interactions between the carriers (of the trion) change the eigenfunctions of the system (see Chapter 7.12). In a single-particle basis, the initial state contains admixtures of Slater determinants [236, 237] of higher single-particle shells. The optical recombination removes an electron-hole pair from the initial trion state, leading to a final state which is a superposition of single-electron single-particle states. Every state in that superposition consists of an electron in a particular shell along with a photon of a certain energy. Since the initial state is always the same, the energy separations between the different emission lines correspond to precise single-particle splittings. The ratio of radiative Auger emission and resonance fluorescence reflects the expansion of the trion state in single-particle states. Compared to the resonance fluorescence, the radiative Auger emission is weaker, by about two to three orders of magnitude, for both types of dots. It is slightly stronger for the larger GaAs dots. The trion wavefunctions are close, yet not equal to, single-particle states.

In conclusion, we experimentally studied negatively-charged trions in two different types of semiconductor quantum dots and observed a radiative Auger process in the optical recombination spectrum. We employ the radiative Auger process to determine the properties of a single electron in the quantum dot – the energy quantisation and its relaxation and tunnelling dynamics – using the precise, sensitive and fast tools of quantum optics. The radiative Auger process only requires significant Coulomb interactions within the trion, a very general feature. Therefore, this process should also occur for the positively-charged trion and other quantum emitters in the solid state.

## 7.10 Supplementary note I: Methods

The samples are grown by molecular beam epitaxy. Sample A contains InGaAs quantum dots embedded in a *p-i-n-i-n*-diode structure [101, 238–240]. Sample B contains GaAs quantum dots in AlGaAs, which are grown by GaAs-infilling of Al-droplet etched nano-holes [103, 221]. The photon out-coupling is enhanced by a distributed Bragg mirror below the dots. For both samples, the dots are placed between a *p*-doped top gate and an *n*-type doped back gate. The quantum dots are tunnel-coupled to the back gate. This configuration stabilises the charge environment of the dots and enables tuning the quantum dot charge state by applying a voltage between top and back gate [241, 242]. For the InGaAs dots, the back gate has a distance of 40 nm to the dots, 30 nm for the GaAs dots. In a magnetic field, there is optical spin-pumping in the centre of the trion charge plateau [205, 243] (see Chapter 7.13). Therefore, we perform all experiments at the plateau edges, where co-tunnelling randomises the electron spin [244].

All time-resolved measurements are performed by using superconducting single-photon detectors. The overall timing resolution for the  $g^{(2)}$ -measurements is IRF  $\simeq$  35 ps (full width at half maximum). Optical measurements are carried out at 4.2 K in a helium bath cryostat. Resonant excitation of the quantum dots is performed with a narrow-bandwidth ( $\sim$  1 MHz) tunable diode laser (Toptica DLpro), which is additionally filtered with a home-built grating setup in order to remove any background from the gain medium of the laser. The resonance fluorescence of individual dots is measured by suppressing the reflected laser light with a cross-polarisation technique.



## 7.11 Supplementary note II: List of definitions

**Table 7.3:** List of definitions. HO: Harmonic oscillator.

Label	Description
$\hbar$	reduced Planck constant
$\mu_B$	Bohr magneton
$\epsilon_0, \epsilon_r$	permittivity of vacuum, relative permittivity
$g_e, g_h$	electron and hole g-factor
$E_0$	bandgap of the QD-material
$m_e^*, m_h^*$	electron, hole effective mass
$\hbar\omega_c = \frac{\hbar e B}{m_e^*}$	electron cyclotron energy
$\hbar\omega_x, \hbar\omega_y$	confinement energies of the asymmetric HO
$\hbar\omega_0 \equiv \hbar\omega_x + \Delta_p \equiv \hbar\omega_p - \Delta_p$	confinement energy of the symmetric HO
$n, L$	quantum numbers for the symmetric HO
$n_x, n_y$	quantum numbers for the asymmetric HO
$E_{n,l}$	eigenenergies of the symmetric HO
$\Delta_{pd}$	coupling between $p_-$ - and the $d_+$ -shell
$\Omega_R$	Rabi frequency
$\Gamma_R = \tau_r^{-1}$	radiative decay rate
$\Gamma_A = \tau_A^{-1}$	radiative Auger decay rate
$\Gamma_p = \tau_p^{-1}$	relaxation rate from $p$ - to $s$ -shell
$\Gamma_{\text{out}} = \tau_{\text{out}}^{-1}$	tunnel rate out of the QD
$\Gamma_{\text{in}} = \tau_{\text{in}}^{-1}$	tunnel rate into the ionised QD
$E_f^{p\pm}, E_f^{d\pm}$ , and $E_f^{d_0}$	final state energies after Auger excitation
$\Delta_{LO}, \Delta_{TO}$	energies of LO and TO phonons

## 7.12 Supplementary note III: Radiative Auger process theory

To explain the radiative Auger process, we consider the interactions between the three particles forming the trion. We determine the multi-particle eigenstates,  $\Psi$ , for several carriers in the same dot by numerically solving the time-independent Schrödinger equation,  $\hat{H}\Psi = E\Psi$ , via exact diagonalisation. The Hamiltonian,  $\hat{H}$ , of the system is:

$$\hat{H} = \sum_{i=1}^N \left[ \frac{-\hbar^2}{2m_i^*} \Delta_i + V(\vec{x}) \right] + \hat{C}. \quad (7.9)$$

$\hat{C}$  is the Coulomb operator, which is given by:

$$\hat{C} = \frac{1}{4\pi\epsilon_0\epsilon_r} \sum_{i,j,i<j}^N \frac{c_i \cdot c_j}{|r_i - r_j|}. \quad (7.10)$$

The term  $c_i = \pm e$  is the charge of a particle (electron or hole). As we are considering fermionic particles, the overall wavefunction is antisymmetric under particle exchange. Therefore, we consider  $\hat{H}$  in a basis,  $\{\Psi_{\mathbf{n}}\}$ , of antisymmetrised Slater determinants:

$$\Psi_{\mathbf{n}} = \hat{A} \prod_{i=1}^N \phi_{n_i}(x_i, \sigma_i). \quad (7.11)$$

The Slater determinants are constructed from the single-particle solutions,  $\phi_{n_i}(x_i, \sigma_i)$ , of Eq. 7.9. The index  $\mathbf{n}$  represents the quantum numbers required to describe all particles. The asymmetrisation operator,  $\hat{A}$ , constructs a Slater-determinant, which is asymmetric under the exchange of identical particles. To express  $\hat{H}$  in the basis  $\{\Psi_{\mathbf{n}}\}$ , the matrix elements  $\langle \Psi_{\mathbf{n}} | \hat{H} | \Psi_{\mathbf{m}} \rangle$  are computed. The Slater-Condon rules [236, 245] transform these multi-particle matrix elements into two-particle Coulomb matrix elements. The Slater-Condon rules for the two-particle Coulomb operator,  $\hat{C}$ , are:

$$\langle \Psi_{\mathbf{n}} | \hat{C} | \Psi_{\mathbf{n}} \rangle = \frac{1}{2} \sum_{i,j,i \neq j}^N [V_{ijij} - V_{ijji}] \quad (7.12)$$

$$\langle \Psi_{\mathbf{n}} | \hat{C} | \Psi_{\mathbf{n}(h,k)} \rangle = \sum_{i=1}^N [V_{hiki} - V_{hiik}] \quad (7.13)$$

$$\langle \Psi_{\mathbf{n}} | \hat{C} | \Psi_{\mathbf{n}(h,k,l,m)} \rangle = V_{hklm} - V_{hlmk}. \quad (7.14)$$

The index  $\mathbf{n}(h,k)$  indicates that this wavefunction is obtained from  $\Psi_{\mathbf{n}}$  by replacing the single-particle wavefunction  $\phi_h$  of particle number  $h$  by  $\phi_k$ . The index  $\mathbf{n}(h,k,l,m)$  means that two wavefunctions are changed correspondingly. The two-particle Coulomb matrix elements,  $V_{hklm}$ , are given by the following integral:

$$\begin{aligned} V_{hklm} &= \langle \phi_h \phi_k | \hat{C} | \phi_l \phi_m \rangle \\ &\equiv \frac{e^2}{4\pi\epsilon_0\epsilon_r} \int \int \frac{\phi_h(\mathbf{r}_1)^* \phi_k(\mathbf{r}_2)^* \phi_l(\mathbf{r}_1) \phi_m(\mathbf{r}_2)}{|\mathbf{r}_1 - \mathbf{r}_2|} d\mathbf{r}_1 d\mathbf{r}_2. \end{aligned} \quad (7.15)$$

Depending on the order of the indices, these integrals include the direct Coulomb and the Coulomb exchange terms. For a symmetric harmonic confinement potential, analytic solutions for the Coulomb integrals can be found e.g. in Refs. [229, 230].

The eigenfunctions of Eq. 7.9 are obtained by diagonalising  $\hat{H}$  in the basis  $\{\Psi_{\mathbf{n}}\}$ . The trion ground state has a small admixture of higher single-particle shells, which is the origin of the radiative Auger process. Upon optical recombination of one electron and a hole, the remaining electron of the trion is in a superposition including these higher shells. Detection of the frequency of the emitted photon projects the state of the remaining electron to the corresponding shell. For the trion, it is sufficient to carry out exact diagonalisation for the initial state only since the final states are single-particle states.

In the dipole approximation, the emission spectrum can be computed with Fermi's golden rule [80, 246]:

$$I(\omega) \propto \sum_f \left| \langle \Psi^{(f)} | \hat{P} | \Psi^{(i)} \rangle \right|^2 \cdot \delta(E_i - E_f - \hbar\omega) \cdot D(\omega), \quad (7.16)$$

where  $\Psi^{(i)}$  is the initial state,  $\Psi^{(f)}$  are the possible final states, and  $D(\omega)$  is the density of states for an emitted photon.  $\hat{P} = \sum d_{ij} \hat{h}_{i,\sigma} \hat{e}_{j,-\sigma}$  adds up all dipole-matrix ( $d_{ij}$ ) allowed electron-hole recombinations, where  $i, j$  sum over orbital and  $\sigma$  over spin degrees of freedom [80, 246].

With the presented formalism, we estimate that the intensity of the radiative Auger transition from  $s$ - to the  $d_0$ -shell is about a hundred times weaker than the resonance fluorescence. However, this intensity is tendentially overestimated compared to the experimentally obtained values. The issue could be that the exact diagonalisation only converges when taking into account very high single-particle shells. In reality, not all of these states exist due to close-by continuum states. Furthermore, the envelope wave approximation is a simplification compared to a fully atomistic treatment [247]. Finally, this approach assumes that angular momentum is a good quantum number, allowing radiative Auger with the  $d_0$ -shell but not with  $p$ -shells. In the experiment, radiative Auger with the  $p$ -shells is clearly observed, also in the limit of high magnetic field, suggesting that angular momentum is not a good quantum number.

## 7.13 Supplementary note IV: Spin pumping and Rabi oscillations

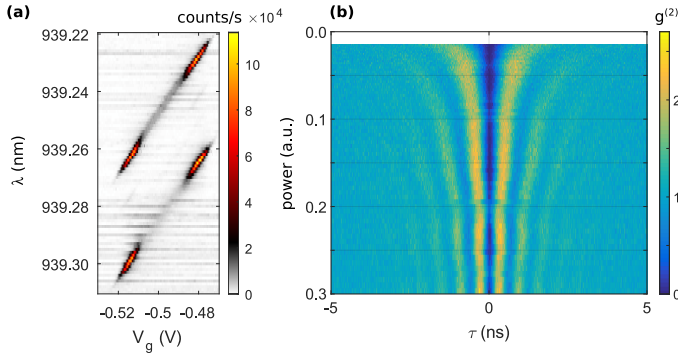


**Figure 7.10: Additional quantum dot characterisation.** (a) The charge plateau of the resonantly excited trion at a magnetic field of 0.6 T. This measurement is carried out on the InGaAs quantum dot (QD) shown in Fig. 7.1(b). At the edges of the charge plateau, a strong resonance fluorescence is detected. In the plateau center, the resonance fluorescence intensity is strongly reduced due to electron spin pumping. All radiative Auger measurements are performed at the plateau edges. (b) Power dependent  $g^{(2)}$ -measurement on the negative trion of the same dot.

Fig. 7.10(a) shows a measurement of the resonance fluorescence of the negative trion as a function of the gate voltage and the laser wavelength. This measurement is performed on the quantum dot which is presented in Fig. 7.1(b). The trion is stable in the gate voltage range between  $V_g = -0.52$  V and  $V_g = -0.48$  V. This charge plateau splits into two due to the electron spin Zeeman energy. We perform the measurements of the radiative Auger emission on one Zeeman branch. No Zeeman splitting is observed in the emission spectrum, which shows that the radiative Auger process is spin-conserving. In the center of the charge plateau, the resonance fluorescence disappears due to optical spin pumping. At the edges of the charge plateau, the resonance fluorescence is strong due to spin co-tunnelling with the back gate [205, 244]. For this reason, we perform all measurements in the co-tunnelling regime.

Fig. 7.10(b) shows resonantly driven Rabi oscillations as a function of the excitation power. The measurement is performed on the trion state of the same dot. These coherent oscillations in the auto-correlation ( $g^{(2)}$ ) measurement show that the quantum dot can be approximately described by a two-level system [5]. However, radiative Auger is a fundamental process that limits this two-level approximation in the case of a trion.



---

## Optically driving the radiative Auger transition

---

**The content of this chapter is adapted from:**

C. Spinnler, L. Zhai, G. N. Nguyen, J. Ritzmann, A. D. Wieck, A. Ludwig, A. Javadi, D. E. Reiter, P. Machnikowski, R. J. Warburton, and M. C. Löbl, “**Optically driving the radiative Auger transition**”, *Nature Communications* **12**, 6575 (2021).

## 8.1 Introduction

As discussed in detail in the previous chapter, the radiative Auger process promotes carriers to an excited state, resulting in weak red-shifted satellite peaks in the emission spectrum. The appearance of radiative Auger in the emission directly leads to the question if the process can be inverted: simultaneous photon absorption and electronic demotion. However, resonant excitation of the radiative Auger transition has not been shown, neither on atoms nor on solid-state quantum emitters. Here, we demonstrate the optical driving of the radiative Auger transition, linking few-body Coulomb interactions and quantum optics. We perform our experiments on a trion in a semiconductor quantum dot, where the radiative Auger and the fundamental transition form a  $\Lambda$ -system. On driving both transitions simultaneously, we observe a reduction of the fluorescence signal by up to 70%. Our results suggest that radiative Auger could be used as a resonance fluorescence switch as well as for THz spectroscopy (using optics close to the visible regime).

Non-radiative Auger processes have been observed in both atoms [210] and solid-state quantum emitters [212, 248]. They play an important role in determining the efficiency of semiconductor light-emitting diodes and lasers [249]. In the non-radiative Auger process, one electron reduces its energy by transferring it to a second electron that is promoted to a high-energy state. In the radiative Auger process (shake-up), in contrast, one electron makes an optical decay, creating a photon. Part of the photon energy is transferred to a second electron such that the radiative Auger emission is red-shifted with respect to the main emission line. Both radiative and non-radiative Auger processes arise as a consequence of the Coulomb interactions between electrons in close proximity [79, 250, 251]. Non-radiative Auger is a purely Coulomb scattering process. In contrast, radiative Auger involves both Coulomb scattering and electron-photon interactions. It can either be viewed as a higher-order scattering process or interpreted in terms of Coulomb-induced admixtures of higher single-particle states to the multi-electron wave function [251, 252]. What appears to be an optical relaxation of one electron in the single-particle picture involves in fact a sudden change of the many-particle configuration.

Radiative Auger emission has been observed over a large spectral range: in the X-ray emission of atoms [208]; close to visible frequencies on donors in semiconductors [217] and quantum emitters [253, 254]; and at infrared frequencies as shake-up lines in two-dimensional systems [218, 219, 255–257]. Furthermore, radiative Auger connects carrier dynamics to the quantum optical properties of the emitted photons [253], making it a powerful probe of multi-particle systems. Driving the fundamental transition between the electron ground state and an optically excited state is an important technique in quantum optics [1, 5]. In contrast, driving the radiative Auger transition would significantly increase the number of quantum optics techniques that can be employed. However, this has not been achieved, neither with atoms nor with solid-state systems.

## 8.2 Driving the radiative Auger transition

We demonstrate driving the radiative Auger transition on an epitaxial GaAs quantum dot embedded in AlGaAs [66, 103]. Quantum dot forms a potential minimum which

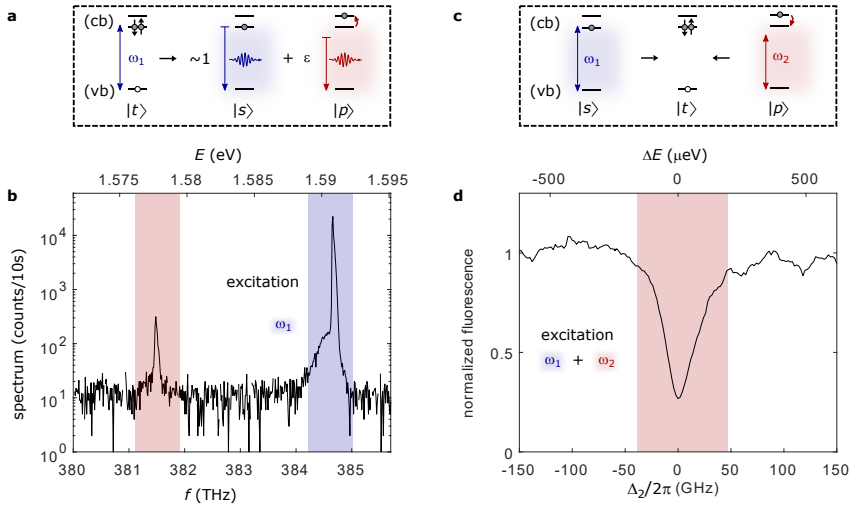


**Figure 8.1: Radiative Auger emission and excitation of the radiative Auger transition.** (a) Schematic illustration of the fundamental transition and the radiative Auger process. The trion state  $|t\rangle$  optically decays by recombination of one electron in the conduction band (cb) with a hole in the valence band (vb). The second electron either stays in its ground state  $|s\rangle$  (fundamental transition), or is left in a higher shell  $|p\rangle$  (radiative Auger). The radiative Auger photon is red-shifted from the fundamental transition by the energy transferred to the Auger electron. (b) Emission spectrum from a negatively charged quantum dot upon optical excitation at the fundamental transition. In addition to the fundamental transition (highlighted in blue), there is a red-shifted satellite line (highlighted in red). This emission arises from the radiative Auger process where the trion state  $|t\rangle$  decays to the excited electron state  $|p\rangle$ . (c) Two possible absorption channels in the presence of one confined conduction band electron. When the electron is in the ground state  $|s\rangle$ , a laser resonant with the fundamental transition (blue, frequency  $\omega_1$ , Rabi frequency  $\Omega_1$ ) excites a valence band electron and brings the system to the trion state,  $|t\rangle$ . When the conduction band electron is in an excited state  $|p\rangle$ , a red-shifted laser (frequency  $\omega_2$ , Rabi frequency  $\Omega_2$ ) can excite the system to the same trion state  $|t\rangle$ . In this inverted radiative Auger process, the missing energy is provided by the excited electron. (d) Resonance fluorescence from the fundamental transition in the presence of a strong second laser. When the second laser ( $\omega_2$ ) is on resonance with the radiative Auger transition ( $\Delta_2 = 0$ ), the resonance fluorescence intensity is strongly reduced.

confines charge carriers (see Chapter 2), resulting in discrete energy levels (similar to atoms). Without optical illumination, a single electron is trapped in the conduction band of the quantum dot and occupies the lowest possible shell (the  $s$ -shell,  $|s\rangle$ ). Upon resonant excitation of the fundamental transition, a second electron is promoted from the filled valence band to the conduction band and a negative trion  $X^{1-}$  ( $|t\rangle$ ) is formed. This trion consists of two electrons in the conduction band and one electron vacancy (hole) in the valence band. Fig. 8.1(a) shows the possible optical decay paths: in a fundamental transition, one electron decays, removing the valence band hole, while the other electron remains in the conduction band ground state  $|s\rangle$ ; in a radiative Auger process, the remaining electron is left in an excited state  $|p\rangle$ . The



emitted photon is red-shifted by the energy separation between  $|p\rangle$  and  $|s\rangle$  [79, 253]. Fig. 8.1(b) shows a typical emission spectrum from the trion decay. This spectrum is measured on resonantly driving the fundamental transition  $|s\rangle-|t\rangle$  at 384.7 THz (1.591 eV) with a narrow-bandwidth laser [253]. Red-shifted by 3.2 THz (13.2 meV) from the fundamental transition a weak satellite line arises from the radiative Auger process.

Photons at the radiative Auger frequency have insufficient energy to excite the fundamental transition  $|s\rangle-|t\rangle$ . Figure 8.1(c) shows how the trion state  $|t\rangle$  still can be excited with a laser at the Auger transition. The missing energy is provided by the electron which initially occupies the excited state  $|p\rangle$ . However, driving the radiative Auger transition is experimentally challenging for two main reasons: first, there is a fast non-radiative relaxation from the excited single-electron state  $|p\rangle$  back to  $|s\rangle$  [253, 258], and the state  $|p\rangle$  is not occupied at thermal equilibrium. Second, the dipole moment of the radiative Auger transition is small. Therefore, it is difficult to achieve high Rabi frequencies on driving the transition, plus the radiative Auger emission is very weak and hard to distinguish from the back-reflected laser light.

We perform a two-laser experiment revealing optical driving of the radiative Auger transition. The fundamental transition  $|s\rangle-|t\rangle$  (at  $\sim 1.591$  eV) is driven with one laser (labelled by  $\omega_1$ ) while the radiative Auger transition (at  $\sim 1.578$  eV) is simultaneously driven with a second laser (labelled by  $\omega_2$ ). This  $\Lambda$ -configuration has the following advantages: First, on driving  $|s\rangle-|t\rangle$  with  $\omega_1$ , there is a small chance of initialising the system in state  $|p\rangle$  via the radiative Auger emission. Additionally, driving the  $|p\rangle-|t\rangle$ -transition with  $\omega_2$ , while transferring population to  $|t\rangle$  with  $\omega_1$ , also leads to a finite occupation of  $|p\rangle$ . Second, the small dipole matrix element of the radiative Auger transition is compensated by using high power for  $\omega_2$ . The high power causes a high laser background when detecting the fluorescence from the radiative Auger transition. Instead, we tune the second laser over the Auger transition while measuring just the fluorescence originating from the fundamental transition  $|s\rangle-|t\rangle$ . Fig. 8.1(d) shows the result of this two-laser experiment. We observe a strong reduction in fluorescence on addressing the transition  $|p\rangle-|t\rangle$  which is characteristic of two-colour excitation of a  $\Lambda$ -configuration. Our approach has a conceptual similarity to the driving of weak phonon sidebands of mechanical resonators resulting in optomechanically induced transparency [155, 156].

### 8.3 Autler-Townes splitting in single-laser experiments

We consider initially the situation where the fundamental transition ( $|s\rangle-|t\rangle$ ) is strongly driven by a single laser. If radiative Auger and fundamental transition form a  $\Lambda$ -system, one would expect an Autler-Townes splitting in the radiative Auger emission. Fig. 8.2(a) shows the corresponding level scheme including the dressed states  $\frac{1}{\sqrt{2}}(|N+1, s\rangle \pm |N, t\rangle)$  and  $\frac{1}{\sqrt{2}}(|N, s\rangle \pm |N-1, t\rangle)$ , where  $N$  is the photon number. The dressed-state splitting leads to the Mollow triplet in the resonance fluorescence [4, 5, 118]. For a decay into a third level, the Autler-Townes splitting [2, 259] in the emission is expected to be  $\Omega_1$ . Fig. 8.2(b) shows the radiative Auger emission of a quantum dot (QD1). In this measurement, the laser is in resonance with the fundamental transition. The Rabi frequency ( $\Omega_1 = 2\pi \times 31.9$  GHz, red bar in

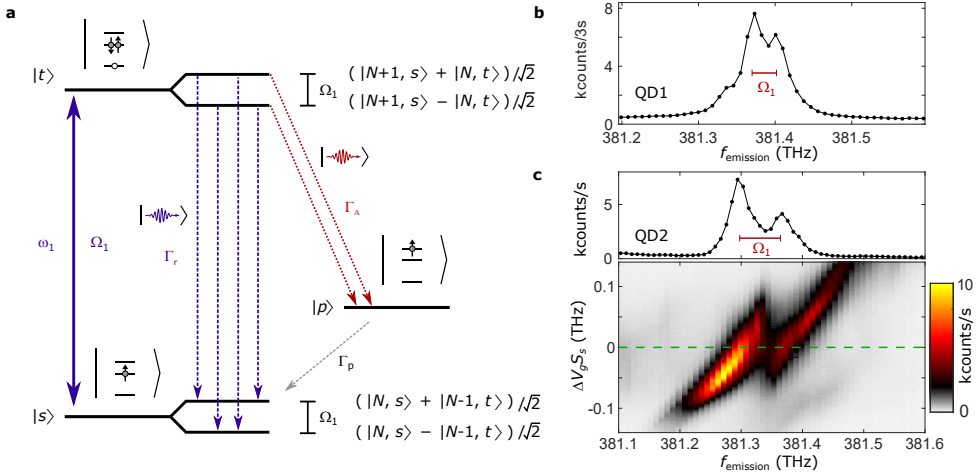


**Figure 8.2: Autler-Townes splitting in the radiative Auger emission.** (a) Level scheme under strong resonant driving of the fundamental transition ( $|s\rangle$ – $|t\rangle$ ). The energy levels of the transition are split into dressed states. The splitting between the dressed states is given by the Rabi frequency,  $\Omega_1$ . In the radiative Auger emission (red arrows), the dressed-state splitting creates two decay paths leading to an Autler-Townes splitting. (b) Radiative Auger emission from the main quantum dot (QD1) on driving the transition  $|s\rangle$ – $|t\rangle$  with  $\omega_1$ . The Rabi frequency of  $\Omega_1 = 2\pi \times 31.9$  GHz (red bar) is determined from a power saturation curve. The measured Autler-Townes splitting in the emission matches the Rabi frequency. (c) Emission spectrum from a second quantum dot (QD2), measured for a set of different detunings ( $\Delta_1 = \Delta V_g \cdot S_s$ ) between fundamental transition and laser frequency. The upper part of the plot is a line cut along the dashed green line at zero detuning ( $\Delta_1 = 0$ ). In this case, the measured Autler-Townes splitting agrees with the independently determined Rabi frequency ( $\Omega_1 = 2\pi \times 67.7$  GHz).

Fig. 8.2(b)) is estimated independently by measuring the fluorescence intensity as a function of laser power, see Fig. 8.6(b). We observe an Autler-Townes splitting that agrees well with this Rabi frequency. For this quantum dot, we also observe an additional weak emission appearing on the low energy side of the spectrum when using high Rabi frequencies (see [Supplementary note II](#)). We speculate that this emission is connected to optical coupling between  $|p\rangle$  and an excited trion state,  $|t^*\rangle$ . Figure 8.2(c) shows radiative Auger emission from a second quantum dot (QD2). For this quantum dot, we measure the radiative Auger emission as a function of detuning between the quantum dot transition and the laser (see [Supplementary note II](#), Fig. 8.2 for the corresponding measurement on QD1). On applying a gate voltage  $\Delta V_g$ , the quantum dot transition  $|s\rangle$ – $|t\rangle$  is detuned from the fixed laser by  $\Delta_1 = \Delta V_g \cdot S_s$  via the quantum-confined Stark shift.  $S_s$  parameterises the Stark shift of the fundamental transition. At zero detuning, the observed Autler-Townes splitting again agrees with the Rabi frequency obtained from a power saturation curve ( $\Omega_1 = 2\pi \times 67.7$  GHz).

## 8.4 Two-laser experiments in a $\Lambda$ -configuration

We now consider the experiments with the second laser (labelled as  $\omega_2$ ) at the radiative Auger transition. Fig. 8.3(a) shows the corresponding level scheme. We set  $\omega_1$  to a modest Rabi frequency ( $\Omega_1 = 2\pi \times 0.08$  GHz) compared to the decay rate of the trion ( $\Gamma_R = 2\pi \times 0.50$  GHz). The frequency of the radiative Auger transition is estimated from the trion emission spectrum (Fig. 8.1(b)). We sweep the frequency  $\omega_2$  and simultaneously monitor the resonance fluorescence intensity from the fundamental transition. Fig. 8.3(b) shows this measurement for different powers of the laser on the Auger transition. On increasing the power of  $\omega_2$  to several orders of magnitude higher than the power of  $\omega_1$ , there is a pronounced dip in the fluorescence intensity. This intensity dip appears precisely when the laser frequency  $\omega_2$  matches the radiative Auger transition ( $|p\rangle$ – $|t\rangle$ ) and is characteristic for a  $\Lambda$ -system that is driven with two lasers. We estimate the Rabi frequency  $\Omega_2$  driving  $|p\rangle$ – $|t\rangle$  by simulating the resonance fluorescence intensity as a function of  $\Delta_2$  (see Chapter 8.5 for the quantum optics simulation). In this simulation we keep the decay rate from  $|p\rangle$  to  $|s\rangle$  ( $\gamma_p \sim 2\pi \times 9.3$  GHz) fixed to the value that we determine from independent auto- and cross-correlation measurements [253] (see Fig. 8.5). The value for  $\Omega_2$  can then be determined by a corresponding fit to the two-laser experiment. Additionally, we fit a constant pure dephasing,  $\gamma_p$ , for the state  $|p\rangle$  which leads to an additional broadening of the fluorescence dip. We estimate  $\gamma_p \sim 2\pi \times 8.8$  GHz from the fit and a Rabi frequency of  $\Omega_2 = 2\pi \times 3.2$  GHz ( $\omega_2$ ) for the strongest fluorescence dip. Note that additional excitation-induced dephasing via phonons is expected to be weak for such Rabi-frequencies [122, 260].

In Fig. 8.3(c), we plot the minimum of the resonance fluorescence dip as a function of  $\Omega_2$ . The  $\Lambda$ -system model with two driving lasers fits this data set well. For the highest value of  $\Omega_2$ , we achieve a reduction of the resonance fluorescence intensity by up to 70%. The intensity reduction is limited by the power that we can reach in our optical setup. The measurement shows that resonance fluorescence can be switched on and off by using the radiative Auger transition. In our system, part of the fluorescence dip is due to the reduction of the overall absorption via the formation of a dark state. This effect is related to electromagnetically induced transparency (EIT) [261] and coherent population trapping (CPT) [16, 262]. An additional reduction of the signal comes from the fact that there is a fast decay rate  $\gamma_p$  from state  $|p\rangle$  to  $|s\rangle$ . Thus, after the laser-induced transition from state  $|t\rangle$  to  $|p\rangle$ , the system quickly decays to the ground state  $|s\rangle$ . This de-excitation channel reduces the population of the trion state and therefore the fluorescence intensity. We can distinguish the contributions of the two mechanisms by our quantum optics simulation. The density matrix element  $\rho_{tt}$  (occupation of state  $|t\rangle$ ) is proportional to the overall fluorescence intensity. The term  $\text{Im}(\rho_{st})$  (coherence between the states  $|s\rangle$  and  $|t\rangle$ ) is proportional to the absorption and reflects the coherent part of the intensity reduction. The contribution of both mechanisms is comparable for the parameter regime in which we operate (see Fig. 8.4(b)).

The measurements so far were performed with  $\omega_1$  on resonance ( $\Delta_1 = 0$ ). We repeat the two-laser experiments while detuning of  $\omega_1$  from the fundamental transition. Fig. 8.3(d) shows the fluorescence intensity for positive, zero, and negative detuning  $\Delta_1$ . For non-zero detuning, the fluorescence dip is asymmetric as a function of  $\Delta_2$ . The asymmetry is an important result as it cannot be explained by a rate equation

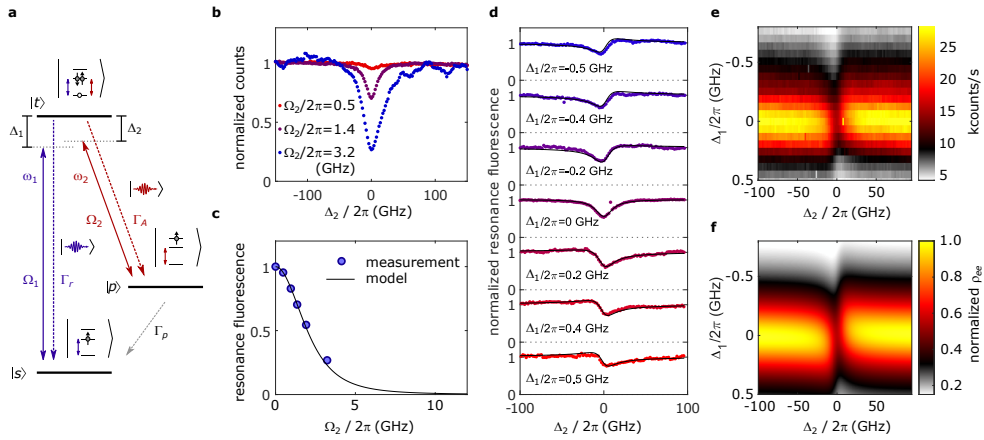


**Figure 8.3: Optically driving the radiative Auger transition.** (a) The level scheme where one laser ( $\omega_1$ ) with Rabi frequency  $\Omega_1$  drives the fundamental transition ( $|s\rangle$ – $|t\rangle$ ) while a second laser ( $\omega_2$ ) drives the radiative Auger transition ( $|p\rangle$ – $|t\rangle$ ) with Rabi frequency  $\Omega_2$ . (b) Resonance fluorescence ( $\Omega_1 = 2\pi \times 0.08$  GHz) as a function of detuning  $\Delta_2$  (detuning of  $\omega_2$ ). At low values of  $\Omega_2$ , the resonance fluorescence intensity is almost constant for different values of  $\Delta_2$ . For the highest value of  $\Omega_2$ , the resonance fluorescence drops by up to  $\sim 70\%$  on bringing  $\omega_2$  into resonance with the radiative Auger transition. The strong fluorescence dip at a particular frequency is a characteristic feature of a  $\Lambda$ -system driven with two lasers that are detuned in frequency by the ground state splitting. (c) Resonance fluorescence at  $\Delta_2 = 0$  as a function of  $\Omega_2$ . The resonance fluorescence intensity (blue dots) drops with increasing  $\Omega_2$ , fitting well to the theoretical model (black line). (d) Fluorescence intensity as a function of detuning  $\Delta_2$ . The Rabi frequencies are  $\Omega_1 = 2\pi \times 0.27$  GHz,  $\Omega_2 = 2\pi \times 2.1$  GHz. The same measurement is repeated for a series of fixed detunings  $\Delta_1$  (detuning of  $\omega_1$  from the fundamental transition). Detuning  $\omega_1$  leads to an asymmetric fluorescence dip. This asymmetry is well captured by our quantum optics simulations (black lines) based on the level scheme shown in (a). (e) Fluorescence intensity as a function of laser detunings  $\Delta_1$ ,  $\Delta_2$ . (f) Simulation of the fluorescence intensity as a function of the laser detunings.

description, but depends on the quantum coherences in the master equation model (see Chapter 8.5). The full dependence of the resonance fluorescence intensity as a function of  $\Delta_1$  and  $\Delta_2$  is plotted in Fig. 8.3(e). This data set matches well to the corresponding quantum optics simulation in Fig. 8.3(f) using the parameters from the previous measurements. The following chapter will discuss the quantum optics simulations in detail.

## 8.5 Modelling the $\Lambda$ -system

The level scheme to describe the two-laser experiments is shown in Fig. 8.4. It consists of the electron ground state  $|s\rangle$ , an excited electron state  $|p\rangle$ , and the trion state  $|t\rangle$ . The laser driving the fundamental transition is labelled as  $\omega_1$  and the laser driving the radiative Auger transition is labelled as  $\omega_2$ . The corresponding Rabi frequencies are given by  $\Omega_1$ ,  $\Omega_2$  and the detunings of the lasers from the corresponding transitions

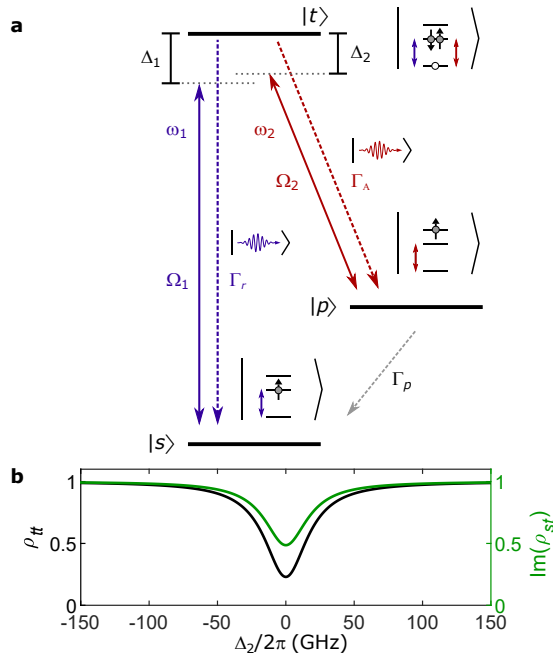


**Figure 8.4: Level scheme and quantum optics simulation.** (a) Fundamental transition and radiative Auger transition form a  $\Lambda$ -system where both transitions can be driven by two independent lasers. The Rabi-frequency of the laser on the fundamental transition ( $\omega_1$ ) is given by  $\Omega_1$ , the Rabi frequency of the laser on the radiative Auger transition ( $\omega_2$ ) is given by  $\Omega_2$ . The corresponding laser detunings are  $\Delta_1$  and  $\Delta_2$ , the corresponding spontaneous decay rates from the trion state  $|t\rangle$  are  $\Gamma_R$  (fundamental transition),  $\Gamma_A$  (radiative Auger). The parameter  $\gamma_p$  is the relaxation rate from the electron excited state  $|p\rangle$  to the electron ground state  $|s\rangle$ . (b) Comparison of the density matrix elements  $\rho_{tt}$  and  $\text{Im}(\rho_{st})$  as a function of  $\Delta_2$ . The parameters are identical to those used to describe the deepest fluorescence dip shown in Fig. 8.3(b).

are  $\Delta_1$ ,  $\Delta_2$ . The spontaneous decay rates are the decay rate via the fundamental transition ( $\Gamma_R$ ), the decay rate via radiative Auger ( $\Gamma_A$ ), and the  $p$ -to- $s$  decay rate ( $\gamma_p$ ). We simulate the system with a standard quantum optics approach, following the formalism from Chapter 2. Making the dipole and the rotating-wave approximations, the Hamiltonian of the system is given by [16, 261]:

$$\hat{H} = \frac{\hbar}{2} [2(\Delta_2 - \Delta_1) |p\rangle \langle p| - 2\Delta_1 |t\rangle \langle t| + \Omega_1 |t\rangle \langle s| + \Omega_2 |t\rangle \langle p| + \Omega_1 |s\rangle \langle t| + \Omega_2 |p\rangle \langle t|]. \quad (8.1)$$

The Hamiltonian describes the coherent evolution of the system. The incoherent decay paths are taken into account by the Lindblad collapse operators for the spontaneous emission from the fundamental transition ( $L_1 = \sqrt{\Gamma_R} |s\rangle \langle t|$ ), the spontaneous radiative Auger emission ( $L_2 = \sqrt{\Gamma_A} |p\rangle \langle t|$ ), the  $p$ -to- $s$  relaxation ( $L_3 = \sqrt{\gamma_p} |s\rangle \langle p|$ ), and the  $p$ -shell dephasing ( $L_4 = \sqrt{\gamma_p} |p\rangle \langle p|$ ). The dynamics of the system are described

by the following master equation:

$$i\hbar \frac{d\rho}{dt} = [\hat{H}, \rho] + i\hbar \sum_i \left( L_i \rho L_i^\dagger - \frac{1}{2} \{L_i^\dagger L_i, \rho\} \right), \quad (8.2)$$

where  $\rho$  is the density matrix, see Chapter 2. Using this equation, we determine the steady state of the system ( $\frac{d\rho}{dt} = 0$ ). The steady state occupation of the trion state is used for simulating the experiments as it is proportional to the fluorescence intensity.

This simulation fits well to our experimental results in Fig. 8.3. We also use it to estimate the Rabi frequency  $\Omega_2$  and the dephasing  $\gamma_p$ : when  $\Delta_2$  is close to zero, the resonance fluorescence depends on  $\Omega_2$ . Due to the small dipole moment of the radiative Auger transition, strong laser powers are required to achieve high values of  $\Omega_2$ . For the strongest laser power of  $\omega_2$  (increasing the power of  $\omega_1$  by a factor of  $\sim 8 \times 10^3$ ), we estimate  $\Omega_2 = 2\pi \times 3.2$  GHz from the simulation. Alternatively, one could estimate the ratio of the corresponding dipole moments by using the intensity ratio between resonance fluorescence and radiative Auger emission ( $\sim 50 : 1$ ).  $\Omega_2$  could then be obtained by using this estimation together with the power saturation curve of the resonance fluorescence. We find that this method underestimates  $\Omega_2$  compared to the simulation. Since effects such as chromatic aberration make this second approach more prone to systematic errors, we always use the two-laser experiment and the corresponding simulation to determine  $\Omega_2$ . The dephasing term  $\gamma_p$  is also estimated by simulating the two-laser experiment. We find that it mainly affects the width of the fluorescence dip.  $\Gamma_R$ ,  $\gamma_p$ , and  $\Omega_1$  are determined from independent measurements and kept fixed in the simulation.

There are two mechanisms that contribute to the fluorescence reduction when driving the Auger transition with  $\omega_2$ : a coherent part related to EIT/CPT and dark state formation [261], an incoherent part due to a fast de-excitation channel from  $|t\rangle$  to  $|p\rangle$  via radiative Auger and from  $|p\rangle$  to  $|s\rangle$  by two-phonon emission [258]. The incoherent decay path is irrelevant in systems where the ground state lifetime is long [261]. To distinguish these two mechanisms we compare the density matrix element  $\rho_{tt}$  (proportional to the overall fluorescence signal) to  $\text{Im}(\rho_{st})$  (proportional to the susceptibility). The susceptibility determines the system's absorption [261] and is associated with the coherent contribution of the fluorescence reduction. In Fig. 8.4(b) we plot  $\rho_{tt}$  and  $\text{Im}(\rho_{st})$  as a function of  $\Delta_2$ . This comparison shows that the coherent contribution to the fluorescence reduction (EIT/CPT mechanism) is only part of the overall fluorescence reduction.

## 8.6 Cross-correlation measurements

Time-resolved correlation measurements ( $g^{(2)}$ -measurements) are used to determine the relaxation time  $\tau_p = 1/\gamma_p$ , as explained in detail in Chapter 7. The corresponding setups are shown in Fig. 8.5(a-c). An auto-correlation of the resonance fluorescence from the fundamental transition and a cross-correlation between emission from the fundamental transition and radiative Auger emission are shown in Fig. 8.5(d). As shown in Fig. 8.5(e), the theoretical model fits well with the data. In these measurements, only a single laser at  $\omega_1$  is used. The system is described by Eqs. 8.1 and 8.2, with the parameter  $\Omega_2$  set to zero. We use the Python quantum toolbox

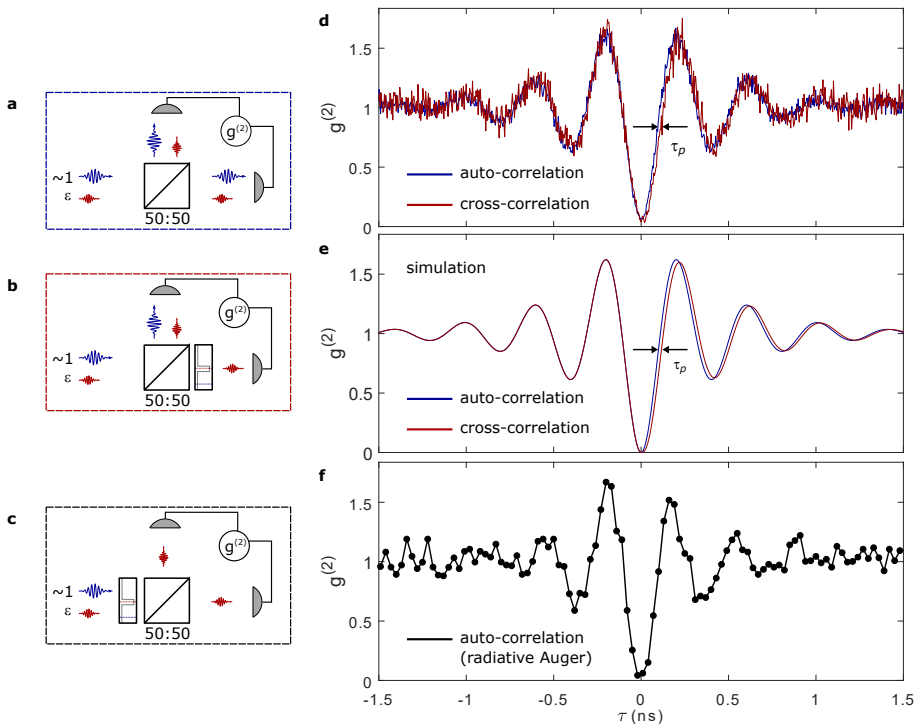


**Figure 8.5: Time-resolved correlation measurements.** (a) Schematic measurement setup for the auto-correlation of resonance fluorescence from the fundamental transition. (b) Schematic setup for the cross-correlation between resonance fluorescence and radiative Auger emission. (c) Schematic setup for the auto-correlation of the radiative Auger emission. (d) Comparison between the auto-correlation of the resonance fluorescence (blue) and the cross-correlation between resonance fluorescence and radiative Auger emission (red, data from QD1). Both correlation-measurements ( $g^{(2)}$ ) are performed with a single laser on the fundamental transition and show Rabi oscillations due to the strong driving ( $\Omega_1$ ). The cross-correlation has a small offset given by the  $|p\rangle$ -to- $|s\rangle$  relaxation time ( $\tau_p = 1/\gamma_p = 17$  ps). This offset measures the finite time for which the Auger electron remains in the excited state after a radiative Auger process has occurred [253]. The origin of the relaxation  $\gamma_p$  is probably a phonon-assisted decay [258] but further investigations are needed. (e) Simulation of the measurements shown in (d). (f) Auto-correlation of the radiative Auger emission. Since the radiative Auger emission is relatively weak (count rates: 630 Hz on the first, 530 Hz on the second detector), a long integration time ( $\sim 50$  h) is needed to resolve the Rabi oscillations in this measurement. The excitation power and Rabi frequency are slightly different with respect to the auto- and cross-correlation shown in (d).

Qutip [116, 117] to compute the steady-state density matrix. With the resulting density matrix, we then compute the auto- and the cross-correlation. The auto-correlation is:

$$g^{(2)}(\tau) = \frac{\langle \hat{a}^\dagger(t) \hat{a}^\dagger(t + \tau) \hat{a}(t + \tau) \hat{a}(t) \rangle}{\langle \hat{a}^\dagger(t) \hat{a}(t) \rangle^2}, \quad (8.3)$$

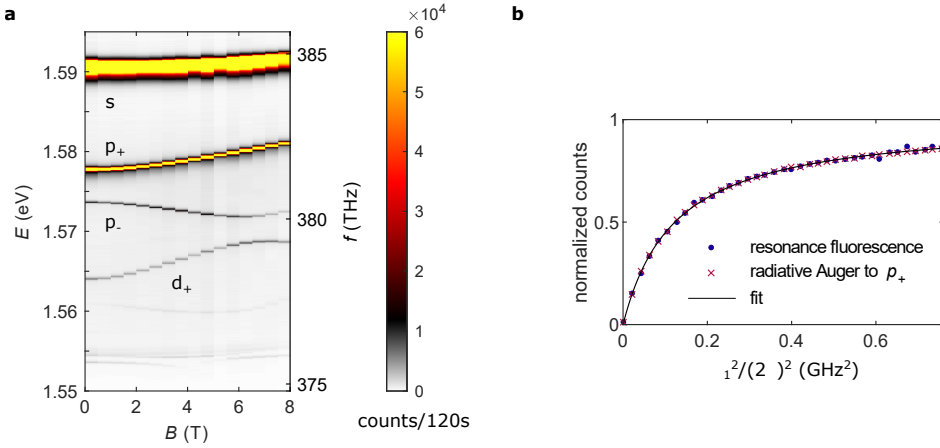


**Figure 8.6: Magnetic field dependence of the different emission lines.** (a) Resonance fluorescence from the fundamental transition and radiative Auger emission as a function of the magnetic field  $B$  (data from QD1). The strong magnetic field dispersion of the radiative Auger lines enables direct identification of the final electron states of the Auger electron. (b) Normalised fluorescence intensity of the different emission lines as a function of Rabi frequency  $\Omega_1$ .  $\omega_2$  is turned off for this measurement ( $\Omega_2 = 0$ ). The power dependence of the radiative Auger intensity coincides with that of the resonance fluorescence from the fundamental transition and matches the power curve of a two-level system. From a fit to the power curve we determine  $\Omega_1$  in our measurements. For fitting, the radiative decay is fixed to a value that we determine from an independent lifetime measurement ( $\Gamma_R = 2\pi \times 0.50$  GHz) [66].

and the cross-correlation is:

$$g^{(2)}(\tau) = \frac{\langle \hat{a}_A^\dagger(t) \hat{a}^\dagger(t+\tau) \hat{a}(t+\tau) \hat{a}_A(t) \rangle}{\langle \hat{a}^\dagger(t) \hat{a}(t) \rangle \langle \hat{a}_A^\dagger(t) \hat{a}_A(t) \rangle}. \quad (8.4)$$

In both cases,  $t \rightarrow \infty$  for the steady-state solution and  $\tau$  is the time delay between two subsequently detected photons.  $\hat{a}^\dagger$  describes the creation of a photon via decay into the  $s$ -shell (fundamental transition), and  $\hat{a}_A^\dagger$  describes the creation of a photon via radiative Auger decay into the excited electron state,  $|p\rangle$ .

## 8.7 Magnetic field dispersion

The magnetic field dispersion of the radiative Auger emission is significantly stronger than that of the emission from the fundamental transition (see Fig. 8.6). The reason is the different final state after the optical decay: the electron ground state  $|s\rangle$  ( $s$ -shell) has a weak magnetic field dispersion and, in contrast, higher shells such as the excited state  $|p\rangle$  ( $p$ -shell) have a much stronger dependence on the magnetic field. Since the optical emission energy is given by the energy of the trion minus the energy of the final state, the strong magnetic field dispersion is transferred to the radiative Auger lines. The strong dispersion of the radiative Auger emission is an important feature allowing



it to be distinguished unambiguously from phonon replicas. For a two-dimensional harmonic confinement potential, the magnetic field dispersions of the different shells form the Fock-Darwin spectrum [225]. The dispersion of the radiative Auger emission is, therefore, typically close to an inverted Fock-Darwin spectrum [253]. A detailed discussion of the magnetic field dispersion (including the model) can be found in Chapter 7.

## 8.8 Conclusion and future directions

Upon the optical transition of a carrier, radiative Auger leaves other carriers in an excited orbital state, and the emitted photon is red-shifted. We show here that this process can be inverted: radiative Auger exists in absorption and the corresponding transition can be optically driven. In both emission and absorption, the process has conceptual similarities to phonon scattering. For radiative Auger emission, the electronic configuration is left in an excited state, for the phonon sideband, the lattice configuration [224, 263]. We demonstrate that the resonance fluorescence can be strongly reduced by addressing the radiative Auger transition: a modulated laser on the radiative Auger transition could be used for fast optical gating of the emitter's absorption. As an outlook, we suggest that an effective coupling between orbital states, split by frequencies in the THz band, can be created by two lasers at optical frequencies. The idea here is to establish a Raman-like process: the lasers are equally detuned from their resonances and an exciton is not created. This scheme facilitates control of the orbital degree of freedom with techniques that have been developed for manipulating spin-states [16, 264]. Further quantum optics experiments with radiative Auger photons are conceivable: by using a two-colour Raman-scheme [265], it might be possible to create deterministically highly excited shake-up states that are also subject of recent theoretical [266] and experimental [23] investigations. Adding a third laser with a THz-frequency at the transition  $|s\rangle-|p\rangle$  [258] might even allow close-contour driving schemes [267]. In analogy to experiments on spins [268], the radiative Auger process could lead to an entanglement between the frequency of the emitted photon and the orbital state of the Auger electron.

## 8.9 Supplementary note I: Methods

For all our measurements, the quantum dot sample is kept in a liquid helium bath cryostat at 4.2 K. The quantum dots used in this work are GaAs quantum dots in AlGaAs grown by molecular beam epitaxy. Their decay rates  $\Gamma_R$  (typically in the range  $2\pi \times (0.5 - 0.6)$  GHz) were determined by lifetime measurements using pulsed resonant excitation [66]. The decay rate of the radiative Auger transition,  $\Gamma_A \sim \Gamma_R/100$ , is estimated by comparing its emission intensity to the fundamental transition. QD1 is identical to the second quantum dot in Ref. [66]. The quantum dots presented in this work have a strong radiative Auger emission compared to other III-V quantum dots [253] indicating a stronger dipole-moment of the radiative Auger transition. We use radiative Auger lines where the final state of the Auger electron,  $|p\rangle$ , is a quantum dot  $p$ -shell. In particular, we investigate the transition associated with the lower  $p$ -shell ( $p_+$ ) for QD1 and the higher  $p$ -shell ( $p_-$ ) for QD2. We can assign further emission lines to the corresponding higher electronic shells by measuring the magnetic field dispersion of the emission spectrum [253] (see Fig. 8.6(a)).

To excite the quantum dots, we use a tunable diode laser with a narrow bandwidth ( $\sim 100$  kHz) far below the quantum dot linewidth. Resonant excitation is not necessary to observe the radiative Auger emission: above-band excitation is also sufficient [251, 254]. It is also possible to observe radiative Auger on systems that suffer from much more charge noise than ours [254]. However, resonant excitation has the advantage that no continuum states are excited making it easier to identify all emission lines. Furthermore, low charge noise makes resonant excitation a lot easier to perform. For this work, resonant excitation is crucial to optically address a single radiative Auger transition. To suppress the reflected excitation laser, we use a cross-polarisation scheme [112].

To determine the relaxation rate  $\gamma_p$  ( $\sim 2\pi \times 9.3$  GHz) from  $|p\rangle$  to  $|s\rangle$ , we make use of a technique developed in Ref. [253]: on driving  $|s\rangle\text{--}|t\rangle$  ( $\Omega_2 = 0$ ), we measure an auto-correlation of the resonance fluorescence from the fundamental transition and compare it to the cross-correlation between resonance fluorescence from the fundamental transition and radiative Auger emission. The corresponding measurement setups are shown in Fig. 8.5(a,b). To resolve the auto- and cross-correlations with high time resolution, we use two superconducting nanowire single-photon detectors (SingleQuantum) with a timing jitter below 20 ps (FWHM) in combination with correlation hardware (Swabian Instruments).

Compared to the auto-correlation, the cross-correlation has a small time offset when a radiative Auger photon is followed by a photon from the fundamental transition (see Fig. 8.5(d,e)). This time scale corresponds to the relaxation time,  $\tau_p = 1/\gamma_p$ , describing the relaxation from  $|p\rangle$  to  $|s\rangle$ . The relaxation time appears in the cross-correlation: when a radiative Auger event is detected by the first detector, there is an additional waiting time of  $\tau_p$  before the excited Auger electron relaxes to the ground state and the system can be optically re-excited. Therefore, it takes longer before a second photon is detected. The additional waiting time is only present for the cross-correlation. For the auto-correlation, the system decays directly to the ground state  $|s\rangle$  and there is no additional waiting time.

Finally, we also measure the auto-correlation of the radiative Auger emission (see Fig. 8.5(c) for the setup). The measurement is shown in Fig. 8.5(e). We observe

a pronounced anti-bunching at zero delay proving the single-photon nature of the radiative Auger photons. Going beyond the results in Ref. [253], we observe the Rabi oscillation from strongly driving the transition  $|s\rangle-|t\rangle$  in the photon-statistics of the radiative Auger photons from the transition  $|p\rangle-|t\rangle$ .

## 8.10 Supplementary note II: Additional Autler-Townes splitting

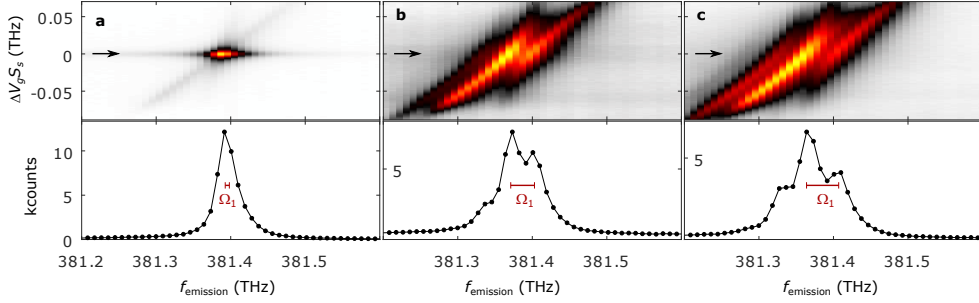


**Figure 8.7: Radiative Auger emission upon excitation of the fundamental transition.** (a) Radiative Auger emission from QD1 (see also Fig. 8.2(b)). The emission frequency (x-axis) is plotted as a function of detuning between laser and the  $|s\rangle - |t\rangle$  transition (y-axis). In the measurements shown here, the Autler-Townes splitting is not resolved since the Rabi frequency is too small ( $\Omega_1 = 2\pi \times 5.5$  GHz). (b, c) The same measurements as before performed at higher Rabi frequencies ( $\Omega_1 = 2\pi \times 31.9$  GHz,  $\Omega_1 = 2\pi \times 43.2$  GHz) where the Autler-Townes splittings are resolved.

In Fig. 8.7 we show additional measurements of the Autler-Townes splitting on QD1. The measurements are performed for different Rabi frequencies  $\Omega_1$  and the detuning  $\Delta_1$  between laser and fundamental transition is varied. The quantum dot transitions are detuned from the fixed laser by applying a gate voltage,  $V_g$ . The detuning from the fundamental transition is  $\Delta V \cdot S_s$ , where  $S_s$  is the Stark-shift of the fundamental transition and  $\Delta V_g$  the difference in gate voltage. The Rabi frequencies at zero laser detuning are independently determined from a power saturation curve (red bars in Fig. 8.7). They match the measured Autler-Townes splittings in the emission spectra. Furthermore, on detuning the quantum dot resonance from the laser ( $\Delta V_g \neq 0$ ), there is a small probability to excite the trion via the phonon sideband giving rise to a weak “diagonal” emission line. In the case of a red-detuned quantum dot ( $\Delta V_g < 0$ ), the laser has more energy than the quantum dot transition and the additional energy can be transferred to LA-phonons. In the case of a blue-detuned quantum dot, the laser energy is too small and the missing energy can be provided by phonon absorption.



## CHAPTER 9

---

### Summary

---

The four optomechanical chapters (Chapter 3-6) showed an in-depth characterisation of the mechanical-membrane platform. Three different mechanical resonator designs were presented. Starting with a cantilever resonator with up to 20 MHz mechanical frequencies, the exciton-phonon coupling in the unresolved-sideband regime was investigated. The resonator was then detached from the under-etch and suspended freely with four tethers. This minor change to the mechanical design enabled frequencies of up to 600 MHz. This is higher than the decay rate of the quantum dot, yet still smaller than the inhomogeneously-broadened linewidth. The final mechanical design presented was a phononic-crystal resonator with a highly confined mode at 1.5 GHz. This is not only ten times higher than the decay rate of the quantum dot but also more than double its linewidth. More importantly, the mechanical quality factor stays at a high level of  $\sim 2000$ , even though there are a lot of potential mechanical loss channels. Therefore, we claim to have developed a high-quality mechanical resonator with frequencies in the sideband-resolved regime [64, 65].

The coupling to the mechanical resonators is measured using the emission of single quantum dots. A hallmark of this thesis presents the Brownian motion measurement [20]. This is achieved for all three mechanical resonators. However, we also showed that these measurements can get very difficult for small mechanical resonators due to unstable laser suppression. Using the electric-field antenna the mechanical resonators are mechanically driven which is used for a series of optical and mechanical characterisation measurements. This includes the observation of acoustic sidebands in the emission spectrum of the quantum dot.

The interesting part, compared to other optomechanical systems, is the non-linear response of the quantum dot to the optical field. If a red or blue shifted photon is detected in the emission (at  $\pm\Omega_m$ ) it directly means that simultaneously a single phonon was emitted or absorbed by the dot. To prove this point we confirmed the single-photon emission of the quantum dots for all mechanical resonators, even under strong mechanical driving. A further interesting aspect of quantum dots is that many of them can be coupled to the same mechanical mode. Furthermore, the quantum dot emission frequency can be tuned over many linewidths which is not straightforward with other optical systems, for example, optical cavities. This is advantageous for experiments involving more than one optomechanical system, such as optomechanical teleportation [70] or entanglement [157].

We stress that it is important to further increase the exciton-phonon coupling rate (at least five- to ten-fold) while keeping the mechanical frequency roughly the same. Then, effects due to optomechanical cooling could become visible. However, this is not trivial. The current mechanical mode of the phononic-crystal beam shows small areas (around the first air holes) of enhanced strain, up to three-fold compared to the centre of the resonator. This means that the limit of the deformation potential is not yet reached and with careful design optimisation, the exciton-phonon coupling can be increased further. If, however, enough coupling can be reached to observe optomechanical cooling remains an open question.

Another improvement in this direction could be to reduce the inhomogeneous broadening by optimising the heterostructure design. This would highly increase the sensitivity to the mechanical interaction. Finally, the membrane platform is highly suitable for on-chip applications and could be combined with photonic-crystal cavities [71] and waveguides [72–75, 199].

With the two radiative Auger chapters of this thesis (Chapter 3-6) the radiative Auger process was studied in detail. The measurements present the first observation of radiative Auger on a single quantum emitter. We showed that the radiative Auger process is present for different species of quantum dots. Furthermore, the strength of the radiative Auger emission varied from dot to dot. This gives an insight into the quantum dot composition and geometry [81]. Moreover, we showed that radiative Auger can be used to study single-carrier dynamics inside the dot, which was so far inaccessible [21]. It is not only possible to measure the emission of such processes but also to optically drive the radiative Auger transition. By doing so, a dark state was generated: a coherent superposition of the Auger electron being in the s- and p-shell [22]. This opens up the path to coherent control of the orbital degree of freedom of the Auger carrier [23].

Overall, this thesis showed two examples of how the quantum dot can be used to study coupled systems. The optomechanical and the radiative Auger parts both showed that a large coupling rate is needed to control the state of the coupled system. If the coupling rate is high enough, both of the systems can be studied in a similar way, namely, in a  $\Lambda$ -type configuration. Whereas this was already possible for the radiative Auger experiments, it is not yet the case for the optomechanical system. Nevertheless, it shows that the quantum dot is a versatile tool and that with some clever tricks, a weak spot (unwanted interaction) can be turned into a strength (controlled coupled system).





---

## Bibliography

---

- [1] A. Muller, E. B. Flagg, P. Bianucci, X. Y. Wang, D. G. Deppe, W. Ma, J. Zhang, G. J. Salamo, M. Xiao, and C. K. Shih, *Resonance fluorescence from a coherently driven semiconductor quantum dot in a cavity*, *Phys. Rev. Lett.* **99**, 187402 (2007). [Cited on page: 2, 14, 144]
- [2] X. Xu, B. Sun, P. R. Berman, D. G. Steel, A. S. Bracker, D. Gammon, and L. J. Sham, *Coherent optical spectroscopy of a strongly driven quantum dot*, *Science* **317**, 929 (2007). [Cited on page: 2, 146]
- [3] S. Ates, S. M. Ulrich, S. Reitzenstein, A. Löffler, A. Forchel, and P. Michler, *Post-Selected Indistinguishable Photons from the Resonance Fluorescence of a Single Quantum Dot in a Microcavity*, *Phys. Rev. Lett.* **103**, 167402 (2009). [Cited on page: 2]
- [4] A. Ulhaq, S. Weiler, S. M. Ulrich, R. Roßbach, M. Jetter, and P. Michler, *Cascaded single-photon emission from the Mollow triplet sidebands of a quantum dot*, *Nat. Photon.* **6**, 238 (2012). [Cited on page: 2, 82, 146]
- [5] E. B. Flagg, A. Muller, J. Robertson, S. Founta, D. Deppe, M. Xiao, W. Ma, G. Salamo, and C.-K. Shih, *Resonantly driven coherent oscillations in a solid-state quantum emitter*, *Nat. Phys.* **5**, 203 (2009). [Cited on page: 2, 82, 118, 141, 144, 146]
- [6] C. Matthiesen, A. N. Vamivakas, and M. Atatüre, *Subnatural Linewidth Single Photons from a Quantum Dot*, *Phys. Rev. Lett.* **108**, 093602 (2012). [Cited on page: 2]
- [7] H. S. Nguyen, G. Sallen, C. Voisin, P. Roussignol, C. Diederichs, and G. Cassaboïs, *Ultra-coherent single photon source*, *Appl. Phys. Lett.* **99**, 261904 (2011). [Cited on page: 2]
- [8] L. Zhai, G. N. Nguyen, C. Spinnler, J. Ritzmann, M. C. Löbl, A. D. Wieck, A. Ludwig, A. Javadi, and R. J. Warburton, *Quantum interference of identical photons from remote GaAs quantum dots*, *Nat. Nanotechnol.* **17**, 829 (2022). [Cited on page: 2, 8, 22, 52]
- [9] R. Uppu, L. Midolo, X. Zhou, J. Carolan, and P. Lodahl, *Quantum-dot-based deterministic photon-emitter interfaces for scalable photonic quantum technology*, *Nat. Nanotechnol.* **16**, 1308 (2021). [Cited on page: 2, 8, 116]
- [10] S. Shutts, C. P. Allford, C. Spinnler, Z. Li, A. Sobiesierski, M. Tang, H. Liu, and P. M. Snowton, *Degradation of  $iii-v$  quantum dot lasers grown directly on silicon substrates*, *IEEE J. Sel. Top. Quantum. Electron.* **25**, 1 (2019). [Cited on page: 2]
- [11] P. Senellart, G. Solomon, and A. White, *High-performance semiconductor quantum-dot single-photon sources*, *Nat. Nanotechnol.* **12**, 1026 (2017). [Cited on page: 2, 8]
- [12] D. Najer, I. Söllner, P. Sekatski, V. Dolique, M. C. Löbl, D. Riedel, R. Schott, S. Starosielec, S. R. Valentin, A. D. Wieck, N. Sangouard, A. Ludwig, and R. J. Warburton, *A gated quantum dot strongly coupled to an optical microcavity*, *Nature* **575**, 622 (2019). [Cited on page: 2]
- [13] R. Uppu, F. T. Pedersen, Y. Wang, C. T. Olesen, C. Papon, X. Zhou, L. Midolo, S. Scholz, A. D. Wieck, A. Ludwig, and P. Lodahl, *Scalable integrated single-photon source*, *Sci. Adv.* **6**, eabc8268 (2020). [Cited on page: 2, 9, 23, 116]

- [14] S. Kotal, A. Artioli, Y. Wang, A. D. Osterkryger, M. Finazzo, R. Fons, Y. Genuist, J. Bleuse, J.-M. Gérard, N. Gregersen, and J. Claudon, *A nanowire optical nanocavity for broadband enhancement of spontaneous emission*, *Applied Physics Letters* **118** (2021). [Cited on page: 2, 8]
- [15] M. Munsch, G. Wüst, A. V. Kuhlmann, F. Xue, A. Ludwig, D. Reuter, A. D. Wieck, M. Poggio, and R. J. Warburton, *Manipulation of the nuclear spin ensemble in a quantum dot with chirped magnetic resonance pulses*, *Nat. Nanotechnol.* **9**, 671 (2014). [Cited on page: 2]
- [16] J. H. Prechtel, A. V. Kuhlmann, J. Houel, A. Ludwig, S. R. Valentin, A. D. Wieck, and R. J. Warburton, *Decoupling a hole spin qubit from the nuclear spins*, *Nat. Mater.* **15**, 981 (2016). [Cited on page: 2, 148, 150, 154]
- [17] G. Wüst, M. Munsch, F. Maier, A. V. Kuhlmann, A. Ludwig, A. D. Wieck, D. Loss, M. Poggio, and R. J. Warburton, *Role of the electron spin in determining the coherence of the nuclear spins in a quantum dot*, *Nat. Nanotechnol.* **11**, 885 (2016). [Cited on page: 2]
- [18] D. M. Jackson, U. Haeusler, L. Zaporski, J. H. Bodey, N. Shofer, E. Clarke, M. Hugues, M. Atatüre, C. Le Gall, and D. A. Gangloff, *Optimal Purification of a Spin Ensemble by Quantum-Algorithmic Feedback*, *Phys. Rev. X* **12**, 031014 (2022). [Cited on page: 2]
- [19] E. V. Denning, J. Iles-Smith, N. Gregersen, and J. Mork, *Phonon effects in quantum dot single-photon sources*, *Opt. Mater. Express* **10**, 222 (2020). [Cited on page: 2, 15]
- [20] M. Munsch, A. V. Kuhlmann, D. Cadeddu, J.-M. Gérard, J. Claudon, M. Poggio, and R. J. Warburton, *Resonant driving of a single photon emitter embedded in a mechanical oscillator*, *Nat. Commun.* **8**, 76 (2017). [Cited on page: 2, 8, 17, 22, 24, 25, 26, 34, 36, 38, 42, 48, 55, 160]
- [21] M. C. Löbl, C. Spinnler, A. Javadi, L. Zhai, G. N. Nguyen, J. Ritzmann, L. Midolo, P. Lodahl, A. D. Wieck, A. Ludwig, and R. J. Warburton, *Radiative Auger process in the single-photon limit*, *Nat. Nanotechnol.* **15**, 558 (2020). [Cited on page: 2, 3, 15, 51, 161]
- [22] C. Spinnler, L. Zhai, G. N. Nguyen, J. Ritzmann, A. D. Wieck, A. Ludwig, A. Javadi, D. E. Reiter, P. Machnikowski, R. J. Warburton, and M. C. Löbl, *Optically driving the radiative Auger transition*, *Nat. Commun.* **12**, 6575 (2021). [Cited on page: 2, 3, 22, 51, 161]
- [23] J.-Y. Yan, C. Chen, X.-D. Zhang, Y.-T. Wang, H.-G. Babin, A. D. Wieck, A. Ludwig, Y. Meng, X. Hu, H. Duan, W. Chen, W. Fang, M. Cygorek, X. Lin, D.-W. Wang, C.-Y. Jin, and F. Liu, *Coherent control of a high-orbital hole in a semiconductor quantum dot with near-unity fidelity*, [arXiv:2212.10749](https://arxiv.org/abs/2212.10749) (2023). [Cited on page: 2, 3, 5, 154, 161]
- [24] I. Wilson-Rae, P. Zoller, and A. Imamoglu, *Laser cooling of a nanomechanical resonator mode to its quantum ground state*, *Phys. Rev. Lett.* **92**, 075507 (2004). [Cited on page: 2, 3, 72, 104, 116]
- [25] O. Arcizet, P.-F. Cohadon, T. Briant, M. Pinard, and A. Heidmann, *Radiation-pressure cooling and optomechanical instability of a micromirror*, *Nature* **444**, 71 (2006). [Cited on page: 2]
- [26] J. D. Thompson, B. M. Zwickl, A. M. Jayich, F. Marquardt, S. M. Girvin, and J. G. E. Harris, *Strong dispersive coupling of a high-finesse cavity to a micromechanical membrane*, *Nature* **452**, 72 (2008). [Cited on page: 2]
- [27] J. Chan, T. P. M. Alegre, A. H. Safavi-Naeini, J. T. Hill, A. Krause, S. Gröblacher, M. Aspelmeyer, and O. Painter, *Laser cooling of a nanomechanical oscillator into its quantum ground state*, *Nature* **478**, 89 (2011). [Cited on page: 2, 22, 49, 104]
- [28] E. Verhagen, S. Deléglise, S. Weis, A. Schliesser, and T. J. Kippenberg, *Quantum-coherent coupling of a mechanical oscillator to an optical cavity mode*, *Nature* **482**, 63 (2012). [Cited on page: 2]
- [29] M. Aspelmeyer, T. J. Kippenberg, and F. Marquardt, *Cavity optomechanics*, *Rev. Mod. Phys.* **86**, 1391 (2014). [Cited on page: 2, 15, 16, 17, 41, 48, 49, 52, 53]
- [30] T. P. Purdy, R. W. Peterson, and C. A. Regal, *Observation of Radiation Pressure Shot Noise on a Macroscopic Object*, *Science* (2013). [Cited on page: 2]
- [31] J. D. Teufel, T. Donner, D. Li, J. W. Harlow, M. S. Allman, K. Cicak, A. J. Sirois, J. D. Whittaker, K. W. Lehnert, and R. W. Simmonds, *Sideband cooling of micromechanical motion to the quantum ground state*, *Nature* **475**, 359 (2011). [Cited on page: 2]
- [32] J.-M. Pirkkalainen, E. Damskägg, M. Brandt, F. Massel, and M. A. Sillanpää, *Squeezing of Quantum Noise of Motion in a Micromechanical Resonator*, *Phys. Rev. Lett.* **115**, 243601 (2015). [Cited on page: 2]

- [33] E. E. Wollman, C. U. Lei, A. J. Weinstein, J. Suh, A. Kronwald, F. Marquardt, A. A. Clerk, and K. C. Schwab, *Quantum squeezing of motion in a mechanical resonator*, **Science** **349**, 952 (2015). [Cited on page: 2]
- [34] S. Barzanjeh, E. S. Redchenko, M. Peruzzo, M. Wulf, D. P. Lewis, G. Arnold, and J. M. Fink, *Stationary entangled radiation from micromechanical motion*, **Nature** **570**, 480 (2019). [Cited on page: 2]
- [35] Y. Chu, P. Kharel, W. H. Renninger, L. D. Burkhardt, L. Frunzio, P. T. Rakich, and R. J. Schoelkopf, *Quantum acoustics with superconducting qubits*, **Science** **358**, 199 (2017). [Cited on page: 2]
- [36] Y. Chu, P. Kharel, T. Yoon, L. Frunzio, P. T. Rakich, and R. J. Schoelkopf, *Creation and control of multi-phonon Fock states in a bulk acoustic-wave resonator*, **Nature** **563**, 666 (2018). [Cited on page: 2, 22]
- [37] A. A. Clerk, K. W. Lehnert, P. Bertet, J. R. Petta, and Y. Nakamura, *Hybrid quantum systems with circuit quantum electrodynamics*, **Nat. Phys.** **16**, 257 (2020). [Cited on page: 2]
- [38] K. W. Murch, K. L. Moore, S. Gupta, and D. M. Stamper-Kurn, *Observation of quantum-measurement backaction with an ultracold atomic gas*, **Nat. Phys.** **4**, 561 (2008). [Cited on page: 2]
- [39] F. Brennecke, S. Ritter, T. Donner, and T. Esslinger, *Cavity Optomechanics with a Bose-Einstein Condensate*, **Science** **322**, 235 (2008). [Cited on page: 2]
- [40] M. H. Schleier-Smith, I. D. Leroux, H. Zhang, M. A. Van Camp, and V. Vuletić, *Optomechanical Cavity Cooling of an Atomic Ensemble*, **Phys. Rev. Lett.** **107**, 143005 (2011). [Cited on page: 2]
- [41] D. A. Golter, T. Oo, M. Amezcua, K. A. Stewart, and H. Wang, *Optomechanical Quantum Control of a Nitrogen-Vacancy Center in Diamond*, **Phys. Rev. Lett.** **116**, 143602 (2016). [Cited on page: 2, 8]
- [42] K. W. Lee, D. Lee, P. Ovarthaiyapong, J. Minguzzi, J. R. Maze, and A. C. Bleszynski Jayich, *Strain coupling of a mechanical resonator to a single quantum emitter in diamond*, **Phys. Rev. Appl.** p. 034005 (2016). [Cited on page: 2, 8]
- [43] R. Ohta, L. Herpin, V. M. Bastidas, T. Tawara, H. Yamaguchi, and H. Okamoto, *Rare-Earth-Mediated Optomechanical System in the Reversed Dissipation Regime*, **Phys. Rev. Lett.** **126**, 047404 (2021). [Cited on page: 2, 8]
- [44] S. Lazić, A. Espinha, S. Pinilla Yanguas, C. Gibaja, F. Zamora, P. Ares, M. Chhowalla, W. S. Paz, J. J. P. Burgos, A. Hernández-Mínguez, P. V. Santos, and H. P. van der Meulen, *Dynamically tuned non-classical light emission from atomic defects in hexagonal boron nitride*, **Commun. Phys.** **2**, 1 (2019). [Cited on page: 2, 8]
- [45] S. D. Patel, K. Parto, M. Choquer, S. Umezawa, L. Hellman, D. Polishchuk, and G. Moody, *Surface acoustic wave cavity optomechanics with WSe<sub>2</sub> single photon emitters*, **arXiv:2211.15811** (2022). [Cited on page: 2, 8]
- [46] D. Jaeger, F. Fogliano, T. Ruelle, A. Lafranca, F. Braakman, and M. Poggio, *Mechanical Mode Imaging of a High-Q Hybrid hBN/Si<sub>3</sub>N<sub>4</sub> Resonator*, **Nano Lett.** **23**, 2016 (2023). [Cited on page: 2, 8]
- [47] S. G. Carter, A. S. Bracker, G. W. Bryant, M. Kim, C. S. Kim, M. K. Zalalutdinov, M. K. Yakes, C. Czarnocki, J. Casara, M. Scheibner, and D. Gammon, *Spin-mechanical coupling of an inas quantum dot embedded in a mechanical resonator*, **Phys. Rev. Lett.** **121**, 246801 (2018). [Cited on page: 2, 8, 22, 31]
- [48] S. G. Carter, A. S. Bracker, M. K. Yakes, M. K. Zalalutdinov, M. Kim, C. S. Kim, B. Lee, and D. Gammon, *Tunable coupling of a double quantum dot spin system to a mechanical resonator*, **Nano Lett.** **19**, 6166 (2019). [Cited on page: 2, 22]
- [49] X. Yuan, M. Schwendtner, R. Trotta, Y. Huo, J. Martín-Sánchez, G. Piredda, H. Huang, J. Edlinger, C. Diskus, O. G. Schmidt, B. Jakoby, H. J. Krenner, and A. Rastelli, *A frequency-tunable nanomembrane mechanical oscillator with embedded quantum dots*, **Appl. Phys. Lett.** **115** (2019). [Cited on page: 2, 22]
- [50] A. Vogeles, M. M. Sonner, B. Mayer, X. Yuan, M. Weiß, E. D. S. Nysten, S. F. Covre da Silva, A. Rastelli, and H. J. Krenner, *Quantum dot optomechanics in suspended nanophononic strings*, **Adv. Quantum Technol.** **3**, 1900102 (2020). [Cited on page: 2, 8, 22]

- [51] M. Montinaro, G. Wüst, M. Munsch, Y. Fontana, E. Russo-Averchi, M. Heiss, A. Fontcuberta i Morral, R. J. Warburton, and M. Poggio, *Quantum dot opto-mechanics in a fully self-assembled nanowire*, **Nano Lett.** **14**, 4454 (2014). [Cited on page: 2, 8, 22]
- [52] I. Yeo, P.-L. de Assis, A. Gloppe, E. Dupont-Ferrier, P. Verlot, N. S. Malik, E. Dupuy, J. Claudon, J.-M. Gérard, A. Auffèves, G. Nogues, S. Seidelin, J.-P. Poizat, O. Arcizet, and M. Richard, *Strain-mediated coupling in a quantum dot-mechanical oscillator hybrid system*, **Nat. Nanotechnol.** **9**, 106 (2014). [Cited on page: 2, 22]
- [53] I. Yeo, H. J. Kim, J. D. Song, and K. S. Yi, *Hybrid quantum optomechanics with a quantum-dot single photon source*, **Phys. Rev. B** **94**, 165422 (2016). [Cited on page: 2, 22]
- [54] P.-L. de Assis, I. Yeo, A. Gloppe, H. A. Nguyen, D. Tumanov, E. Dupont-Ferrier, N. S. Malik, E. Dupuy, J. Claudon, J.-M. Gérard, A. Auffèves, O. Arcizet, M. Richard, and J.-P. Poizat, *Strain-gradient position mapping of semiconductor quantum dots*, **Phys. Rev. Lett.** **118**, 117401 (2017). [Cited on page: 2, 8, 22, 62]
- [55] J. Kettler, N. Vaish, L. M. de Lépinay, B. Besga, P.-L. de Assis, O. Bourgeois, A. Auffèves, M. Richard, J. Claudon, J.-M. Gérard, B. Pigeau, O. Arcizet, P. Verlot, and J.-P. Poizat, *Inducing micromechanical motion by optical excitation of a single quantum dot*, **Nat. Nanotechnol.** **16**, 283 (2021). [Cited on page: 2, 3, 17, 22, 48, 60]
- [56] M. Finazzo, R. Tanos, Y. Curé, A. Artioli, S. Kotal, J. Bleuse, Y. Genuist, J.-M. Gérard, F. Donatini, and J. Claudon, *On-Chip Electrostatic Actuation of a Photonic Wire Antenna Embedding Quantum Dots*, **Nano Lett.** **23**, 2203 (2023). [Cited on page: 2, 8, 22, 89, 116]
- [57] S. G. Carter, A. S. Bracker, M. K. Yakes, M. K. Zalalutdinov, M. Kim, C. S. Kim, C. Czarnocki, M. Scheibner, and D. Gammon, *Sensing flexural motion of a photonic crystal membrane with InGaAs quantum dots*, **Appl. Phys. Lett.** **111** (2017). [Cited on page: 2, 22]
- [58] J. R. Gell, M. B. Ward, R. J. Young, R. M. Stevenson, P. Atkinson, D. Anderson, G. a. C. Jones, D. A. Ritchie, and A. J. Shields, *Modulation of single quantum dot energy levels by a surface-acoustic-wave*, **Appl. Phys. Lett.** **93**, 081115 (2008). [Cited on page: 2, 22]
- [59] M. Metcalfe, S. M. Carr, A. Muller, G. S. Solomon, and J. Lawall, *Resolved sideband emission of InAs/GaAs quantum dots strained by surface acoustic waves*, **Phys. Rev. Lett.** **105**, 037401 (2010). [Cited on page: 2, 22]
- [60] B. Villa, A. J. Bennett, D. J. P. Ellis, J. P. Lee, J. Skiba-Szymanska, T. A. Mitchell, J. P. Griffiths, I. Farrer, D. A. Ritchie, C. J. B. Ford, and A. J. Shields, *Surface acoustic wave modulation of a coherently driven quantum dot in a pillar microcavity*, **Appl. Phys. Lett.** **111**, 011103 (2017). [Cited on page: 2, 22]
- [61] D. Wigger, M. Weiß, M. Lienhart, K. Müller, J. J. Finley, T. Kuhn, H. J. Krenner, and P. Machnikowski, *Resonance-fluorescence spectral dynamics of an acoustically modulated quantum dot*, **Phys. Rev. Res.** **3**, 033197 (2021). [Cited on page: 2, 22, 67, 84]
- [62] M. Weiß, D. Wigger, D. Wigger, D. Wigger, M. Nägele, K. Müller, J. J. Finley, T. Kuhn, P. Machnikowski, and H. J. Krenner, *Optomechanical wave mixing by a single quantum dot*, **Optica** **8**, 291 (2021). [Cited on page: 2, 22, 24, 67, 84, 86]
- [63] D. D. Bühler, M. Weiß, A. Crespo-Poveda, E. D. S. Nysten, J. J. Finley, K. Müller, P. V. Santos, M. M. de Lima, and H. J. Krenner, *On-chip generation and dynamic piezo-optomechanical rotation of single photons*, **Nat. Commun.** **13**, 1 (2022). [Cited on page: 2, 22]
- [64] R. A. DeCrescent, Z. Wang, P. Imany, R. C. Boutelle, C. A. McDonald, T. Autry, J. D. Teufel, S. W. Nam, R. P. Mirin, and K. L. Silverman, *Large Single-Phonon Optomechanical Coupling Between Quantum Dots and Tightly Confined Surface Acoustic Waves in the Quantum Regime*, **Phys. Rev. Appl.** **18**, 034067 (2022). [Cited on page: 2, 22, 84, 105, 160]
- [65] P. Imany, P. Imany, P. Imany, Z. Wang, Z. Wang, R. A. DeCrescent, R. C. Boutelle, C. A. McDonald, C. A. McDonald, T. Autry, S. Berweger, P. Kabos, S. W. Nam, R. P. Mirin, K. L. Silverman, and K. L. Silverman, *Quantum phase modulation with acoustic cavities and quantum dots*, **Optica** **9**, 501 (2022). [Cited on page: 2, 22, 84, 105, 160]
- [66] L. Zhai, M. C. Löbl, G. N. Nguyen, J. Ritzmann, A. Javadi, C. Spinnler, A. D. Wieck, A. Ludwig, and R. J. Warburton, *Low-noise GaAs quantum dots for quantum photonics*, **Nat. Commun.** **11**, 4745 (2020). [Cited on page: 2, 8, 9, 48, 74, 116, 144, 153, 155]
- [67] T. Descamps, T. Schetelat, J. Gao, P. J. Poole, D. Dalacu, A. W. Elshaari, and V. Zwiller, *Dynamic strain modulation of a nanowire quantum dot compatible with a thin-film lithium niobate photonic platform*, **arXiv:2306.05798** (2023). [Cited on page: 2]

- [68] P. Stepanov, M. Elzo-Aizarna, J. Bleuse, N. S. Malik, Y. Curé, E. Gautier, V. Favre-Nicolin, J.-M. Gérard, and J. Claudon, *Large and Uniform Optical Emission Shifts in Quantum Dots Strained along Their Growth Axis*, **Nano Letters** **16**, 3215 (2016). [Cited on page: 2, 22]
- [69] D. Tumanov, N. Vaish, H. A. Nguyen, Y. Curé, J.-M. Gérard, J. Claudon, F. Donatini, and J.-P. Poizat, *Static strain tuning of quantum dots embedded in a photonic wire*, **Applied Physics Letters** **112** (2018). [Cited on page: 2, 22]
- [70] N. Fiaschi, B. Hensen, A. Wallucks, R. Benevides, J. Li, T. P. M. Alegre, and S. Gröblacher, *Optomechanical quantum teleportation*, **Nat. Photon.** **15**, 817 (2021). [Cited on page: 2, 38, 160]
- [71] B.-y. Zhou and G.-x. Li, *Ground-state cooling of a nanomechanical resonator via single-polariton optomechanics in a coupled quantum-dot-cavity system*, **Phys. Rev. A** **94**, 033809 (2016). [Cited on page: 2, 116, 160]
- [72] I. Söllner, L. Midolo, and P. Lodahl, *Deterministic single-phonon source triggered by a single photon*, **Phys. Rev. Lett.** **116**, 234301 (2016). [Cited on page: 2, 22, 104, 116, 160]
- [73] A. Zivari, N. Fiaschi, R. Burgwal, E. Verhagen, R. Stockill, and S. Gröblacher, *On-chip distribution of quantum information using traveling phonons*, **Sci. Adv.** **8**, eadd2811 (2022). [Cited on page: 2, 116, 160]
- [74] A. Zivari, R. Stockill, N. Fiaschi, and S. Gröblacher, *Non-classical mechanical states guided in a phononic waveguide*, **Nat. Phys.** **18**, 789 (2022). [Cited on page: 2, 116, 160]
- [75] O. Florez, G. Arregui, M. Albrechtsen, R. C. Ng, J. Gomis-Bresco, S. Stobbe, C. M. Sotomayor-Torres, and P. D. Garcia, *Engineering nanoscale hypersonic phonon transport*, **Nat. Nanotechnol.** **17**, 947 (2022). [Cited on page: 2, 107, 116, 160]
- [76] N. Tomm, A. Javadi, N. O. Antoniadis, D. Najer, M. C. Löbl, A. R. Korsch, R. Schott, S. R. Valentini, A. D. Wieck, A. Ludwig, and R. J. Warburton, *A bright and fast source of coherent single photons*, **Nat. Nanotechnol.** **16**, 399 (2021). [Cited on page: 2, 8, 22]
- [77] P. Lodahl, A. Ludwig, and R. J. Warburton, *A deterministic source of single photons*, **Physics Today** **75**, 44 (2022). [Cited on page: 2, 8]
- [78] F. Bloch and P. A. Ross, *Radiative Auger effect*, **Phys. Rev.** **47**, 884 (1935). [Cited on page: 3, 122]
- [79] F. Bloch, *Double electron transitions in X-ray spectra*, **Phys. Rev.** **48**, 187 (1935). [Cited on page: 3, 122, 144, 146]
- [80] P. Michler, *Single quantum dots: Fundamentals, applications and new concepts*, volume 90 (Springer Science & Business Media) (2003). [Cited on page: 3, 122, 140]
- [81] K. Gawarecki, C. Spinnler, L. Zhai, G. N. Nguyen, A. Ludwig, R. J. Warburton, M. C. Löbl, D. E. Reiter, and P. Machnikowski, *Structural symmetry-breaking to explain radiative Auger transitions in self-assembled quantum dots*, **arXiv:2208.12069** (2022). [Cited on page: 3, 161]
- [82] J. Beugnon, M. P. A. Jones, J. Dingjan, B. Darquié, G. Messin, A. Browaeys, and P. Grangier, *Quantum interference between two single photons emitted by independently trapped atoms*, **Nature** **440**, 779 (2006). [Cited on page: 8]
- [83] P. Maunz, D. L. Moehring, S. Olmschenk, K. C. Younge, D. N. Matsukevich, and C. Monroe, *Quantum interference of photon pairs from two remote trapped atomic ions*, **Nat. Phys.** **3**, 538 (2007). [Cited on page: 8]
- [84] L. J. Stephenson, D. P. Nadlinger, B. C. Nichol, S. An, P. Drmota, T. G. Ballance, K. Thirumalai, J. F. Goodwin, D. M. Lucas, and C. J. Ballance, *High-Rate, High-Fidelity Entanglement of Qubits Across an Elementary Quantum Network*, **Phys. Rev. Lett.** **124**, 110501 (2020). [Cited on page: 8]
- [85] T. T. Tran, K. Bray, M. J. Ford, M. Toth, and I. Aharonovich, *Quantum emission from hexagonal boron nitride monolayers*, **Nat. Nanotechnol.** **11**, 37 (2016). [Cited on page: 8]
- [86] Y.-M. He, G. Clark, J. R. Schaibley, Y. He, M.-C. Chen, Y.-J. Wei, X. Ding, Q. Zhang, W. Yao, X. Xu, C.-Y. Lu, and J.-W. Pan, *Single quantum emitters in monolayer semiconductors*, **Nat. Nanotechnol.** **10**, 497 (2015). [Cited on page: 8]
- [87] S. Michaelis de Vasconcelos, D. Wigger, U. Wurstbauer, A. W. Holleitner, R. Bratschitsch, and T. Kuhn, *Single-Photon Emitters in Layered Van der Waals Materials*, **physica status solidi (b)** **259**, 2100566 (2022). [Cited on page: 8]
- [88] T. Schröder, F. Gädeke, M. J. Banholzer, and O. Benson, *Ultrabright and efficient single-photon generation based on nitrogen-vacancy centres in nanodiamonds on a solid immersion lens*, **New J. Phys.** **13**, 055017 (2011). [Cited on page: 8]



- [89] E. Neu, D. Steinmetz, J. Riedrich-Möller, S. Gsell, M. Fischer, M. Schreck, and C. Becher, *Single photon emission from silicon-vacancy colour centres in chemical vapour deposition nano-diamonds on iridium*, *New J. Phys.* **13**, 025012 (2011). [Cited on page: 8]
- [90] S. Castelletto, B. C. Johnson, V. Ivády, N. Stavrias, T. Umeda, A. Gali, and T. Ohshima, *A silicon carbide room-temperature single-photon source*, *Nat. Mater.* **13**, 151 (2014). [Cited on page: 8]
- [91] B. Lienhard, T. Schröder, S. Mouradian, F. Dolde, T. T. Tran, I. Aharonovich, and D. Englund, *Bright and photostable single-photon emitter in silicon carbide*, *Optica* **3**, 768 (2016). [Cited on page: 8]
- [92] M. J. Holmes, K. Choi, S. Kako, M. Arita, and Y. Arakawa, *Room-Temperature Triggered Single Photon Emission from a III-Nitride Site-Controlled Nanowire Quantum Dot*, *Nano Lett.* **14**, 982 (2014). [Cited on page: 8]
- [93] X. Zhou, L. Zhai, and J. Liu, *Epitaxial quantum dots: a semiconductor launchpad for photonic quantum technologies*, *Photonics Insights* **1**, R07 (2022). [Cited on page: 8]
- [94] I. Aharonovich, D. Englund, and M. Toth, *Solid-state single-photon emitters*, *Nat. Photon.* **10**, 631 (2016). [Cited on page: 8]
- [95] S. Strauf, N. G. Stoltz, M. T. Rakher, L. A. Coldren, P. M. Petroff, and D. Bouwmeester, *High-frequency single-photon source with polarization control*, *Nat. Photon.* **1**, 704 (2007). [Cited on page: 8]
- [96] F. Liu, A. J. Brash, J. O'Hara, L. M. Martins, C. L. Phillips, R. J. Coles, B. Royall, E. Clarke, C. Bentham, N. Prtljaga, I. E. Itskevich, L. R. Wilson, M. S. Skolnick, and A. M. Fox, *High purcell factor generation of indistinguishable on-chip single photons*, *Nat. Nanotechnol.* **13**, 835 (2018). [Cited on page: 8]
- [97] L. Midolo, T. Pregolato, G. Kiršanskè, and S. Stobbe, *Soft-mask fabrication of gallium arsenide nanomembranes for integrated quantum photonics*, *Nanotechnology* **26** (2015). [Cited on page: 8, 20, 23, 48]
- [98] I. Yeo, P.-L. de Assis, A. Gloppe, E. Dupont-Ferrier, P. Verlot, N. S. Malik, E. Dupuy, J. Claudon, J.-M. Gérard, A. Auffèves, G. Nogues, S. Seidelin, J.-P. Poizat, O. Arcizet, and M. Richard, *Strain-mediated coupling in a quantum dot-mechanical oscillator hybrid system*, *Nat. Nanotechnol.* **9**, 106 (2014). [Cited on page: 8, 16, 17, 24, 29, 42]
- [99] I. N. Stranski and L. Krastanow, *Zur Theorie der orientierten Ausscheidung von Ionenkristallen aufeinander*, *Monatsh. Chem.* **71**, 351 (1937). [Cited on page: 8]
- [100] D. Leonard, K. Pond, and P. M. Petroff, *Critical layer thickness for self-assembled InAs islands on GaAs*, *Phys. Rev. B* **50**, 11687 (1994). [Cited on page: 8]
- [101] M. C. Löbl, I. Söllner, A. Javadi, T. Pregolato, R. Schott, L. Midolo, A. V. Kuhlmann, S. Stobbe, A. D. Wieck, P. Lodahl, A. Ludwig, and R. J. Warburton, *Narrow optical linewidths and spin pumping on charge-tunable close-to-surface self-assembled quantum dots in an ultrathin diode*, *Phys. Rev. B* **96**, 165440 (2017). [Cited on page: 8, 137]
- [102] M. C. Löbl, S. Scholz, I. Söllner, J. Ritzmann, T. Denneulin, A. Kovács, B. E. Kardynał, A. D. Wieck, A. Ludwig, and R. J. Warburton, *Excitons in InGaAs quantum dots without electron wetting layer states*, *Commun. Phys.* **2**, 1 (2019). [Cited on page: 8, 10, 48, 127]
- [103] Z. M. Wang, B. L. Liang, K. A. Sablon, and G. J. Salamo, *Nanoholes fabricated by self-assembled gallium nanodrink on GaAs(100)*, *Appl. Phys. Lett.* **90**, 113120 (2007). [Cited on page: 8, 137, 144]
- [104] L. Jacak, *Semiconductor quantum dots - towards a new generation of semiconductor devices*, *Eur. J. Phys.* **21**, 487 (2000). [Cited on page: 8]
- [105] D. A. B. Miller, D. S. Chemla, T. C. Damen, A. C. Gossard, W. Wiegmann, T. H. Wood, and C. A. Burrus, *Band-Edge Electroabsorption in Quantum Well Structures: The Quantum-Confined Stark Effect*, *Phys. Rev. Lett.* **53**, 2173 (1984). [Cited on page: 9]
- [106] R. J. Warburton, C. Schäfflein, D. Haft, F. Bickel, A. Lorke, K. Karrai, J. M. Garcia, W. Schoenfeld, and P. M. Petroff, *Optical emission from single, charge-tunable quantum rings*, *Physica E Low Dimens. Syst. Nanostruct.* **9**, 124 (2001). [Cited on page: 9]
- [107] J. J. Finley, M. Sabathil, P. Vogl, G. Abstreiter, R. Oulton, A. I. Tartakovskii, D. J. Mowbray, M. S. Skolnick, S. L. Liew, A. G. Cullis, and M. Hopkinson, *Quantum-confined Stark shifts of charged exciton complexes in quantum dots*, *Phys. Rev. B* **70**, 201308 (2004). [Cited on page: 9]

- [108] C. Gerry and P. Knight, *Introductory Quantum Optics*, pp. i–vi (Cambridge University Press) (2004). [Cited on page: 9, 11, 13]
- [109] M. C. Löbl, I. Söllner, A. Javadi, T. Pregnolato, R. Schott, L. Midolo, A. V. Kuhlmann, S. Stobbe, A. D. Wieck, P. Lodahl, A. Ludwig, and R. J. Warburton, *Narrow optical linewidths and spin pumping on charge-tunable close-to-surface self-assembled quantum dots in an ultrathin diode*, *Phys. Rev. B* **96**, 165440 (2017). [Cited on page: 9, 48, 66]
- [110] R. J. Warburton, C. Schäfflein, D. Haft, F. Bickel, A. Lorke, K. Karrai, J. M. Garcia, W. Schoenfeld, and P. M. Petroff, *Optical emission from a charge-tunable quantum ring*, *Nature* **405**, 926 (2000). [Cited on page: 10, 122]
- [111] X.-Q. Li, H. Nakayama, and Y. Arakawa, *Phonon bottleneck in quantum dots: Role of lifetime of the confined optical phonons*, *Phys. Rev. B* **59**, 5069 (1999). [Cited on page: 10, 130]
- [112] A. V. Kuhlmann, J. Houel, D. Brunner, A. Ludwig, D. Reuter, A. D. Wieck, and R. J. Warburton, *A dark-field microscope for background-free detection of resonance fluorescence from single semiconductor quantum dots operating in a set-and-forget mode*, *Rev. Sci. Instrum.* **84**, 073905 (2013). [Cited on page: 10, 12, 46, 155]
- [113] M. O. Scully and M. S. Zubairy, *Quantum Optics* (Cambridge University Press) (1997). [Cited on page: 11]
- [114] M. Fox and M. Fox, *Quantum Optics: An Introduction*, Oxford Master Series in Physics (Oxford University Press, Oxford, New York) (2006). [Cited on page: 11, 12]
- [115] K. Karrai and R. J. Warburton, *Optical transmission and reflection spectroscopy of single quantum dots*, *Superlattices and Microstructures* **33**, 311 (2003). [Cited on page: 12]
- [116] J. R. Johansson, P. D. Nation, and F. Nori, *QuTiP: An open-source Python framework for the dynamics of open quantum systems*, *Comput. Phys. Commun.* **183**, 1760 (2012). [Cited on page: 14, 78, 82, 131, 152]
- [117] J. R. Johansson, P. D. Nation, and F. Nori, *Qutip 2: A python framework for the dynamics of open quantum systems*, *Comput. Phys. Commun.* **184**, 1234 (2013). [Cited on page: 14, 78, 82, 131, 152]
- [118] B. R. Mollow, *Power spectrum of light scattered by two-level systems*, *Phys. Rev.* **188**, 1969 (1969). [Cited on page: 14, 82, 146]
- [119] F. Schuda, C. R. S. Jr, and M. Hercher, *Observation of the resonant Stark effect at optical frequencies*, *J. Phys. B: At. Mol. Opt. Phys.* **7**, L198 (1974). [Cited on page: 14]
- [120] F. Y. Wu, R. E. Grove, and S. Ezekiel, *Investigation of the Spectrum of Resonance Fluorescence Induced by a Monochromatic Field*, *Phys. Rev. Lett.* **35**, 1426 (1975). [Cited on page: 14]
- [121] A. N. Vamivakas, Y. Zhao, C.-Y. Lu, and M. Atatüre, *Spin-resolved quantum-dot resonance fluorescence*, *Nat. Phys.* **5**, 198 (2009). [Cited on page: 14]
- [122] D. E. Reiter, T. Kuhn, and V. M. Axt, *Distinctive characteristics of carrier-phonon interactions in optically driven semiconductor quantum dots*, *Adv. Phys.: X* **4**, 1655478 (2019). [Cited on page: 15, 148]
- [123] L. Besombes, K. Kheng, L. Marsal, and H. Mariette, *Acoustic phonon broadening mechanism in single quantum dot emission*, *Phys. Rev. B* **63**, 155307 (2001). [Cited on page: 15]
- [124] J. L. Skinner and D. Hsu, *Pure dephasing of a two-level system* (2002). [Cited on page: 15]
- [125] A. V. Kuhlmann, J. Houel, A. Ludwig, L. Greuter, D. Reuter, A. D. Wieck, M. Poggio, and R. J. Warburton, *Charge noise and spin noise in a semiconductor quantum device*, *Nat. Phys.* **9**, 570 (2013). [Cited on page: 15, 33, 52, 69, 101]
- [126] W. P. Bowen and G. J. Milburn, *Quantum Optomechanics*, volume 1 (CRC Press) (2015). [Cited on page: 15]
- [127] S. Schmid, L. G. Villanueva, and M. L. Roukes, *Fundamentals of nanomechanical resonators* (Springer International Publishing) (2016). [Cited on page: 15, 16, 48, 50, 51, 53, 56, 57, 58]
- [128] B. D. Hauer, C. Doolin, K. S. D. Beach, and J. P. Davis, *A general procedure for thermomechanical calibration of nano/micro-mechanical resonators*, *Ann. Phys.* **339**, 181 (2013). [Cited on page: 15, 17, 41]
- [129] A. N. Cleland, *Foundations of nanomechanics* (Springer International Publishing) (2003). [Cited on page: 15]
- [130] M. Poot and H. van der Zant, *Mechanical systems in the quantum regime*, *Phys. Rep.* **511**, 273 (2012). [Cited on page: 15]



- [131] J. F. Vignola, J. A. Judge, J. Jarzynski, M. Zalalutdinov, B. H. Houston, and J. W. Baldwin, *Effect of viscous loss on mechanical resonators designed for mass detection*, *Appl. Phys. Lett.* **88**, 041921 (2006). [Cited on page: 15, 48]
- [132] K. Wang, A.-C. Wong, and C.-C. Nguyen, *Vhf free-free beam high-q micromechanical resonators*, *J. Microelectromechanical Syst.* **9**, 347 (2000). [Cited on page: 15]
- [133] K. Yasumura, T. Stowe, E. Chow, T. Pfafman, T. Kenny, B. Stipe, and D. Rugar, *Quality factors in micron- and submicron-thick cantilevers*, *J. Microelectromech. Sys.* **9**, 117 (2000). [Cited on page: 15, 26, 58]
- [134] C. Zener, *Internal Friction in Solids II. General Theory of Thermoelastic Internal Friction*, *Phys. Rev.* **53**, 90 (1938). [Cited on page: 16]
- [135] R. Lifshitz and M. L. Roukes, *Thermoelastic damping in micro- and nanomechanical systems*, *Phys. Rev. B* **61**, 5600 (2000). [Cited on page: 16, 48]
- [136] H. Okamoto, D. Ito, K. Onomitsu, and H. Yamaguchi, *Thermoelastic damping in GaAs micromechanical resonators*, *physica status solidi c* **5**, 2920 (2008). [Cited on page: 16, 45]
- [137] A. A. Kiselev and G. J. Iafrate, *Phonon dynamics and phonon assisted losses in Euler-Bernoulli nanobeams*, *Phys. Rev. B* **77**, 205436 (2008). [Cited on page: 16]
- [138] I. Vurgaftman, J. R. Meyer, and L. R. Ram-Mohan, *Band parameters for III-V compound semiconductors and their alloys*, *J. Appl. Phys.* **89**, 5815 (2001). [Cited on page: 17, 42]
- [139] C. G. Van de Walle, *Band lineups and deformation potentials in the model-solid theory*, *Phys. Rev. B* **39**, 1871 (1989). [Cited on page: 17, 42]
- [140] R. Leijssen, G. R. La Gala, L. Freisem, J. T. Muhonen, and E. Verhagen, *Nonlinear cavity optomechanics with nanomechanical thermal fluctuations*, *Nat. Commun.* **8**, ncomms16024 (2017). [Cited on page: 17]
- [141] F. R. Braakman and M. Poggio, *Force sensing with nanowire cantilevers*, *Nanotechnology* **30**, 332001 (2019). [Cited on page: 22]
- [142] D. Halg, T. Gisler, Y. Tsaturyan, L. Catalini, U. Grob, M.-D. Krass, M. Heritier, H. Mattiat, A.-K. Thamm, and R. Schirhagl, *Membrane-based scanning force microscopy*, *Phys. Rev. Applied* **15**, L021001 (2021). [Cited on page: 22]
- [143] M. A. Page, M. Goryachev, H. Miao, Y. Chen, Y. Ma, D. Mason, M. Rossi, C. D. Blair, L. Ju, D. G. Blair, A. Schliesser, M. E. Tobar, and C. Zhao, *Gravitational wave detectors with broadband high frequency sensitivity*, *Commun. Phys.* **4**, 27 (2021). [Cited on page: 22]
- [144] B.-B. Li, L. Ou, Y. Lei, and Y.-C. Liu, *Cavity optomechanical sensing*, *Nanophotonics* **10**, 2799 (2021). [Cited on page: 22]
- [145] M. Forsch, R. Stockill, A. Wallucks, I. Marinkovic, C. Gartner, R. A. Norte, F. van Otten, A. Fiore, K. Srinivasan, and S. Groblacher, *Microwave-to-optics conversion using a mechanical oscillator in its quantum ground state*, *Nat. Phys.* **16**, 69 (2020). [Cited on page: 22, 116]
- [146] e. Aasi, J., *Advanced LIGO*, *Class. Quantum Grav.* **32**, 074001 (2015). [Cited on page: 22, 48]
- [147] R. J. Warburton, *Single spins in self-assembled quantum dots*, *Nat. Mater.* **12**, 483 (2013). [Cited on page: 22]
- [148] A. K. Huttel, H. B. Meerwaldt, G. A. Steele, M. Poot, B. Witkamp, L. P. Kouwenhoven, and H. S. J. van der Zant, *Single electron tunnelling through high-Q single-wall carbon nanotube NEMS resonators*, *Phys. Stat. Solidi B* **247**, 2974 (2010). [Cited on page: 24]
- [149] A. Javadi, D. Ding, M. H. Appel, S. Mahmoodian, M. C. Lobl, I. Sollner, R. Schott, C. Papon, T. Pregnolato, S. Stobbe, L. Midolo, T. Schroder, A. D. Wieck, A. Ludwig, R. J. Warburton, and P. Lodahl, *Spin-photon interface and spin-controlled photon switching in a nanobeam waveguide*, *Nat. Nanotechnol.* **13**, 398 (2018). [Cited on page: 27, 31]
- [150] J. Houel, A. V. Kuhlmann, L. Greuter, F. Xue, M. Poggio, B. D. Gerardot, P. A. Dalgarno, A. Badolato, P. M. Petroff, A. Ludwig, D. Reuter, A. D. Wieck, and R. J. Warburton, *Probing single-charge fluctuations at a GaAs/AlAs interface using laser spectroscopy on a nearby InGaAs quantum dot*, *Phys. Rev. Lett.* **108**, 107401 (2012). [Cited on page: 33]
- [151] A. Barg, L. Midolo, G. Kirsanske, P. Tighineanu, T. Pregnolato, A. Imamođlu, P. Lodahl, A. Schliesser, S. Stobbe, and E. S. Polzik, *Carrier-mediated optomechanical forces in semiconductor nanomembranes with coupled quantum wells*, *Phys. Rev. B* **98**, 155316 (2018). [Cited on page: 38, 45, 60, 72]
- [152] A. H. Safavi-Naeini and O. Painter, *Design of optomechanical cavities and waveguides on a simultaneous bandgap phononic-photonic crystal slab*, *Opt. Express* **18**, 14926 (2010). [Cited on page: 38, 104, 105]

- [153] T. P. M. Alegre, A. Safavi-Naeini, M. Winger, and O. Painter, *Quasi-two-dimensional optomechanical crystals with a complete phononic bandgap*, *Opt. Express* **19**, 5658 (2011). [Cited on page: 38, 104, 105]
- [154] J. Chan, A. H. Safavi-Naeini, J. T. Hill, S. Meenehan, and O. Painter, *Optimized optomechanical crystal cavity with acoustic radiation shield*, *Appl. Phys. Lett.* **101**, 081115 (2012). [Cited on page: 38, 104, 105]
- [155] S. Weis, R. Rivière, S. Deléglise, E. Gavartin, O. Arcizet, A. Schliesser, and T. J. Kippenberg, *Optomechanically induced transparency*, *Science* **330**, 1520 (2010). [Cited on page: 38, 146]
- [156] A. H. Safavi-Naeini, T. P. M. Alegre, J. Chan, M. Eichenfield, M. Winger, Q. Lin, J. T. Hill, D. E. Chang, and O. Painter, *Electromagnetically induced transparency and slow light with optomechanics*, *Nature* **472**, 69 (2011). [Cited on page: 38, 146]
- [157] R. Riedinger, A. Wallucks, I. Marinković, C. Löschnauer, M. Aspelmeyer, S. Hong, and S. Gröblacher, *Remote quantum entanglement between two micromechanical oscillators*, *Nature* **556**, 473 (2018). [Cited on page: 38, 160]
- [158] E. Meyer, R. Bennowitz, and H. J. Hug, *Scanning probe microscopy: the lab on a tip* (Springer International Publishing) (2021). [Cited on page: 48]
- [159] P. Mohanty, D. A. Harrington, K. L. Ekinci, Y. T. Yang, M. J. Murphy, and M. L. Roukes, *Intrinsic dissipation in high-frequency micromechanical resonators*, *Phys. Rev. B* **66**, 085416 (2002). [Cited on page: 48]
- [160] K. Brueckner, V. Cimalla, F. Niebelschütz, R. Stephan, K. Tonisch, O. Ambacher, and M. A. Hein, *Strain- and pressure-dependent RF response of microelectromechanical resonators for sensing applications*, *J. Micromech. Sys.* **17**, 2016 (2007). [Cited on page: 48]
- [161] K. Yasumura, T. Stowe, E. Chow, T. Pfafman, T. Kenny, B. Stipe, and D. Rugar, *Quality factors in micron- and submicron-thick cantilevers*, *J. of Microelectromech. Sys.* **9**, 117 (2000). [Cited on page: 48, 58]
- [162] F. Pan, K. Cui, G. Bai, X. Feng, F. Liu, W. Zhang, and Y. Huang, *Radiation-pressure-antidamping enhanced optomechanical spring sensing*, *ACS Photonics* **5**, 4164 (2018). [Cited on page: 48, 52]
- [163] F. Pan, K. Cui, Y. Huang, Z. Chen, N. Wu, G. Bai, Z. Huang, X. Feng, F. Liu, and W. Zhang, *Phonon lasing enhanced mass sensor with zeptogram resolution under ambient conditions*, *Chip* p. 100050 (2023). [Cited on page: 48]
- [164] K. Cui, K. Cui, Z. Huang, N. Wu, N. Wu, Q. Xu, Q. Xu, F. Pan, F. Pan, J. Xiong, J. Xiong, X. Feng, X. Feng, F. Liu, F. Liu, W. Zhang, W. Zhang, W. Zhang, Y. Huang, Y. Huang, and Y. Huang, *Phonon lasing in a hetero optomechanical crystal cavity*, *Photon. Res.* **9**, 937 (2021). [Cited on page: 49, 53]
- [165] A. G. Primo, C. M. Kersul, R. Benevides, N. C. Carvalho, M. Ménard, N. C. Frateschi, P.-L. de Assis, G. S. Wiederhecker, and T. P. Mayer Alegre, *Accurate modeling and characterization of photothermal forces in optomechanics*, *APL Photonics* **6**, 086101 (2021). [Cited on page: 50]
- [166] H. Okamoto, D. Ito, K. Onomitsu, H. Sanada, H. Gotoh, T. Sogawa, and H. Yamaguchi, *Vibration amplification, damping, and self-oscillations in micromechanical resonators induced by optomechanical coupling through carrier excitation*, *Phys. Rev. Lett.* **106**, 036801 (2011). [Cited on page: 52]
- [167] P. K. Shandilya, D. P. Lake, M. J. Mitchell, D. D. Sukachev, and P. E. Barclay, *Optomechanical interface between telecom photons and spin quantum memory*, *Nat. Phys.* **17**, 1420 (2021). [Cited on page: 53, 55]
- [168] M. Dresselhaus, G. Dresselhaus, S. B. Cronin, and A. Gomes Souza Filho, *Electron and phonon scattering*, in *Solid state properties: from bulk to nano* (Springer) (2018). [Cited on page: 55]
- [169] Z. Lindenfeld and R. Lifshitz, *Damping of mechanical vibrations by free electrons in metallic nanoresonators*, *Phys. Rev. B* **87**, 085448 (2013). [Cited on page: 55]
- [170] Y. Taturyan, A. Barg, E. S. Polzik, and A. Schliesser, *Ultraslow nanomechanical resonators via soft clamping and dissipation dilution*, *Nat. Nanotechnol.* **12**, 776 (2017). [Cited on page: 55, 115]
- [171] A. H. Ghadimi, S. A. Fedorov, N. J. Engelsens, M. J. Breyhi, R. Schilling, D. J. Wilson, and T. J. Kippenberg, *Elastic strain engineering for ultralow mechanical dissipation*, *Science* **360**, 764 (2018). [Cited on page: 55]

- [172] S. A. Fedorov, N. J. Engelsen, A. H. Ghadimi, M. J. Beryhi, R. Schilling, D. J. Wilson, and T. J. Kippenberg, *Generalized dissipation dilution in strained mechanical resonators*, **Phys. Rev. B** **99**, 054107 (2019). [Cited on page: 55]
- [173] A. Beccari, D. A. Visani, S. A. Fedorov, M. J. Beryhi, V. Boureau, N. J. Engelsen, and T. J. Kippenberg, *Strained crystalline nanomechanical resonators with quality factors above 10 billion*, **Nat. Phys.** **18**, 436 (2022). [Cited on page: 55]
- [174] G. Arregui, M. F. Colombano, J. Maire, A. Pitanti, N. E. Capuj, A. Griol, A. Martínez, C. M. Sotomayor-Torres, and D. Navarro-Urrios, *Injection locking in an optomechanical coherent phonon source*, **Nanophotonics** **10**, 1319 (2021). [Cited on page: 55]
- [175] S. Gigan, H. R. Böhm, M. Paternostro, F. Blaser, G. Langer, J. B. Hertzberg, K. C. Schwab, D. Bäuerle, M. Aspelmeyer, and A. Zeilinger, *Self-cooling of a micromirror by radiation pressure*, **Nature** **444**, 67 (2006). [Cited on page: 56]
- [176] L. Villanueva and S. Schmid, *Evidence of surface loss as ubiquitous limiting damping mechanism in SiN micro- and nanomechanical resonators*, **Phys. Rev. Lett.** **113**, 227201 (2014). [Cited on page: 58]
- [177] I. Lekavicius, T. Oo, and H. Wang, *Diamond Lamb wave spin-mechanical resonators with optically coherent nitrogen vacancy centers*, **J. Appl. Phys.** **126**, 214301 (2019). [Cited on page: 60, 72, 74]
- [178] G. D. Cole, I. Wilson-Rae, K. Werbach, M. R. Vanner, and M. Aspelmeyer, *Phonon-tunnelling dissipation in mechanical resonators*, **Nat. Commun.** **2**, 231 (2011). [Cited on page: 60, 62]
- [179] T. Hahn, D. Groll, H. J. Krenner, T. Kuhn, P. Machnikowski, and D. Wigger, *Photon scattering from a quantum acoustically modulated two-level system*, **AVS Quantum Science** **4**, 011403 (2022). [Cited on page: 67]
- [180] D. A. Golter, T. Oo, M. Amezcua, I. Lekavicius, K. A. Stewart, and H. Wang, *Coupling a Surface Acoustic Wave to an Electron Spin in Diamond via a Dark State*, **Phys. Rev. X** **6**, 041060 (2016). [Cited on page: 67, 84]
- [181] T. Kaldewey, S. Lüker, A. V. Kuhlmann, S. R. Valentin, J.-M. Chauveau, A. Ludwig, A. D. Wieck, D. E. Reiter, T. Kuhn, and R. J. Warburton, *Demonstrating the decoupling regime of the electron-phonon interaction in a quantum dot using chirped optical excitation*, **Phys. Rev. B** **95**, 241306 (2017). [Cited on page: 75]
- [182] T. Kaldewey, S. Lüker, A. V. Kuhlmann, S. R. Valentin, A. Ludwig, A. D. Wieck, D. E. Reiter, T. Kuhn, and R. J. Warburton, *Coherent and robust high-fidelity generation of a biexciton in a quantum dot by rapid adiabatic passage*, **Phys. Rev. B** **95**, 161302 (2017). [Cited on page: 75]
- [183] J.-P. Jahn, M. Munsch, L. Béguin, A. V. Kuhlmann, M. Renggli, Y. Huo, F. Ding, R. Trotta, M. Reindl, O. G. Schmidt, A. Rastelli, P. Treutlein, and R. J. Warburton, *An artificial Rb atom in a semiconductor with lifetime-limited linewidth*, **Phys. Rev. B** **92**, 245439 (2015). [Cited on page: 78, 92, 132]
- [184] D. M. Lukin, A. D. White, R. Trivedi, M. A. Guidry, N. Morioka, C. Babin, O. O. Soykal, J. Ul-Hassan, N. T. Son, T. Ohshima, P. K. Vasireddy, M. H. Nasr, S. Sun, J.-P. W. MacLean, C. Dory, E. A. Nanni, J. Wrachtrup, F. Kaiser, and J. Vučković, *Spectrally reconfigurable quantum emitters enabled by optimized fast modulation*, **Npj Quantum Inf.** **6**, 1 (2020). [Cited on page: 83]
- [185] A. Artioli, S. Kotal, N. Gregersen, P. Verlot, J.-M. Gérard, and J. Claudon, *Design of Quantum Dot-Nanowire Single-Photon Sources that are Immune to Thermomechanical Decoherence*, **Phys. Rev. Lett.** **123**, 247403 (2019). [Cited on page: 84]
- [186] Q. P. Unterreithmeier, E. M. Weig, and J. P. Kotthaus, *Universal transduction scheme for nanomechanical systems based on dielectric forces*, **Nature** **458**, 1001 (2009). [Cited on page: 89, 116]
- [187] A. Schliesser, R. Rivière, G. Anetsberger, O. Arcizet, and T. J. Kippenberg, *Resolved-sideband cooling of a micromechanical oscillator*, **Nat. Phys.** **4**, 415 (2008). [Cited on page: 104]
- [188] R. Riedinger, S. Hong, R. A. Norte, J. A. Slater, J. Shang, A. G. Krause, V. Anant, M. Aspelmeyer, and S. Gröblacher, *Non-classical correlations between single photons and phonons from a mechanical oscillator*, **Nature** **530**, 313 (2016). [Cited on page: 104, 116]
- [189] M. Pechal, P. Arrangoiz-Arriola, and A. H. Safavi-Naeini, *Superconducting circuit quantum computing with nanomechanical resonators as storage*, **Quantum Sci. Technol.** **4**, 015006 (2018). [Cited on page: 104]

- [190] A. Wallucks, I. Marinković, B. Hensen, R. Stockill, and S. Gröblacher, *A quantum memory at telecom wavelengths*, *Nat. Phys.* **16**, 772 (2020). [Cited on page: 104]
- [191] L. Van Hove, *The Occurrence of Singularities in the Elastic Frequency Distribution of a Crystal*, *Phys. Rev.* **89**, 1189 (1953). [Cited on page: 107]
- [192] J. Chan, *Laser Cooling of an Optomechanical Crystal Resonator to Its Quantum Ground State of Motion*, *Phd thesis*, California Institute of Technology (2012). [Cited on page: 115]
- [193] K. Kuruma, Y. Ota, M. Kakuda, S. Iwamoto, and Y. Arakawa, *Surface-passivated high-Q GaAs photonic crystal nanocavity with quantum dots*, *APL Photonics* **5** (2020). [Cited on page: 115]
- [194] D. Najer, N. Tomm, A. Javadi, A. R. Korsch, B. Petrak, D. Riedel, V. Dolique, S. R. Valentin, R. Schott, A. D. Wieck, A. Ludwig, and R. J. Warburton, *Suppression of Surface-Related Loss in a Gated Semiconductor Microcavity*, *Phys. Rev. Applied* **15**, 044004 (2021). [Cited on page: 115]
- [195] J.-J. Li and K.-D. Zhu, *An efficient optical knob from slow light to fast light in a coupled nanomechanical resonator-quantum dot system*, *Opt. Express* **17**, 19874 (2009). [Cited on page: 116]
- [196] J.-J. Li and K.-D. Zhu, *Mechanical vibration-induced coherent optical spectroscopy in a single quantum dot coupled to a nanomechanical resonator*, *J. Phys. B: At. Mol. Opt. Phys.* **43**, 155504 (2010). [Cited on page: 116]
- [197] J.-J. Li and K.-D. Zhu, *Generalized Optomechanics and Its Applications: Quantum Optical Properties of Generalized Optomechanical System* (WORLD SCIENTIFIC) (2013). [Cited on page: 116]
- [198] N. Lauk, N. Sinclair, S. Barzanjeh, J. P. Covey, M. Saffman, M. Spiropulu, and C. Simon, *Perspectives on quantum transduction*, *Quantum Sci. Technol.* **5**, 020501 (2020). [Cited on page: 116]
- [199] G. Calajó, M. J. A. Schuetz, H. Pichler, M. D. Lukin, P. Schneeweiss, J. Volz, and P. Rabl, *Quantum acousto-optic control of light-matter interactions in nanophotonic networks*, *Phys. Rev. A* **99**, 053852 (2019). [Cited on page: 116, 160]
- [200] M. Arcari, I. Söllner, A. Javadi, S. Lindskov Hansen, S. Mahmoodian, J. Liu, H. Thyrrstrup, E. H. Lee, J. D. Song, S. Stobbe, and P. Lodahl, *Near-Unity Coupling Efficiency of a Quantum Emitter to a Photonic Crystal Waveguide*, *Phys. Rev. Lett.* **113**, 093603 (2014). [Cited on page: 116]
- [201] I. Söllner, S. Mahmoodian, S. L. Hansen, L. Midolo, A. Javadi, G. Kiršanskė, T. Pregolato, H. El-Ella, E. H. Lee, J. D. Song, S. Stobbe, and P. Lodahl, *Deterministic photon-emitter coupling in chiral photonic circuits*, *Nat. Nanotechnol.* **10**, 775 (2015). [Cited on page: 116]
- [202] C. Papon, X. Zhou, H. Thyrrstrup, Z. Liu, S. Stobbe, R. Schott, A. D. Wieck, A. Ludwig, P. Lodahl, and L. Midolo, *Nanomechanical single-photon routing*, *Optica* **6**, 524 (2019). [Cited on page: 116]
- [203] C. Papon, Y. Wang, R. Uppu, S. Scholz, A. D. Wieck, A. Ludwig, P. Lodahl, and L. Midolo, *Independent operation of two waveguide-integrated single-photon sources*, *arXiv:2210.09826* (2022). [Cited on page: 116]
- [204] M. Mirhosseini, A. Sipahigil, M. Kalaei, and O. Painter, *Superconducting qubit to optical photon transduction*, *Nature* **588**, 599 (2020). [Cited on page: 116]
- [205] J. Dreiser, M. Atatüre, C. Galland, T. Müller, A. Badolato, and A. Imamoglu, *Optical investigations of quantum dot spin dynamics as a function of external electric and magnetic fields*, *Phys. Rev. B* **77**, 075317 (2008). [Cited on page: 116, 137, 141]
- [206] A. V. Khaetskii and Y. V. Nazarov, *Spin-flip transitions between Zeeman sublevels in semiconductor quantum dots*, *Phys. Rev. B* **64**, 125316 (2001). [Cited on page: 116]
- [207] L. M. Woods, T. L. Reinecke, and Y. Lyanda-Geller, *Spin relaxation in quantum dots*, *Phys. Rev. B* **66**, 161318 (2002). [Cited on page: 116]
- [208] T. Åberg and J. Utriainen, *Evidence for a "radiative Auger effect" in X-ray photon emission*, *Phys. Rev. Lett.* **22**, 1346 (1969). [Cited on page: 122, 144]
- [209] T. Åberg, *Theory of the radiative Auger effect*, *Phys. Rev. A* **4**, 1735 (1971). [Cited on page: 122]
- [210] W. Bambynek, B. Crasemann, R. W. Fink, H. U. Freund, H. Mark, C. D. Swift, R. E. Price, and P. V. Rao, *X-ray fluorescence yields, Auger, and Coster-Kronig transition probabilities*, *Rev. Mod. Phys.* **44**, 716 (1972). [Cited on page: 122, 144]

- [211] M.-G. Barthés-Labrousse, *The Auger effect*, *Microsc. Microanal.* **6**, 253 (1995). [Cited on page: 122]
- [212] A. Kurzmann, A. Ludwig, A. D. Wieck, A. Lorke, and M. Geller, *Auger recombination in self-assembled quantum dots: Quenching and broadening of the charged exciton transition*, *Nano Lett.* **16**, 3367 (2016). [Cited on page: 122, 144]
- [213] B. Han, C. Robert, E. Courtade, M. Manca, S. Shree, T. Amand, P. Renucci, T. Taniguchi, K. Watanabe, X. Marie, L. E. Golub, M. M. Glazov, and B. Urbaszek, *Exciton states in monolayer MoSe<sub>2</sub> and MoTe<sub>2</sub> probed by upconversion spectroscopy*, *Phys. Rev. X* **8**, 031073 (2018). [Cited on page: 122]
- [214] P. Siyushev, H. Pinto, M. Vörös, A. Gali, F. Jelezko, and J. Wrachtrup, *Optically controlled switching of the charge state of a single nitrogen-vacancy center in diamond at cryogenic temperatures*, *Phys. Rev. Lett.* **110**, 167402 (2013). [Cited on page: 122]
- [215] P. Blood, *Quantum Confined Laser Devices: Optical gain and recombination in semiconductors*, volume 23 (OUP Oxford) (2015). [Cited on page: 122]
- [216] T. A. Carlson, *Electron shake-off following the beta decay of Ne<sup>23</sup>*, *Phys. Rev.* **130**, 2361 (1963). [Cited on page: 122]
- [217] P. J. Dean, J. D. Cuthbert, D. G. Thomas, and R. T. Lynch, *Two-electron transitions in the luminescence of excitons bound to neutral donors in gallium phosphide*, *Phys. Rev. Lett.* **18**, 122 (1967). [Cited on page: 122, 144]
- [218] M. S. Skolnick, K. J. Nash, D. J. Mowbray, M. K. Saker, T. A. Fisher, D. M. Whittaker, D. W. Peggs, N. Miura, S. Sasaki, R. S. Smith, and S. J. Bass, *Fermi sea shake-up in quantum well luminescence spectra*, *Solid-State Electronics* **37**, 825 (1994). [Cited on page: 122, 144]
- [219] M. J. Manfra, B. B. Goldberg, L. Pfeiffer, and K. West, *Anderson-Fano resonance and shake-up processes in the magnetophotoluminescence of a two-dimensional electron system*, *Phys. Rev. B* **57**, R9467 (1998). [Cited on page: 122, 144]
- [220] N. A. J. M. Kleemans, J. van Bree, A. O. Govorov, J. G. Keizer, G. J. Hamhuis, R. Nötzel, A. Y. Silov, and P. M. Koenraad, *Many-body exciton states in self-assembled quantum dots coupled to a Fermi sea*, *Nat. Phys.* **6**, 534 (2010). [Cited on page: 122]
- [221] Y. H. Huo, A. Rastelli, and O. G. Schmidt, *Ultra-small excitonic fine structure splitting in highly symmetric quantum dots on GaAs (001) substrate*, *Appl. Phys. Lett.* **102**, 152105 (2013). [Cited on page: 122, 137]
- [222] J. Hansom, C. H. H. Schulte, C. Matthiesen, M. J. Stanley, and M. Atatüre, *Frequency stabilization of the zero-phonon line of a quantum dot via phonon-assisted active feedback*, *Appl. Phys. Lett.* **105**, 172107 (2014). [Cited on page: 123]
- [223] Z. X. Koong, D. Scerri, M. Rambach, T. S. Santana, S. I. Park, J. D. Song, E. M. Gauger, and B. D. Gerardot, *Fundamental limits to coherent photon generation with solid-state atomlike transitions*, *Phys. Rev. Lett.* **123**, 167402 (2019). [Cited on page: 123]
- [224] A. J. Brash, J. Iles-Smith, C. L. Phillips, D. P. S. McCutcheon, J. O'Hara, E. Clarke, B. Royall, L. R. Wilson, J. Mørk, M. S. Skolnick, A. M. Fox, and A. Nazir, *Light scattering from solid-state quantum emitters: Beyond the atomic picture*, *Phys. Rev. Lett.* **123**, 167403 (2019). [Cited on page: 123, 154]
- [225] L. P. Kouwenhoven, D. G. Austing, and S. Tarucha, *Few-electron quantum dots*, *Rep. Prog. Phys.* **64**, 701 (2001). [Cited on page: 124, 127, 154]
- [226] V. Fock, *Bemerkung zur Quantelung des harmonischen Oszillators im Magnetfeld*, *Zeitschrift für Physik* **47**, 446 (1928). [Cited on page: 124, 126, 127]
- [227] C. G. Darwin, *The diamagnetism of the free electron*, *Proc. Camb. Phil. Soc.* **27**, 86 (1930). [Cited on page: 124, 126, 127]
- [228] A. V. Madhav and T. Chakraborty, *Electronic properties of anisotropic quantum dots in a magnetic field*, *Phys. Rev. B* **49**, 8163 (1994). [Cited on page: 127]
- [229] R. J. Warburton, B. T. Miller, C. S. Dürr, C. Bödefeld, K. Karrai, J. P. Kotthaus, G. Medeiros-Ribeiro, P. M. Petroff, and S. Huant, *Coulomb interactions in small charge-tunable quantum dots: A simple model*, *Phys. Rev. B* **58**, 16221 (1998). [Cited on page: 127, 140]
- [230] S.-J. Cheng, W. Sheng, and P. Hawrylak, *Theory of excitonic artificial atoms: InGaAs/GaAs quantum dots in strong magnetic fields*, *Phys. Rev. B* **68**, 235330 (2003). [Cited on page: 127, 140]



- [231] B. Ohnesorge, M. Albrecht, J. Oshinowo, A. Forchel, and Y. Arakawa, *Rapid carrier relaxation in self-assembled  $In_xGa_{1-x}As/GaAs$  quantum dots*, *Phys. Rev. B* **54**, 11532 (1996). [Cited on page: 130]
- [232] H. Kurtze, J. Seebeck, P. Gartner, D. R. Yakovlev, D. Reuter, A. D. Wieck, M. Bayer, and F. Jahnke, *Carrier relaxation dynamics in self-assembled semiconductor quantum dots*, *Phys. Rev. B* **80**, 235319 (2009). [Cited on page: 130]
- [233] K. Müller, A. Bechtold, C. Ruppert, T. Kaldewey, M. Zecherle, J. S. Wildmann, M. Bichler, H. J. Krenner, J. M. Villas-Bôas, G. Abstreiter, M. Betz, and J. J. Finley, *Probing ultrafast carrier tunneling dynamics in individual quantum dots and molecules*, *Ann. Phys.* **525**, 49 (2013). [Cited on page: 130]
- [234] J. Hansom, C. H. H. Schulte, C. Le Gall, C. Matthiesen, E. Clarke, M. Hugues, J. M. Taylor, and M. Atatüre, *Environment-assisted quantum control of a solid-state spin via coherent dark states*, *Nat. Phys.* **10**, 725 (2014). [Cited on page: 132]
- [235] R. Loudon, *The quantum theory of light* (OUP Oxford) (2000). [Cited on page: 135]
- [236] J. C. Slater, *The theory of complex spectra*, *Phys. Rev.* **34**, 1293 (1929). [Cited on page: 136, 139]
- [237] H. A. Bethe and R. Jackiw, *Intermediate quantum mechanics*, (CRC Press) (2018). [Cited on page: 136]
- [238] P. M. Vora, A. S. Bracker, S. G. Carter, T. M. Sweeney, M. Kim, C. S. Kim, L. Yang, P. G. Brereton, S. E. Economou, and D. Gammon, *Spin-cavity interactions between a quantum dot molecule and a photonic crystal cavity*, *Nat. Commun.* **6**, 7665 (2015). [Cited on page: 137]
- [239] A. Javadi, D. Ding, M. H. Appel, S. Mahmoodian, M. C. Löbl, I. Söllner, R. Schott, C. Papon, T. Pregnolato, S. Stobbe, L. Midolo, T. Schröder, A. D. Wieck, A. Ludwig, R. J. Warburton, and P. Lodahl, *Spin-photon interface and spin-controlled photon switching in a nanobeam waveguide*, *Nat. Nanotechnol.* **13**, 398 (2018). [Cited on page: 137]
- [240] J. Q. Grim, A. S. Bracker, M. Zalalutdinov, S. G. Carter, A. C. Kozen, M. Kim, C. S. Kim, J. T. Mlack, M. Yakes, B. Lee, and D. Gammon, *Scalable in operando strain tuning in nanophotonic waveguides enabling three-quantum-dot superradiance*, *Nat. Mater.* **18**, 963 (2019). [Cited on page: 137]
- [241] R. B. Patel, A. J. Bennett, I. Farrer, C. A. Nicoll, D. A. Ritchie, and A. J. Shields, *Two-photon interference of the emission from electrically tunable remote quantum dots*, *Nat. Photonics* **4**, 632 (2010). [Cited on page: 137]
- [242] G. Kiršanskė, H. Thyrestrup, R. S. Daveau, C. L. Dreeßen, T. Pregnolato, L. Midolo, P. Tighineanu, A. Javadi, S. Stobbe, R. Schott, A. Ludwig, A. D. Wieck, S. I. Park, J. D. Song, A. V. Kuhlmann, I. Söllner, M. C. Löbl, R. J. Warburton, and P. Lodahl, *Indistinguishable and efficient single photons from a quantum dot in a planar nanobeam waveguide*, *Phys. Rev. B* **96**, 165306 (2017). [Cited on page: 137]
- [243] M. Kroutvar, Y. Ducommun, D. Heiss, M. Bichler, D. Schuh, G. Abstreiter, and J. J. Finley, *Optically programmable electron spin memory using semiconductor quantum dots*, *Nature* **432**, 81 (2004). [Cited on page: 137]
- [244] J. M. Smith, P. A. Dalgarno, R. J. Warburton, A. O. Govorov, K. Karrai, B. D. Gerardot, and P. M. Petroff, *Voltage control of the spin dynamics of an exciton in a semiconductor quantum dot*, *Phys. Rev. Lett.* **94**, 197402 (2005). [Cited on page: 137, 141]
- [245] E. U. Condon, *The theory of complex spectra*, *Phys. Rev.* **36**, 1121 (1930). [Cited on page: 139]
- [246] D. Chithrani, M. Korkusinski, S.-J. Cheng, P. Hawrylak, R. L. Williams, J. Lefebvre, P. J. Poole, and G. C. Aers, *Electronic structure of the p-shell in single, site-selected  $InAs/InP$  quantum dots*, *Physica E Low Dimens. Syst. Nanostruct.* **26**, 322 (2005). [Cited on page: 140]
- [247] M. Cygorek, M. Korkusinski, and P. Hawrylak, *Atomistic theory of electronic and optical properties of  $InAsP/InP$  nanowire quantum dots*, *Phys. Rev. B* **101**, 075307 (2020). [Cited on page: 140]
- [248] A. L. Efros and M. Rosen, *Random telegraph signal in the photoluminescence intensity of a single quantum dot*, *Phys. Rev. Lett.* **78**, 1110 (1997). [Cited on page: 144]
- [249] R. Vaxenburg, E. Lifshitz, and A. L. Efros, *Suppression of Auger-stimulated efficiency droop in nitride-based light emitting diodes*, *Appl. Phys. Lett.* **102**, 031120 (2013). [Cited on page: 144]

- [250] P. Hawrylak, *Resonant magnetoexcitons and the fermi-edge singularity in a magnetic field*, *Phys. Rev. B* **44**, 11236 (1991). [Cited on page: 144]
- [251] J. Llusar and J. I. Climente, *Nature and control of shakeup processes in colloidal nanoplatelets*, *ACS Photonics* **7**, 3086 (2020). [Cited on page: 144, 155]
- [252] J. Stöhr, *NEXAFS Spectroscopy*, volume 25 (Springer Science & Business Media) (2013). [Cited on page: 144]
- [253] M. C. Löbl, C. Spinnler, A. Javadi, L. Zhai, G. N. Nguyen, J. Ritzmann, L. Midolo, P. Lodahl, A. D. Wieck, A. Ludwig, and R. J. Warburton, *Radiative Auger process in the single-photon limit*, *Nat. Nanotechnol.* **15**, 558 (2020). [Cited on page: 144, 146, 148, 152, 154, 155, 156]
- [254] F. V. Antolinez, F. T. Rabouw, A. A. Rossinelli, J. Cui, and D. J. Norris, *Observation of electron shakeup in CdSe/CdS core/shell nanoplatelets*, *Nano Lett.* **19**, 8495 (2019). [Cited on page: 144, 155]
- [255] K. J. Nash, M. S. Skolnick, M. K. Saker, and S. J. Bass, *Many body shakeup in quantum well luminescence spectra*, *Phys. Rev. Lett.* **70**, 3115 (1993). [Cited on page: 144]
- [256] G. Finkelstein, H. Shtrikman, and I. Bar-Joseph, *Mechanism of shakeup processes in the photoluminescence of a two-dimensional electron gas at high magnetic fields*, *Phys. Rev. B* **56**, 10326 (1997). [Cited on page: 144]
- [257] L. Bryja, A. Wójs, J. Misiewicz, M. Potemski, D. Reuter, and A. Wieck, *Magneto-optical probing of weak disorder in a two-dimensional hole gas*, *Phys. Rev. B* **75**, 035308 (2007). [Cited on page: 144]
- [258] E. Zibik, T. Grange, B. Carpenter, N. Porter, R. Ferreira, G. Bastard, D. Stehr, S. Winnerl, M. Helm, H. Liu *et al.*, *Long lifetimes of quantum-dot intersublevel transitions in the terahertz range*, *Nat. Mater.* **8**, 803 (2009). [Cited on page: 146, 151, 152, 154]
- [259] S. H. Autler and C. H. Townes, *Stark effect in rapidly varying fields*, *Phys. Rev.* **100**, 703 (1955). [Cited on page: 146]
- [260] A. J. Ramsay, T. M. Godden, S. J. Boyle, E. M. Gauger, A. Nazir, B. W. Lovett, A. M. Fox, and M. S. Skolnick, *Phonon-induced Rabi-frequency renormalization of optically driven single InGaAs/GaAs quantum dots*, *Phys. Rev. Lett.* **105**, 177402 (2010). [Cited on page: 148]
- [261] M. Fleischhauer, A. Imamoglu, and J. P. Marangos, *Electromagnetically induced transparency: Optics in coherent media*, *Rev. Mod. Phys.* **77**, 633 (2005). [Cited on page: 148, 150, 151]
- [262] A. Aspect, E. Arimondo, R. Kaiser, N. Vansteenkiste, and C. Cohen-Tannoudji, *Laser cooling below the one-photon recoil energy by velocity-selective coherent population trapping*, *Phys. Rev. Lett.* **61**, 826 (1988). [Cited on page: 148]
- [263] J. H. Quilter, A. J. Brash, F. Liu, M. Glässl, A. M. Barth, V. M. Axt, A. J. Ramsay, M. S. Skolnick, and A. M. Fox, *Phonon-assisted population inversion of a single InGaAs/GaAs quantum dot by pulsed laser excitation*, *Phys. Rev. Lett.* **114**, 137401 (2015). [Cited on page: 154]
- [264] D. Press, T. D. Ladd, B. Zhang, and Y. Yamamoto, *Complete quantum control of a single quantum dot spin using ultrafast optical pulses*, *Nature* **456**, 218 (2008). [Cited on page: 154]
- [265] D. A. Gangloff, G. Éthier-Majcher, C. Lang, E. V. Denning, J. H. Bodey, D. M. Jackson, E. Clarke, M. Hugues, C. Le Gall, and M. Atatüre, *Quantum interface of an electron and a nuclear ensemble*, *Science* **364**, 62 (2019). [Cited on page: 154]
- [266] N. P. Bauman, H. Liu, E. J. Bylaska, S. Krishnamoorthy, G. H. Low, C. E. Granade, N. Wiebe, N. A. Baker, B. Peng, M. Roetteler *et al.*, *Towards quantum computing for high-energy excited states in molecular systems: quantum phase estimations of core-level states*, *J. Chem. Theory Comput.* **17**, 201 (2020). [Cited on page: 154]
- [267] A. Barfuss, J. Kölbl, L. Thiel, J. Teissier, M. Kasperczyk, and P. Maletinsky, *Phase-controlled coherent dynamics of a single spin under closed-contour interaction*, *Nat. Phys.* **14**, 1087 (2018). [Cited on page: 154]
- [268] W. B. Gao, P. Fallahi, E. Togan, J. Miguel-Sanchez, and A. Imamoglu, *Observation of entanglement between a quantum dot spin and a single photon*, *Nature* **491**, 426 (2012). [Cited on page: 154]

---

## Acknowledgements

---

First of all, I would like to thank Prof. Richard J. Warburton for letting me conduct my research in his group and for his supervision throughout the past years. I am very grateful for his deep physics knowledge, not only in semiconductor physics but also in all other fields. I further would like to thank Prof. Martino Poggio for being my second supervisor. He inspired one of the main achievements of this thesis (electric field antenna) without which, many of the experiments would not have been possible. I also would like to thank Prof. Julien Claudon for being the external expert and for finding the time to come to Basel. Furthermore, I would like to thank the QCQT PhD-school for its support during my studies.

On an equally important basis I would like to thank the people who worked together with me in the lab on a daily basis, namely, Nam Nguyen, Liang Zhai, Matthias Löbl and Alisa Javadi, as well as Caroline Schrader. I learned a lot and I appreciate that we managed to work together and keep a good relationship, which is not for granted. Together, we managed very nice results and I hope that the lab will continue like that. I also would like to thank Nam Nguyen and Liang Zhai for proofreading this thesis and Lukas Sponfeldner for taking the SEM pictures of the suspended beam resonator.

I highly appreciated the discussions with Hinrich Mattiat and Dr. Thibaud Ruelle from the Poggio lab and Gianni Buser and Dr. Roberto Mottola from the Treutlein group who helped us with technical questions in the lab.

I am very grateful to work together with such skilled collaborators. Without them, most of this work would not have been possible. First I would like to thank Sven Scholz, Julian Ritzmann, Hans-Georg Babin, Dr. Arne Ludwig, and Prof. Andreas D. Wieck at the Lehrstuhl für Angewandte Festkörperphysik at the Ruhr-Universität Bochum (Germany) for the growth of the wafer material. Furthermore, I would like to thank Dr. Ying Wang, Prof. Leonardo Midolo, and Prof. Peter Lodahl at the Niels Bohr Institute in Copenhagen (Denmark) for fabricating the mechanical resonators. I also thank the whole rest, current and former members, of the Bochum and Copenhagen teams for all the good exchanges during the past years. It was always a pleasure to work together with them. I am also very thankful for the theoretical support from Dr. Krzysztof Gawarecki, Prof. Doris E. Reiter, and Prof. Paweł Machnikowski for the radiative Auger experiments.



A big thanks goes to the current and also former members of the Nano-photonics group. This team was one of the main reasons why I was going to work every day: Lukas Sponfeldner, Simon Geyer, Sigurd Flågan, Nadia Antoniadis, Viktoria Yurgens, Nam Nguyen, Alisa Javadi, Yannik Fontana, Marcel Erbe, Natasha Tomm, Daniel Najer, Jonas G. Roch, Nadine Leisgang, Malwina Anna Marczak, Andrea Corazza, Rahel Kaiser, Timon Baltisberger, Matthias C. Löbl, Liang Zhai, Mark Hogg, Rafael Egli, and Andreas V. Kuhlmann. I am very grateful for all the good times we spent together, from hiking to skiing and just enjoying time with good food and playing games, or brewing beers together. I also thank the group for endless physics discussions which helped me to understand what we are doing in our labs. I also had the best office time together with Tomasz Jakubczyk, Yannik Fontana, and Malwina Marczak which I will miss a lot.

A very warm thanks goes to my family, my friends and my love. They spend ours and ours listening to either (boring) physics lectures or complaints about things that did not work as I wished for.

Finally I thank the whole staff of the Physics department of the University of Basel: the mechanical workshop, the electronics lab, the cleanroom team, the administrative, and the safety staff.

For financial support I thank the University of Basel, the Swiss National Science Foundation (SNF), the Swiss Nanoscience Institute (SNI), and the NCCR Quantum Science and Technology (QSIT).

---

## List of publications

---

1. G. N. Nguyen, C. Spinnler, M. R. Hogg, L. Zhai, A. Javadi, C. A. Schrader, M. Erbe, M. Wyss, J. Ritzmann, H.-G. Babin, A. D. Wieck, A. Ludwig, R. J. Warburton, *Enhanced electron spin coherence in a GaAs quantum emitter*, [arXiv:2307.02323](#) (2023).
2. K. Gawarecki, C. Spinnler, L. Zhai, G. N. Nguyen, A. Ludwig, R. J. Warburton, M. C. Löbl, D. E. Reiter, P. Machnikowski, *Structural symmetry-breaking to explain radiative Auger transitions in self-assembled quantum dots*, [arXiv:2208.12069](#) (2022).
3. L. Zhai, G. N. Nguyen, C. Spinnler, J. Ritzmann, M. C. Löbl, A. D. Wieck, A. Ludwig, A. Javadi, and R. J. Warburton, *Quantum interference of identical photons from remote GaAs quantum dots*, [Nature Nanotechnology](#) **17**, 829–833 (2022).
4. C. Spinnler, L. Zhai, G. N. Nguyen, J. Ritzmann, A. D. Wieck, A. Ludwig, A. Javadi, D. E. Reiter, P. Machnikowski, R. J. Warburton, and M. C. Löbl, *Optically driving the radiative Auger transition*, [Nature Communications](#) **12**, 6575 (2021).
5. H. G. Babin, J. Ritzmann, N. Bart, M. Schmidt, T. Kruck, L. Zhai, M. C. Löbl, G. N. Nguyen, C. Spinnler, L. Ranasinghe, R. J. Warburton, C. Heyn, A. D. Wieck, A. Ludwig, *Charge tunable GaAs quantum dots in a photonic n-i-p diode*, [Nanomaterials](#) **11**, 2703 (2021).
6. L. Zhai, M. C. Löbl, G. N. Nguyen, J. Ritzmann, A. Javadi, C. Spinnler, A. D. Wieck, A. Ludwig, and R. J. Warburton, *Low-noise GaAs quantum dots for quantum photonics*, [Nature Communications](#) **11**, 4745 (2020).
7. M. C. Löbl, C. Spinnler, A. Javadi, L. Zhai, G. N. Nguyen, J. Ritzmann, L. Midolo, P. Lodahl, A. D. Wieck, A. Ludwig, and R. J. Warburton, *Radiative Auger process in the single-photon limit*, [Nature Nanotechnology](#) **15**, 558–562 (2020).

8. S. Shutts, C. P. Allford, C. Spinnler, Z. Li, A. Sobiesierski, M. Tang, H. Liu, and P. M. Smowton, *Degradation of III-V quantum dot lasers grown directly on silicon substrates*, *IEEE Journal of Selected Topics in Quantum Electronics* **25**, 1-6 (2019).

## Clemens Spinnler

### Personal information

Email address: cspinnler@bluewin.ch  
Date of birth: 23rd May 1993  
Place of birth: Basel, Switzerland  
Citizenship: Swiss

### Education

2019 – 2023 **PhD in Experimental Physics**, University of Basel, Switzerland  
Thesis: *Exploiting phonon and Coulomb interactions in semiconductor quantum dots*  
Advisors: Prof. Richard J. Warburton, Prof. Martino Poggio

2018 **Math Teacher**, Secondary School Reinach, Switzerland

2016 – 2018 **M.Sc. in Nanosciences**, University of Basel, Switzerland  
Thesis: *Optical characterisation of p-doped 1.3  $\mu\text{m}$  InAs QD laser material grown on GaAs and on silicon substrates*, Cardiff University, Wales, UK  
Advisors: Dr. Samuel Shutts, Prof. Peter M. Smowton  
Project: *Influence of Hydrogen and catalyst composition on VA-CNT surface properties*, ETH (IBM Labs Rueschlikon)  
Advisors: Dr. Carin Lightner, Dr. Ali Altun  
Project: *Immobilization of self-assembled nanoreactors on PEG-modified magnetic  $\mu$ -particles by thiol-ene reaction*  
Advisors: Dr. Gesine Gunkel-Grabole, Prof. Wolfgang Meier

2013 – 2016 **B.Sc. in Nanosciences**, University of Basel, Switzerland

2012 – 2013 **Swiss Civil Service**, TSM School Centre for Children

- with Disabilities, WohnWerk Basel  
2007 – 2012 **Gymnasium Kirschgarten**, Basel, Switzerland  
Main subject: Physics and Mathematics  
Supplementary subject: Chemistry
- 2000 – 2007 **Primary and Orientation School**, Basel, Switzerland